

BULGARIAN CHEMICAL COMMUNICATIONS

2019 Volume 51 / Special Issue F

Selected papers presented on the Second International Scientific Conference
Alternative Energy Sources, Materials & Technologies AESMT'19,
Sofia, Bulgaria, June 3 - 4, 2019

*Journal of the Chemical Institutes
of the Bulgarian Academy of Sciences
and of the Union of Chemists in Bulgaria*

BULGARIAN CHEMICAL COMMUNICATIONS

A quarterly published by

THE BULGARIAN ACADEMY OF SCIENCES

and

THE UNION OF CHEMISTS IN BULGARIA

Volume 51, Special Issue F

ИЗВЕСТИЯ ПО ХИМИЯ

Тримесечно издание на

БЪЛГАРСКА АКАДЕМИЯ НА НАУКИТЕ

и

СЪЮЗ НА ХИМИЦИТЕ В БЪЛГАРИЯ

Том 51, Специален брой F

2019

Editor-in-Chief:

V. Beschkov

Guest editors:

A. G. Georgiev and D. B. Dzhonova-Atanasova

EDITORIAL BOARD

Ch. Bonev, L. Boyadzhiev, I. Gutzow, I. Havezov, E. Ivanova, P. Peshev, K. Petkov, K. Petrov, L. Petrov, I. Pojarlieff, S. Rakovsky, D. Stoychev, P. Petrov, D. Tsalev, D. Vladikova, D. Yankov, V. Kurteva

Members from abroad:

J. M. Albella (Spain), S. Berger (Germany), J. C. Breakman (Belgium), J. Etourneau (France), M. Farina (Italy), K. Friedrich (Germany), J. Gyenis (Hungary), A. J. Kirby (United Kingdom), T. Kowalska (Poland), K. Kutchitsu (Japan), A. Lasia (Canada), O. V. Mazurin (Russia), B. Mutaftshiev (France), E. Peter Kündig (Switzerland), S. De Rosa (Italy), T. F. Tadros (United Kingdom), K. Valko (Hungary)

The annual subscription (for 4 issues) for vol. 51 (2019) is € 160. – including postage, handling and packaging charge.

Payments should be delivered to:

*Editorial Board of Bulgarian Chemical Communications, Institute of Chemical Engineering,
Unicredit Bulbank, IBAN: BG65UNCR 7630 3400 0017 48; BIC - UNCRBGSF (for Euro €).*

Unicredit Bulbank, IBAN: BG18UNCR 9660 3119 9033 12; BIC - BACXBGSF (for local currency BGN).

BULGARIAN CHEMICAL COMMUNICATIONS

2019 Volume 51 / Special Issue F

Selected papers presented on the Second International Scientific Conference
Alternative Energy Sources, Materials & Technologies AESMT'19,
Sofia, Bulgaria, June 3 - 4, 2019

*Journal of the Chemical Institutes
of the Bulgarian Academy of Sciences
and of the Union of Chemists in Bulgaria*

PREFACE

The Second International Scientific Conference “Alternative Energy Sources, Materials & Technologies AESMT’18” was held between 3rd and 4th June 2019 in Sofia, Bulgaria. Representatives of 21 countries (Bulgaria, China, Kazakhstan, Turkey, Lebanon, Romania, United Kingdom, Spain, Serbia, Latvia, India, Belarus, Germany, Hong Kong, Italy, Norway, Poland, Russia, Slovenia, USA, Yemen) sent their works to the conference. Some of the reports (16 works) have been selected and are published after international peer-review in the present Special Issue of the journal “Bulgarian Chemical Communications”.

It is our pleasure to be guest editors of the presented articles, which focus on new international scientific results in the field of Alternative Energy Sources, Materials and Technologies (Energy Materials Science, Energy Efficiency, Biotechnologies, Solar Photovoltaic Systems, Hydrogen Energy, and Mechanical Engineering and Technologies).

Prof. Aleksandar Georgiev, PhD (European Polytechnic University, Pernik, Bulgaria)

Assoc. Prof. Daniela Dzhonova-Atanasova (Bulgarian Academy of Sciences, Sofia, Bulgaria)

Guest editors of the present Special Issue

Research of specific destruction energy of the porous coatings at power units

A. A. Genbach¹, K. K. Shokolakov¹, D. Yu. Bondartsev¹, I. K. Iliev^{2*}, A. K. Terziev³

¹ Almaty University of Energy and Communications, Faculty of Heat & Power Units

²University of Ruse, Dept. of Thermal Engineering, Hydraulics and Ecology, 8 Studentska str., 7017 Ruse, Bulgaria,
³ Technical University of Sofia, Dept. of Power Engineering and Power Machines, 8 Kliment Ohridski blvd., 1000 Sofia, Bulgaria

Methods and devices of the capillary porous system were developed for the turbine equipment of power plants. The scientific methodology of their research was established and study was carried out for the limit heat flows at metal and poor conductive porous structures as granite coatings working under joint action of gravity and capillary forces. Mathematical model is based on the thermoelasticity problem. Mechanism of the destruction process for analogy of heat exchange of poor conductive coatings of minor porosity and metal base was also described. The revealed values of specific destruction energy allow extending the critical cases in the porous system of cooling and ensuring the most suitable choice of porous coatings of minor porosity and heat conductivity.

Keywords: heat exchange, porous structure, heat power plants

INTRODUCTION

The main problem determining the development of the energy industry is the problem of uneconomic production and use of energy. One of the ways to reduce losses from external irreversibility of thermal processes in gas turbine plants is to reduce the temperature between the media. The main tendency emerging at the present stage of development of both domestic and foreign stationary gas turbine unit (GTU) is the increase of initial gas parameters before the turbine – it is this tendency that determines the steady growth of efficiency of newly designed powerful GTUs.

Application of porous materials in the steam turbine equipment has motivated many researches to develop new devices. The intensity of heat discharging systems and boosting of processes [1-2] inside them was observed. Application of porous materials apart from cooling systems help to develop devices and solve problems of explosion safety, health and durability [3-4]. It was possible to control processes of steam generation due to the excessive liquid in porous and capillary structures formed by capillary and mass forces [1-4].

At heat and power units (HPU) capillary porous materials are used for cooling highly boosted detonation burners [1], forming steam coolers in steam boilers [3], oil coolers that avoid oil and water penetration into the cooling water

and bearing system, labyrinth sealing, and other devices [4].

Previously, using the methods of photoelasticity and holography, the destruction mechanism of the porous cooling system of the fire-jet burners' combustion chambers and nozzles was investigated [1]. It is interesting to compare the intensity of heat transfer [5-7] and the surface limit state [8, 9, 12], as well as to evaluate possible mechanisms for the destruction of heating surfaces covered with capillary-porous structures [1-4]. This is in relation to the tasks of increasing the capacity of the thermal power equipment of power plants [10, 11]. Such a problem is long overdue in connection with the modernization and extension of the life of gas turbine power plants.

EXPERIMENTAL STUDY

The process of destruction of capillary-porous coatings of granite, quartz and tesenite is investigated. Coatings were applied to a heat exchange surface (metal wall) with a gas flame rocket burner at a temperature of $2500 \div 3000$ °C and a flow velocity of 2000 m/s, using a fine fraction (husk). It was obtained by treating rocks with a rocket-type burner. The porosity of the coatings was (3÷30) %. Their destruction was carried out using the torch of a thermoset burner (Fig.1).

The burner, combustion chamber and nozzle were protected by porous coatings (they simulate similar devices of gas turbines). For measurement of the heat flux, a heat receiver was used,

* To whom all correspondence should be sent:
iiliev@enconservices.com

consisting of a copper cylinder, which perceived the action of a gas jet from one end, and was cooled by water from the other.



Fig.1. General view of the experimental plant in the form of a rocket flame-jet rocket burner torch

Ceramic made of zirconium dioxide was used as an insulator. The chromel-kopel thermocouples were placed in a copper cylinder. The thermal balance mismatch did not exceed $\pm 12\%$, and the maximum relative error in determining q_i did not exceed $\pm 7\%$. The coordinate device mounted on the burner made it possible to establish a stagnation spot (spreading) of the gas stream in the area of the temperature sensor.

The most difficult part of the experiment was the ability to determine of the size of the detached particles at the time of the limiting state of the coatings. To cope with the issue a filming method using the SKS-1M camera was used (Fig.2 and Fig.3).

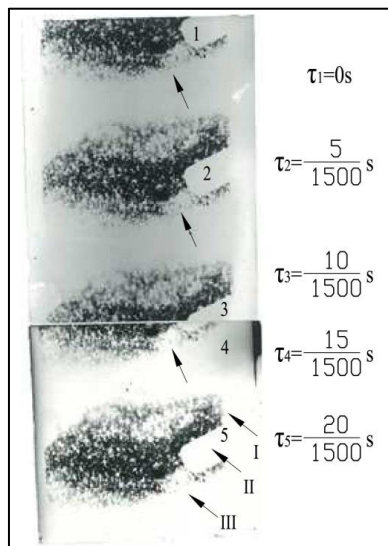


Fig.2. Record of the husk flight of size $\delta = 2,5 \cdot 10^{-3}$ m at destruction of the granite coating particle by the rocket burner ($q = 1,2 \cdot 10^6$ W/m²): I – capillary porous coating; II – trunk of burner where the supersonic high temperature pulse detonation gas flow comes from; III – particle pulled from coating

Refrigerant was supplied from the pressure tank under a slight overpressure $(0,2 \div 0,25) \cdot 10^5$ Pa. Its consumption is reduced by 60 \div 70 times, because heat removal is carried out by vaporization. Heat flow is transmitted through the walls of the chamber and the nozzle, the value of which varies widely (by one to two orders of magnitude).

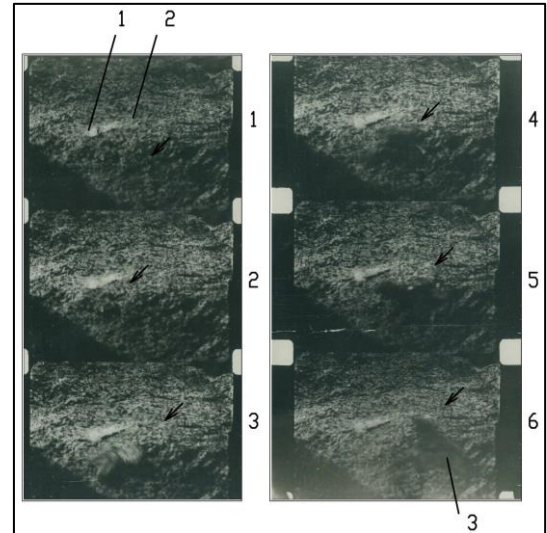


Fig.3. Fragment of a high-speed shooting of the destruction of a teshenite with a rocket flame-jet burner with a specific heat flux equal to $1,2 \cdot 10^6$ W/m². A shell with a size of $2,5 \cdot 10^{-3}$ forms for 2,2 s. A line of destruction of "equal possibilities" is clearly visible (arrow): 1 – capillary-porous coating; 2 – particle (shell) detached from the coating; 3 – line of destruction of "equal possibilities". Cinemagram of particle flight in time: τ_1 to τ_6 : 1 = 0 s; 2 = 5/1500 s; 3 = 10/1500 s; 4 = 15/1500 s; 5 = 20/1500 s; 6 = 25/1500 s

It reaches the highest value in the zone of the critical section of the nozzle. However, the self-adaptive ability of the system successfully copes with this working mode and ensures uniform distribution of the temperature field in the cooled walls. Stagnation or formation of a vapour bubble in narrow cooling channels, leading to burnout of the walls, as is the case with a once-through cooling system, is eliminated. The requirements for sealing the connection of the combustion chamber with the distribution head of the burner are reduced.

SIMPLIFIED BURNER DESIGN AND OPERATION

The capillary - porous structure is removable, for which it is enough to unscrew it from the distribution head together with the combustion chamber. In a detached form, the structure can be cleaned from mechanical and chemical deposits

and again easily installed on the burner, i.e. repeatedly restored with a minimum investment in time (several minutes). A very low water flow rate, for example $(3 \div 4) \cdot 10^{-3}$ kg / s for a TR-14/22 - 5M kerosene-oxygen burner instead of 2 kg/s, allows steam to be emitted into the atmosphere, which greatly simplifies the system and its operation.

The average particle formation time was selected as the initial parameter for frame rate and aperture size, which was assumed to be $1/50 \div 1/4000$ s depending on the heat load. The shooting speed is $250 \div 500$ frames/s, the shutter speed is $1/1250$ or $1/2500$, and the duration of the process is up to 20 s. Granulometric composition of the peel was determined by sieve analysis.

MODEL OF A CAPILLARY-POROUS COATING

Carrying out highly heat-stressed processes is associated with the occurrence of the limiting state of a heated surface. In one case, targeted destruction of the material is carried out, for example, using rocket-type fire blast burners, from whose nozzles supersonic high-temperature flows flow, and in the other, it is necessary to create a cooling system of the nozzles and combustion chambers themselves in order to avoid a heat exchange crisis and the destruction of a steam-generating surface coated with a porous structure.

-surface melting:

$$q_1 = \frac{T_f}{\frac{M}{2(c\rho\lambda)_w}\tau + \frac{2}{3M} - \frac{4}{\pi^2 M} \sum_{n=1}^{\infty} \frac{(-1)^n}{n^2} \exp\left[-n^2 \frac{\pi^2 M^2}{4(c\rho\lambda)_w} \tau\right] \cos(n\pi)} \quad (2)$$

- creation of limiting compression stresses:

$$q_2 = \frac{\frac{(1-\nu)\sigma_{comp.stress}}{\alpha E}}{\frac{M}{2(c\lambda\rho)_w}\tau + \frac{3z^2 + 6z}{h^2 + h} - 1 - \frac{4}{\pi^2 M} \sum_{n=1}^{\infty} \frac{(-1)^n}{n^2} \exp\left[-n^2 \frac{\pi^2 M^2}{4(c\lambda\rho)_w} \tau\right] \cos\left[\frac{n\pi}{z}\left(\frac{z}{h} + 1\right)\right]} \quad (3)$$

- creation of limiting tensile stresses:

$$q_3 = \frac{\frac{(1-\nu)\sigma_{tens.stress}}{\alpha E}}{\frac{M}{2(c\lambda\rho)_w}\tau} \quad (4)$$

The functional dependences of q_1 , q_2 , q_3 on time for fixed values of the particle size for the coating rock, or the penetration depth of temperature disturbances for the metal, were calculated on a PC as applied to plates made of quartz, granite, tesenite, and metal. Thermo-

To determine the critical thermal flows and stresses, the thermoelasticity problem [2] is solved under the secondary limiting conditions for the one-dimensional equation of nonstationary heat conductivity.

Let us consider a plate with the thickness of $2h$. The constant ultimate thermal flow q is supplied to the surface $z = +h$, starting from the time point $t = 0$. The bottom surface $z = -h$ and the plate side edges are thermally insulated.

Thermal conductivity equation with limiting and initial conditions can be written in the form:

$$\alpha_w \frac{\partial^2 T}{\partial z^2} = \frac{\partial T}{\partial \tau}, \quad T = 0, \quad \tau < 0;$$

$$\lambda_w \frac{\partial T}{\partial z} = q, \quad z = +h; \quad (1)$$

$$\lambda_w \frac{\partial T}{\partial z} = 0, \quad z = -h;$$

Solution to the equation (1): If we are given the limiting values of tension and compression stresses for the rock (porous coatings from the natural mineral medium) and the metal, we obtain the dependence of the thermal flow required for destruction on the time of delivery and the depth of penetration. In addition, equating the temperatures on the plate surface to the rock and metal melting temperature, we find the values of the ultimate thermal flows necessary for melting the surface layer for a different period of their action:

mechanical characteristics of rock coatings and metals are summarized in Tab.1.

The wall material influences the q_{cr} value by means of the complex $(\rho c \lambda)_w$, where ρ , c , λ is the density, heat capacity and thermal conductivity of the wall respectively, but it is not appropriate to state this unambiguously, because it is practically impossible to withstand the same conditions for processing purity and microstructure.

Table 1. Thermomechanical properties of the studied material

Material	$\rho, \text{kg/m}^3 \times 10^3$	$\alpha, 1/\text{K} \times 10^{-5}$	$C, \text{J}/(\text{kg}\cdot\text{K})$	$\lambda, \text{W}/(\text{m}\cdot\text{K})$	$T_f, ^\circ\text{C}$	ν	$E, \text{N/m}^2 \times 10^{10}$	$\bar{\sigma}_{ult.tens}, \text{N/m}^2 \times 10^6$	$\bar{\sigma}_{ult.comp}, \text{N/m}^2 \times 10^6$
quartz	2,65	1,56	1172	10,8	1788	0,17	7,3	3,92	78,5
granite	2,58	1,16	921	3,15	1230	0,22	2,8	20,5	260
tesenite	2,7	5,44	937	1,44	1140	0,27	4,97	7,6	159
copper (Cu+0,56Fe)	8,9	1,6	390	390	1100	0,34	11,8	220	1570
Stainless steel 1X18H9T	7,8	1,1	516	16	1300	0,35	21,6	700	2500

When designing the combustion chamber and especially the nozzle, it is necessary to take into account a certain margin on the thickness of the heating surface. A boiling crisis will occur earlier on thin heaters, since in the pre-crisis boiling area the size of the “dry” spot at the base of the bubbles will increase, the heat transfer process will deteriorate sharply, and the wall temperature will increase. Surfaces having a large thickness will require more time to heat them up [3].

When solving the problem of thermoelasticity for the limiting state of heat transfer, the characteristic value was the thickness of detached particles (peel) δ , and when solving the same problem (heat equation (1)) for a metal surface based on the law of similar phenomena, this quantity is the penetration depth of the heat wave, which is critical in the event of a heat transfer crisis. Since the heat fluxes from the torch are destructive, in this case they also lead to the ultimate state of the enclosing elements of the burner structure (chamber and nozzle) at the time of crisis. Thus, the law of analogy allows us to use the same heat equation (1) to solve the problem of the limiting state of coatings and heat transfer surface.

ANALYTICAL STUDY

Results from the study are shown at Fig.4 and 6. The maximum thickness of the particles detaching under the action of compression forces for coatings made of quartz and granite is $(0,25 \div 0,3) \cdot 10^{-2}$ m.

Fig.4 gives the calculation of the specific energy Q of the destruction of a granite coating volume unit. The energy Q is calculated depending on the thickness δ of the particles being detached. The curves have pronounced minima.

The range of critical values of the specific heat fluxes in the heated layer determines the limiting

and stable conduct of the cooling process at high power plant performance.

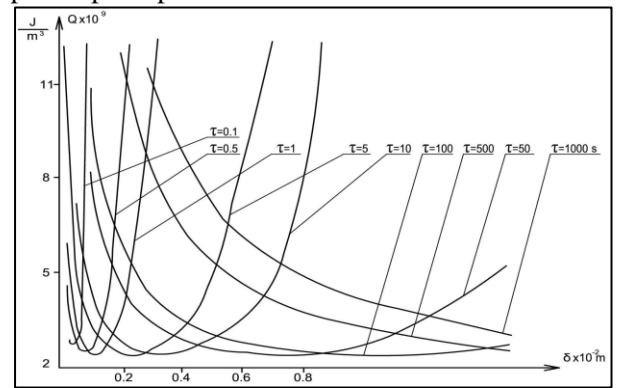


Fig.4. Change in the specific destruction energy of the granite coating Q depending on δ for different τ . $Q = q \cdot \tau / \delta$

The upper limit of the limiting values for tensile coating is not more than $0,08 \cdot 10^7 \text{ W/m}^2$, for granite - up to $0,5 \cdot 10^7 \text{ W/m}^2$, for quartz - up to 10^7 W/m^2 , and the lower limit, at which particle separation is still observed under the influence of thermal stresses of compression, for quartz coating it will be $0,25 \cdot 10^7 \text{ W/m}^2$, for granite five times less ($0,05 \cdot 10^7 \text{ W/m}^2$), and for tensitic - respectively ten times less ($0,025 \cdot 10^7 \text{ W/m}^2$). Lower specific heat fluxes will cause tensile failure of the coatings [2].

The presence of microcracks in the capillary porous system reduces the compressive strength of the coating in the vicinity of this crack so that the compressive strength can only be 2 times the tensile strength. In a continuous coating monolith, this ratio is 10 to 20 times greater.

The coating always has a fracture. Consequently, the ratio $\sigma_{lim.comp} / \sigma_{lim.tens}$ will be in the range from 2 to $10 \div 20$.

In this regard, the specific energy consumption Q will vary within certain limits, which is well illustrated by the curves (Figs. 4-6) (similar

curves are obtained for a quartz coating). Then, the previously determined limiting region q and Q for coatings of their quartz, granite, and tesenite will be between the values corresponding to the ratios $\sigma_{lim.comp.}/\sigma_{lim.tens.}$ from 2 to $10 \div 20$.

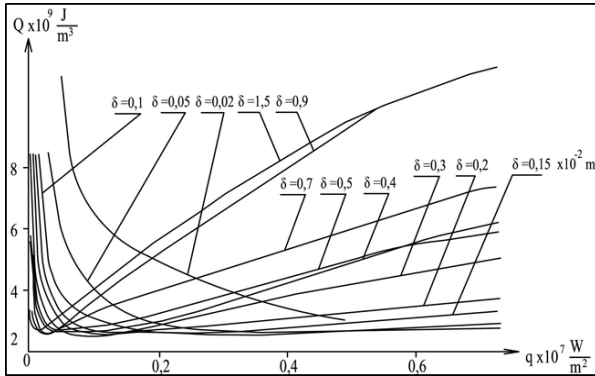


Fig.5. Change of specific destruction energy of granite coating due to q for various δ

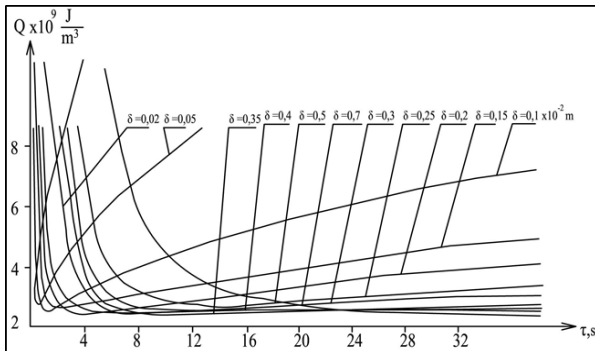


Fig.6. Change of specific destruction energy of granite coating due to τ for various δ

Since the oxygen cooler in the burners allows to develop specific heat fluxes in the stream at the main working area up to $4 \cdot 10^7 \text{ W/m}^2$ and air - up to $0,6 \cdot 10^7 \text{ W/m}^2$, which corresponds to specific heat fluxes in the coating of $0,74 \cdot 10^7 \text{ W/m}^2$ and $0,06 \cdot 10^7 \text{ W/m}^2$ - respectively, then using the proposed method, it is possible to follow the mechanism of destruction of brittle coatings from heating and to control this process.

The heated layer of rocks whilst increasing in volume, starts affecting the neighboring less heated layers. Since extension at all other directions is blocked by reaction of non-heated layers, then rocks begin freely extend at open side and due to its overextension is getting separated and broken-off.

If cavities of vacancies could transfer to dislocation, then surface under review gets plastic properties and is not destructed under influence of flame. All metals are like that. Some rocks also have these properties. Trial was carried out with

the steam generating metal surfaces of heat during the boiling crisis [1].

In terms of metals crystals are destructed under directions up to 10^{-5} V . The destruction process consists of stages of the fracture birth and their development.

Under the thermal energy impact micro fractures are born in area of stress concentrators (inclusions, discontinuity, fractures). High internal stresses also could happen due to the discontinuous process of plastic deformation, after that a fragile destruction begins. Plastic deformation is considered as the initial cause of destruction, though it can stop a growth of fractures. On one side, in centre of destruction there are ruptured links caused by heat fluctuations. On the other hand, destruction is a kinetic heat activating process which is based on transfer of vacancies towards fractures, where their growth determines destruction kinetic.

Based on the performed researches in case of irradiation by flame of the kerosene-oxygen burner of the porous coating at working area we have up to $4 \cdot 10^7 \text{ W/m}^2$, which conforms to q of coating $0,4 \cdot 10^7 \text{ W/m}^2$. Mechanism of the metal destruction differs crucially from mechanism of the rock destruction. Notwithstanding, based on analogy of the heat flow dependencies revealed from time of action and permeability depth of temperature perturbation that help avoid the boiling crisis in cooling system and ensure the most appropriate selection of porous coatings of minor porosity and heat conductivity. In future research of the other porous natural materials is required.

The danger of the appearance of limit thermal stresses is great at the moment of start-up and shutdown of power equipment at power plants. These stresses arise primarily in the places of concentrators, which are active vapour phase centres or condensate formation centres. The capillary-porous structure can be both of natural origin (salt deposits, tarnishes) and artificially created with well and poorly heat-conducting materials in a wide range of porosity and permeability of 3% to 90%. Structures can play a modelling role and serve as a high-intensity and forced cooling system. For example, teschenite porous coatings with a 5-fold greater lineal expansion coefficient and a 10-fold lower thermal conductivity factor and approximately the same melting point in comparison with energy steels serve as a modelling material. They are the most viscous with a porosity of up to 30%.

CONCLUSIONS

1. Using the heat balance method, functional dependencies have been established that describe the process of thermal destruction of capillary-porous coatings as a result of reaching tensile stresses or compression of limiting values, as well as in the case of surface melting.

2. It was found that for large heat fluxes and a short heating time, the compression curves are “screened” by the melting curve, and in the case of small heat fluxes and a significant time interval, by a tensile curve.

3. High-speed filming made it possible to determine the size of detached particles of capillary-porous coatings for the macroprocessing area. For example, for tessenite, their size was $2,5 \div 3,0$ mm with a heat flux of $1,2 \cdot 10^6$ W/m²; particle formation time – 2,2 s.

4. For quartz coating, the limits of destructive heat fluxes were $8 \cdot 10^4 \div 7 \cdot 10^7$ W/m² and for granite coating respectively $21 \cdot 10^4 \div 1 \cdot 10^7$ W/m².

5. The minimum fracture energy, for example, for a tense coating is $0,5 \cdot 10^9$ J/m³ with a heat supply time of $0,1 \div 5$ s and a particle size of $1 \div 4$ mm.

6. The described approach can be useful for modelling salt deposits, assessing the possible occurrence of fatigue cracks during commissioning, as well as in calculating capillary-porous cooling systems for turbine equipment in power plants.

NOMENCLATURE

δ – thickness of the structure (depth of wave propagation, particles size), m;
 λ – thermal conductivity, W/(m.K);
 ν – Poisson ratio (lateral contraction);
 τ – time, s;
 ρ – density, kg/m³;
 σ – stress, N/m²;
 z – coordinate, m;
 q – thermal load, W/m²;
 Q – specific crushing energy, J/m³
 T – temperature, K;
 E – Young's modulus (elasticity modulus), Pa;
 h – film height, thickness, m;
 c – thermal capacity, J/(kg.K);
 a – thermal diffusivity, m²/s;
 $2h$ – plate thickness, m;
 Q_{cr} – heat load, W/m²;
 $\sigma_{lim.stress}$ – limited tensile stress, N/m²;
 $\sigma_{lim.compr.}$ – limited compression stress, N/m²

REFERENCES

- [1] A.A. Genbach, D. Yu. Bondartsev, I. K. Iliev, Investigation of a high-forced cooling system for the elements of heat power installations, *J. of machine Eng.* **18**, 106-117 (2018).
- [2] A. A. Genbach, D. Yu. Bondartsev, I. K. Iliev, Modelling of capillary coatings and heat exchange surfaces of elements of thermal power plants, *Bulg.Chem.Comm.* **50**, 133 – 139 (2018).
- [3] A. A. Genbach, D. Yu. Bondartsev, I. K. Iliev, Heat transfer crisis in the capillary-porous cooling system of elements of heat and power installations. *Thermal Science.* **23** (2A), 849-860. (2019).
- [4] A. A. Genbach, K. K. Shokolakov, Development of an experimental plant of a non-nozzle porous foam generator for producing with foam generating and defoaming structures. News of the National Academy of Sciences of the Republic of Kazakhstan, *Series of Geology and Technical Sciences*, **3**, № 429, 300 – 308 (2018).
- [5] E. G. Shklover, Experimental study of heat transfer from porous surface in pool and forced – convection boiling at low pressures, *Phase Change Heat Transfer ASME*, **159**, 75-80 (1991).
- [6] A.S. Surtaev, V.S. Serdyukov, A.N. Pavlenko, D.V. Kozlov, D.S. Selishchev. Characteristics of boiling heat transfer on hydrophilic surface with SiO₂ coating. *Bulgarian Chemical Communications*, **50**, 36 – 44 (2018).
- [7] L.L. Tovazhnyanskyy, P.O. Kapustenko, O.A. Vasilenko, S.K. Kusakov, O.P. Arsenyeva, P.Y. Arsenyev, Mathematical model of a plate heat exchanger for condensation of steam in the presence of non-condensing gas, *Bulgarian Chemical Communications*, **50**, 76 – 82, (2018).
- [8] M. Jamialahmadi, H. Müller-Steinhagen, H. Abdollahi, A. Shariati, Experimental and theoretical studies on subcooled flow boiling of pure liquids and multicomponent mixtures, *Int. J. Heat and Mass Transfer*, **51**, (2008).
- [9] E. Krepper, B. Koncar, Yu Egorov. CFD modelling of subcooled boiling - Concept, validation and application to fuel assembly design, *Nucl. Eng. & Design* **7**, 716-731 (2007).
- [10] M. Kupetz, J. Heiew, F. Hiss, Modernization and extension of the life of steam turbine power plants in Eastern Europe and Russia, *Heat Power Engineering*, **6**, 35-43 (2014).
- [11] E. A. Grin, The possibilities of fracture mechanics in relation to the problems of strength, resource and justification for the safe operation of thermal mechanical equipment, *Heat Power Engineering*, **1**, 25-32 (2014).
- [12] [12] Z. Q. Yu, G. S. Zhou, S. D. Zhu, J. M. Li, L. J. Li, Influence of sensitizing treatment on the corrosion resistance of Incoloy 028 alloy. *Bulg. Chem. Comm.*, **49**, 4, 943 – 47 (2017).

3D computer simulation of heat and mass transfer processes to improve the energy efficiency of combustion chambers

A.S. Askarova¹⁻², S.A. Bolegenova¹⁻², S.A. Bolegenova¹⁻², R.K. Manatbayev¹, V.Yu. Maximov¹, Zh.K. Shortanbayeva¹, A.O. Nugymanova¹, A.S. Bergaliyeva^{1*}

¹Al-Farabi Kazakh National University, Faculty Physics and Technical, Almaty, ave. Al-Farabi 71, Kazakhstan

²Scientific Research Institute of Experimental and Theoretical Physics, ave. Al-Farabi 71a, 050040 Almaty, Kazakhstan
050040 Almaty, Kazakhstan

Thermal power plants are the main producers of electricity in the most countries of the world and will remain so for at least the next 50 years. To optimize the combustion of solid fuels, to develop and implement "clean" technologies and to protect the environment and ensure the efficiency of power plants, research of the complex physical and chemical processes in combustion chambers is required. It is also necessary to build adequate physical, mathematical, and chemical models and develop an accurate method for solving the system of differential equations that describes the real technological process of pulverized coal combustion. The results of 3D computer simulation make it possible to obtain data without conducting full-scale experiments, which can be used to substantiate the parameters and modes of thermal and hydro aerodynamic processes in the preparation of subsequent experimental studies on real energy facilities.

Keywords: computer simulation, heat and mass transfer, energy efficiency, combustion

INTRODUCTION

To ensure the energy efficiency of combustion chambers and reduce emissions of harmful substances into the atmosphere, it is necessary to study the problems of solid fuel combustion in heating chambers of thermal power plants (TPPs). Numerical simulation of heat and mass transfer processes in high-temperature reactive media is the main tool for theoretical study of nonlinear heat and mass transfer processes, taking into account various physical phenomena. For numerical simulation of complex physicochemical processes occurring in combustion chambers of operating TPPs, it is necessary to have: an adequate mathematical and physical-chemical model; an exact method for solving a system of differential equations that describe a real technological process of pulverized flame combustion in an existing power plant; a multiprocessor computing system [1-8].

MATHEMATICAL MODEL

Since most practical flows are turbulent, the conservation equations must be considered in averaged and time-filtered or spatial forms, which must be closed using additional turbulent models.

To formulate a mathematical model, we consider the basic equations.

The mass conservation equation can be written:

$$\frac{\partial p}{\partial t} + \frac{\partial}{\partial x_i} (p u_i) = S_i \quad (1)$$

where

S_i - the source of mass. It determines the mass added to the continuous phase and any other sources determined by a specific physical task.

The mass conservation equation or the continuity equation takes the form:

$$\frac{\partial p}{\partial t} + \frac{\partial}{\partial x_i} (p u_i) = 0 \quad (2)$$

The momentum conservation equation can be written by the Navier-Stokes equation in the form:

$$\frac{\partial (p u_i)}{\partial t} + \frac{\partial}{\partial x_j} (p u_i u_j) = - \frac{\partial p}{\partial x_i} + \frac{\partial \tau_{ij}}{\partial x_j} + \quad (3)$$

$$+ p g_i + F_i$$

The stress tensor can be expressed as:

$$\tau_{ij} = \mu \left(\frac{\partial u_i}{\partial x_j} + \frac{\partial u_j}{\partial x_i} \right) - \frac{2}{3} \mu \frac{\partial u_l}{\partial x_l} \delta_{ij} \quad (4)$$

The energy conservation equation takes into account energy transfer due to conductivity, diffusion, and viscous dissipation:

* To whom all correspondence should be sent:
bergaliyeva.saltanat@gmail.com

$$\frac{\partial(ph)}{\partial t} + \frac{\partial}{\partial x_i}(phu_i) = \frac{\partial p}{\partial t} + u_i \frac{\partial p}{\partial t} - \frac{\partial}{\partial x_i} \left(k_{eff} \frac{\partial T}{\partial x_i} \right) - \frac{\partial}{\partial x_{ij}} h_i H_j + (\tau_{ij})_{eff} \frac{\partial u_j}{\partial x_j} \quad (5)$$

where

$h = \sum_{j'} m_{j'} h_{j'}$ – heat content for ideal gases;

$h = \sum_{j'} m_{j'} h_{j'} + \frac{p}{\rho}$ for incompressible gas flows;

$h_{j'} T_{ref} C_{p,j'} dT$ – j' substance heat content of $J_{j'}$ diffusion flow;

$k_{eff} = k_l + k_t$ – effective thermal conductivity (the sum of laminar and turbulent thermal conductivity);

$(\tau_{ij})_{eff}$ – effective stress tensor;

S_h – source member, which takes into account heat from chemical reactions and other bulk energy sources (heat from radiation, convective exchange between particles and the gas phase and calorific value) [9-17].

When solving the problem, the mathematical model should include specific initial and boundary conditions for the desired functions (velocity, temperature, concentration of the mixture components, etc.) corresponding to the geometry of the selected combustion chamber and the actual technological process of fuel combustion at TPPs.

To solve the problem, the following boundary conditions for the velocity were chosen:

- Input: u_i – input velocity,
- Exit: $-\frac{\partial u_i}{\partial x_i} \Big|_{\infty} = 0$
- Symmetry plane: $u_i|_{no} = 0, \frac{\partial u_i}{\partial x_i} \Big|_{\infty} = 0$
- Hard surface: $u_i|_{no} = 0, \frac{\partial u_i}{\partial x_i} \Big|_{\infty} = 0, \frac{\partial u_i}{\partial x_i} \Big|_{no} = 0, u_i|_{ta} = 0$

The following relation was used for the friction stress on the wall:

$$\tau_W = \frac{\rho C_{\mu}^{0.25} k_{WP}^{0.5} k}{\ln[EE_{y*}]} u_{i,WP}|_{ta} \quad (6)$$

To solve the energy equation, we chose the following boundary conditions:

- Input: $h = C_p T$ – inlet flow temperature is set,
- Exit: $\frac{\partial h}{\partial x_i} \Big|_{no} = 0,$

- Symmetry plane: $\frac{\partial h}{\partial x_i} \Big|_{no} = 0, \frac{\partial h}{\partial x_i} \Big|_{ta} = 0$

On solid walls, various types of boundary conditions for temperature can be specified. For adiabatic walls, the heat flux q_w is equal to zero; in this case, boundary conditions are used as in the plane of symmetry. In the case of heat exchange between the wall and the liquid, you can set the wall temperature or heat flux. If the convective heat transfer coefficient a is experimentally or analytically determined, then we can use the condition:

$$q_W = \alpha(T_{WP} - T_W) \quad (7)$$

For the equation for the transfer of the concentration of components, the following boundary conditions can be specified:

- Input: C_p – component concentration value,
- Exit: $\frac{\partial c_{\beta}}{\partial x_i} \Big|_{no} = 0$
- Symmetry plane: $\frac{\partial c_{\beta}}{\partial x_i} \Big|_{no} = 0$
- Hard surface: $\frac{\partial c_{\beta}}{\partial x_i} \Big|_{no} = 0.$

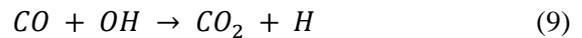
PHYSICAL-CHEMICAL MODEL

Due to the consumption of huge amounts of coal, coal-burning objects annually emit various pollutants into the atmosphere - oxides of sulfur and nitrogen, particulate matter, trace elements (including arsenic, lead, mercury, fluorine, selenium and radionuclides) and organic compounds - that can cause health problems [18-20].

Describing the process of CO formation, the combustion of volatile components, which also include CO and CO_2 , can be represented as a two-step reaction. Then the direct reaction between CO and O_2 will be:



The formed oxygen atom O does not lead to any fast chain branched reactions, but even with the minimal presence of hydrogen, OH radicals form. In this case, the formation of CO_2 occurs through the reaction:



When carbon burning, two primary direct heterogeneous oxidation reactions are possible:





As a result of the formation of CO_2 and CO , two secondary reactions can take place:

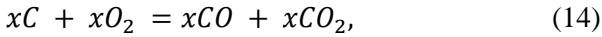
a) carbon monoxide oxidation



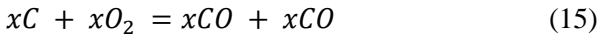
carbon dioxide reduction



The ratio between CO and CO_2 at the surface of a particle depends on the temperature of gases in this region. For example, according to experimental studies, the reaction proceeds at 1200°C:

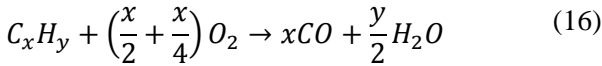


at temperatures above 1500°C, the reaction is:



CO will be formed in large amount if there is a lack of oxygen required for complete combustion, if the temperature range is not enough to fully respond CO to CO_2 , and if the residence time in the combustion zone with the appropriate temperature and sufficient oxygen content for complete combustion is not enough.

In numerical calculations, since only velocity and heat release during oxidation are in the main interest, at high temperatures and sufficient oxygen the formation of CO can be represented as a generalized reaction of hydrocarbon components with oxygen, assuming that the decomposition of the fuel molecules to CO and H_2O occurs:



The velocity of CO formation is determined by the ratio:

$$\left(\frac{d\xi_{CO}}{dt}\right) = \xi_{CO} * 10^{-3} * \left(\frac{\xi_{O_2}}{M_{O_2}}\right)^{\frac{1}{2}} * \left(\frac{\xi_{H_2O}}{M_{H_2O}}\right)^{\frac{1}{2}} * 1.3 * 10^{14} * \exp\left(-\frac{15155}{T}\right) \quad (17)$$

The expression of complete reaction, taking into account the law of Arrhenius and the entry of water vapor into the reaction, will look as follows:

$$\frac{d\bar{c}_{x,CO}}{dt} = -k_{0,co} * \bar{c}_{x,CO}^{-1.0} * \bar{c}_{x,H_2O}^{-0.5} * \bar{c}_{x,O_2}^{-0.25} * e^{-\frac{E_{\alpha,CO}}{RT_G}} * p_{gem}^{0.75} \quad (18)$$

where

$$k_{0,co} = 2.2179 \cdot 10^{12} \text{ 1/s;}$$

$$E_{\alpha,CO} = 1.6914 \cdot 10^5 \text{ kJ/kmol.}$$

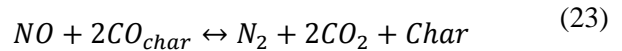
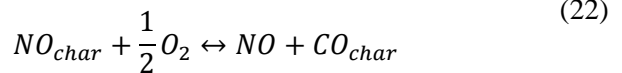
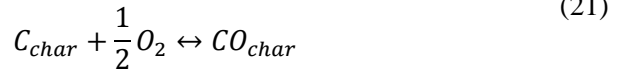
During coal combustion, nitrogen oxides are produced by dozens of species. The total amount of NO_x emissions from burning solid fuels can be described by summing up the three main identified ways of reactions: thermal NO_x , fuel NO_x , and fast NO_x .

Thermal NO_x results from the oxidation of nitrogen present in the air at high temperatures available in the combustion zone. They typically range from 20% to 50% of the total generated NO_x . For this purpose, the necessary temperatures prevail predominantly in the secondary combustion zone. Zeldovich described the oxidation of nitrogen and revealed the following mechanism:



The first reaction requires high activation energy, so it is slow at low temperatures. The burning of stable bound nitrogen N_2 requires a very high activation energy, which needs a temperature above 1200°C. Therefore, the main formation of thermal NO_x occurs in parts of the flame close to the burner, where the peak temperature of the flame is highest in combination with the available oxygen [21-25].

During the formation of fuel NO_x , fuel-bound organic nitrogen reacts with existing hydrocarbons (C_xH_y). Organic nitrogen, which is chemically bound to fuel, is the main source for total NO_x emissions from coal flame. The production of nitrogen oxides NO and molecular nitrogen N_2 can form either as a homogeneous gas phase reaction or as a result of a heterogeneous reaction that includes the surface of the char. In this regard, the most important reactions on the surface of coke are described by the following reaction equations:



In order to implement the mechanism of fast NO_x formation, bound nitrogen reacts with hydrocarbons or available hydrocarbon fragments, which are formed as a result of thermal

decomposition in a reducing atmosphere. There is another chemical mechanism of rapid NO_x at temperatures of 1600-2100°C. Formation is initiated by various fragments of hydrocarbon fuels, such as CH and CH_2 , which appear during the release of volatile substances. Molecular nitrogen is attacked by these hydrocarbons. Fenimore [26] described this phenomenon as follows:



This reaction takes place mainly in fuel-rich areas where hydrocarbon radicals increase the formation of HCN using the following reactions:



Nitrogen is oxidized in the composition of the fuel and becomes oxides of nitrogen NO_x when burned, as well as fuel NO_x , and HCN is oxidized to NO depending on conditions. A significant part of nitrogen compounds is formed during the fast mechanism of conversion to diatomic nitrogen (N_2) inside the boiler. It is assumed that part of the rapid NO_x is less than 5% of the total amount of NO_x generated during coal combustion.

Thus, nitrogen oxides are formed as a result of atmospheric nitrogen oxidation at high temperatures (thermal NO_x) and the oxidation of fuel nitrogen compounds (fuel NO_x). In the case when hydrocarbon components in the flame zone react with nitrogen with the appearance of a nitrogen atom, forming NO , fast NO_x are formed [27-33].

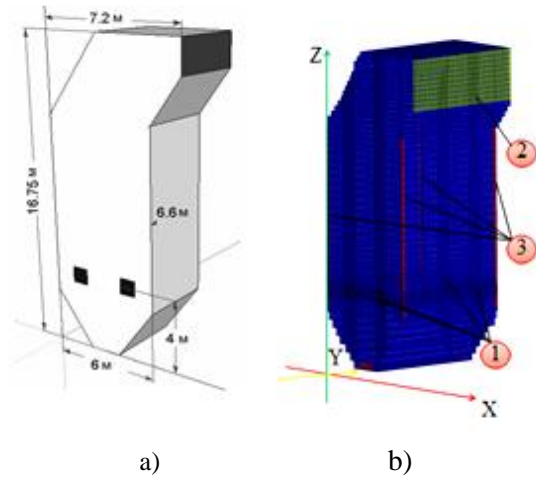
COMPUTATIONAL EXPERIMENTS

The boiler chamber BKZ-75 of the Shakhtinsk TPP operated in the Karaganda region was selected as the object of research [34-35].

To carry out computational experiments, the geometry of the research object was constructed according to a real scheme, and its finite-difference grid was compiled for numerical simulation of solid fuel combustion in the combustion chamber of the BKZ-75 boiler. The finite-difference grid has steps along the X, Y, Z axes: $59 \times 32 \times 67$, which is 126.496 control volumes (Fig.1).

Figs.2-6 show the aerodynamic characteristics of the process (distribution of the total velocity along the height of the furnace, three-dimensional distributions of the total velocity vector in longitudinal and cross sections of the combustion

chamber, at the exit from it, and in the region of the rotating chamber).



1- burners, 2-chamber outlet area, 3-suction cups; X-width of the furnace, Y-depth of the furnace, Z-height of the combustion chamber

Fig.1. General view of the boiler BKZ-75 of the Shakhtinsk TPP (a) and its discretization for control volumes (b)

Fig.2 shows the curves of the maximum, minimum and average values of the full velocity vector along the height of the combustion chamber of the BKZ-75 boiler. It clearly shows the region of maximum values (~ 20 m/s) of the flow velocity, which falls on the places where the burner devices are installed ($Z = 4$ m), from which an air mixture is injected with the primary air.

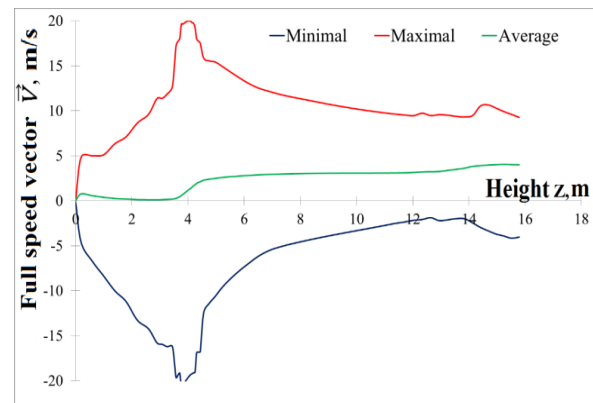


Fig.2. Distribution of full velocity at the height of the combustion chamber of the boiler BKZ-75 Shakhtinsk TPP

From the analysis of Fig.2 that as the flow of the air mixture and combustion products moves towards the exit, the velocity monotonously decreases, except for the turning area ($Z=14.6$ m) of the boiler combustion chamber, where its surge is observed. This is due to the fact that at this height the geometry of the combustion chamber

changes, and the flow, due to a change in its direction, becomes unsteady, forming an additional vortex, increasing the flow turbulence, which leads to a velocity change in this area of the furnace space.

Fig.3 shows the three-dimensional distributions of the full velocity vector over the cross sections: longitudinal sections of the first and second pair of burners ($X = 1.76$ and 4.22 m); in cross section at the outlet of the furnace ($X=7$ m); longitudinal radial-central section ($Y=3.19$ m); in the cross section of the burner area ($Z=4$ m) and in the turning area ($Z=12.65$ m). From the analysis of Fig.3, it can be said that the flow of the air mixture with combustion products has a vortex character in the region of the burners and in the lower part of the combustion chamber at a height of Z from 2 m to 8 m. It can be seen that the full velocity vector has its maximum values (~ 16 m/s) in the region of the burner (Fig.3a).

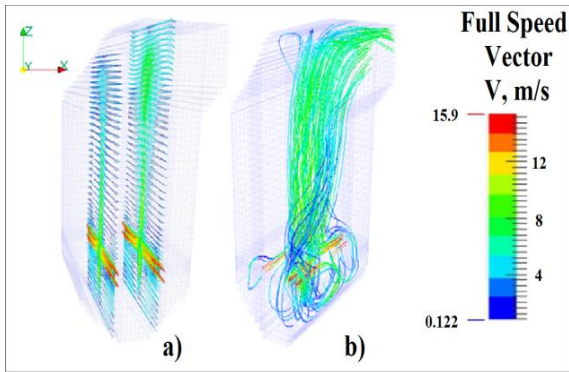


Fig.3. Three-dimensional distribution of the overall velocity in longitudinal sections ($X = 1.76$ and 4.22 m) and over the volume of the combustion chamber of the boiler BKZ-75 of the Shakhtinsk TPP

This is explained by the fact that the countercurrent flows injected from the burner devices, heading towards the center of the furnace space, with maximum velocity, collide. And here, dissipating into several whirlwinds, they form a reverse flow up and down (Fig.3b) along the heating space. Such a nature of vortices arises due to turbulence due to the interaction of the air mixture with the oxidizing agent. Above $Z=8$ m in height, towards the exit from the furnace space, there is a gradual smoothing of the currents, the velocity of which lies in the range of $4-8$ m/s.

Fig.4 shows the three-dimensional distribution of the full velocity vector over the depth of the combustion chamber ($Y=3.19$ m) in its central region. In the figure you can see how the threads collide in the center of the furnace, here the velocity is greatest. A part of the flows with maximum velocity (about 11 m/s) descends to the

area of the cold funnel, forming eddy currents, and the other part goes up to the exit from the combustion chamber.

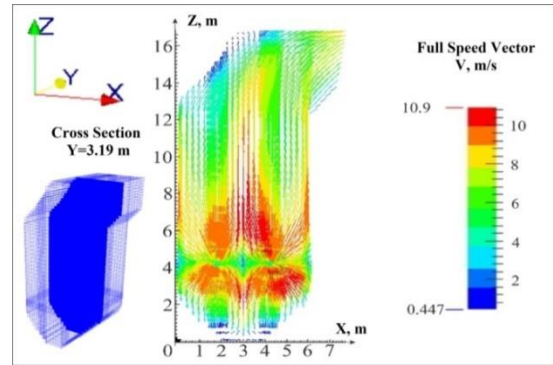


Fig.4. Three-dimensional distribution of the full-velocity vector in the longitudinal central section over the depth of the combustion chamber ($Y=3.19$ m) of the BKZ-75 boiler at the Shakhtinsk TPP

Fig.5 shows the aerodynamics of the flow in cross section in the area of the burners ($Z=4$ m), it can be seen that some flow symmetry is preserved, which confirms the distribution of the full velocity over the height of the combustion chamber (Fig.2).

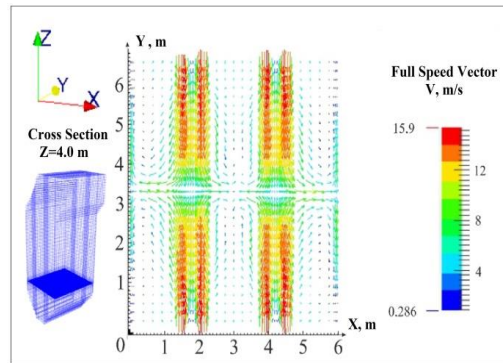


Fig.5. Three-dimensional distribution of the full velocity vector in the cross section in the burner area of the combustion chamber ($Z = 4$ m) of the BKZ-75 boiler at the Shakhtinsk TPP

Fig.6 shows the field of the overall velocity in the area of the rotating chamber ($Z=12.65$ m) and in the outlet section ($X=7$ m) from the boiler combustion chamber. Analysis of Fig.6 shows that as the turbulent flow moves towards the exit from the combustion chamber, the vortex nature of the flow weakens, then it increases in the region of the rotating section of the boiler and an almost uniform velocity profile is observed at the exit from the chamber.

It is noticeable that in the cross section of the furnace's turning area the maximum velocity (9 m/s) are concentrated in the central part and in the near-wall area, which to some extent can be

explained by the asymmetric geometry of the furnace in this area. At the exit from the furnace space, the velocity is practically equalized, no mixing of the flows is observed and its average value is ~ 4 m/s.

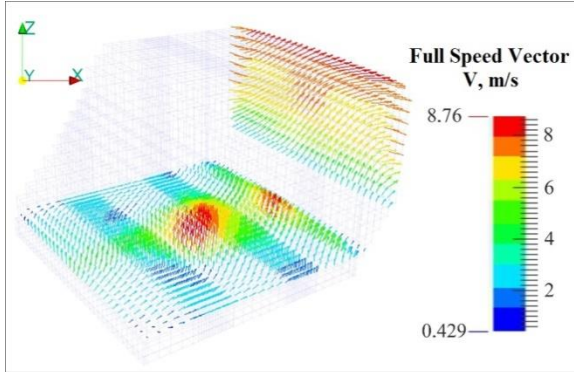


Fig.6. Three-dimensional distribution of the full velocity vector in the rotary region of the combustion chamber ($Z = 12.65$ m) and at the exit from the furnace ($X = 7$ m) of the BKZ-75 boiler at the Shakhtinsk TPP

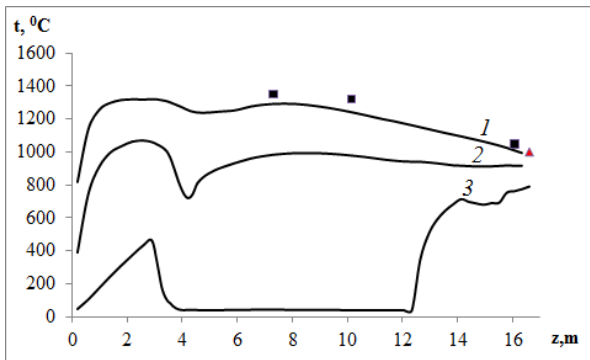


Fig.7. Distribution of the temperature T along the height of the combustion chamber of the BKZ-75 boiler: 1-maximum; 2-average; 3- minimum;

■ - experimental data at TPPs [36]; ▲ - is theoretical values obtained by the method of thermal calculation (CBTI – Central Boiler-and-Turbine Institute) [37]

The analysis of the curves in Fig.7 shows that the behavior of the temperature curves and the measured temperature values coincide qualitatively, however, the experimental data have higher values in the torch region, as well as at the outlet from the furnace space. The temperature at the outlet of the combustion chamber (base version) is confirmed by experimental data at TPPs and theoretical value calculated by the method of CBTI (Central Boiler-and-Turbine Institute) for direct-flow supplying of air mixture [37].

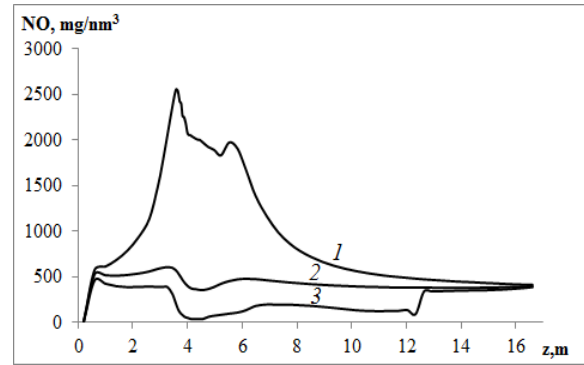


Fig.8. Distribution of concentration nitrogen oxide NO along the height of the combustion chamber of the BKZ-75 boiler: 1-maximum; 2-average; 3- minimum

Fig.8 shows the distribution curves of the maximum, minimum and average values of the concentrations of nitrogen oxide NO over the height of the combustion chamber of the boiler BKZ-75. From the analysis of the figure it is seen that the maximum values of the concentration of nitrogen oxide NO are in the area of the burners. This is due to the fact that in the studied problem, coal dust combustion occurs at a temperature of 1000-1700K; therefore, the main source of formation of nitrogen oxides is nitrogen NO contained in the fuel.

At the outlet nitrogen oxide NO concentrations are less than the maximum permissible concentration (MPC) accepted in Kazakhstan. Thus, we can conclude that the vortex method of supplying air mixtures in the combustion chambers of energy boilers significantly improves the environmental performance of thermal power plants.

CONCLUSIONS

- Using modern numerical 3D computer simulation methods, the research of thermal processes, aerodynamic and concentration characteristics of the combustion chamber of the boiler BKZ-75 of the Shakhtinsk TPP (Kazakhstan) were carried out.
- Physical and chemical processes were investigated during the combustion of high-ash energy fuel in the combustion chamber of an industrial energy facility, taking into account the main stages of coal combustion, the formation and destruction of harmful dust and gas emissions.
- Geometric and technical characteristics for 3D computational experiments on the combustion of low-quality high-ash Kazakhstan coal in the combustion chambers of existing power plants were determined. A program Preproz for introducing the initial parameters for conducting

3D computational experiments on the combustion of high-ash coal was created. The chemical composition of low-quality high-ash Karaganda coal has been studied.

ACKNOWLEDGEMENTS

The Ministry of Education supported this work and Science of the Republic of Kazakhstan (grants AP05132988, AP05133590 and BR05236730).

REFERENCES

- [1] V. Maximov, P. Safarik Investigation of heat and mass transfer processes in the combustion chamber of industrial power plant boiler. Part 2. Distribution of concentrations of O₂, CO, CO₂, NO. *Journal Applied and Computational Mechanics* **12**, 127-138 (2018).
- [2] H. Muller, R. Leithner Combustion of low-rank coals in furnaces of Kazakhstan coal-firing power plants. *VDI Berichte*, 497-502 (2007).
- [3] V.E. Messerle, A.S. Askarova, A.B. Ustimenko Reduction of noxious substance emissions at the pulverized fuel combustion in the combustor of the BKZ-160 boiler of the Almaty heat electro power station using the "Overfire Air" technology. *Thermophysics and Aeromechanics* **231**, 125-134 (2016).
- [4] K.S. Baktybekov, S.A. Bolegenova, A.B. Syzdykov Investigation of the different Reynolds numbers influence on the atomization and combustion processes of liquid fuel. *Bulgarian Chemical Communications* **50**, 68-77 (2018).
- [5] A. Georgiev, Zh.T. Baizhuma, A.O. Nugymanova The use of a new "clean" technology for burning low-grade coal in on boilers of Kazakhstan TPPs. *Bulgarian Chemical Communications* **50**, 53-60 (2018).
- [6] M. Buchmann, A. Askarova. Structure of the flame of fluidized-bed burners and combustion processes of high-ash coal. *Proceedings of 18th Dutch-German Conference on Flames, VDI Berichte* **1313**, 241-244 (1997).
- [7] I.V. Loktionova, V.E. Messerle, A.B. Ustimenko 3D Modeling of the two-stage combustion of ekibastuz coal in the furnace chamber of a PK-39 Boiler at the Ermakovo district power station. *Journal Thermal Engineering* **50**, 633-638 (2003).
- [8] Sh. Ospanova, R. Manatbayev, N. Mazhrenova 3D modelling of heat and mass transfer processes during the combustion of liquid fuel, Proceedings of 15th International Scientific Conference on Renewable Energy and Innovative Technologies, Tech Coll Smolyan, Smolyan, Bulgaria. *Bulgarian Chemical Communications* **48**, 229-235 (2016).
- [9] R. Leithner, H. Muller, A. Askarova CFD code FLOREAN for industrial boilers simulations. *WSEAS Transactions on Heat and Mass Transfer* **4**, 98-107 (2009).
- [10] S.A. Bolegenova, E.I. Heierle CFD study of harmful substances production in coal-fired power plant of Kazakhstan. *Bulgarian chemical communications* **48**, 260-265 (2016).
- [11] V.E. Messerle, A.S. Askarova, Yu.V. Maximov 3D-modelling of Kazakhstan low-grade coal burning in power boilers of thermal power plant with application of plasma gasification and stabilization technologies. *Journal of Physics: Conference Series* **1261-1**, 12-22 (2009).
- [12] M. Beketayeva, Z. Gabitova, A. Bekmukhamet Control harmful emissions concentration into the atmosphere of megacities of Kazakhstan Republic. *Int. conf. on Future Information Engineering, Beijing, Peoples China* **10**, 252-258 (2014).
- [13] A.S. Askarova, P. Safarik, M.T. Beketayeva Modern computing experiments on pulverized coal combustion processes in boiler furnaces. *News of the national academy of sciences of the Republic of Kazakhstan-series Physico-mathematical* **6-322**, (2018).
- [14] Z. Gabitova, A. Yergaliyeva, Zh. Shortanbayeva Simulation of the aerodynamics and combustion of a turbulent pulverized-coal flame. *Proc. of 4th Int. Conf. on Mathematics and Computers in Sciences and in Industry (MCSI 2017). Corfu Island, Greece*, 92-97 (2017).
- [15] A.S. Askarova, S.A. Bolegenova, Sh.S. Ospanova Investigation of aerodynamics and heat and mass transfer in the combustion chambers of the boilers PK-39 and BKZ-160. *News of the national academy of sciences of the Republic of Kazakhstan-series physico-mathematical* **2-312**, 27-38 (2017).
- [16] S. Bolegenova, A. Askarova, ZhK Shortanbaeva Numerical modeling of burning pulverized coal in the combustion chamber of the boiler PK 39. *News of the national academy of sciences of the Republic of Kazakhstan-series physico-mathematical* **2-312**, 58-63 (2017).
- [17] A. Bekmukhamet, Z. Gabitova, S. Ospanova Using 3D modeling technology for investigation of conventional combustion mode of BKZ-420-140-7C combustion chamber. *J. of Engineering and Applied Sciences* **9-1**, 24-28 (2014).
- [18] V.Yu. Maximov, S.A. Bolegenova, A. Bekmukhamet Mathematical simulation of pulverized coal in combustion chamber. *Procedia Engineering* **42**, 1150-1156 (2012).
- [19] I.V. Loktionova, E.I. Karpenko, V.E. Messerle Optimization of the combustion of power station coals using plasma technologies. *J. Thermal Engineering* **51-6**, 488-493 (2004).

- [20] S.A. Bolegenova, S. Ospanova, Z. Gabitova Investigation of turbulence characteristics of burning process of the solid fuel in BKZ 420 combustion chamber. *WSEAS Transactions on Heat and Mass Transfer* **9**, 39-50 (2014).
- [21] S.A. Bolegenova, V.Yu. Maximov, A. Bekmuhamet Mathematical simulation of pulverized coal in combustion chamber. *Procedia Engineering* **42**, 1250-1259 (2012).
- [22] R. Leithner, A. Ergalieva, A. Nugymanova Computational modeling of heat and mass transfer processes in combustion chamber at power plant of Kazakhstan. *MATEC Web of Conferences* **5**. (2016).
- [23] A. Chtab-Desportes, M. Gorohovski, I. Voloshina Stochastic simulation of the spray formation assisted by high pressure. *AIP Conference Proceeding* **1207**, 66-73 (2010).
- [24] A.N. Aldiyarova, S. Bolegenova, A.E. Boranbayeva Mathematical modeling of heat and mass transfer in the presence of physical chemical processes. *Bulgarian Chemical Communications* **48**, 272-277 (2016).
- [25] J. Zeldovich The oxidation of nitrogen in combustions and explosions. *J. Acta Physicochemica* **21**, 557-628 (1946).
- [26] C.P. Fenimore Formation of nitric oxide in premixed hydrocarbon flames. *Symposium (International) on Combustion - Elsevier* **13-1**, 373-380 (1971).
- [27] P. Safarik, V.Yu. Maximov, S.A. Bolegenova 3D modeling of combustion thermochemical activated fuel. *News of the national academy of sciences of the Republic of Kazakhstan-series physico-mathematical* **2-324**, 9-16 (2019).
- [28] A.S. Askarova, S.A. Bolegenova, M.T. Beketayeva Numerical modeling of turbulence characteristics of burning process of the solid fuel in BKZ-420-140-7c combustion chamber. *Int. J. of Mechanics* 343-352 (2013).
- [29] Sh.S. Ospanova, V.Yu. Maximov, R.K. Manatbayev The computational study of heat and mass transfer processes at combustion of pulverized Kazakh coal in real conditions of energy objects. *Bulgarian Chemical Communications* **50**, 61-67 (2018).
- [30] H.Muller Numerische Berechnung Dreidimensionaler Turbulenter Strömungen in Dampferzeugern Mit Wärmeübergang und Chemischen Reaktionen am Beispiel des SNCR-Verfahrens und der Kohleverbrennung. *Fortschritt-Berichte VDI-Verlag*. **6-268**, 158. (1992).
- [31] Sh. Ospanova, S. Bolegenova, A. Ergalieva 3D modeling of heat and mass transfer during combustion of solid fuel in BKZ-420-140-7C combustion chamber of Kazakhstan. *J. of Applied Fluid Mechanics* 699-709 (2016).
- [32] A.S. Askarova, S.A. Bolegenova, M.T. Beketayeva Modeling of heat mass transfer in high-temperature reacting flows with combustion. *J. High Temperature* **56-5**, 738-743 (2018).
- [33] M.T. Beketayeva A.S. Askarova, S.A. Bolegenova 3D modeling of the aerodynamics and heat transfer in the combustion chamber of the BKZ-75 boiler of the Shakhtinsk cogeneration plant. *Thermophysics and Aeromechanics* **26-2**, 295-311 (2019).
- [34] P. Safarik, S. Bolegenova, A. Nugymanova Simulation of low-grade coal combustion in real chambers of energy objects. *J. Acta Polytechnica* **59-2**, 98-108 (2019).
- [35] P. Safarik, M. Beketayeva, V. Maximov Numerical modeling of pulverized coal combustion at thermal power plant boilers. *Journal Thermal Science* **24-3**, 275-282 (2015).
- [36] B.K. Alijarov, and M.B. Alijarova Combustion of Kazakh coals in thermal power stations and large-power boiler houses, Almaty, (2011).
- [37] Thermal calculation of boilers (normative method). Publishing House AOOT "NCPO Central Boiler-and-Turbine Institute", (1998).

Numerical simulation of turbulent combustion of pulverized coal flame

A. S. Askarova¹, S. A. Bolegenova¹, V. Yu. Maximov², S. A. Bolegenova², N. R. Mazhrenova¹,
Zh. K. Shortanbayeva¹, R. K. Manatbayev^{1*}, M. R. Mamedova¹

¹Al-Farabi Kazakh National University, Faculty Physics and Technical, Almaty, ave. Al-Farabi 71, Kazakhstan

²Scientific Research Institute of Experimental and Theoretical Physics, ave. Al-Farabi 71a, 050040 Almaty, Kazakhstan

The increased demand for solid fuels is accompanied by the need to reduce emissions of pollutants into the atmosphere and to increase the efficiency of fuel combustion process. Thus, research in the field of advanced technologies to improve pulverized coal combustion plants and the use of alternative methods of organizing the combustion process of various types of fuel are currently the most relevant for the entire energy sector of the Republic of Kazakhstan. The main direction in improving pulverized coal combustion and the use of alternative fuels is to meet stringent environmental requirements for specific emissions of harmful substances with exhaust gases, for which there are standards defined.

Keywords: combustion, coal, combustion chamber, boiler, burners, fuel

INTRODUCTION

The fundamental and applied prospects of the tasks that are proposed for solution in this paper are determined by the prevalence of turbulent flows in nature and technology, as well as the difficulty of their experimental and theoretical research. The prospectivity of the proposed research lies in updating the tasks associated with the development of numerical methods as applied to the study of complex practical problems. The practical value of the study is determined by the universality of the proposed research method, which can be widely used at various energy facilities of the Republic of Kazakhstan.

JUSTIFICATION OF RESEARCH TASK

Along with the energy consumption growth, the environmental danger is progressively increasing due to the emissions of harmful substances and industrial waste, which resulted in the development of the Kyoto Protocol that established quotas for these emissions and penalties for their violation.

To solve the problems of modern power engineering and ecology it is especially important to study the processes of heat-and-mass transfer in the high-temperature reacting media and to simulate physical and chemical processes that occur during the combustion of pulverized coal. These problems are related, on the one hand, to the concept of “energy safety” of the country and, on

the other hand, to the development of processes of “clean” fuel combustion under strict standards of emission of harmful substances into the environment.

In the conditions of depletion of natural power resources and environmental pollution, implementation of technological processes with the rational use of fossil fuels, increase in the efficiency of energy generation and solution of environmental problems are actual and important tasks [1-5].

Expensive experimental studies on reduced fire models do not strictly comply with all the conditions that correspond to the actual combustion process, as it is necessary to achieve the geometrical and physical resemblance of the objects and to observe basic parameters and operation conditions corresponding to the technological combustion scheme used at the real power facility.

Theoretical investigations of heat-and-mass transfer in the presence of physical and chemical transformations in moving high-temperature responsive environment also cannot answer all the questions. This is because such flows are described by a complex system of non-autonomous nonlinear multidimensional partial differential equations. That corresponds to the transfer of momentum, distribution of heat, components of the reaction mixture and the reaction products, which must take into account a considerable turbulence, multi-phase medium and source terms related to chemical kinetics of the processes.

Analytical solutions of this complex system of equations have not yet been found, and they can be

* To whom all correspondence should be sent:
rustem1977@mail.ru

solved only numerically. Recently, the main methods used to study such processes, particularly in the areas of real geometry, are the methods of numerical modeling and on their basis numerical experiments that adequately reflect the actual physical processes occurring in the combustion chambers. Progress in the development of computational models, in the creation of efficient computational algorithms and problem-oriented software packages allows us to solve many problems that are of great practical application in various industries [6-10].

Therefore, it is important to carry out a comprehensive study of physical and chemical processes of heat transfer in the high-temperature environment. This study will be based on the achievements of modern thermal physics, the use of new numerical methods of 3D modeling, construction of efficient computational algorithms and new computational models that enable scientists to describe with high degree of accuracy real physical processes that occur during combustion of power-plant fuels in the combustion chambers of operating power stations.

It should be noted that more than 80% of all energy produced in the world is produced by burning fossil fuels. Other sources of energy: nuclear power, hydropower, solar and wind power plants in the coming decades will not be able to compete with traditional methods of its production.

The limited fossil fuels resources necessitate the search for more cost-efficient methods of its combustion, while the scale of industrial production is such that the problem of generation of harmful substances during combustion comes to the fore.

Combustion of pulverized coal has the greatest environmental impact: toxic and greenhouse gases, particulate matter, waste and seepage water, slag waste ash, heat waste and much more. Moreover, the development of the energy complex is associated with a large-scale transformation of environmental components, the negative effects of which can manifest for a long time. Coal pits change the topography and form specific soil conditions in dumps, hydroelectric reservoirs cause changes in seismicity, flood the most productive valley ecosystems, and change the landscape structure of the regions [11-15].

Coal industry of Kazakhstan is one of the largest sectors of the country's economy. Today, coal industry of the republic provides 80% of electricity in Kazakhstan. In terms of proven coal reserves, Kazakhstan ranks 8th in the world and contains 4% of the global reserves in its depths. The most

valuable for industry power and coking coals are concentrated in 16 deposits [16-21]. Coal reserves of are estimated at 75 billion tons. The Republic of Kazakhstan is among the ten largest coal producers in the world market, ranks third in terms of reserves and production among the CIS countries, and is first in terms of coal mining per capita.

The main power plant coals of Kazakhstan are mined by open-pit method, resulting in their low cost. Coal of Kazakhstan is a cheap energy fuel, and its reserves will be sufficient for many hundreds of years. However, it should be noted their low sulfur and low nitrogen content (less than one percent). Nevertheless, Kazakhstan's coal, being a good energy fuel for its reactivity, have one big disadvantage - high ash content. The ash content of coal supplied from separate Kazakhstan's fields to CHP plants sometimes exceeds 70%. While in the UK it is 22% in accordance with the law, 9% in the USA, and 8% in Germany [22].

Many of Kazakhstan's CHP plants primarily use cheap high-ash Ekibastuz coal, which is mined by open-pit method. The adopted coal mining technology and its use without prior enrichment leads to a considerable anthropogenic pressure on the ecosystem. The ash component of coal is a mixture of minerals that are in a free state or are associated with fuel.

BASIC EQUATIONS OF THE MATHEMATICAL MODEL

The problem of modeling is very complex, as it involves the interaction of turbulent combustion of many chemical components with multiphase processes (particles of gaseous or solid fuel and carbon in the flow field) and with radiant heat transfer.

During particles combustion, it is necessary to take into account the rates of heterogeneous reactions and it is required to know particles distribution by sizes and in space. Emission of pollutants, such as hydrocarbons, soot and nitrogen oxides, can be reduced by appropriately controlling temperature and concentration changes patterns in the combustion area.

For three-dimensional fluid motion with variable physical properties, the field of velocity, temperature and concentration is described by a differential equations system (1 - 4)

a) The continuity equation:

$$\frac{\partial \rho}{\partial t} = - \frac{\partial}{\partial x_i} (\rho u_i), \quad (1)$$

b) The equation of motion:

$$\frac{\partial}{\partial t}(\rho u_i) = -\frac{\partial}{\partial x_j}(\rho u_i u_j) + \frac{\partial}{\partial x_j}(\tau_{i,j}) - \frac{\partial \rho}{\partial x_j} + \rho f_i, \quad (2)$$

Here: f_i – volume forces; u_i – components of velocity, m/s; $\tau_{i,j}$ – viscous stress tensor.

d) The energy equation:

$$\frac{\partial}{\partial t}(\rho h_i) = -\frac{\partial}{\partial x_i}(\rho u_i h) - \frac{\partial q_i}{\partial x_i} + u_i \frac{\partial \rho}{\partial x_i} + \tau_{ij} \frac{\partial u_j}{\partial x_i} + S_q \quad (3)$$

Here: h – enthalpy; q_i – energy flux density due to molecular heat transfer, S_q – energy source.

c) Conservation law for a component of a substance:

$$\frac{\partial}{\partial t}(\rho c_\beta) = -\frac{\partial}{\partial x_i}(\rho c_\beta u_j) + \frac{\partial}{\partial x_i} R_\beta, \quad (4)$$

where $I = 1,2,3$; $j = 1,2,3$; $\beta=1,2,3,\dots,N$; R_β – source of substance.

To model turbulent viscosity, the well-known k - ε turbulence model was used. Consisting of the equation of conservation of the kinetic energy of turbulence k , its dissipation rate ε and the model relation for turbulent viscosity. The k - ε turbulence model is the standard model for forced and natural convection flows.

a) The standard k - ε turbulence model:

$$\frac{\partial(\overline{\rho k})}{\partial t} = -\frac{\partial(\overline{\rho u_j k})}{\partial x_j} + \frac{\partial}{\partial x_j} \left[\frac{\mu_{eff}}{\sigma_k} \frac{\partial k}{\partial x_j} \right] + P - \rho \varepsilon, \quad (5)$$

Where P is the production of kinetic energy of turbulence, which is determined by the following relation:

$$P = \left[\mu_{turb} \left(\frac{\partial \overline{u_i}}{\partial x_j} + \frac{\partial \overline{u_j}}{\partial x_i} \right) \right] \frac{\partial \overline{u_i}}{\partial x_j} - \left[\frac{2}{3} \rho k \delta_{ij} \right] \frac{\partial \overline{u_i}}{\partial x_j} \quad (6)$$

and the equation for the dissipation of turbulent kinetic energy ε :

$$\frac{\partial(\overline{\rho \varepsilon})}{\partial t} = -\frac{\partial(\overline{\rho u_j \varepsilon})}{\partial x_j} + \frac{\partial}{\partial x_j} \left[\frac{\mu_{eff}}{\sigma_\varepsilon} \frac{\partial \varepsilon}{\partial x_j} \right] + C_{\varepsilon,1} \frac{\varepsilon}{k} P - C_{\varepsilon,2} \frac{\varepsilon^2}{k} \rho, \quad (7)$$

Here, is the conversion of the kinetic energy of the pulsating motion into internal energy (dissipation).

Initial conditions: $u = 0$, $v = 0$, $w = 0$, $P = 0$, at $t = 0$.

The boundary conditions must be set on the free surfaces, which are the burners, the exit from the combustion chamber of the boiler and the plane of symmetry.

For velocity, we set the values of its normal and tangential component and their gradient:

At the input: u_i – velocity values at the inlet.

At the output: $\frac{\partial u_i}{\partial x_i} \Big|_{\text{ino}} = 0$, in the plane of symmetry: $u_i \Big|_{\text{ino}} = 0$, $\frac{\partial u_i}{\partial x_i} \Big|_{\text{ino}} = 0$.

PHYSICAL STATEMENT OF PROBLEM

The computing experiment in the work was carried out for the combustion chamber of the BKZ-160 boiler at Almaty Thermal Power Plant (Kazakhstan), with a steam capacity of 160 t/h, a pressure of 9,8 MPa and a superheating temperature of 540°C.

Steam heating capacity $Q = 119,5$ MW (97,8 Gcal/h), thermal power of the furnace $N = 124,4$ MW (107 Gcal/h). The boiler is designed to burn coal.

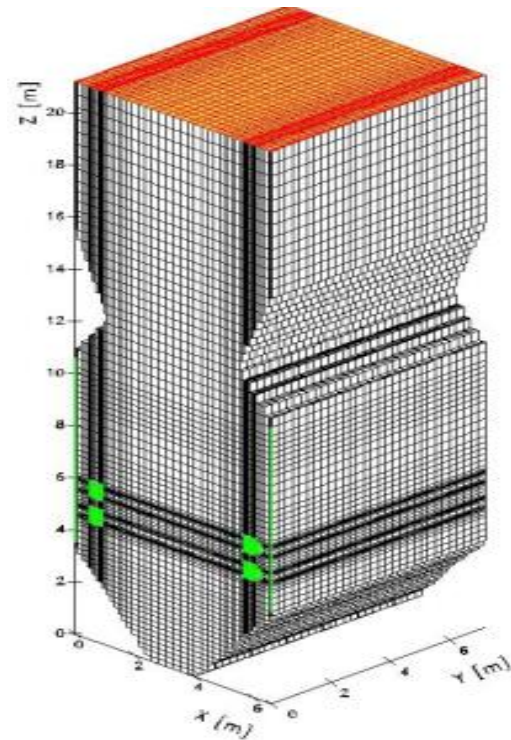


Fig.1. General view of the combustion chamber of the boiler BKZ-160 and its breakdown into control volumes

There are 4 blocks of direct-flow slot burners (2 burners per block), directed tangentially to a circle with a diameter of 60x4 with a step of 64 mm on the sides of the furnace chamber. The screens are divided into 12 separate circulation circuits. Front and rear screen pipes form a cold funnel in the bottom part, while in the upper part the rear screen pipes are bent into combustion chamber, forming an "aerodynamic" nose. After the "aerodynamic" nose the rear screen pipe run into chambers, from where steam-water mixture is sent to the boiler drum through the slag screen.

A radiation-convective steam superheater is installed on the boiler. The radiation part of the super-heater is made in the form of screen heating surfaces located behind the aerodynamic nose, and ceiling superheater pipes.

Convective surfaces of the superheater are in the upper exhaust duct. In the convective part, behind the convective superheater, a water economizer and a tubular air preheater of 2 and 1 stages are arranged in series.

The pulverized-coal system with a dust bunker has got 2 ball-pulverized mills ShBM-250 and 2 mill exhausters BM-50/1000. Dust is dried by hot air. Dust is supplied from dust bins through eight ULPP-1 dust feeders and then transported through pulverized fuel pipes to the burners.

Air is supplied to air heater through two blower fans VD 15.5. 2 exhaust fans are used to remove flue gas. Ash extraction from the furnace is dry. Fly ash is trapped in wet fly ash collectors.

8 straight-through slot burners of the BKZ-160 boiler furnace are located on the side walls of the furnace in a tangential pattern. Every two burners are combined into a burner assembly.

Each burner has one air-and-fuel mixture channel and two secondary air channels above and below air-and-fuel mixture channel and separated by lined walls. The upper and lower burners are also separated by a partition in the center of which a fuel oil nozzle is mounted for flame kindling and lighting.

Fuel capacity of one burner is 4 t/h. Secondary air flow rate through the burner is $V = 6000 \text{ nm}^3/\text{h}$ with an excess air coefficient $\alpha=0.38$. The secondary air heating temperature is $t=380^\circ\text{C}$. The cross-sectional area of secondary air channels at the burner outlet is $F=0.2\text{m}^2$, which ensures secondary air velocities level at the burner outlet of $W = 40 \text{ m/s}$.

Coal dust is supplied to the burners with hot air. Air consumption for transporting dust per burner is $V=4850 \text{ nm}^3/\text{h}$. The primary excess air coefficient

is $\alpha=0.3$. The balance temperature of the air mixture at the burner outlet is $t = 250^\circ\text{C}$. The cross-sectional area of the air-and-fuel mixture channel is $F=0.105 \text{ m}^2$, which ensures the speed of the air mixture at the burner outlet $W_1=25 \text{ m/s}$. The ratio of the velocities of secondary and primary air is $W_2/W_1 = 1.64$. The excess air coefficient in the burners is $\alpha_g = \alpha_1 + \alpha_2 = 0.68$.

Hot air consumption per mill is $12,000 \text{ nm}^3/\text{h}$. After the mill, exhaust air is fed into the furnace through 4 waste burners located from the rear and from the front of the boiler.

Based on the air balance with the excess air coefficient at the furnace outlet being $\alpha_t = 1.27$, false air inflow into the furnace and dust systems make up about 40%, which deteriorates the efficiency of the boiler.

In the burners' area, where the ignition takes place, the flame is essentially non-uniform. However, at a distance from the burners, the concentrations of dust, oxygen and combustion products are equalized, as well as the temperature over the cross section of the flame.

Almaty TPP-3 is equipped with six BKZ-160 boilers with steam capacity of 160t/h each.

COMPUTING EXPERIMENT RESULTS

This section presents the results of computer simulation of the turbulent combustion of a pulverized coal flame in the BKZ-160 boiler chamber.

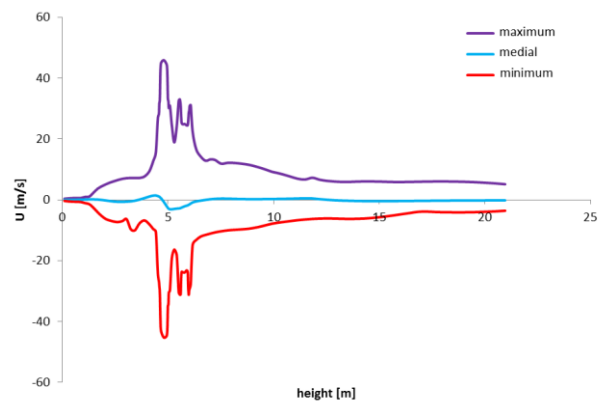


Fig.2. Distribution of velocity component U along the height of the combustion chamber

Graphs analysis (Fig.2 and Fig.3) of the maximum, minimum and medial values of full velocity components: U, V, indicates the symmetry of flows distribution in each section of combustion chamber.

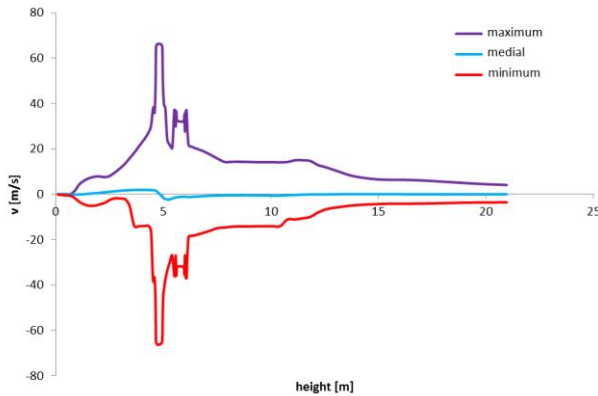


Fig.3. Distribution of velocity component V along the height of the combustion chamber

Figs.3-4 shows the minimum, maximum and average values of the full velocity vector along the height of the combustion chamber. At a height of four meters, the vector of full velocity reaches its maximum value. It is at this height that burner devices are installed through which the aerosol is injected at a maximum velocity reaching its value.

From a physical point of view, the velocity value cannot be negative, therefore, in the above figure, the negative values of the total velocity vector should be interpreted as the outflow of the mixture flow from opposite burners, where, according to the initial physical conditions, the flows have the same velocities, which is reflected in Figs.3-4.

As the flow reaches fuel mixture and the combustion products to the output speed falls monotonically, except for the deflection of the boiler chamber, in which we observe a certain peak area distribution vector full speed. In this region, the flow again becomes unsteady and therefore the velocity undergoes minor changes. This reflects the real aerodynamic picture of the physical and chemical processes occurring in the studied configuration of the combustion chamber.

The kinetic energy of turbulence k and the dissipation of turbulent energies ε , determined by relations (5) and (7) through the pulsating velocity components.

When the maximum turbulent kinetic energy k and its dissipation ε reach the central region opposite the burners. This is understandable, since in this region there is a collision of dust and gas flows from opposite tangentially located burner devices, which leads to a maximum perturbation of the flow in this region of the combustion chamber and to a high level of turbulence here. And this, in turn, provides high values of turbulent kinetic energy and its dissipation directly depend on the

pulsations of the velocity (disturbances) and the level of turbulence.

Significant turbulization of the flow occurs with good filling of the combustion space, therefore, with an increased residence time of the combustible mixture in the combustion space.

Due to the slightly rarefied filling of the chamber section above the burners, vortices develop at the front and rear walls. Part of the upward flow is directed to the exit from the furnace. Excess flow recycles, forming vortex regions near the walls in the area above the burners.

The presence of rotation of flows in the near-wall zone promotes uniform heating of surfaces and a decrease in slagging of screens, which allows reducing corrosion and thermal overheating. To the exit from the combustion chamber, the upward flow expands intensively and at the exit is evenly distributed over the entire cross section.

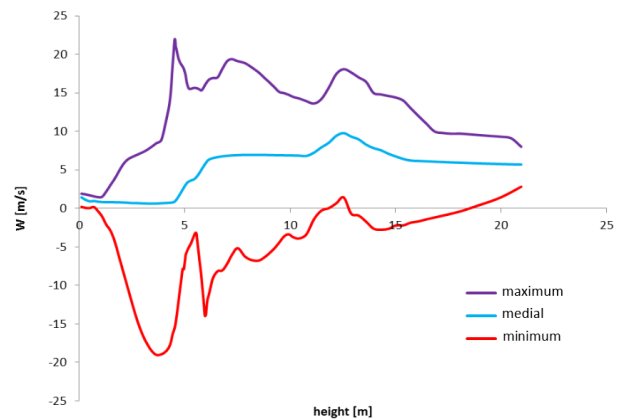


Fig.4. Distribution of velocity component W along the height of the combustion chamber

Only in the distribution of velocity component W is there no symmetry (Fig.4). From the analysis of the graphs obtained, we can draw the following conclusion: in the area where the burners are located, the fuel and air supply speed reaches its highest values.

Areas with a steep increase in pressure can be determined from the distribution of maximum, minimum and medial pressure values over the cross section (XY) ($Z=\text{const}$) (Fig.5). Naturally, these are areas where the burner tiers are located, which is due to the maximum velocity values.

The strongest pressure change occurs in the area of the burners, i.e. in the field of fuel and oxidizer supply. As the burners move away from this area, the pressure monotonously decreases.

The maximum convective transfer is observed in the blended fuel plane supply and in the combustion chamber symmetry plane. Combustion

reactions here are the most intense, resulting in significant temperature changes in this area.

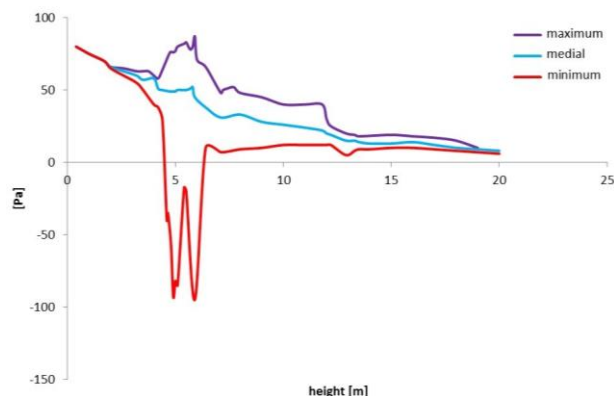


Fig.5. P pressure distribution along the height of the combustion chamber

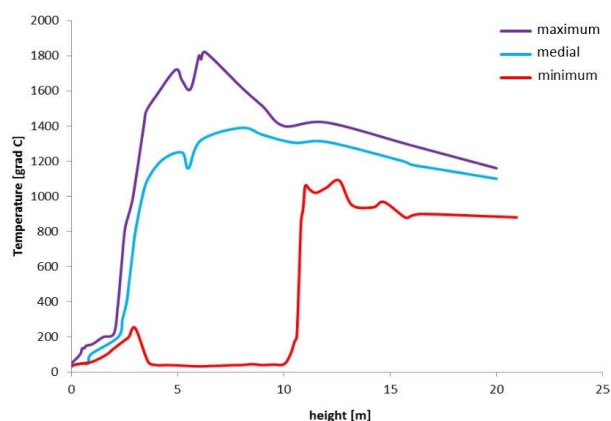


Fig.6. Distribution of temperature along the height of the combustion chamber

Fig.6 shows the distribution of the maximum, minimum and medial temperatures in cross-sections (X, Y) along the height of the boiler. The minima on all curves are related to the low temperature of the fuel mixture entering this area of combustion chamber through burners. Temperature maxima are observed directly in sections passing through the burner axis. Near the reaction zone, peaks in the distribution of temperature and its gradient are detected in the flame. As you move toward the outlet of combustion chamber, the temperature drops evenly.

CONCLUSIONS

The work has developed physical and mathematical model of combustion chamber of the Kazakhstan power boiler BKZ-160 at Almaty

thermal power plant with a tangential supply of pulverized coal, which adequately reflects the main elements, the configuration of combustion chamber, the arrangement of its burners and the real high-ash coal combustion process therein.

Computational experiments were carried out to simulate pulverized coal flame combustion process in combustion chamber of the BKZ-160 power boiler, and determine key characteristics of the flow aerodynamics: the full velocity and pressure P field.

The obtained results of numerical simulations of the aerodynamics process correctly reflects the real flow pattern that occurs in the combustion chambers of existing industrial boilers with a tangential supply of dust and gas mixture.

The results of numerical modeling of aerodynamics of the BKZ-160 furnace boiler showed that in the combustion chambers with the tangential supply of fuel and oxidizer, the organization of the vertical directional rotational movement of the flue gases occurs.

ACKNOWLEDGMENT

This work was supported by the Ministry of Education and Science of the Republic of Kazakhstan (grants AP05132988, AP05133590 and BR05236730).

REFERENCES

- [1] V. Maksimov, V. Messerle. Numerical simulation of the coal combustion process initiated by a plasma source. *Thermophysics and aeromechanics* **21**, 747-754 (2014).
- [2] A.S. Askarova, E.I. Karpenko, V.E. Messerle Plasma enhancement of combustion of solid fuels. *Journal of High Energy Chemistry* **40**, 111-118 (2006).
- [3] V.E. Messerle, A.B. Ustimenko, Z.Kh. Gabitova Numerical simulation of pulverized coal combustion in a power boiler furnace. *High temperature* **53**, 445-452 (2015).
- [4] A.S. Askarova, S.A. Bolegenova Computational method for investigation of solid fuel combustion in combustion chambers of a heat power plant. *High temperature* **53**, 751-757 (2015).
- [5] S.A. Bolegenova, Sh.S. Ospanova Numerical research of aerodynamic characteristics of combustion chamber BKZ-75 mining thermal power station. *Procedia Engineering* **42**, 1250-1259 (2012).
- [6] A.S. Askarova, S.A. Bolegenova 3D modeling of heat and mass transfer during combustion of solid fuel in BKZ-420-140-7c combustion chamber of Kazakhstan. *Journal of Applied Fluid Mechanics* 699-709 (2016).

- [7] A. Ergalieva, A.B. Ustimenko, V.E. Messerle Reduction of noxious substance emissions at the pulverized fuel combustion in the combustor of the BKZ-160 boiler of the Almaty heat electropower station using the “Overfire Air” technology. *Thermophysics and aeromechanics* **23**, 125-134 (2016).
- [8] Z. Kh. Gabitova, M. Beketayeva Control of Harmful Emissions Concentration into the Atmosphere of Megacities of Kazakhstan Republic. International Conference on Future Information Engineering. *IERI Procedia* 252-258 (2014).
- [9] R. Leithner, S. Vockrodt, A. Schiller Firing technique measures for increased efficiency and minimization of toxic emissions in Kazakh coal firing. 19th German Conference on Flames. Germany. VDI Gesell Energietechn; Verein Deutsch Ing. Combustion and Incineration. VDI Berichte, **1492**, 93 (1999).
- [10] H. Müller Numerische Berechnung dreidimensionaler turbulenter Strömungen in Dampferzeugern mit Wärmeübergang und chemischen Reaktionen am Beispiel des SNCR-Verfahrens und der Kohleverbrennung. Fortschritt-Berichte VDI-Verlag, **6-268**, 158 (1992).
- [11] R. Leithner Energy Conversion Processes with CO₂-Separation Not Reducing Efficiency. Handbook of Combustion. Wiley VCH Verlag GmbH & Co. (2010).
- [12] B. Eppler, R. Leithner, W. Linzer, H. Walter . Simulation von Kraftwerken und wärmetechnischen Anlagen. Springer-Verlag: Vienna (2009).
- [13] S.V. Patankar Numerical Heat Transfer and Fluid Flow. Hemisphere Publishing Corporation. (1980).
- [14] M.A. Leschziner Practical Evaluation of three finite difference schemes for the Computation of Steady State Recirculation Flows. Computer *Methods and Applied Mechanics an Engineering* **23**, 293-312 (1980).
- [15] V.E. Messerle, A.B. Ustimenko, O.A. Lavrichshev Comparative study of coal plasma gasification. *Fuel* **64**, 172-179 (2016).
- [16] V.E. Messerle, A.B. Ustimenko Mathematical modeling of the processes of solid fuel ignition and combustion at combustors of the power boilers. 7th Int. Fall Seminar on Propellants, Explosives and Pyrotechnics. Xian, 672-683 (2007).
- [17] M.A. Buchmann, A.S. Askarova Structure of the flame of fluidized-bed burners and combustion processes of high-ash coal. Gesell Energietechn, Combustion and incineration – eighteenth dutch-german conference on flames. VDI Berichte, 241-244 (1997).
- [18] A.S. Askarova, E.I. Karpenko, V.E. Messerle, A.B. Ustimenko Plasma-supported coal combustion in boiler furnace. *IEEE Transactions on Plasma Science* **35(6)**, 1607-1616 (2007).
- [19] R. Leithner, A. Ergalieva, A. Nugymanova Computational modeling of heat and mass transfer processes in combustion chamber at power plant of Kazakhstan. *MATEC Web of Conferences* **5**. (2016).
- [20] A. Askarova, A. Boranbayeva, S. Bolegenova, K. Berdikhan Application of numerical methods for calculating the burning problems of coal-dust flame in real scale. *Int. J. of Applied Engineering Research* **11-8**, 5511-5515 (2016).
- [21] A. Askarova, S. Bolegenova Influence of boundary conditions to heat and mass transfer processes. *Int. J. of Mechanics* **10**. 320-325. (2016).
- [22] P. Safarik, V. Maximov 3D modeling of heat and mass transfer processes during the combustion of liquid fuel. *J. of thermal science* **24-3**, 275-282 (2015).

Influence of the initial structure on the critical points in solid-state phase transformation of some hypoeutectoid steels

C. Dulucleanu¹, T.L. Severin^{1,*}, A. Potorac¹, L. Irimescu¹, J. Javorova²

¹University "Stefan cel Mare" of Suceava, Faculty of Mechanical Engineering, Mechatronics and Management & Research Center MANSiD, 13 University Street, 720229 Suceava, Romania

²University of Chemical Technology and Metallurgy, Boulevard Sveti Kliment Ohridski 8, 1756 Studentski Kompleks, Sofia, Bulgaria

This study allowed, by dilatometric analyses, both to highlight the solid state transformations that occurred during the continuous heating of three hypoeutectoid steels (with 0.087% C - 0.511% Mn, 0.101% C - 0.529% Mn and 0.093% C - 1.922% Mn), as well as to investigate the effect of the initial ferrite-pearlite structure on the critical points at which these transformations occurred. Dilatometric analyses were performed on specimens of steels with unmodified structures (as-delivered structures) and on specimens with structures obtained from full annealing (heating at 980 °C for 60 minutes and slow cooling in the furnace). These structures (with different grain size indices, mean diameters and mean area of grain) have influenced both the aspect of the dilatometric and the first derivative curves, as well as the values of the critical points in solid-state phase transformation.

Keywords: critical point, dilatometric analysis, structure, grain size index, dual-phase steel

INTRODUCTION

The behaviour of a steel in the basic operations of the various heat treatment technologies, the structures and the properties obtained therefrom, are influenced both by the homogeneity of the austenite grains and by their dimensions. The size of the austenitic grains formed by heating depends not only on the parameters of the heating regime (temperature, time), but also on the initial structure of the steel. According to the Fe-C equilibrium diagram, when heating a hypoeutectoid Fe-C binary alloy, results austenite (γ) through two transformations, namely, the pearlite (P) dissolution which represents an eutectoid transformation ($P \rightarrow \gamma$) and the transformation of proeutectoid ferrite (α) which is an allotropic transformation ($\alpha \rightarrow \gamma$); the temperatures at which these transformations take place are considered critical points, being noted as Ac_1 , respectively Ac_3 . In conditions of thermodynamic equilibrium, in the Fe-C binary alloys, the pearlite dissolution into austenite (eutectoid transformation) occurs at a constant temperature of 727 °C [1-5]. Commercial steels, unlike Fe-C binary alloys, are metallic materials which have in their composition also other chemical elements (such as impurities or alloying elements), elements which modify the position of the critical points; in addition, in the commercial

steels, under industrial heating conditions (different from thermodynamic equilibrium), the pearlite dissolution into austenite (eutectoid transformation) no longer occurs at 727 °C (at constant temperature), but in a range of temperatures, namely, between Ac_1 temperature (pearlite dissolution start temperature) and pearlite dissolution finish temperature, denoted Ac_{fp} . The temperature Ac_{fp} indicates the beginning of ferrite and austenite coexistence range during heating (beginning of the allotropic transformation of ferrite into austenite, $\alpha \rightarrow \gamma$), range that stretches up to the temperature of the Ac_3 point, the determination of this range of coexistence of the ferrite and austenite ($Ac_{fp} - Ac_3$) being of great importance for the technologies of manufacturing dual-phase steels [1-7]. These steels have a low carbon content and a structure formed of a soft and ductile ferrite matrix in which are homogeneously dispersed, martensite (10 to 35 %) and a small amount of residual austenite (1 to 2 %); the main technology for producing such steels consists of the intercritical quenching. The structure obtained, for a given chemical composition, is the result of combined action of the technological parameters of intercritical heat treatment (heating temperature, cooling rate etc.), their influence on the structure of the material being directly reflected on its properties. Consequently, for designing and developing a dual-phase steel production technology, it is necessary to know both the temperatures of the critical points Ac_1 , Ac_{fp} and Ac_3 ,

* To whom all correspondence should be sent:
severin.traian@usm.ro

as well as the influence of certain technological parameters (heating rate, grain size of ferrite and austenite etc.) on these points [4, 5, 8]. A quick and convenient method for determining the temperature of critical points in solid-state phase transformation when heating a steel lies in the use of mathematical models that take into account the chemical composition (equations obtained by statistical processing of experimental results), but these equations can generate large errors [1, 2, 4, 5]. A high precision in determining these temperatures is obtained by dilatometric analyses; modern dilatometers, connected to computerised systems, collect the signals of change in the length of a specimen as a function of temperature, plot a dilatometric curve, $\Delta L/L_0 = f(T)$, calculate and generate its corresponding derivative, $d(\Delta L/L_0)/dT = f'(T)$, and allow the identification of both critical points Ac_1 and Ac_3 , as well as the pearlite dissolution finish temperature (the Ac_{fp} point) and therefore, the determination of the temperatures range ($Ac_{fp} - Ac_3$) [2, 7, 9, 10]. Unfortunately, the literature is relatively poor in information on the results of dilatometric analyses performed in order to identify the temperatures of the critical points in solid-state phase transformation of dual-phase steels or to establish the influence of some technological parameters (heating speed, initial structure, grain size etc.) on these critical temperatures.

This article describes some of the researches carried out at University "Stefan cel Mare" of Suceava, Romania, in order to obtain and characterise dual-phase steels; the results of the dilatometric analyses performed on specimens made from three of the alloys used in the research are presented. As a result of these researches, the temperatures of the critical points in solid-state phase transformation were identified and the influence of the initial structures on these temperatures was established.

EXPERIMENTAL DETAILS

The chemical compositions of the investigated three Fe-C alloys (denoted A_Steel, B_Steel and C_Steel in this article) were determined with a FOUNDRY-MASTER Xpert spectrometer (Oxford Instruments Analytical GmbH, Germany), and led to the next values (weight %):

- A_Steel: Fe, 0.087 C, 0.511 Mn, 0.091 Si, 0.0036 P, 0.0039 S, 0.029 Cr, 0.005 Mo, 0.049 Ni, 0.003 Al, 0.082 Cu, 0.003 V, 0.003 W;

- B_Steel: Fe, 0.101C, 0.529 Mn, 0.091 Si, 0.0032 P, 0.0037 S, 0.036 Cr, 0.005 Mo, 0.015 Ni, 0.003 Al, 0.015 Cu, 0.003 V, 0.003 W, 0.011 Pb;

- C_Steel: Fe, 0.093 C, 1.922 Mn, 0.065 Si, 0.0191 P, 0.0116 S, 0.111 Cr, 0.036 Mo, 0.092 Ni, 0.012 Al, 0.154 Cu.

The influence of the initial structure on the critical points in solid-state phase transformation was studied on:

- specimens with as-delivered structure, denoted D_A for A_Steel, D_B for B_Steel and D_C for C_Steel;

- specimens with structure obtained by full annealing, denoted FA_A for A_Steel, FA_B for B_Steel and FA_C for C_Steel.

The heat treatments (full annealing) were performed in a Nabertherm LT 40/11/P330 electrical laboratory furnace (Nabertherm GmbH, Germany) and consisted of heating to 980 °C (for 60 minutes), followed by cooling slowly, in furnace.

The metallographic analyses, which allowed the identification and characterization of the structures, were performed with a LEXT OLS4100 Laser Microscope (Olympus Corporation, Japan). The surfaces needed metallographic analyses (three samples for each structure and each steel) were obtained by processing with Hot Mounting Press OPAL 410 and Grinding/Polishing Machine SAPHIR 530 (ATM GmbH, Germany). The quantitative characterization of the structures was achieved by the planimetric method (in compliance with EN ISO 643:2003 [11]), with OLYMPUS Stream MOTION Image Analysis Software.

The dilatometric analyses, aimed to reveal the critical points in the solid-state phase transformation of the three steels, were made with a DIL 402 Expedis-SUPREME Dilatometer (NETZSCH Gerätebau GmbH, Germany), on cylindrical specimens with a diameter of 5 mm and a length of 25 mm, continuous heated in (30 ÷ 980) °C temperature range, with a heating rate of 3 °C/min, in nitrogen atmosphere (100 ml/min N₂) and with a load at the specimen of 200 mN; for each initial structure and each steel, three analyses were made (three specimens for each initial structure and each steel). Finally, the signals provided by the dilatometer were processed with NETZSCH Proteus[®] Software 7.1.0.

RESULTS AND DISCUSSION

Micrographic determination of grain size

After highlighting the structures, five micrographs were achieved (in different regions) on

each metallographic sample (Figs.1-3); all the structures of the three steels were made of ferrite and pearlite (ferrite-pearlite structures). Finally, on each micrograph the grain size index (G), the mean diameter of grain (\bar{d}) and the mean area of grain (\bar{a}) were determined; for each parameter (G, \bar{d} and \bar{a}), three determinations were made. The results obtained (average values) are presented in Tab.1.

Table 1. Characterization of grain size

Steel	As-delivered structure		
	G	\bar{d} μm	\bar{a} μm^2
A_Steel	10.16	10.49	109.44
B_Steel	9.77	12.06	143.87
C_Steel	8.69	17.62	304.43
Steel	Full annealing structure		
	G	\bar{d} μm	\bar{a} μm^2
A_Steel	7.48	26.83	702.98
B_Steel	7.28	28.65	809.06
C_Steel	8.39	19.57	373.02

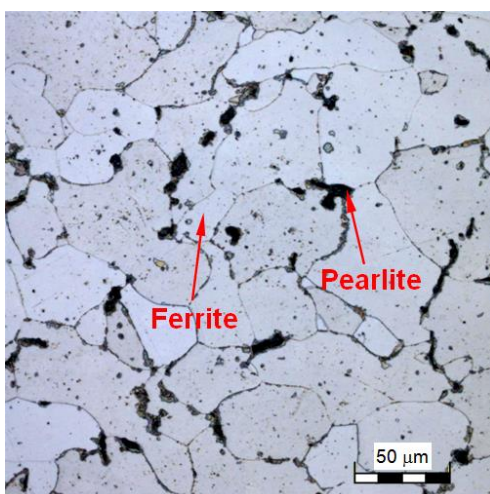
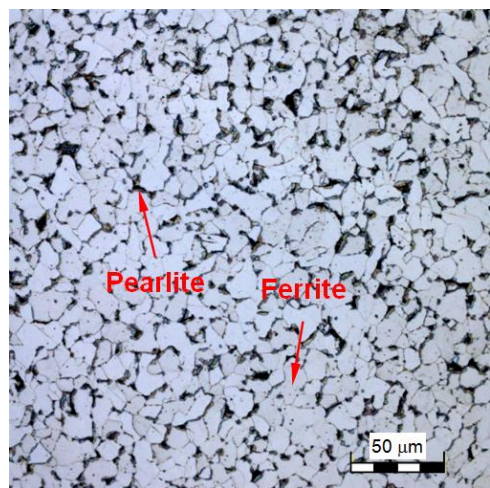


Fig.1. Structures of the A_Steel (etchant 2% Nital): a) D_A ; b) FA_A

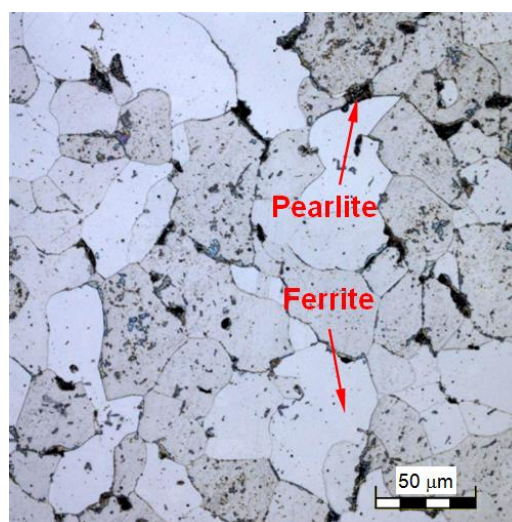
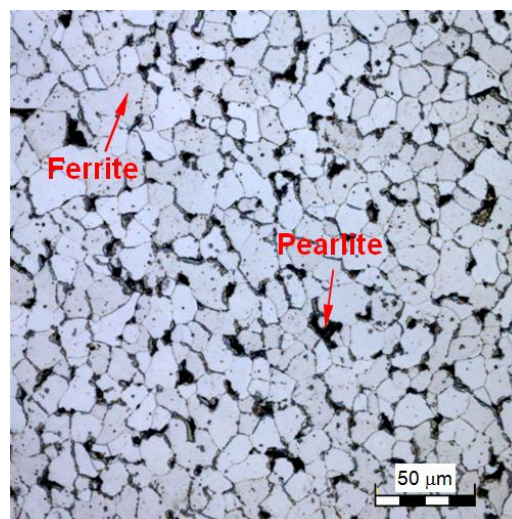


Fig.2. Structures of the B_Steel (etchant 2% Nital): a) D_B ; b) FA_B

The data in Tab.1 shows that, for each steel, the full annealing structures had grains larger than those in the as-received structures, the biggest differences being highlighted at structures of the A_Steel and B_Steel; for example, the mean diameter of grain (\bar{d}) was 2.56 times greater for A_Steel, 2.38 times for B_Steel and 1.11 times for C_Steel.

The grain size indice (G) diminished with 26.38% (from 10.16 for as-received structure to 7.48 for full annealing structure) for A_Steel, with 25.49% (from 9.77 for as-received structure to 7.28 for full annealing structure) for B_Steel and with only 3.45% (from 8.69 for as-received structure to 8.39 for full annealing structure) for C_Steel (Fig.4).

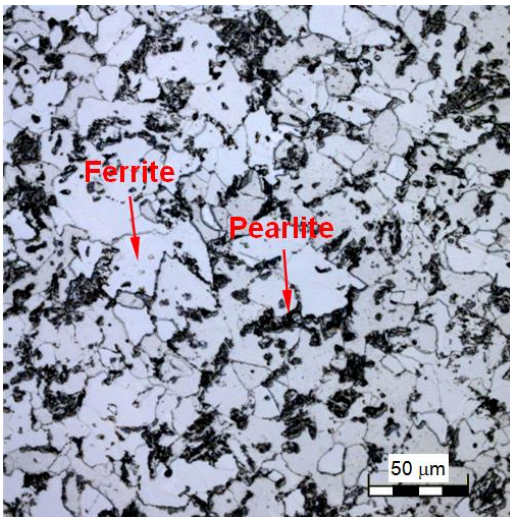
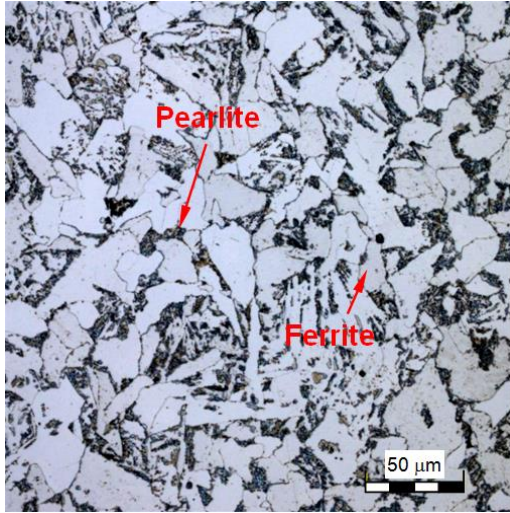


Fig.3. Structures of the C_Steel (etchant 2% Nital): a) D_C ; b) FA_C

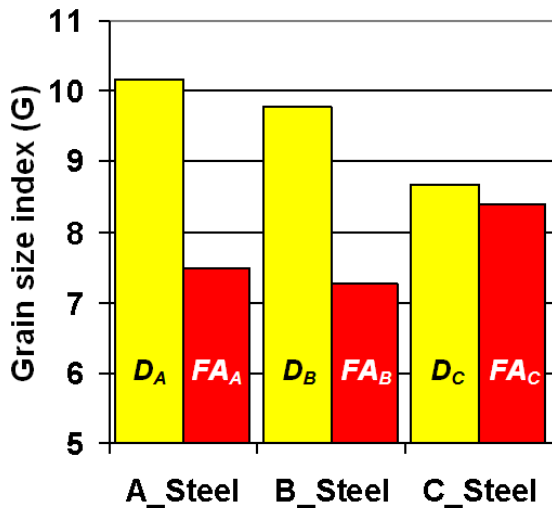


Fig.4. The grain size index (G) of the structures

Influence of the initial structure on the critical points in solid-state phase transformation

The signals of change in the length of the specimens as a function of temperature, collected during dilatometric analyses with the computerised systems of the DIL 402 Expedis-SUPREME Dilatometer, have led to the plotting of the dilatometric curves, as well as to the calculation and graphic representation of their derivatives (Figs.5-7).

Normally, no difference between the eutectoid transformation (the pearlite dissolution in austenite, $P \rightarrow \gamma$) and the allotropic transformation of ferrite into austenite ($\alpha \rightarrow \gamma$) is detected on the continuous heating dilatometric curve obtained for a hypoeutectoid Fe-C binary alloy. However, all the dilatometric curves drawn for the specimens of the three steels with as-delivered structures (D_A , D_B and D_C) present an unusual anomaly at the onset of the austenitization; this obvious anomaly is a contraction associated to the pearlite dissolution (Figs.5.a, 6.a, 7a) [2-7, 9, 10, 12, 13].

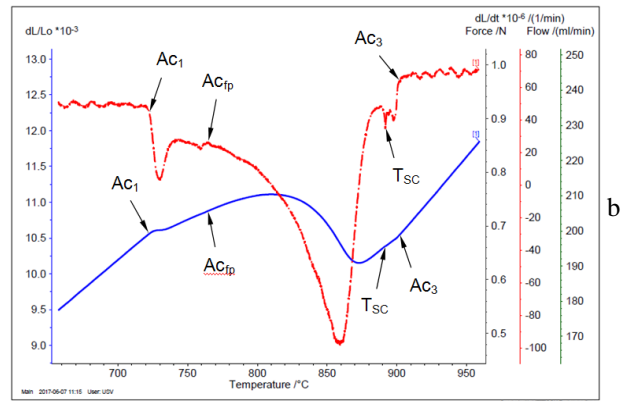
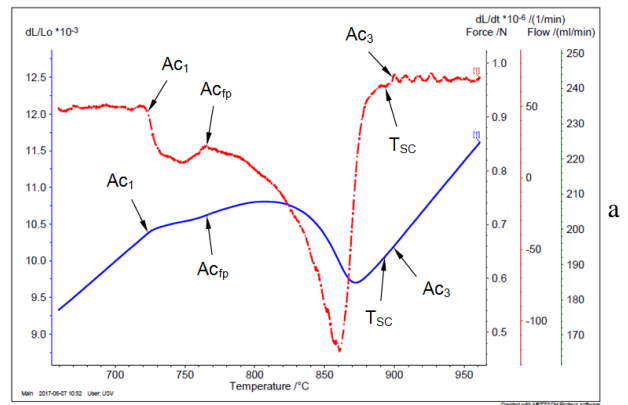


Fig.5. Dilatometric curve (continuous line) and its corresponding derivative (dashed line) of the A_Steel: a) D_A ; b) FA_A

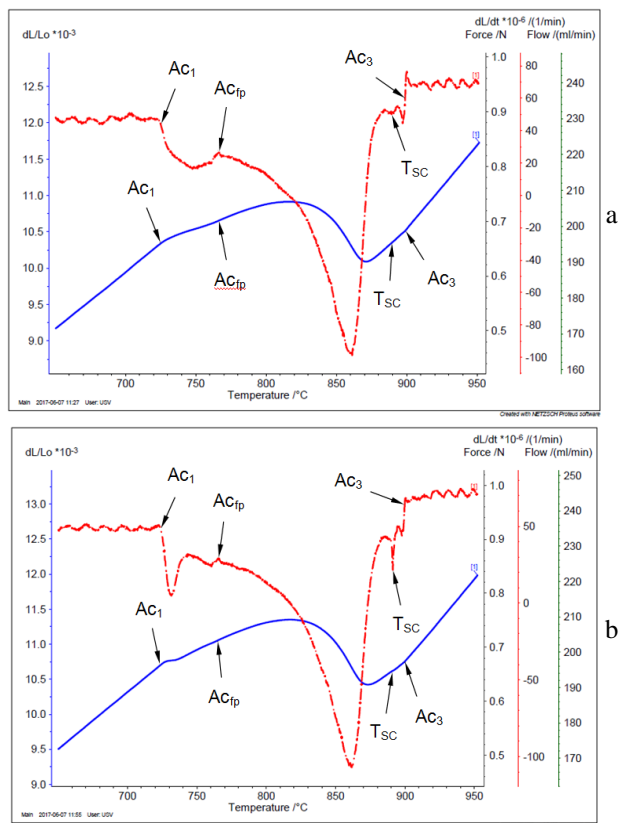


Fig.6. Dilatometric curve (continuous line) and its corresponding derivative (dashed line) of the B_Steel: a) D_B ; b) FA_B

The high resolution dilatometry, which highlights precisely the two processes that take place when heating a hypoeutectoid steel (the pearlite dissolution into austenite and the allotropic transformation of ferrite into austenite), permits the determination of the Ac_{fp} temperature (the pearlite dissolution finish temperature). Ac_{fp} is the temperature at which the first contraction on the dilatometric curve, due to pearlite to austenite transformation, finishes, being also a transition temperature between the two transformations, ($P \rightarrow \gamma$) and ($\alpha \rightarrow \gamma$); this temperature is much easier to highlight on the first derivative curve, curve that has two peaks which indicates the contractions caused by ($P \rightarrow \gamma$) and ($\alpha \rightarrow \gamma$) transformations (Figs.5.a, 6.a, 7.a) [2, 4, 5, 9, 10]. Immediately after finishing pearlite dissolution ($P \rightarrow \gamma$) the allotropic transformation of ferrite in austenite ($\alpha \rightarrow \gamma$) begins, transformation that determine also a decrease in the specific volume (a contraction). After achieving a minimum in the variation of the relative length of the specimen, on the dilatometric curves drawn for A_Steel and B_Steel with as-delivered structures (D_A and D_B), at a temperature noted T_{SC} , there is a small contraction which is

better highlighted on the first derivative curves, which have a small peak at T_{SC} temperature (Figs.5.a, 6.a) [4, 5]. This modification of volume is difficult to explain, being determined, probably, either through the formation of austenite from a ferrite that remains untransformed in structure (which transforms almost instantaneously due to the change in ferrite-to-austenite transformation kinetics) [3-5, 13], either through a diffusion of carbon from rich-carbon austenite (formed of pearlite) in less-carbon austenite (formed of ferrite) [4, 5, 14]. The modification of volume of the specimens highlighted for A_Steel and B_Steel, at T_{SC} temperature, does not appear on the dilatometric curves and their corresponding derivatives obtained for C_Steel (specimens with as-delivered structures, D_C), Fig.7.a [5].

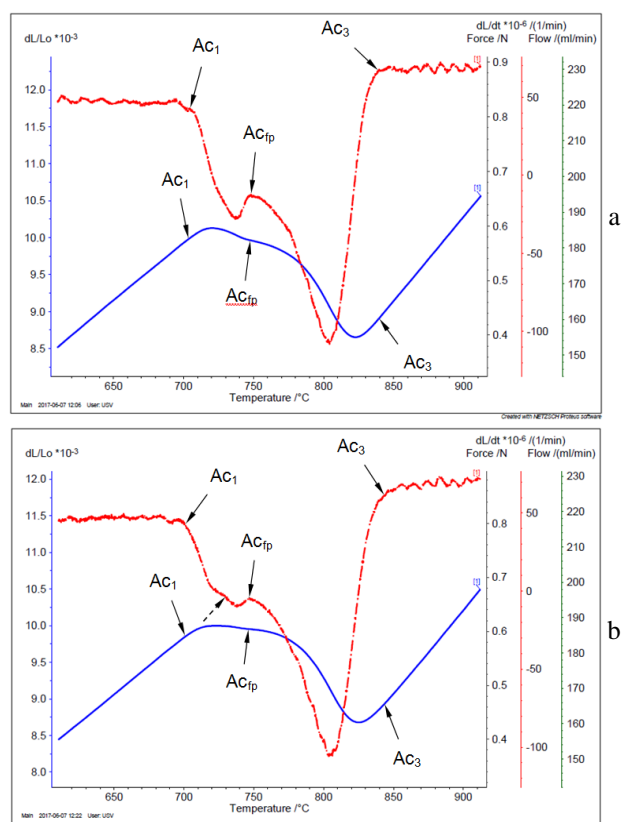


Fig.7. Dilatometric curve (continuous line) and its corresponding derivative (dashed line) of the C_Steel: a) D_C ; b) FA_C

The dilatometric curves and its corresponding derivative for the specimens with full annealing structures (FA_A , FA_B and FA_C) have modified shapes as compared to those designed for as-received structures (D_A , D_B and D_C), Figs.5.b, 6.b., 7.b. Thus, in the case of A_Steel and B_Steel, on the dilatometric curves the contraction to the onset

of austenitisation appears better outlined (Figs.5.b, 6.b), and on the first derivative curve, between the temperatures Ac_1 and Ac_{fp} , there are two peaks. The first peak (higher than the second one) corresponds to the eutectoid transformation (the pearlite dissolution in austenite), but the presence of the second peak is difficult to explain; either in the austenite formed by the pearlite dissolution would remain a small amount of undissolved cementite particles which then dissolved, either homogenization of the austenite (which was formed by the pearlite dissolution) was produced. In the case of C_Steel, there are no highlighted the modifications or aspects noticed for the other two steels; only a small anomaly appears on the first derivative curve, marked with a dashed arrow in Fig.7.b. The contraction observed at T_{SC} temperature on the dilatometric curves plotted for the A_Steel and B_Steel specimens with as-received structures also appears on the curves plotted for specimens with full annealing structures (Figs.5.b, 6.b); it is better emphasized on both the dilatometric curves and the first derivative curve. In the case of C_Steel, this contraction from T_{SC} temperature, does not even occur in the specimens with full annealing structures (Fig.7.b).

Tab.2 shows, depending on the initial structure, the results of the dilatometric analyses, which were obtained through processing with NETZSCH Proteus® Software 7.1.0. of the signals of variation in the length of the specimens, provided by the dilatometer, during tests.

Table 2. The results of the dilatometric analyses

Steel	Specimens with as-received structures			
	Ac_1 °C	Ac_{fp} °C	Ac_3 °C	$(Ac_{fp} - Ac_3)$ °C
A_Steel	724.00	765.60	899.40	133.80
B_Steel	725.10	766.30	898.90	132.60
C_Steel	703.80	747.70	839.70	92.00
Steel	Specimens with full annealing structures			
	Ac_1 °C	Ac_{fp} °C	Ac_3 °C	$(Ac_{fp} - Ac_3)$ °C
A_Steel	722.70	764.70	901.90	137.20
B_Steel	723.80	765.20	899.70	134.50
C_Steel	700.90	746.60	843.60	97.00

Data in Tab.2 show that the temperatures of the critical points in solid-state phase transformation determined for the specimens with full annealing structures have lower values for Ac_1 (with 1.30 °C for A_Steel and B_Steel, 2,90 °C for C_Steel) and Ac_{fp} (with 0,90 °C for A_Steel, 1,10 °C for B_Steel and C_Steel) and higher for Ac_3 (with 2,50 °C for A_Steel, 0,80 °C for B_Steel and 3,90 °C for

C_Steel) than those established for the specimens with as-received structures (Figs.8-10). This has led to a slight increase in the temperature range ($Ac_{fp} - Ac_3$), with 3,40 °C for A_Steel, 1,90 °C for B_Steel and 5,0 °C for C_Steel (Fig.11), range which is important for the dual-phase steels production technologies.

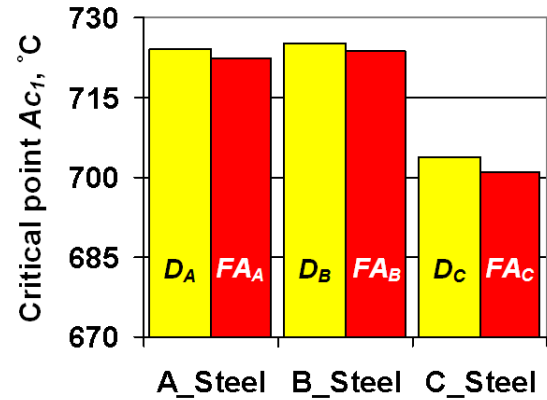


Fig.8. Influence of the initial structure on critical point Ac_1

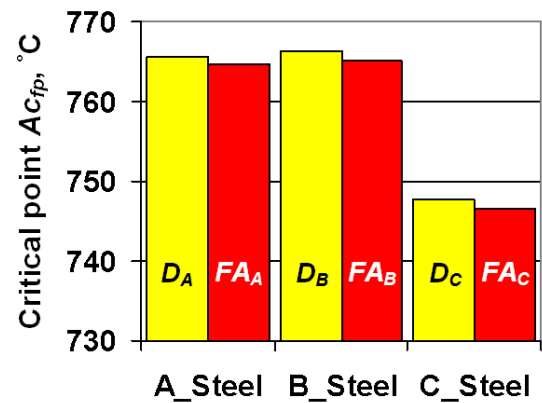


Fig.9. Influence of the initial structure on critical point Ac_{fp}

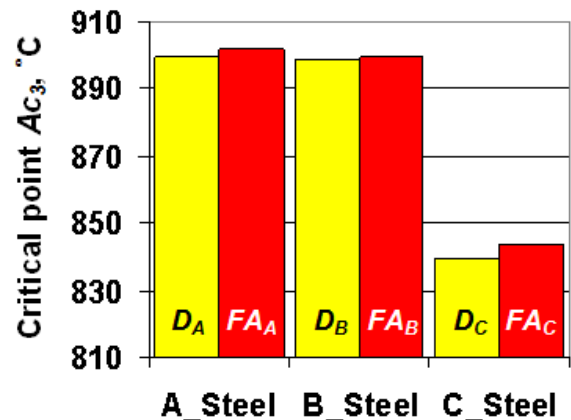


Fig.10. Influence of the initial structure on critical point Ac_3

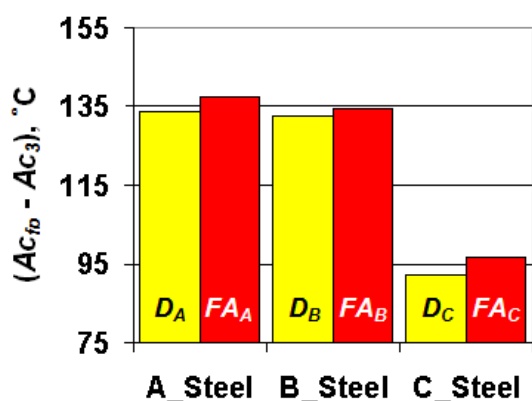


Fig.11. Influence of the initial structure on the temperature range ($Ac_{1f} - Ac_3$)

CONCLUSIONS

Dilatometric analyses performed on a DIL 402 Expedis-SUPREME dilatometer, allowed to highlight the solid-state phase transformations that occurred during the continuous heating of three hypoeutectoid steels, 0.087% C - 0.511% Mn, 0.101% C - 0.529% Mn and 0.093% C - 1.922% Mn (the dissolution of the pearlite in austenite and the allotropic transformation of proeutectoid ferrite into austenite), as well as to determine the critical temperatures (points) at which these transformations occurred.

All the specimens used had ferrite-pearlite structures, but with the grain size index (G) different: those with as-received structures had grain size index (G) between 8.69 and 10.16, and those with a full annealing structures between 7.28 and 8.39. The pearlite dissolution into austenite (eutectoid transformation) was carried out in a temperature interval ranging between pearlite dissolution start temperature (critical point Ac_1) and pearlite dissolution finish temperature (denoted Ac_{fp}); allotropic transformation of ferrite into austenite occurred between the Ac_{fp} temperature and the ferrite to austenite transformation finish temperature (critical point Ac_3).

The dilatometric curves and its corresponding derivative for the specimens with full annealing structures have modified shapes as compared to those designed for as-received structures, both in the region of the pearlite dissolution into austenite (eutectoid transformation), and in the region of the allotropic transformation of ferrite into austenite.

The temperatures of the critical points in solid-state phase transformation determined for the specimens with full annealing structures had lower values for Ac_1 and Ac_{fp} and higher for Ac_3 than

those established for the specimens with as-received structures. This has led to a slight increase in the temperature range ($Ac_{fp} - Ac_3$), range which is important for the dual-phase steels production technologies.

ACKNOWLEDGEMENTS

This work was partially supported from contract no. 18 PFE/16.10.2018 funded by Ministry of Research and Innovation within Program 1 - Development of national research and development system, Subprogram 1.2 - Institutional Performance - RDI excellence funding projects, The infrastructure used for this work was partially supported from the projects "Integrated Center for research, development and innovation in Advanced Materials, Nanotechnologies, and Distributed Systems for fabrication and control (MANSiD)", Contract No. 671/2015.

NOMENCLATURE

Ac_1 - pearlite dissolution start temperature (lower temperature of the ferrite-austenite field during heating), °C;

Ac_3 - ferrite to austenite transformation finish temperature (upper temperature of the ferrite-austenite field during heating), °C;

Ac_{fp} - pearlite dissolution finish temperature (ferrite to austenite transformation start temperature), °C;

T_{SC} - small contraction temperature, °C;

α - proeutectoid ferrite;

γ - austenite;

P - pearlite;

\bar{d} - mean diameter of grain;

\bar{a} - mean area of grain;

G - grain size index.

REFERENCES

- [1] B. Pawlowski, Critical points of hypoeutectoid steel - prediction of the pearlite dissolution finish temperature Ac_{1f} , *Journal of Achievements in Materials and Manufacturing Engineering* **49**, 2, 331-337 (2011).
- [2] B. Pawlowski, Dilatometric examination of continuously heated austenite formation in hypoeutectoid steels, *Journal of Achievements in Materials and Manufacturing Engineering* **54**, 2, 185-193 (2012).
- [3] C. García de Andrés, F.G. Caballero, C. Capdevila, L.F. Álvarez, Application of dilatometric analysis to study of solid-solid phase

- transformation in steels, *Materials Characterization* **48**, 1, 101-111 (2002).
- [4] C. Dulucheanu, T. Severin, A. Potorac, L. Irimescu, Critical points in solid-state phase transformation of a steel with 0.087% C and 0.511% Mn, determined through dilatometric analyses, *Bulgarian Chemical Communications* **50**, Special Issue G, 158-164 (2018).
- [5] C. Dulucheanu, T. Severin, A. Potorac, L. Irimescu, Determination of the critical points in solid-state phase transformation of some hypoeutectoid steels, *E3S Web of Conference* **95**, 04004 (2019).
- [6] C. García de Andrés, F.G. Caballero, C. Capdevila, Dilatometric characterization of pearlite dissolution in 0.1C-0.5Mn low carbon low manganese steel, *Scripta materialia* **38**, 12, 1835-1842 (1998).
- [7] D. San Martin, T. De Cock, A. García-Junceda, F.G. Caballero, C. Capdevila, C. García de Andrés, The effect of heating rate on the reaustenitisation of a low carbon niobium microalloyed steel, *Materials Science and Technology* **24**, 3, 266-272 (2008).
- [8] S.A. Golovanenko, N.M. Fonshteyn, Dual-phase alloyed steels, Metallurgy, 1986.
- [9] B. Pawlowski, Determination of critical points of hypoeutectoid steels, *Archives of Metallurgy and Materials* **57**, 4, 957-962 (2012).
- [10] F.L.G. Oliveira, M.S. Andrade, A.B. Cota, Kinetics of austenite formation during continuous heating in a low carbon steel, *Materials Characterization* **58**, 256 - 261 (2007).
- [11] EN ISO 643:2003, Steel - Micrographic determination of the apparent grain size.
- [12] D. San Martin, P.E.J. Rivera-Diaz-del-Castillo, C. García de Andrés, In-situ Study of Austenite Formation by Dilatometry in a Low Carbon Microalloyed Steel, *Scripta Materialia* **58**, 926-929 (2008).
- [13] F.G. Caballero, C. Capdevila, C. García de Andrés, Modelling of kinetics of austenite formation in steel with different initial microstructures, *ISIJ International* **41**, 10, 1093-1102 (2001).
- [14] B. Pawlowski, P. Bała, J. Krawczyk, Some factors influencing, the determination of eutectoid transformation start and finish temperatures in hypoeutectoid steels, *Metallurgy and Foundry Engineering* **35**, 2, 121-128 (2009).

Comparison of antiviral activity of realgar and nano-realgar against herpes simplex virus type II (HSV-2) *in vitro*

Dan Wang^{1†}, Li Wang^{3†}, Rui Xu³, Xingan Wu⁴, Yunlan Li^{1,2*}

¹School of Pharmaceutical Science, Shanxi Medical University, Taiyuan 030001, P. R. China, *Corresponding author: Yun-lan Li: liyunlanrr@163.com

²Shanxi University of Chinese Medicine, Key Laboratory of Innovative Drug for the Treatment of Serious Diseases Basing on the Chronic Inflammation

³The First Affiliated Hospital, Xi'an Medical University, Xi'an 710077, P. R. China

⁴Department of Pathogenic Microorganism, School of Preclinical Medicine, Airforce Medical University, Xi'an 710032, P. R. China

† These authors contributed equally to the present work.

In traditional folk prescriptions, realgar, as a traditional Chinese medicine, has been widely used to treat herpes caused by virus. To compare the antiviral activity of realgar and nano-realgar against herpes simplex virus type II (HSV-2) *in vitro*, the Vero cells model of HSV-2 infection was established, and cytotoxicity of realgar and nano-realgar on Vero cells were determined by the cell counting kit-8 (CCK8) in this study. Subsequently, the antiviral effects of realgar and nano-realgar on infected cells were also evaluated by CCK8 method under the three modes including prevention, treatment and direct inactivation. The results showed that the 50% cytotoxic concentration (CC₅₀) of realgar and nano-realgar on Vero were 18.75 µg/mL and 150 µg/mL, respectively. In the preventive mode, 50% effective concentration (EC₅₀) of realgar on HSV-2 infected cells was 10.19 µg/mL, while nano-realgar had an EC₅₀ value of 2.26 µg/mL for infected cells. Under treatment mode, the EC₅₀ value of realgar and nano-realgar on infected cells were 3.94 µg/mL and 1.13 µg/mL, respectively. In the direct inactivation mode, the EC₅₀ of realgar on infected cells was 10.23 µg/mL, while the EC₅₀ value of nano-realgar on infected cells was 2.92 µg/mL. In conclusion, the cytotoxicity of nano-realgar was lower than realgar's. Both realgar and nano-realgar can play a good antiviral activity on HSV-2 infected cells in the three ways of prevention, treatment and direct inactivation modes. Meanwhile, in prevention, treatment and direct inactivation modes, nano-realgar has an EC₅₀ value lower than that realgar on HSV-2 infected cells, so the anti-HSV-2 efficacy of nano-realgar on infected cells is better than realgar's antiviral efficacy in three modes.

Keywords: Realgar, nano-realgar, herpes simplex virus type II (HSV-2), antiviral

INTRODUCTION

There is increasing awareness of the importance of the skin infection disease caused by herpes simplex virus type II (HSV-2). Furthermore, several of emerging rare cases [1, 2] were found continuously in recent years, which indicated an upward trend in their incidence. HSV-2 can typically cause serious afflictions in a significant proportion of individuals, mainly because of the generation of genital lesions and severe infections like life-threatening encephalitis and disseminated infections in neonates [3-5]. Additionally, HSV-2 infection also significantly increased the risk of the host to acquire HIV [6]. Clinically, the most common drugs used for treating viral infection are acyclovir (ACV) and its derivatives. With the wide use of them, the disadvantages of narrow antiviral spectrum, drug resistance and high costs were more concerned, because of its huge burden on people's life [7-9]. Beyond that, the reserves shortage of

ACV had been also extremely concerned in America [10]. Besides, no effective HSV-2 vaccine is available until now in the world. For these reasons, there is a need for the development of novel antiherpes drugs which are safe and preferably inexpensive with limiting the primary infection and supporting further treatment.

Realgar, as a traditional Chinese medicine, has been used for treating diseases more than many years owning a wide range of sources and has good antitumor, antibacterial, antiviral effects, and so on [11-14]. The main component of realgar is As₄S₄, with disadvantages of large particles, low bioavailability, and insolubility in water [15]. In order to increase the solubility of realgar, enhance antiviral efficacy and reduce toxicity, nano-realgar whose average particle size was about 72.79 nm was therefore gifted by Li huijie, a teacher from shandong traditional Chinese medicine university [16, 17]. The existing clinical data shown that, as the main drug in the prescription, realgar had a significant effect on herpetic lesions appearing on the human surface [18]. But until now, there is no

* To whom all correspondence should be sent: liyunlanrr@163.com

relevant experimental study on separately realgar anti-HSV-2 activity. Therefore, the anti-HSV-2 activities of realgar and nano-realgar were compared to elucidate their activity more clearly in this study. Cell culture technology was used to investigate the antiviral activities of realgar and nano-realgar against HSV-2 *in vitro*, which can provide a theoretical basis for clinical herpes treatment and the invention of an antiviral drug that is widely available and cheap enough for Chinese people.

EXPERIMENTAL

Cell lines, virus strain, traditional chinese medicine and reagents

African green monkey kidney cells (Vero) and HSV-2 virus G strain, kindly donated by prof.X.A WU from department of pathogenic microorganism of airforce medical university. Monkey kidney cells Vero were incubated under dulbecco-modified eagle's medium (DMEM, high glucose) with 10% fetal bovine serum (FBS) at 37°C in atmosphere containing 5% CO₂ in CO₂ incubator (KZX00016904, obtained from Thermo). HSV-2 virus G strain were grown for 3 ~ 4 days on Vero cells in an atmosphere of 5% CO₂ at 37°C, and the virus stock solution was stored at -80°C until use.

Realgar was purchased from shaanxi Conway pharmaceutical co.LTD, and was milled to nanometer level, also known as nano-realgar, by longmai fine grinding machine (Model: LVM-80WE) of shandong longmai technology development co.LTD. And the particles size and size distribution of nano-realgar were determined by the photon-related nano-laser particle size analyzer (Model: Winner801) of jinan micro-nano particle instrument co.LTD. The results showed that the average particle size of nano-realgar was 72.79 nm, which met the requirements of nano-drug preparation [16,17]. Nano-realgar was donated by Li huijie, a teacher from shandong traditional Chinese medicine university.

Crystal violet is purchased from xi'an yongyi biotechnology co.LTD. Sodium carboxymethyl cellulose was purchased from Sigma-Aldrich. All of the high glucose DMEM medium, fetal bovine serum (FBS), dimethyl sulfoxide (DMSO) and cells counting kit-8 (CCK8) were obtained from shanghai sangon bioengineering co.LTD. Ultra-clean bench (SW-CJ-2F) was purchased from Shanghai xinmiao medical equipment manufacturing co.LTD. Other instruments and

equipment are as follows: LABGARD series biosafety cabinet (Nuair, America), Inverted microscope (EKY0014477; OLYMPUS-CKX31), Full wavelength microenzymelabeling apparatus (BioTek).

Cytotoxicity determination of realgar and nano-realgar on Vero cells

The cytotoxicity of both realgar and nano-realgar were determined by cell counting CCK-8 kit-8 [19]. Vero cells were seeded in 96-well plates at a density of 1×10^4 cells/well and cultured in DMEM with 10% FBS overnight. The medium was then removed and the cells were washed twice with phosphate buffered saline (PBS). Realgar and nano-realgar at various concentrations (200, 150, 100, 50, 25, 12.5, 6.25, 3.13, 1.57, 0.78, 0.39, 0 µg/mL) were added to individual well of Vero cells severally in plates and the plates were incubated 24 h under 37°C and 5% CO₂. Cells treated without the realgar and nano-realgar were used as control. After incubation for 24 hours at 37°C, the supernatant medium of each well was replaced with 100 µL DMEM, then 10 µL CCK-8 solution was added to the cells, and cells were cultured for 4 h avoiding light. The absorbance (A) of each well was measured at 450 nm using BioTek synergy 2 microplate reader. The cell viability was calculated using following formula. Cell viability (%) = $(A_s - A_b) / (A_c - A_b) \times 100\%$, where A_s and A_c refer to the absorbance in the presence and absence of realgar or nano-realgar, respectively, and A_b stands for blank control. GraphPad Prism 7.0 software was used to calculate the 50% cytotoxic concentration (CC₅₀) of realgar and nano-realgar on Vero according to bliss principle.

Virus infection and titer determination

The HSV-2 virus stocks were generated by infecting Vero cells monolayer for 2 ~ 3 days in the culture flask, then the infected cells were not lysed by three freeze-thaw cycles between -80°C and room temperature until the cytopathic effect (CPE) up to 90%. The viral lysates, also was called the first generation viral supernatant, were collected and stored at -80°C. A total of five generations viral supernatant were obtained through the above method. The titer of the primary purified HSV-2 virus and the fifth generation viral supernatant on Vero cells were determined by plaque assay [20]. Vero cell monolayer in 6-wells plates was infected with HSV-2 virus at multiple dilutions (10^{-1} , 10^{-2} ,

10^{-3} , 10^{-4} , 10^{-5} , 10^{-6}) and incubated at 37°C with 5% CO_2 for 2 h. The infected cell monolayer was then overlaid with overlapping solution containing 2% carboxymethyl-cellulose sodium salt. After 4 days, cell monolayer was washed three times with PBS and strained with 1% crystal violet solution. Plaques were counted and plaque formation units (PFUs/mL) were calculated as $\bar{x} / (n \times v) \times d$, where \bar{x} , n , v and d refer to the average numbers of plaques, repetitive holes numbers, viral load and dilution factor, respectively.

Antiviral activity of realgar and nano-realgar against HSV-2 under prevention, treatment and direct inactivation modes

In prevention, treatment and direct inactivation assays, the antiviral activities of realgar and nano-realgar on HSV-2 infected cells were assessed by the CCK-8 assay combined with cytopathic observation. For treatment assay, Vero cells cultured in 96-well plates were first infected with HSV-2 at 100 multiple tissue culture infective dose (100 TCID₅₀) for 2 h to allow viral attachment. Following 2 hours' incubation, the realgar or nano-realgar with indicated concentrations (20, 10, 5, 2.5, 1.25, 0.63, 0.31, 0.16, 0.08, 0.04, 0 $\mu\text{g}/\text{mL}$) were added to the infected Vero cells, of which cells without treatment of realgar or nano-realgar was used as a virus control group. Following incubation, the supernatant medium of each well was not replaced with 100 μL DMEM until the virus control group showed 80% ~ 90% cytopathic effects, then 10 μL CCK-8 solution was also added to the cells, and cells were cultured for 4 h avoiding light. The absorbance (A) of each well was measured at 450 nm using BioTek synergy 2 microplate reader. The antiviral activity of realgar or nano-realgar on HSV-2 infected cells was calculated using following formula. Antiviral activity (%) = $(A_s - A_v) / (A_c - A_v) \times 100\%$, where A_s and A_c refer to the absorbance in the presence and absence of realgar or nano-realgar, and A_v stands for the absorbance of virus control group, respectively. GraphPad Prism 7.0 software was used to calculate the 50% effective concentration (EC₅₀) of realgar and nano-realgar on HSV-2 infected Vero cells. For cellular prevention assay, Vero cells monolayer was first treated with realgar or nano-realgar at different concentrations for 2 h at 37°C before HSV-2 infection at 100TCID₅₀ for CCK-8 assay combined with cytopathic observation. For viral direct inactivation assay, the HSV-2 virus supernatant and realgar/ nano-realgar at indicated

concentrations were added to the Vero cell monolayer, simultaneously. The infected cell monolayer was co-cultured with HSV-2 and realgar/ nano-realgar for CCK-8 assay combined with cytopathic observation.

Cell morphology changes

When Vero cells were cultured to a nearly monolayer state at 37°C in atmosphere containing 5% CO_2 , the original culture medium was discarded and the HSV-2 virus solution was added to cells for 2 h to allow viral attachment. After 2 hours' incubation, the HSV-2 virus solution was replaced with the maintenance media (DMEM supplemented with 2% FBS). The state of the Vero cells were observed and photographed under optical microscope 20 \times magnification using Inverted microscope (EKY0014477; OLYMPUS-CKX31) under a visible light.

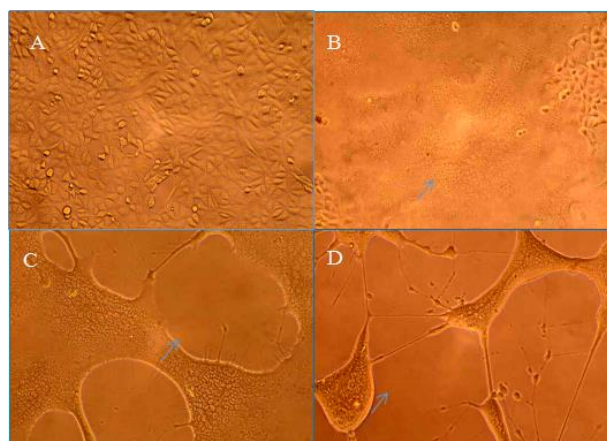


Fig.1. The morphological changes of normal Vero cells and Vero cells infected with HSV-2 ($\times 20$). A. The normal Vero cells, cells were closely arranged with fusiform morphology and intact cytomembrane, and the cell membranes were clearly visible with a strong refractive index; B. Vero cells infected with HSV-2 for 12 h, the cytomembranes of cells were blurred; C. Vero cells infected with HSV-2 for 24 h, multiple cells were gradually merged to form a multinucleated giant cell; D. Vero cells infected with HSV-2 for 30 h, multiple cells were gradually merged to form a multinucleated giant cell.

RESULTS AND DISCUSSIONS

Morphological changes of Vero cells after HSV-2 infection

Morphological changes of the cells can be seen in Fig.1. Normal Vero cells were closely arranged with fusiform morphology and intact

cytomembrane, and the cell membranes were clearly visible with a strong refractive index (Fig.1-A). However, the cytomembranes of Vero cells infected with HSV-2 for 12 h were blurred (Fig.1-B), and multiple cells infected with HSV-2 for 24 h were gradually merged to form a multinucleated giant cell (Fig.1-C), which multiple cells were gradually merged to form a multinucleated giant cell in 30 h (Fig.1-D).

Suspension degree of Nano-realgar is superior to realgar in DMSO solution

Realgar can be suspended in DMSO, and the suspension is dark brown. Realgar tended to settle rapidly to the bottom of the eppendorf (EP) tube, resulting in solution delamination in Fig.2A. However, nano-realgar can be completely suspended in DMSO solution. The solution of nano-realgar in DMSO solution is pale yellow and its sedimentation rate was extremely slow in Fig.2B. These phenomena illustrated that

suspension degree of nano-realgar is superior to realgar in DMSO solution.

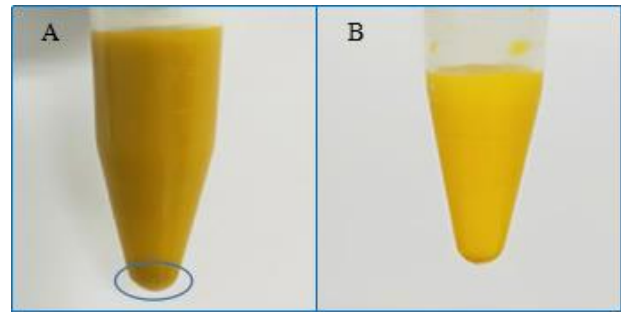


Fig.2. The appearance of realgar and nano-realgar suspensions. A. Realgar suspension; B. Nano-realgar suspension

The cytotoxicity of nano-realgar on Vero was lower than realgar's

In order to evaluate the usability of realgar and nano-realgar on the Vero cells, their cytotoxicity on cells were determined by CCK-8 assay.

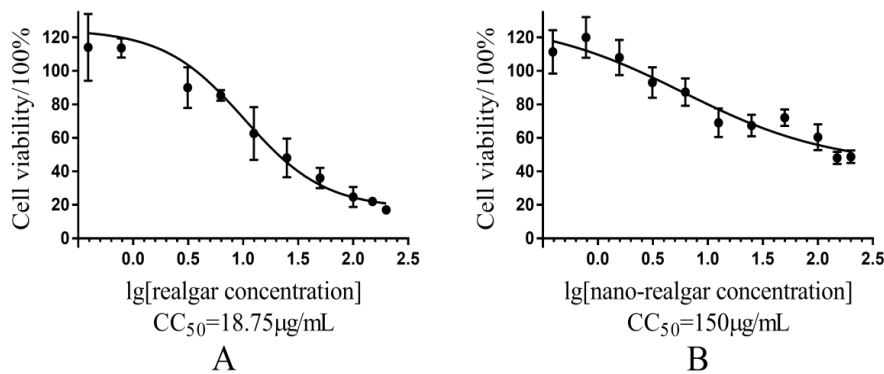


Fig.3. The cytotoxic effects of realgar and nano-realgar on Vero cells. A. realgar; B. nano-realgar

As shown in Fig.3, the cell viabilities of Vero cells treated with realgar at different concentrations were gradually decreased with the dose rising. In other words, the cytotoxicity of realgar on Vero cells was increased in a dose-dependent manner. Similarly, the cell viabilities of Vero cells treated with nano-realgar were also weakened. By calculation, the 50 % cytotoxic concentration (CC₅₀) of realgar and nano-realgar on Vero were 18.75 µg/mL (Fig.3A) and 150 µg/mL (Fig.3B), respectively. There was a significant difference between the cytotoxicity of realgar and nano-realgar on Vero cells ($p < 0.001$). Therefore, the cytotoxicity of nano-realgar on Vero was lower than realgar's. In order to reduce their toxic effects

on normal cells, 20 µg/mL was selected as the maximum initial concentration for subsequent experiments.

The Vero cells model establish of HSV-2 infection for determining the antiviral activity of realgar and nano-realgar against HSV-2 through viral titer by plaque assay

In order to determine the antiviral activity of realgar and nano-realgar against HSV-2, the Vero cells model of HSV-2 infection was established by infecting cells with the fifth generation HSV-2 virus supernatant. The titer of the primary purified HSV-2 virus and the fifth generation viral supernatant on Vero cells were determined by plaque assay.

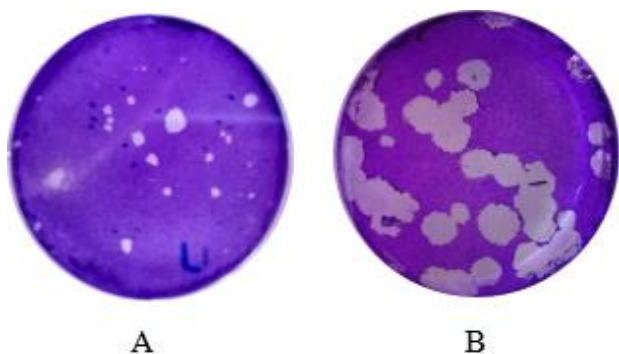


Fig.4. The plaque results of the HSV-2 virus on Vero cells. A. the primary purified HSV-2 virus; B. the fifth generation HSV-2 viral supernatant.

As shown in Fig.4, the plaque result of the Vero cells infected primary purified HSV-2 virus at 10^{-4} dilution showed a total of 17 plaques with small spots, and the titer of primary purified HSV-2 virus on Vero cells was 5.28 logPFUs/mL by calculation.

However, the plaque number of the Vero cells infected the fifth generation HSV-2 virus supernatant was eighteen at viral 10^{-6} dilution, and the spots were large. The titer of the fifth generation HSV-2 virus supernatant on Vero cells was 7.30 logPFUs/mL. The results showed that the virulence of HSV-2 virus was enhanced through generations of HSV-2 infection on Vero cells. Therefore, the Vero cells model of HSV-2 infection was established by infecting cells with the fifth generation HSV-2 virus supernatant at 100TCID₅₀, whose 100TCID₅₀ value was 10^{-5} .

Antiviral activity of realgar and nano-realgar against HSV-2 under prevention, treatment and direct inactivation modes

Antiviral activity of realgar and nano-realgar against HSV-2 under prevention, treatment and direct inactivation modes were shown in Fig.5.

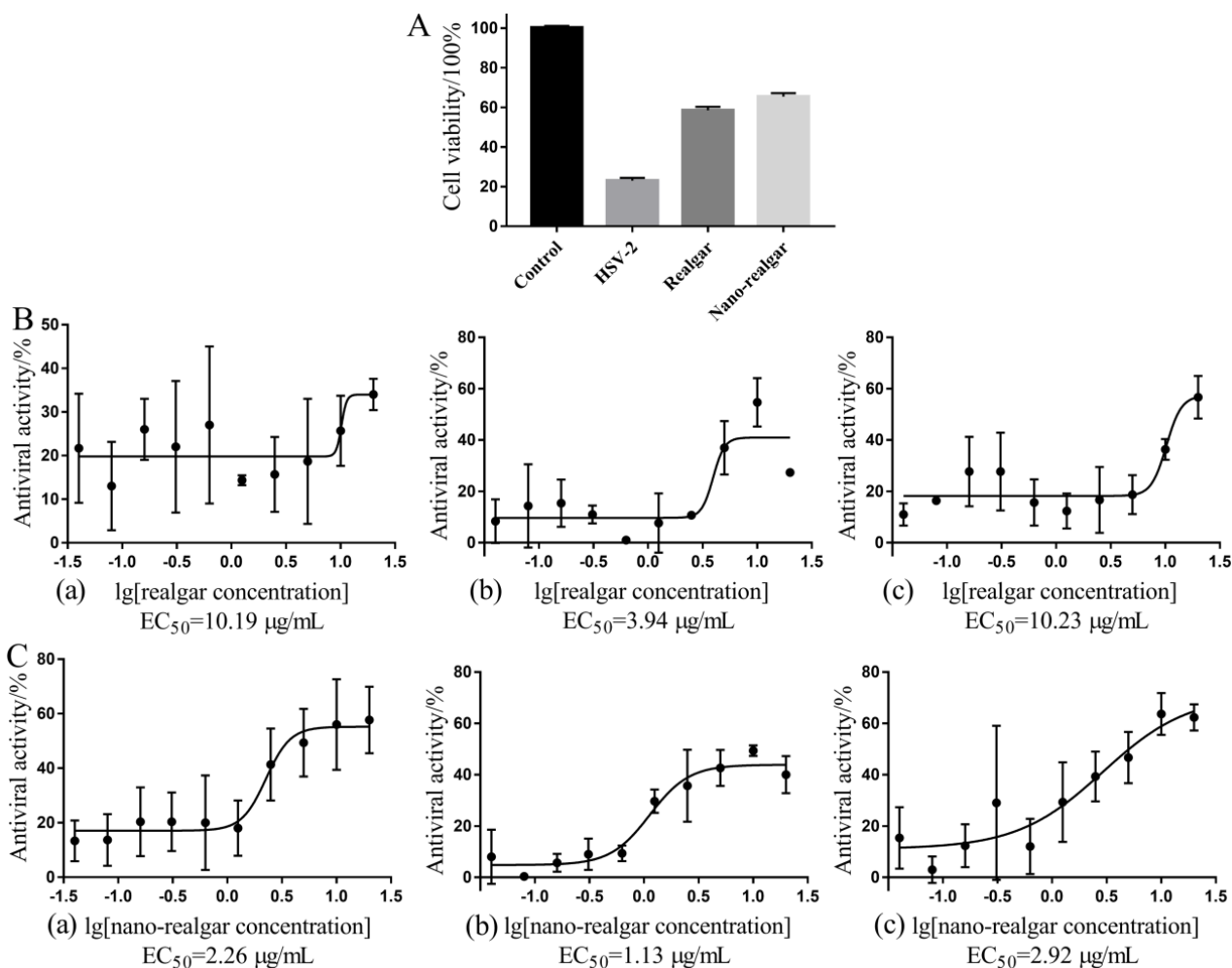


Fig.5. The dose-response curves of realgar and nano-realgar against HSV-2 in prevention, treatment and direct inactivation modes. A. the cellular activities of Vero cell treated with realgar and nano-realgar; B. the dose-response curves of realgar; C. the dose-response curves of nano-realgar; (a) prevention; (b) treatment; (c) direct inactivation

The cell viability of Vero cells infected with HSV-2 was reduced to 23 % compared with that of the normal cells group. However, the cell viability of Vero cells treated with realgar and nano-realgar at 20 µg/mL concentration was decreased to 58 % and 65 %, respectively (Fig.5-A). Therefore, the cytotoxicity of nano-realgar is lower than that of realgar at the same concentration. In the prevention mode, 50 % effective concentration (EC₅₀) of realgar on Vero cells infected with HSV-2 was 10.19 µg/mL, while nano-realgar had an EC₅₀ value of 2.26 µg/mL for infected cells. Under treatment mode, the EC₅₀ value of realgar and nano-realgar on infected cells were 3.94 µg/mL and 1.13 µg/mL, respectively. In the direct inactivation mode, the EC₅₀ of realgar on infected cells was 10.23 µg/mL, while the EC₅₀ value of nano-realgar on infected cells was 2.92 µg/mL. These results showed that both realgar and nano-realgar can exert variously anti-HSV-2 effects in three action modes. And nano-realgar has a lower EC₅₀ value than realgar on HSV-2 infected cells in prevention, treatment and direct inactivation modes, which indicated that the anti-HSV-2 efficacy of nano-realgar on infected cells is better than realgar's antiviral efficacy in three modes.

CONCLUSIONS

In this paper, the antiviral activities of both realgar and nano-realgar on HSV-2 infected Vero cells were investigated and compared *in vitro*. Firstly, the cytotoxicity of nano-realgar on normal Vero cells was lower than that of realgar. Then, the anti-HSV-2 activity experiments *in vitro* indicated that both realgar and nano-realgar can play a good antiviral activity on Vero cells infected HSV-2 in prevention, treatment and direct inactivation modes. And the anti-HSV-2 efficacy of nano-realgar on infected cells is better than realgar's antiviral efficacy in all three modes. This study provides a certain theoretical basis on comparison of antiviral activity of realgar and nano-realgar against herpes simplex virus type II (HSV-2) *in vitro* and demonstrates the potential of nano-realgar as a mineral medicine to control human skin disease caused by HSV-2.

ACKNOWLEDGMENTS

This study was supported in part by grants from National Natural Science Foundation of China (81973411) and Key Research & Development

Projects of Shanxi Province, China (2019SF-163, 2017SF-336) and The Medical Project of Bureau of Science and Technology of Xi'an City, China (2017122SF/YX016 (5)). Financial support funded by Shanxi Key Subjects Construction (FSKSC), National Science and Technology Major Project (2018ZX09101003-001-017), the Top Science and Technology Innovation Teams of Higher Learning Institutions of Shanxi Province, Shanxi Province Key Research and Development Project (201703D111033), the Project of Shanxi Key Laboratory for Innovative Drugs on Inflammation-based major disease "Anti-inflammatory Mechanism of Baihuadexhuangcao Flavone Baogan Capsule" (SXIDL-2018-05), Project of Center of Comprehensive Development, Utilization and Innovation of Shanxi Medicine (2017-JYXT-18), Research subject of graduate education reform in shanxi medical university (20141034) is gratefully acknowledged.

REFERENCES

- [1] Drumm CM, Caufield MC, DeKlotz CM, et al. Intrauterine Herpes Simplex Virus Infection Presenting as a Zosteriform Eruption in a Newborn. *AJP Rep.* **8**, e33-e36 (2018).
- [2] Goettsche LS, Wanat KA. Undisturbed characteristic herpes simplex virus 2 outbreak. *Dermatol Online J.* **23**, 25 (2017).
- [3] Paz-Bailey G, Ramaswamy M, Hawkes SJ, et al. Herpes simplex virus type 2: epidemiology and management options in developing countries. *Sex Transm Infect.* **83**, 16–22 (2007).
- [4] Smith JS, Robinson NJ. Age-specific prevalence of infection with herpes simplex virus types 2 and 1: a global review. *J Infect Dis.* **186**, S3–28 (2002).
- [5] Kimberlin DW. Herpes simplex virus infections in neonates and early childhood. *Semin Pediatr Infect Dis.* **16**, 271–281 (2005).
- [6] Freeman EE, Weiss HA, Glynn JR, Cross PL, Whitworth JA, Hayes RJ. Herpes simplex virus 2 infection increases HIV acquisition in men and women: systematic review and meta-analysis of longitudinal studies. *AIDS.* **20**, 73–83 (2006).
- [7] Li J, Peng F. Research progress of traditional Chinese medicine on anti-herpes simplex virus. *Medical Recapitulate.* **18**, 753-755 (2012).
- [8] Fiele HJ. Herpes simplex antiviral drug resistance-current trends and future prospects. *J Clin Virol.* **21**, 261-269 (2001).
- [9] Piret J, Drouot E, Boivin G. Antiviral drug resistance in herpes viruses. *Rev Med Virol.* **24**, 186-218 (2014).

- [10] Ventola CL. The drug shortage crisis in the united states: causes, impact, and management strategies. *P&T*. **36**, 740-757 (2011).
- [11] Zhang JF, Ding XK. A new method of realgar and cinnabar antiviral infection. *Henan Traditional Chinese Medicine*. **33**, 2013-2015 (2013).
- [12] Ding XK. New cognition of antiviral pharmacological action in cinnabar and realgar. *Chin J of Clinical Rational Drug Use*. **5**, 8-9 (2012).
- [13] Wang ZY. Arsenic compounds as anticancer agents. *Cancer Chemotherapy Pharmacology*. **48**, S72-S76 (2001).
- [14] Prajapati V, Kale RK, Singh RP. Arsenic and its combinations in cancer therapeutics. *Ther Deliv*. **2**, 793-806 (2011).
- [15] Sharma V, Singh NK, Gautam DNS, et al. Challenges for application of realgar: A critical review. *BLDE University Journal of Health Sciences*. **1**, 69-72 (2016).
- [16] Qi YF, Li HJ, Yu LY. The expression of vascular endothelial growth factor and hypoxia-induced factor-1 in A549 lung cancer cells treated with nano-realgar. *Chinese journal of gerontology*. **35**, 720-722 (2015).
- [17] Li XR, Li HJ, Xu YY. Effect of nanometer realgar on breast cancer MCF-7 cells's malignant behavior of invasion and metastasis. *Journal of shandong university of TCM*. **39**, 453-455 (2015).
- [18] Jun HY. Clinical study on the treatment of herpes zoster by western medicine antivirus combined with Chinese medicine external application. *World latest medical information digest*. **17**, 163-164 (2017).
- [19] Munetaka I, Fumio O, Kazumi S, Tomoyuki H, Keiji S and Masami W. A Water soluble Tetrazolium Salt Useful for Colorimetric Cell Viability Assay. *Analytical Communication*. **36**, 47-50 (1999).
- [20] Lai W L, Chuang HS, Lee MH, et al. Inhibition of herpes simplex virus type 1 by thymol-related monoterpenoids. *Planta Med*. **78**, 1636 (2012).

Increasing the efficiency of photovoltaic cells based on Kazakhstan silicon

I. Klinovitskaya^{1*}, D. Kalygulov¹, S. Plotnikov¹, P. Lay²

¹*D. Serikbayev East Kazakhstan Technical University, The Faculty of Energy, 69 Protozanov Street, 070004, Ust-Kamenogorsk, The Republic of Kazakhstan, iklinovitskaya@inbox.ru*

²*ECM Technologies, 46 rue Jean Vaujany – Technisud, F-38029 Grenoble, France*

The study of the solar cells properties is a relevant topic since development of solar energy meets the global demand and complies with the policy of the Government of the Republic of Kazakhstan on its transition to a "green" economy. Various properties of solar cells such carrier lifetime, reflectivity, and quantum efficiency affect the efficiency of solar cells directly. This study is devoted to obtaining and comprehensive study of solar cells manufactured on the basis of the Kazakhstan multicrystalline silicon of solar grade. The study applied: a method of microwave detected photoconductive decay (μ -PCD), a method of Light Beam Induced Current (LBIC), methods for spectrometric analysis of reflection, transmission and photoluminescence coefficients, scanning electron microscopy, and methods for analyzing current-voltage characteristics. Al BSF and PERC solar cells based on Kazakhstan silicon have been produced and analyzed. The study proposes modification of the standard Al-BSF line to the PERC line.

Keywords: solar cells, crystalline silicon, Al-BSF structure, PERC structure, solar energy

INTRODUCTION

Photovoltaic (PV) energy conversion is predicted to play an important part in the future power market, and the interest in this technology is increasing worldwide. Our need for energy will continue to rise, as The United Nations predict the world population growth from 7.7 billion today to 9.2 billion by 2040 [1]. In that regard, the global energy consumption will increase by 28% [2]. Solar energy is the most important and powerful source of energy available to humanity.

Crystalline silicon (c-Si) PV cells are the most common solar cells, accounting for about 90% of the total PV market share. This technology provides the highest energy conversion efficiencies of all commercial solar cells and are expected to continue to play a primary role in the future of PV market.

As part of the transition to a "green" economy, in 2010, Kazakhstan began to implement a project for the production of photovoltaic modules based on the Sarykol quartz deposit. The subject of the research is solar cells production.

The aim of this study is to investigate the properties, possible optimization strategies to achieve high-efficiency solar cells with advanced architecture. Investigation of properties makes it possible to identify the existing reasons for the decrease in the efficiency of solar cells and to determine methods for its improvement.

STANDARD BACK SURFACE FIELD (BSF) CELL ARCHITECTURE AND TECHNOLOGY

The standard BSF cell production technology includes several steps such as surface texturing, p-n junction creation by diffusion, emitter etching and phosphorus silicate glass (PSG) removal, antireflection coating (ARC) depositing by plasma-enhanced chemical vapor deposition (PECVD), metallization by screen-printing and firing. An overview of Standard Al BSF cell is given in Fig.1.

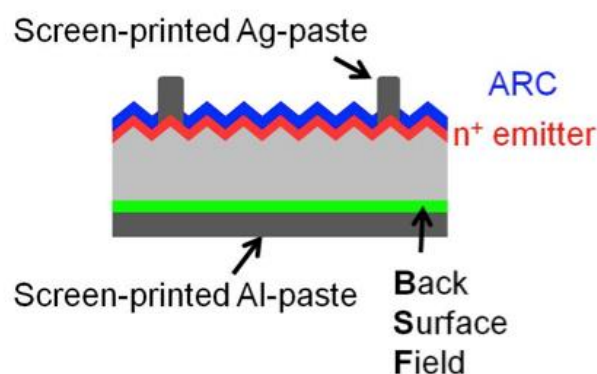


Fig.1. Standard Al BSF cell

Kazakhstan Solar Silicon LLP has implemented traditional production route of multicrystalline silicon (mc-Si) solar cells.

After wafering saw damages are removed and surfaces is normally textured in order to enhance light absorption. The next part of the fabrication is to form the p-n junction of the wafers. The substrate is p-type, so the junction is prepared by

* To whom all correspondence should be sent:
iklinovitskaya@inbox.ru

high-temperature diffusion of the n-type dopant, phosphorus, into the top surface. The dopant is deposited by exposure to nitrogen gas bearing phosphoryl chloride (POCl_3) at high temperature [3]. The front surface of the wafer is further textured to reduce reflectivity, by depositing an anti-reflection coating (ARC). Traditional ARC is silicon nitride (SiN_y) or titanium oxide (TiO_2). Introducing a highly doped region near the back contact will increase I_{sc} and V_{oc} , and the effect is called a back surface field (BSF). This is a way to accomplish low effective recombination [4]. The most efficient technique to produce the BSF has proved to be to screen print an aluminium-based paste onto the rear of the cell and alloy the aluminium into the silicon by a firing process. The last step of the cell fabrication is adding front and back metal contacts.

As is well known, the solar cell industry is facing constant pressure to optimize their cell manufacturing processes, aiming higher efficiencies while not increasing costs significantly.

While in the past most research aimed at increasing the efficiency of solar cells was carried out on the front (sunny) side of the cell, recently the PV industry has shifted its focus to the rear (back) side. Or to be precise, today it is a lot about passivating the rear surface of a solar cell and accordingly modifying the metallization scheme. These rather simple changes adapted to standard solar cell processing entitle the produced silicon slices for a new name – PERC, which stands for Passivated Emitter and Rear Cell. Global trends and the power of energy produced in 2016-2020 are also shifting towards PERC technology. As it was noted in [5], about 50% of all the produced "solar" energy by 2020 would have been attributed to the PERC.

PASSIVATED EMITTER AND REAR CELL (PERC) CELL ARCHITECTURE AND TECHNOLOGY

PERC is gradually becoming the most cost-efficient choice for mass production of cells, and offers a good approach to surpass the 20% cell efficiency level in mass production [6].

An overview of PERC structure is given in Fig.2. Although the conversion to the PERC structure only requires that a few pieces of equipment are added to the standard production line, the improvement of efficiency is not an absolute [6]. Both the emitter and the rear of the cell have to be redesigned because improving only

one of them will not increase the cell efficiency as the recombination losses at the other device part will dominate. Further, if both emitter and rear surface are improved, recombination in the base region becomes important. This is due to boron-oxygen complex formation, which will suppress the FF in the cell. This means that PERC design requires a finetuning of influencing parameters that are not linearly interrelated.

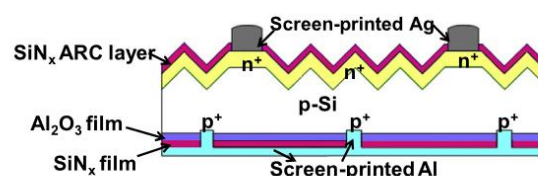


Fig.2. Schematic drawing of the industrial PERC cell structure [7]

The PERC design differs from the conventional full-area rear Al-alloyed BSF. As the recombination of the photo-generated charge carriers at the Al rear contact is only marginally suppressed and the Al layer only partly absorbs infrared light leading to poor light absorption, today's full areal Al-BSF industrial solar cells are limited to around 20% [8]. An important step towards industrialization of the PERC concept was to find a way to obtain low cost and high throughput processes for the deposition of the rear passivation layer. SiN_y deposited by PECVD maintained the most promising candidate for a long time, as this technology had already been established as a successful front side passivation layer of phosphorus doped emitter in industrial solar cells. However, as the rear surface is p type, it was discovered that SiN_y passivation layers induce an inversion of the surface due to the positive fixed charges within the SiN_y layer. This effect was identified by Dauwe et al. in 2002, and parasitic shunting leading to an enhanced carrier recombination was denoted [9].

A rear surface passivation material should have a high fixed negative charge, while at the same time having the ability to provide chemical passivation. Aluminum oxide meets these expectations. Rudolf Hezel and his team from the University of Erlangen-Nuremberg in Germany identified these excellent passivation properties of aluminum oxide back in 1989 [10]. What really makes aluminum oxide so special is its very high density of fixed negative charges of up to $10^{13}/\text{cm}^3$. Most of the other passivation films, such as silicon oxide and silicon nitride, have positive fixed charges. With aluminum oxide, the fixed charges are located right

at the interface between aluminum oxide and the interfacial silicon oxide grown on the silicon wafer during the deposition process, which ensures an effective field effect passivation. Aluminum oxide also scores high in chemical passivation. It acts as an effective hydrogen reservoir supplying hydrogen to saturate dangling bonds on the wafer surface during thermal treatment steps. As for the optical properties, these films with a band gap of 6.4 eV are transparent to the portion of sunlight that is relevant to solar cell applications. The only downside is its rather low refractive index of 1.65, which makes aluminum oxide less suitable for being a single layer antireflection film on the emitter side; however, the dielectric very well fulfills the job of back reflector.

EXPERIMENTS

Al-BSF cell fabrication and characterization

The wafers used for the study were 180–200 μm thick, 2 ohm.cm p-type mc-Si wafers. The wafers were the standard dimensions, 156*156 mm². Al-BSF mc-Si solar cells were fabricated to study the main properties and parameters.

We produced solar cells with a production feasible process flow outlined in Fig.3.

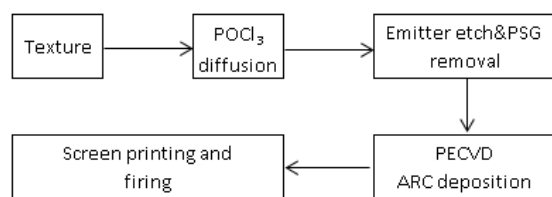


Fig.3. Process flow for industrial mc-Si cell fabrication

A solution of hydrochloric and nitric acids (HCl/HNO₃) was used to texturize the surface of the wafer, resulting in the formation of good textured structure, regardless of the orientation of the crystals. The wafers were treated in a solution of potassium hydroxide (KOH) to etch a layer of porous silicon, then, in order to etch metals, in a solution of hydrofluoric and hydrochloric acids (HF/HCl). The X-Rite SP62 spherical reflectometer was used to measure the reflectivity. Analysis of the surface morphology of silicon wafers before and after texturing was carried out by scanning electron microscopy on a JSM-6390LV microscope.

The emitter was formed using the diffusion method on Lydop equipment from Semco Engineering. Phosphorus doping was carried out at

a pressure slightly below atmospheric and at temperatures of 830–860°C. The phosphorus oxychloride (POCl₃) was used as a source of phosphorus, which is fed into the reactor along with nitrogen. The emitter, formed at a depth of 0.3–0.5 μm , has two functions: the formation of a p / n junction with the base and the transfer of electrons to metal grid. In order to assess the effect of gettering and measuring the lifetime of minority charge carriers, we used the method of measuring photoconductivity decay in the microwave range (μ -PCD) by WT-2000 PVN Semilab measuring system at a laser wavelength of 904 nm.

For the deposition of anti-reflective coating used method of Plasma-Enhanced Chemical Vapor Deposition (PECVD). The deposition of a film of silicon nitride was carried out in a vacuum chamber at a temperature of 350–450°C in the presence of silane (SiH₄) and ammonia (NH₃). The thickness of the obtained antireflection coating, measured by Semilab LE-200PV ellipsometer using the polarization-optical method, is around 75 nm.

A metal grid and busbars were applied by screen printing on Dubuit equipment. Silver-containing conductor paste with a specific resistance of less than 2 m Ω /sq and a viscosity of 16–23 Pa*s was used for front busbars and grids, and for rear current-collecting pads - silver paste with a resistance of 5 m Ω /sq and a viscosity of 89 Pa*s. For applying BSF (backside field), aluminum paste was used, with a resistance of 0.05 Ω /sq and a viscosity of 50 - 70 Pa*s.

PERC cell fabrication and characterization

The experiments were performed on diamond sawed mc-Si wafers. The wafers were the standard dimensions, 156*156 mm². Wafers used for PERC production were gallium doped.

We produced solar cells with a production feasible process flow outlined in Tab.1.

After SDR, wafers were textured and then treated with NaOH solution, creating pyramid-like texture. The front emitter was formed with POCl₃ diffusion. Edge isolation and rear side polishing were performed by a wet chemical process using HNO₃-HF-H₂SO₄ solution. The polishing time was 150 second. The rear polished surface will provide better light trapping and passivation opportunities. Polishing is important because if a uniform surface is achieved, this will improve the MACE with respect to homogeneity of the textured surface, and further achieving a well passivated surface with low enough reflectivity. The goal is to achieve smaller and shallower texture on nanoscale, meaning that

pore depth is reduced and pore diameter is decreased.

Table 1. Overview of production line

Step
1. Saw damage removal (SDR) and texturing
2. POCl ₃ diffusion
3. Wet chemical process of edge isolation and rear side polishing
4. Rear Al ₂ O ₃ + SiN _y coating
5. Front PECVD SiN _y coating
6. Laser ablation (rear contact pattern)
7. Screen printing metallization
8. RTP co-firing

Then the rear side of the cell was passivated by ALD Al₂O₃. The passivation layer was deposited by a trimethylaluminium (TMA)-based thermal ALD process, inducing an Al_xO_y layer. The post anneal process was implemented in a tube furnace. The thickness of the alumina oxide layer was 14 nm. The annealing time and temperature was 1800 seconds and 520°C. SiN_y coating was deposited by PECVD, capping the Al₂O₃-layer and surfaces were locally patterned using laser ablation. Finally, screen printing and co-firing were used for front and rear side metallization to form front Ag/n+-Si ohmic contact, Al-LBSF and rear local A/p+-Si ohmic contact.

RESULTS AND DISCUSSION

Al-BSF solar cells analysis

Fig.4 shows the obtained images of the surface of as cut wafers (Fig.4a), and after texturing (Fig.4b).

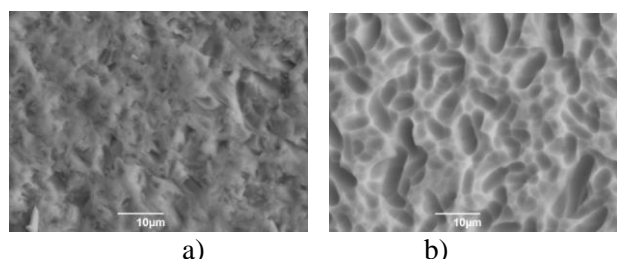


Fig.4. SEM - images of the silicon wafer surface: a) as cut; b) after texturing

As Fig.4a shows, the surface of the source wafer was severely damaged. It contains a huge number of cavities, microcracks and hills - this is the disturbed layer that was formed during the wafer production (wire wafer slicing process). Such a surface is simply destructive for the solar cells performance due to the extremely high surface recombination rate. After texturing and etching of

the wafer surface (Fig.4b), wells were formed, which leads to a significant decrease in reflectivity (Fig.5).

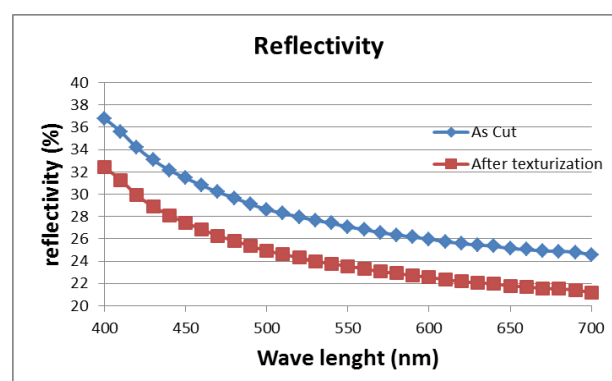


Fig.5. The reflectivity of as cut wafers and wafers after texturing, obtained by spherical spectrometry on an X-Rite SP62 reflectometer

In order to assess the effect of gettering, we carried out the study of the lifetime of charge carriers. The measurements were carried out before and after diffusion process. The lifetime mapping of minority charge carriers, as well as average values, was obtained by measuring the photoconductivity decay in the microwave range (μ -PCD) on the WT-2000 PVN measuring system. The method of measuring the decay of photoconductivity in the microwave range (μ -PCD) is a common method of measuring the lifetime of minority carriers in semiconductors. The method is highly reliable, good reproducibility and speed that provides the possibility of mapping the lifetime of a high-resolution. As the name of the method, it involves the optical excitation and detection of the signal with the microwave system. In this method, a silicon wafer is illuminated by a laser pulse, under the influence of which it generates electron-hole pairs. The transition process of disintegration of the carrier is tracked using a microwave signal. The recombination lifetime is a measure of the quality of the material, that is, the concentration of defects /impurities, which affects the quality of the resulting detectors and their electrical properties. μ PCD – non-destructive testing contactless method, which allows to map the recombination lifetime of the wafer as a whole to its selection for processing in order to obtain devices/detectors.

The study showed that the lifetime of charge carriers increased from 2 μ s (before the diffusion process) to 11.6 μ s (with a formed emitter after diffusion) (Fig.6). The trend shows the effect of gettering by diffusion.

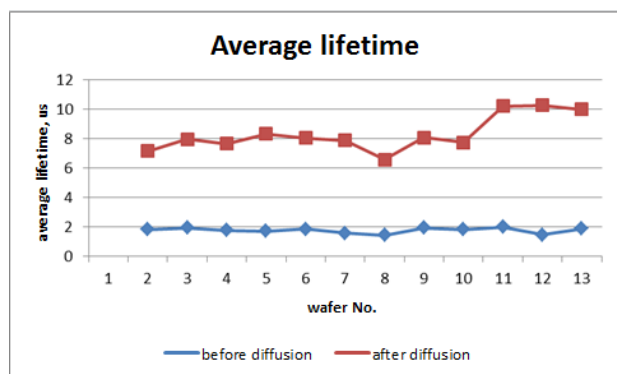


Fig.6. Lifetime trend

As can be seen in Fig.7, the lifetime is distributed more evenly, with the exception of the boundary zones, where an accumulation of lattice defects and recombination zones formed during the crystallization process occurred. It is known [12-15], that the surface of mc-Si wafer is a maximum possible disorder in the crystal lattice symmetry, resulting in increased surface recombination of charge carriers.

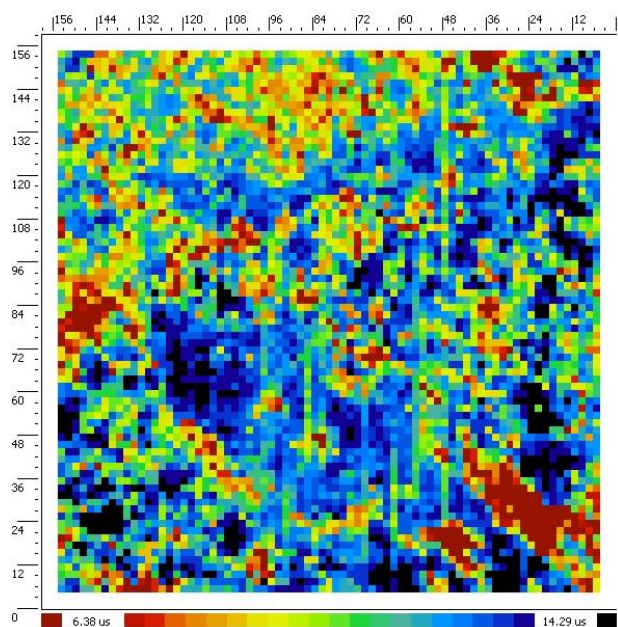


Fig.7. Lifetime Semilab map (scale 6.38-14.29 μs). average: 11.293 μs median: 11.89 μs deviation: 22.545% min: 2.16 μs max: 15.788 μs

Surface recombination can greatly affect the I_{sc} and V_{oc} . Surface recombination has a particularly detrimental effect on the short-circuit current (I_{sc}), since the front surface is also the region with the highest carrier generation in the solar cell. The reduction of high surface recombination is usually achieved by reducing the number of dangling bonds on the surface by passivating it. In this work, the surface was passivated using non-stoichiometric films with a large amount of hydrogen ($Si_xN_y:H$)

applied using the PECVD method. We used an ellipsometer Semilab LE 200PV to measure the thickness and refractive index of the films obtained. The refractive index is 2.05-2.06, and the thickness of the films obtained varies from 73 to 78 nm.

The study of the properties and parameters of silicon wafers and solar cells by the method of spectrometric analysis of photoluminescence was carried out at the National Institute of Solar Energy of France (INES). PL images of silicon wafers (Fig.8) and fabricated solar cells (Fig.9) were obtained by Luminescence Imaging System - Model LIS-R1.

The dark zones present in the PL images of silicon wafers (Fig.8) can be the sites of dislocation accumulations that occur during the crystallization of silicon ingots. These defects adversely affect the performance of solar cells.

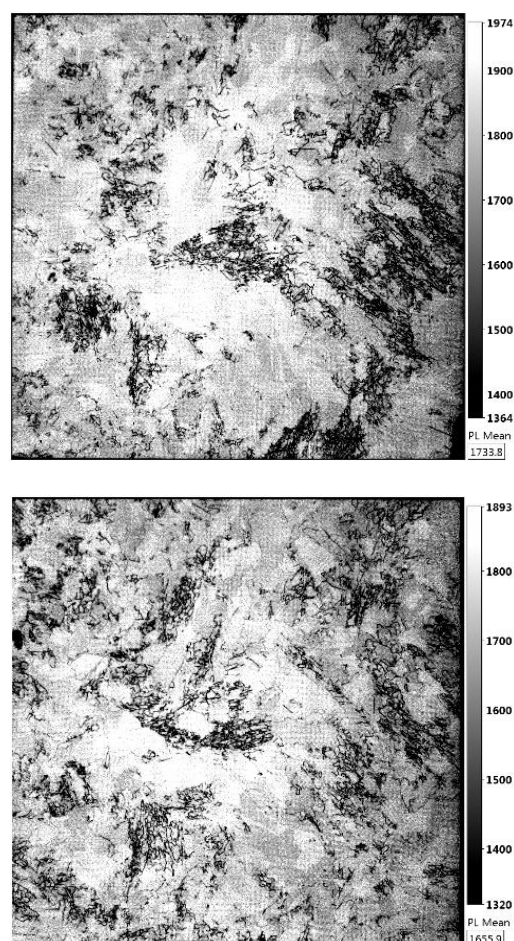


Fig.8. PL images of silicon wafers (samples 1, 10)

Analysis of the obtained PL images of solar cells (Fig.9) proved the assumption that the dark zones are the result of the accumulation of defects arising in the process of crystallization and do not occur as a result of the production of solar cells.

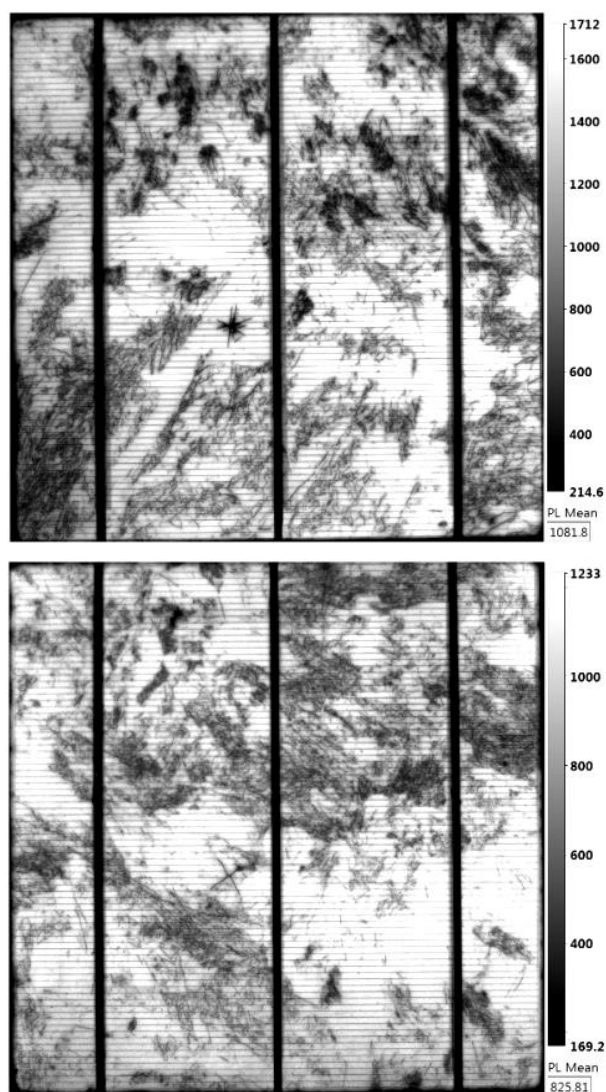


Fig.9. PL images of solar cells (samples 1, 10)

To measure the electrical parameters (current-voltage curves) (Isc short-circuit current, open circuit voltage Uoc, filling factor FF, maximum power Pmpp, efficiency), the Solar simulator ORIEL Sol3A CLASS AAA was used. The measurement results and the obtained current – voltage curves are presented in Tab.2 and in Fig.10.

Table 2. Electrical performance of Al-BSF solar cells

No.	Voc mV	Isc A	FF %	Rsh Ω	Eff %
400	610.3	8.5	76.80	102.3	15.83

Thus, the studied samples of solar cells of Kazakhstan production showed efficiency in the range from 15.6 ÷ 15.9%. Kazakhstan Solar Silicon LLP production requires an upgrade and process tuning.

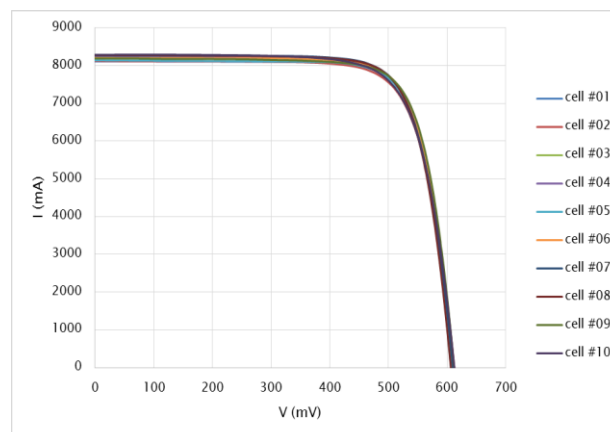


Fig.10. Current - voltage curves

PERC solar cells analysis

The results of PERC cells are presented in Tab. 3. An approximate average of the efficiency of all PERC solar cells is 19.78%.

Table 3. Electrical performance of PERC solar cells

No.	Voc mV	Isc A	FF %	Rsh Ω	Eff %
400	650	9.42	79.30	276.1	19.89

Internal quantum efficiency (IQE) is given in Fig.11. Measurement of short-circuit current in the external quantum efficiency was obtained on the Semilab WT-2000 PVN measuring system. The method is based on the principle of light a very small area of the solar cell with a laser beam that is focused directly on the surface of the solar cell. IQE is the ratio of the number of charge carriers collected by the solar cell to the number of photons of a given energy that shine on the solar cell from outside and are absorbed by the cell. It can be observed that the collection of carriers is higher for the optimized PERC by about 900-1000 nm. This is consistent with the literature, as the introduction of Al_2O_3 has been found to improve the optical reflectivity at the rear of the cell, and thereby to increase the absorption due to improved light-trapping, especially in the IR light region (700-1000 nm).

An important loss mechanism for PERC is bulk recombination. A possible solution to overcome this is to improve the phosphorus diffusion gettering, which can be done by optimizing the emitter doping process.

Further improvement of the PERC production line is necessary to reach the 24% limit. PERC design requires a finetuning of influencing parameters that are not linearly interrelated, thus it is a complicated matter to investigate.

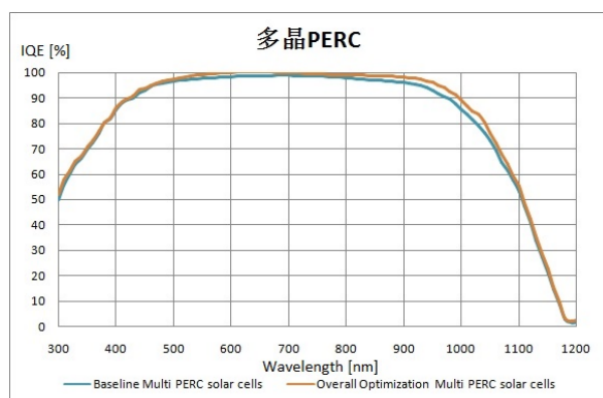


Fig.11. Internal quantum efficiency

Upgrade of standard line to PERC

Processing PERC involves depositing a rear surface passivation film, which is subsequently opened to give way for formation of a rear contact – these are two important additional steps over in Kazakhstan solar cell processing (Fig.12).

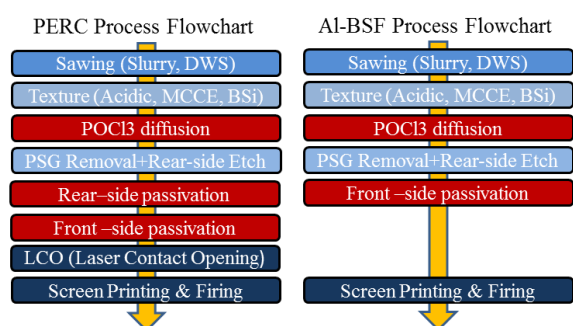


Fig.12. Process sequences for Production of PERC cells

In addition, the chemical wet-bench based edge isolation step is tweaked for rear polishing. That means texturing accomplished on both sides of the wafer is removed only on the rear side by etching off the pyramid structure. The degree of polishing changes from case to case. Thus, a passivation film deposition system and a film opening system - mainly accomplished with PECVD and lasers - are additional tool sets typically hooked up to standard cell processing lines.

A cell line for PERC technology requires only two pieces of additional equipment compared to a standard line – devices for rear passivation and laser structuring. This means upgrades to PERC are simple.

Kazakhstan Solar Silicon LLP has equipment for anti-reflective coating (silicon nitride) deposition TWYN PECVD. The PECVD process consists of the decomposition of a chemical element under the influence of plasma and temperature into individual elements in the reactor,

which then settle to the surface of the wafer and enter a chemical reaction. As a result, the film (up to 80 nm) of silicon nitride, which has the required properties, is “grown” on the front surface of the wafer. PECVD equipment can be modified to apply a rear passivation layer (AlOx + SixNy), while the general principle of deposition remains the same. Introducing a trimethylaluminum (TMA) precursor and adaption of the cleaning mechanism are more or less the two main fundamental changes that PECVD systems are required to undergo to be able to apply aluminum oxide films on the rear side of the cell. Not only the generic deposition principle of PECVD stays the same, which is the radio frequency (RF) power used to dissociate precursors at low pressure and which leads to depositing the required film on the substrate present in the chamber. Even the equipment makers’ proprietary plasma generating mechanisms do not need to be changed. One inherent advantage of PECVD systems over ALD tools is the capability to deposit the silicon nitride capping layer on top of aluminum oxide in one system without breaking the vacuum. That means the complete rear passivation process is executed in one pass.

The easiest way to open the rear passivating layer is to utilize laser technology. This step is generally called laser contact opening (LCO). Today, the photovoltaic industry has a large number of laser solutions offered by companies such as InnoLas Solutions, Rofin, 3D-Micromac, Schmid or Manz.

Like any other advanced cell technology, PERC requires a special metallization paste system. The most critical metallization product is a BSF paste. A suitable aluminum paste does not react on those areas where it covers the passivation layer, but at the same time it establishes contacts at areas opened with lasers to create a local BSF. A nonreactive rear tabbing silver paste is required as well. The attributes for such pastes are twofold: It should not fire through the passivation layer and it should exhibit good adhesion and solderability. Technically speaking, only special rear tabbing and BSF pastes are required for PERC cells, while the standard front contacting paste can be applied on the emitter side as well. However, taking into consideration the fact that PERC cells need to be processed at relatively low temperatures, paste suppliers are also promoting dedicated front contacting paste for this technology. The local BSF can be implemented in many ways. The standard is to have the laser contact opening the line pattern. There is potential to improve efficiency when a dot

or dashed pattern is applied for rear passivation stack opening. This reduces bulk resistivity of the rear contact as the silver paste is not spread all over. Toyo is offering such special aluminum pastes. The company is using silicon doped aluminum pastes which facilitate alloy formation during rear contact realization, thereby improving effectiveness of contact formation. There is another important improvement in the PERC segment, as the first cell manufacturers are working on having aluminum oxide on both sides of the wafer. Adding aluminum oxide on the emitter side requires paste optimization, as the paste has to penetrate through an extra layer of dielectric film.

CONCLUSIONS

The results based on all experiments were combined to investigate the total effect of the upgrading of production line. The results are presented in Tab. 4. It is possible to observe that the upgrade of standard line to PERC was successful, and a champion efficiency above 19% achieved.

Further improvement of the PERC production line is necessary to reach the 24% limit. PERC design requires a finetuning of influencing parameters that are not linearly interrelated.

Table 4. Cell performance of Al-BSF and PERC solar cells based on Kazakhstan Silicon

Group	Voc mV	Isc A	FF %	Rsh Ω	Eff %
PERC	650	9.42	79.30	276.1	19.89
Al-BSF	610.3	8.5	76.80	102.3	15.83

At Kazakhstan Solar Silicon LLP it is possible to switch from Al-BSF standard solar cell production line to the PERC line, which will allow the company to increase the efficiency of the produced solar cells and be competitive in the global market.

REFERENCES

- [1] Department of Economic and Social Affairs. World population prospects: *The 2018 revision*.
- [2] US Energy Information Administration. *International energy outlook 2018*, (2018).
- [3] K. Murugesan, S. Kumbhar, A. K. Kapoor, A. Dhaval, S. Saravanan, R. Pinto, B. M. Arora. POCl diffusion process optimization for the formation of emitters in the crystalline silicon solar cells. *IEEE 40th PV Specialists conf. IEEE*, (2014).
- [4] Martin A Green. *Solar cells: operating principles, technology and system applications*, 1992.
- [5] Jenny Nelson. *The physics of solar cells*. Imperial College Press, London, 2003.
- [6] Matthias Byungul Min, Hannes Muller, Gerd Wagner, Rolf Fischer, Pietro P. Brendel, Holger Altermatt, and Holger Neuhaus. A roadmap toward 24% efficient perc solar cells in industrial mass production. *Photovoltaics, IEEE Journal of*, **7 (6)**, 1541–1550, (2017).
- [7] Haibing Huang, Jun Lv, Yameng Bao, Rongwei Xuan, Shenghua Sun, Sami Sneek, Shuo Li, Chiara Modanese, Hele Savin, Aihua Wang, and Jianhua Zhao. 20.8 efficiency loss mechanisms analysis and roadmap to 24. *Solar Energy Materials and Solar Cells*, **161**, 14–30, (2017).
- [8] Thorsten Dullweber and Jan Schmidt. Industrial silicon solar cells applying the passivated emitter and rear cell (perc) concept, review. *Photovoltaics, IEEE Journal of*, **6 (5)**, 1366–1381, (2016).
- [9] S. Dauwe, L. Mittelstädt, A. Metz, R. Hezel. Exp. evidence of parasitic shunting in silicon nitride rear surface passivated solar cells. *Progress in PV: Research and Appl.*, **10 (4)**, 271–278, (2002).
- [10] R. Hezel, K. Jaeger Low-Temperature Surface Passivation of Silicon for Solar Cells Solid-State Science and Technology - *TECHNICAL PAPERS J. Electrochem. Soc.* **136 (2)**, 518-523 (1989).
- [11] D. Schroder, Semiconductor material and device characterization, *3rd edition ed. Piscataway NJ; Hoboken N.J.: IEEE Press; Wiley*, (2006).
- [12] Jan Schmidt, Robby Peibst, Rolf Brendela Surface passivation of crystalline silicon solar cells: Present and future. *Solar Energy Materials and Solar Cells* **187**, 39-54 (2018).
- [13] Jae Eun Kim, Se Jin Park, Ji Yeon Hyun, Hyomin Park, Soohyun Bae, Kwang-sun Ji Hyunho, Kim Kyung Dong Lee, Yoonmook Kang, Hae-Seok Lee, Donghwan Kim Characterization of SiNx:H thin film as a hydrogen passivation layer for silicon solar cells with passivated contacts. *Thin Solid Films* (2019).
- [14] J. A. Silva, A. Lukianov, R. Bazinette, D. Blanc-Pélissier, Julien Vallade, Sylvain Pouliquen, Laura Gaudy, Mustapha Lemiti, Françoise Massines Feasibility of Antireflection and Passivation Coatings by Atmospheric Pressure PECVD. *Energy Procedia* **55**, 741-749 (2014).
- [15] L. E. Blacka, B. W. H. van de Loo, B. Macco, J. Melskens, W. J. H. Berghuis, W. M. M. Kessels Explorative studies of novel silicon surface passivation materials: Considerations and lessons learned. *Solar Energy Materials and Solar Cells* **188**, 182-189 (2018).
- [16] S. Plotnikov, D. Kalygulov, I. Klinovitskaya Research of the production technology of photovoltaic cells. *Bulletin D. Serikbayev EKSTU* **4 (78)**, 67-73 (2017).

Radiation modification of $\text{BaCe}_{0.85}\text{Nd}_{0.15}\text{O}_{3-\delta}$

I.V. Khromushin¹, Yu.V. Yermolaev^{2,3*}, N.K. Kasmamyrov³, T.I. Aksenova¹,
T. Tusseyev⁴, L.A. Stanbay⁴

¹ Institute of Nuclear Physics of the Republic of Kazakhstan, Almaty, 1 Ibragimov st., Kazakhstan,

² Kazakh National Technical University, Almaty, 22 Satpayev st., Kazakhstan

³ Institute of Physics NAS of the KR, Bishkek, 265-A Chui Ave., Kyrgyzstan

⁴ Al-Farabi Kazakh National University, Almaty, 71 Al-Farabi Ave., Kazakhstan

The effect of irradiation with electrons and ions of inert gases (Ne, Ar, Kr) and oxygen of various energies on the structure, surface state and gaseous components in $\text{BaCe}_{0.85}\text{Nd}_{0.15}\text{O}_{3-\delta}$ has been studied. It was shown that electron irradiation of $\text{BaCe}_{0.85}\text{Nd}_{0.15}\text{O}_{3-\delta}$ results in smoothing-out of the irradiated surface relief, while electron irradiation of BaCeO_3 led to formation of a fine pyramidal (needle-shaped) structure on the irradiated surface. It was noted that in case of $\text{BaCe}_{0.85}\text{Nd}_{0.15}\text{O}_{3-\delta}$ irradiation with high-energy inert gas ions, solid-phase transformations occurred on the surface of $\text{BaCe}_{0.85}\text{Nd}_{0.15}\text{O}_{3-\delta}$. The conclusion was made about the mechanism of the influence of irradiation with high and low energy heavy ions of inert gases on the state of the gaseous components in $\text{BaCe}_{0.85}\text{Nd}_{0.15}\text{O}_{3-\delta}$, based on the features of defects formation under irradiation with the ions of different energies.

Keywords: Proton conductivity, barium cerate, radiation modification, inert gas ions

INTRODUCTION

Currently, active research is being conducted in the area of hydrogen energy. Fuel cells based on solid proton-conducting electrolytes with the ABO_3 perovskite structure, capable of directly converting the chemical energy of hydrogen into electrical energy, are considered as one of the most promising alternative sources of electricity [1, 2].

In the initial state, the perovskite of the ABO_3 type is a dielectric and to give it the properties of proton conductivity, the so-called acceptor doping is traditionally performed, that is, the tetravalent cation at position B is partially replaced by the trivalent rare earth element Re, resulting in formation of oxygen vacancies $\text{V}^{\bullet\bullet}$ with an effective charge of +2 in the lattice. The newly formed compound can be written as follows: $\text{AB}_{1-x}\text{Re}_x\text{O}_{3-\delta}$, where x is the concentration of the trivalent cation or the degree of doping, and $\delta = x/2$ is the concentration of oxygen vacancies. When doped perovskite is exposed in a humid atmosphere, dissociative dissolution of water vapor takes place in the barium cerate lattice in accordance with reaction (1).



The diffusion of protons to the oxygen ions provides the proton conductivity of the oxide.

A deterrent to the widespread use of fuel cells based on proton conductors is currently the high cost of electricity produced due to the high cost of fuel and fuel cell materials, their low stability and efficiency. Therefore, an active search for materials of highly efficient and stable electrolytes is currently in progress. The main focus here is the synthesis of new compounds with the property of proton (ionic) conductivity.

In recent years, there have been proposed to increase the efficiency of ionic conductors through their radiation modification [3-5].

Earlier we have reported some results on influence of irradiation [7] and cation dopant type on structure and properties of barium cerates [9, 10].

In this paper the new results on effect of irradiation with electrons, as well as oxygen, neon, argon and krypton ions of various energies on the structure and properties of $\text{BaCe}_{0.85}\text{Nd}_{0.15}\text{O}_{3-\delta}$ are presented.

EXPERIMENTAL TECHNIQUE

Samples of ceramic $\text{BaCe}_{0.85}\text{Nd}_{0.15}\text{O}_{3-\delta}$ in the form of plates of 10x5x1 mm size were preliminarily annealed in air at the temperature of 650°C for 7 hours.

Some of the samples were irradiated with heavy ions at the accelerator DC-60 of the Institute of Nuclear Physics of the Republic of Kazakhstan, Astana. Tab.1 shows the irradiation characteristics, as well as the ion ranges and

* To whom all correspondence should be sent:
vicnadyerm@mail.ru

damages, calculated using the SRIM - 2013 software [6].

Table 1. Results of calculations of the ion ranges and the concentration of vacancies

High energy			
Ion type	Ion energy, [MeV]	Ion range, [μm]	Vacancy/ion
Ne ⁺	35	12.7	2700
Ar ⁺	70	13.2	8100
Kr ⁺	147	15.3	31000
O ⁺	28	13.3	1740
Low energy			
Ion type	Ion energy, [keV]	Ion range, [μm]	Vacancy/ion
Ne ⁺	40	0.065	320
Ar ⁺	100	0.080	800
Kr ⁺	260	0.108	2500
O ⁺	40	0.080	243

Along with this, some of the samples were irradiated with 1.3 MeV electrons at the accelerator ELV-4 of the INP RK up to doses of 1.0, 5.0, 10.0 and 14 MGy. The calculations showed that the maximum temperature of the irradiated face of the sample did not exceed 372 K.

In this work, the following methods were used: X-ray phase analysis using the diffractometer X'PertPRO, scanning electron microscopy with the microanalyzer JEOL JSM-6490, atomic force microscopy NT-MDT, thermal desorption spectroscopy using the RF mass spectrometer MX-7304, thermal analysis using the thermal analyzer EXSTAR -6000.

RESULTS AND DISCUSSION

X-ray phase analysis of the initial $BaCe_{0.85}Nd_{0.15}O_{3-\delta}$ samples annealed in air at 650°C showed that their structure corresponds to the perovskite structure of undoped $BaCeO_3$. Irradiation of $BaCe_{0.85}Nd_{0.15}O_{3-\delta}$ with low-energy inert gas ions ($E=40 - 260$ keV) to doses of 10^{16} cm⁻² did not have a significant effect on the structure and parameters of the crystal lattice of the material. Also, no changes in the structure of $BaCe_{0.85}Nd_{0.15}O_{3-\delta}$ were found after irradiation with low-energy oxygen ions and electrons. Irradiation of $BaCe_{0.85}Nd_{0.15}O_{3-\delta}$ with the high-energy ions of inert gases led to partial amorphization of the irradiated surface of the material, while the non-irradiated side retained the original structure [7].

The study of the surface morphology of irradiated $BaCe_{0.85}Nd_{0.15}O_{3-\delta}$ by scanning electron microscopy showed that, depending on the type and energy of the ion, the surface of the

ceramics undergoes significant changes. Thus, the irradiation of the samples with low-energy neon ions led to formation of blisters on the surface of the complex oxide (Fig.1).

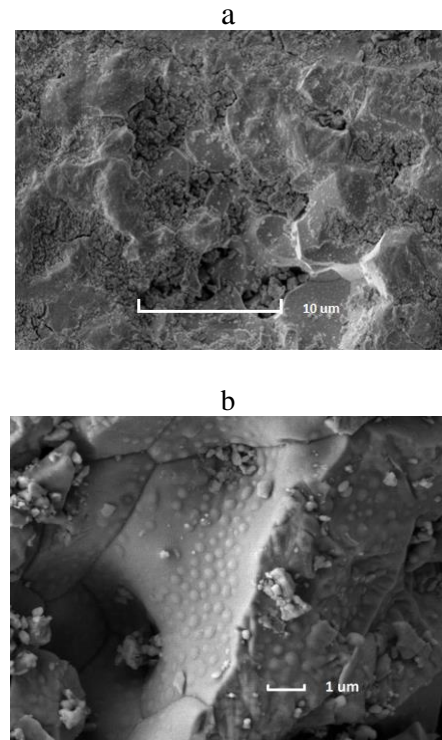
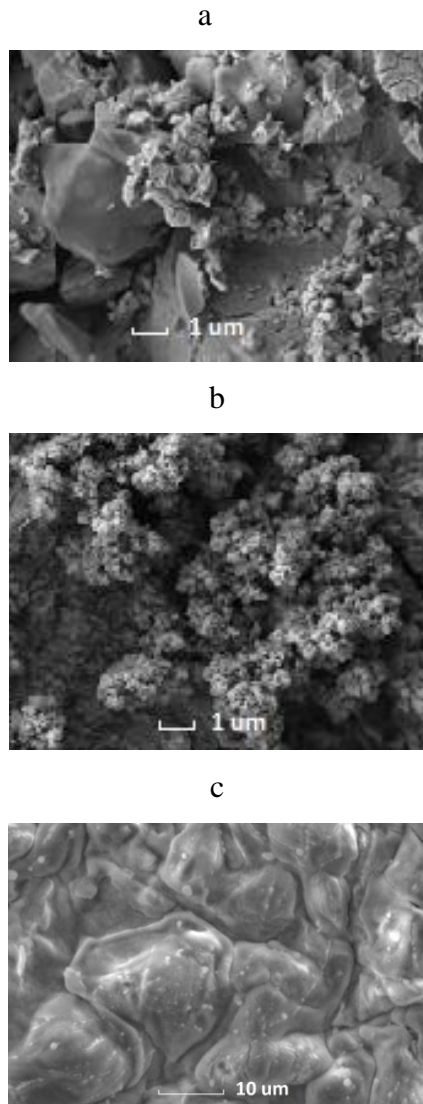


Fig.1. Electron microscopic images of the surface of barium cerate: a - unirradiated sample; b - irradiated with neon ions (40 keV, 10^{16} cm⁻²)

In case of $BaCe_{0.85}Nd_{0.15}O_{3-\delta}$ irradiation with high-energy inert gases, there were changes apparently caused by the solid-state structural transformations on the surface, and in the series Ne, Ar, Kr the surface of the cerate resembled the growth stages of spherulites — nucleation, growth and formation of spherulitic crust (Fig.2).

It should be noted that after irradiation with high-energy oxygen ions, no similar changes in the structure and surface state of the barium cerate were observed, which indicates, apparently, the peculiarities of defect formation in case of cerate irradiation with the ions of inert gases and oxygen and, probably, due to the difference in their solubility. It is assumed that in the first case, the material is oversaturated with lattice defects by means of their stabilization by the ions of inert gas with formation of the “inert gas-vacancy” complexes. These complexes are highly stable due to low solubility of inert gases in the materials. This is confirmed by the absence of inert gases release from the samples in the experiments of thermal desorption up to 1000°C.



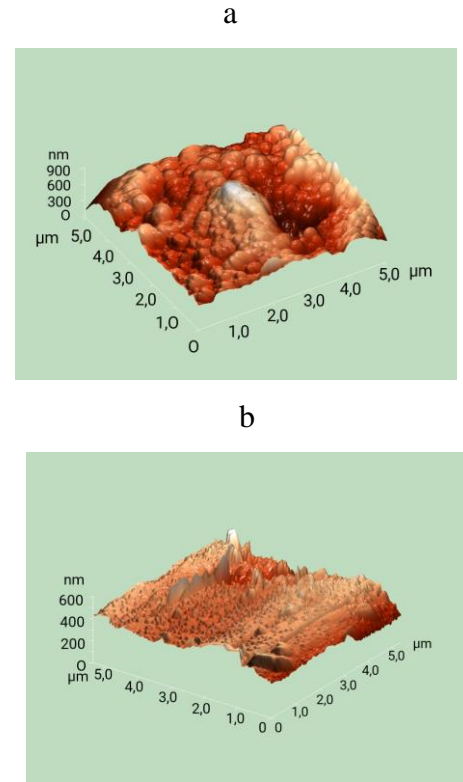
a – Ne, b – Ar, c – Kr ($D = 10^{16} \text{cm}^{-2}$)

Fig.2. Electron microscopic images of the surface of barium cerate irradiated with high-energy inert gas ions

In case of irradiation of the composite oxide with the high-energy ions of oxygen at elevated temperatures, the equilibrium concentration of defects should be significantly lower. Indeed, the solubility of oxygen in cerate is significantly higher than that of inert gases, and when irradiated at elevated temperatures, oxygen can leave the material as a result of its diffusion to the surface and subsequent desorption. In this case, the stabilization of the defect structure does not occur, and a significant part of the defects, formed during irradiation, is annealed under irradiation.

It turned out that the surface relief of the samples, irradiated with electrons, depended substantially on their composition. Thus, electron irradiation of $BaCe_{0,85}Nd_{0,15}O_{3,8}$ led to a smoothing of the surface relief, while electron

irradiation of $BaCeO_3$ led to formation of a small pyramidal (needle) structure on the surface of the complex oxide (Fig.3). The height of the "pyramids" in this case did not exceed 50 nm.



a – unirradiated; b – electron irradiated.

Fig.3. AFM images of undoped barium cerate

Studies of the processes of thermal desorption of gases from barium cerate doped with Nd were carried out at the gas release unit described in details in [7]. Partial pressures of oxygen and water molecules were recorded with mass-spectrometer as a function of temperature during sample heating. This device allows to register up to 6 different gases simultaneously.

The conditions for the experiments on thermal desorption are as follows: the working vacuum in the chamber is no worse than 10^{-8} mm Hg, the heating rate of the samples is $42^\circ\text{C}/\text{min}$.

According to the thermal desorption spectroscopy data, irradiation with low-energy oxygen ions practically did not affect the state of the gaseous components, as evidenced by the fact that irradiation did not affect the thermal desorption of O_2 and H_2O .

At the same time, irradiation of $BaCe_{0,85}Nd_{0,15}O_{3,8}$ with both low-energy and high-energy ions of inert gases had a significant impact on the thermal desorption of oxygen and water molecules. First of all, we should note a

significant rise in the amount of desorbed oxygen from the $BaCe_{0.85}Nd_{0.15}O_{3-\delta}$ samples irradiated with the low-energy ions of inert gas (dose 10^{16} ions/cm²) compared with the non-irradiated samples. As it turned out, the amount of released oxygen from the samples, irradiated with different ions, was approximately the same (Fig.4).

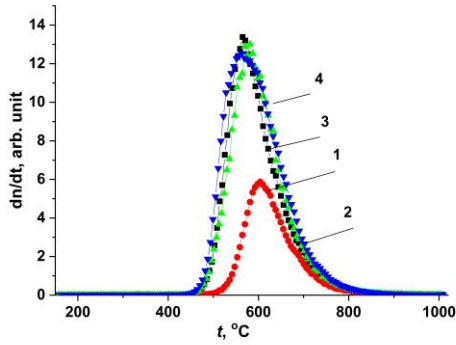


Fig.4. Oxygen release spectra from $BaCe_{0.85}Nd_{0.15}O_{3-\delta}$ after irradiation with low-energy ions: 1 – non-irradiated sample; 2 – irradiated with Ne ions; 3 – Ar; 4 – Kr ($D = 10^{16}$ cm⁻²)

Irradiation of $BaCe_{0.85}Nd_{0.15}O_{3-\delta}$ with high-energy ions of inert gases, on the contrary, caused a decrease in the amount of desorbed oxygen compared to the unirradiated sample. It should be noted that the amount of desorbed oxygen decreased with a decrease in the mass of the implanted ion (Fig.5).

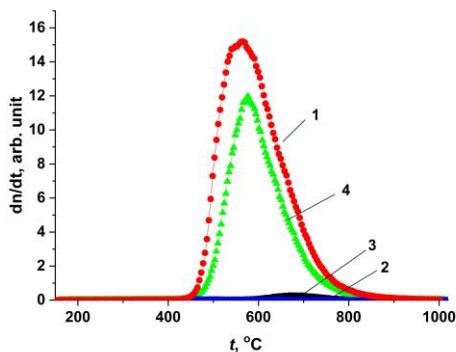


Fig.5. Oxygen release spectra from $BaCe_{0.85}Nd_{0.15}O_{3-\delta}$ after irradiation with high-energy ions: 1 – unirradiated sample, 2 – irradiated with Ne ions, 3 – Ar, 4 – Kr ($D=10^{16}$ cm⁻²)

Irradiation of $BaCe_{0.85}Nd_{0.15}O_{3-\delta}$ samples with the low-energy ions of inert gases led to a significant decrease in the amount of desorbed water compared to the non-irradiated sample. As in the case of desorption of oxygen molecules, the amount of desorbed water from the samples, irradiated with different ions, was also approximately the same (Fig.6).

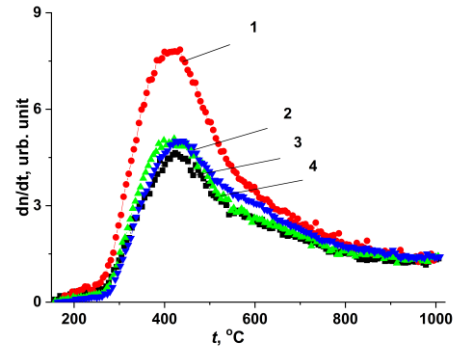


Fig.6. Water release spectra from $BaCe_{0.85}Nd_{0.15}O_{3-\delta}$ after irradiation with low-energy ions: 1 – non-irradiated sample; 2 – irradiated with Ne ions; 3 – Ar; 4 – Kr ($D = 10^{16}$ cm⁻²)

The opposite situation was observed when $BaCe_{0.85}Nd_{0.15}O_{3-\delta}$ was irradiated with the high-energy ions, i.e., the amount of water, desorbed from the irradiated sample, was more than that from the non-irradiated one. It should be noted that the maximum amount of water was released from the sample irradiated with the ions of neon (Fig.7). In this case, an insignificant low-temperature yield of water was observed in the spectra of thermal desorption of the irradiated samples.

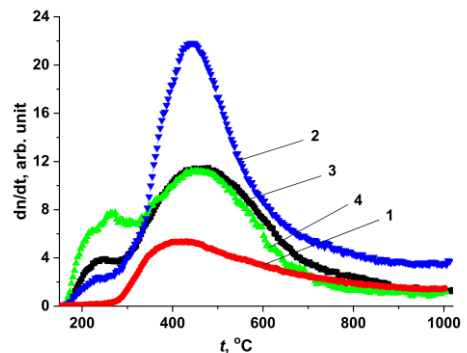
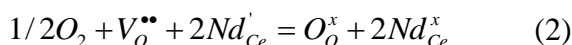


Fig.7. The spectra of water release from $BaCe_{0.85}Nd_{0.15}O_{3-\delta}$ after irradiation with high-energy ions: 1 – non-irradiated sample, 2 – irradiated with Ne ions, 3 – Ar, 4 – Kr ($D=10^{16}$ cm⁻²)

It should be noted that a feature of barium cerate, doped with neodymium, is the presence of superstoichiometric oxygen. This conclusion was first made in [8] when studying the oxygen nonstoichiometry of barium and strontium cerates, doped with neodymium and yttrium, respectively. It was shown that in the dry atmosphere, the oxygen index of $BaCe_{0.9}Nd_{0.1}O_{3-\delta}$ was higher than that expected in a wide range of temperatures and partial pressures of oxygen. At the same time, under similar conditions, the oxygen index of $SrCe_{0.95}Y_{0.05}O_{3-\delta}$ was close to

the expected value of 2.975. The excess oxygen found in BaCe_{0.9}Nd_{0.1}O_{3-δ} was called superstoichiometric by the authors, and its appearance was attempted to be explained by the structural features of this oxide. In [9], we obtained confirmation of the presence of superstoichiometric oxygen in barium cerate doped with neodymium. Later we showed that superstoichiometric oxygen is present only in barium cerate doped with Nd, and absent in barium cerate doped with Sm, Gd or Y [10]. Along with this, it was noticed that the amount of water in the sample, doped with neodymium, was less than in the samples with other dopants. In [11], it was concluded that Nd in these compounds can show a mixed valence of +3 and +4, and when annealing of the neodymium doped barium cerate in the oxygen containing atmosphere, part of the trivalent neodymium is oxidized according to equation (2), reducing the concentration of oxygen vacancies:



As the temperature rises in a reducing atmosphere, neodymium is reduced to Nd⁺³ state. Obviously, reduction of Nd⁺⁴ should be accompanied by the release of oxygen in the temperature range of reduction, as observed in the thermal desorption experiments. At the same time, the amount of superstoichiometric oxygen in the neodymium doped barium cerate should be proportional to the amount of tetravalent neodymium in it.

The obtained regularities of the effect of irradiation with low and high energy ions of inert gases on thermal desorption of oxygen and water molecules from BaCe_{0.85}Nd_{0.15}O_{3-δ} can be explained by the change in Nd³⁺/Nd⁴⁺ ratio in barium cerate during irradiation.

Thus, the revealed increase in the amount of desorbed oxygen after low-energy irradiation probably indicates the increase in the proportion of neodymium in the 4+ state in the irradiated sample. Apparently, this can be explained by the fact that low-energy irradiation leads to a significant increase in concentration of oxygen vacancies, which, in turn, leads to the increase in the equilibrium constant of the quasi-chemical equation (2) and, as a result, the concentration of Nd⁴⁺. Since the amount of released oxygen practically does not depend on the type of ion, it can be concluded that under these irradiation conditions, the concentration of vacancies in the sample reaches saturation. The decrease in the concentration of Nd³⁺ should lead to the decrease in the concentration of protons in the

sample, which is observed in the thermal desorption experiment (Fig.6).

If BaCe_{0.85}Nd_{0.15}O_{3-δ} is irradiated with high-energy ions of inert gas, the observed decrease in the concentration of superstoichiometric oxygen (Fig.5) is probably caused by the decrease in the fraction of Nd⁴⁺ in the series Kr, Ar, Ne. The latter can be explained by the peculiarities of defect formation under irradiation with the high-energy ions, in particular by the fact that at high energies of the ions, electronic defects make a significant contribution to the Nd⁴⁺ fraction. The increase in the fraction of trivalent neodymium should be accompanied by the increase in the concentration of protons in the sample and, as a consequence, the increase in the amount of desorbed water (Fig.7).

CONCLUSIONS

The features of the effect of irradiation type on the state of the BaCe_{0.85}Nd_{0.15}O_{3-δ} surface are revealed.

It was shown that the irradiation of BaCe_{0.85}Nd_{0.15}O_{3-δ} with electrons leads to smoothing of the irradiated surface relief, while electron irradiation of undoped BaCeO₃ led to formation of a small pyramidal structure on the irradiated surface of the complex oxide.

It was noticed that in case of BaCe_{0.85}Nd_{0.15}O_{3-δ} irradiation with the high-energy ions of inert gases, the solid-phase transformations took place on the surface of BaCe_{0.85}Nd_{0.15}O_{3-δ}, and in the series Ne, Ar, Kr the surface of the composite oxide resembled the spherulite growth stages — nucleation, growth and formation of spherulitic crust.

According to the data of thermal desorption spectroscopy, a conclusion was made about the mechanism of influence of irradiation with heavy ions of inert gases of high and low energy on the state of the gaseous components in BaCe_{0.85}Nd_{0.15}O_{3-δ}. The mechanism is based on the features of defect formation under irradiation with the ions of different energies, which determine the Nd³⁺/Nd⁴⁺ ratio in the BaCe_{0.85}Nd_{0.15}O_{3-δ} lattice and, as a consequence, the state of the gaseous components.

Study of the conducting properties of the irradiated BaCe_{0.85}Nd_{0.15}O_{3-δ} is in progress and the results will be reported later.

ACKNOWLEDGEMENTS

This work was supported by the Ministry of Education and Science of the Republic of

Kazakhstan (Grant AP05130148), which is gratefully acknowledged by the authors.

REFERENCES

- [1] H. Iwahara, H. Uchida, N. Maeda. High temperature fuel cell and steam electrolysis cells using proton conducting solid electrolytes. *J. Power Sources* **7**, 293-301 (1982).
- [2] T. Shober. Applications of oxidic high-temperature proton conductors. *Solid State Ionics* **162-163**, 277-281 (2003).
- [3] J.-H. Kim, B. Tsuchiya, S. Nagata, T. Shikama. Effect of ion beam surface modification on proton conductivity of $BaCe_{0.9}Y_{0.1}O_{3-y}$. *Solid State Ionics* **179**, 1182-1186 (2008).
- [4] B. Tsuchiya, A. Morono, E.R. Hodgson, S. Nagata, T. Shikama. Change in hydrogen absorption characteristic of $SrCe_{0.95}Yb_{0.05}O_{3-\delta}$ by electron beam modification. *Solid State Ionics* **179**, 909-912 (2008).
- [5] J.-H. Kim, H. Choib, T. Shikama. Effect of Ar^+ irradiation on the electrical conductivity of $BaCe_{0.9}Y_{0.1}O_{3-\delta}$. *Applied Surface Science* **257**, 8876-8882 (2011).
- [6] J.F. Ziegler, J.P. Biersack, M.D. Ziegler. SRIM - The Stopping and Range of Ions in Matter, 2012, 398 p.
- [7] I.V. Khromushin, T.I. Aksenova, T. Tuseyev, K.K. Munasbaeva, Yu.V. Yermolaev, V.N. Yermolaev, A. S. Seitov. Modification of barium cerate by heavy ion irradiation. *Advance Materials Research* **781-784**, 357-361 (2013).
- [8] K.Kishio, in: Dynamics of Fast Ions in Solids and Its Evolution for Solid State Ionics, Report of a Priority Area Research Program (FY 1995-1997), National Science Foundation, Tokyo Regional Office, 1998 Sept., pp. 23-26.
- [9] T. I. Aksenova, I.V. Khromushin, Zh.R. Zhotabaev, K.D. Bukenov, A.K. Berdauletov, Z.V. Medvedeva. Thermodesorption study of barium and strontium cerates. *Solid State Ionics* **162-163**, 31-36 (2003).
- [10] I.V. Khromushin, T.I. Aksenova, and Yu.M. Baikov. Regularities of oxygen and water thermal desorption from barium cerate doped by neodymium, samarium, and gadolinium. *Russian J. of Electrochemistry* **53**, 647-650 (2017).
- [11] M. Oishi, K. Yashiro, J. Mizusaki, N. Kitamura, K. Ameszawa, T. Kawada, Y. Uchimoto. Oxygen nonstoichiometry of perovskite-type oxides $BaCeMO_{3-y}$ (M= Y, Yb, Sm, Tb and Nd). *Solid State Ionics* **179**, 529-535 (2008).

Simulations of the macroscopic energy migration diffusion characteristics in upconversion core-shell nanostructures

J. F. Liu, T. R. Fu*

Tsinghua University, Department of Energy and Power Engineering, Key Laboratory for Thermal Science and Power Engineering of Ministry of Education, Beijing, China

Lanthanide-doped upconversion nanostructures have attracted much attention due to their excellent upconversion capabilities to convert low energy photons to high energy photons for a wide variety of optical applications. Although classical macroscopic rate equations have been used to describe the dominant upconversion energy transfer mechanism between the sensitizers and activators by assuming infinitely fast energy migration, these models still do not accurately characterize the upconversion dynamics of core-shell nanostructures. Therefore, this paper models the upconversion luminescence in core-shell nanostructures using improved macroscopic rate equations that simultaneously consider the energy migration and energy transfer. The macroscopic model provides an effective way to design the upconversion luminescence characteristics of core-shell nanostructures from fundamental insights that is more convenient than other simulation or microscopic models. The model was used to study NaYF₄: Yb³⁺, Er³⁺ core-shell nanostructures. The energy migration characteristics among the sensitizers in the core-shell nanostructure were analyzed to understand the upconversion emission decay lifetimes, emission intensities and time-resolved spatial gradients of the excited ion population density that depend on the structure, shell thickness and excitation power. The analysis provides further understanding of the energy migration mechanism for improving the upconversion luminescence of core-shell nanostructures.

Keywords: Upconversion, energy transfer, energy migration, Grant's macroscopic rate equations, diffusion

INTRODUCTION

Lanthanide-doped upconversion (UC) materials that convert low energy photons into high energy photons have attracted much attention due to their high photon stability, large anti-Stokes shifts, long lifetimes and sharp band emissions [1, 2]. They are very promising materials for a wide variety of optical applications such as 3D displays [3], super-resolution imaging [4], biomarkers and drug carriers [5, 6], anti-counterfeiting [7] and solar cells [8]. Core multi-shell upconversion nanostructures are in demand for controlling nano-scale interactions among Ln³⁺ ions to manipulate their UC characteristics including their spectra, intensities, lifetimes and efficiencies [9, 10]. Many composite nanosystems have been developed using UC nanostructures and other nanomaterials including quantum dots [11], nano-phosphors [10, 12], and metal nanostructures [13] that offer new opportunities to manipulate the energy emissions and boost the quantum efficiency.

In upconversion systems having sensitizers (S ions) and activators (A ions), the S-A energy transfers (ET) have long been recognized as the major factor producing the upconverted photons, while the energy migration (EM) among the sensitizers has always been modelled as infinitely

fast which neglected Grant's macroscopic rate equations [14]. Although upconversion systems are known to have migration-assisted energy transfer, previous studies have been unable to directly prove its effect on the UC dynamics in the bulk material. The significant effect of energy migration is beginning to become evident in nanostructures. The energy migration design in the nanostructures may provide an effective way to manipulate the UC dynamic characteristics. Wang *et al.* [15] constructed an orthorhombic KYb₂F₇:Er³⁺ nanostructure with Ln³⁺ distributed in tetrad clusters which confined the excitation migration among the Yb³⁺ and minimized the concentration quenching. Chen *et al.* [16] proposed a NaYF₄@NaYF₄:Tm³⁺@NaYF₄ nanostructure in which the excitation migration was confined to the middle layer which produced intense ultraviolet UC emissions. Zuo *et al.* [17, 18] and Zhou *et al.* [19] designed a series of multi-layer nanostructures to illustrate the dependence of the UC luminescence on the shell layer parameters to provide direct evidence of the influence of the energy migration and to demonstrate its usefulness in tuning the emission dynamics in nanostructures. However, the traditional Grant's macroscopic dynamic model and microscopic theoretical models (for example, the Inokuti-Hirayama model, the Zusman model, and the Yokota model) are unable to describe the UC luminescence processes related to the energy migration in core-shell nanostructures. This

* To whom all correspondence should be sent:
trfu@mail.tsinghua.edu.cn

difficulty in developing analytical expressions for UC luminescence processes has been overcome by using Monte-Carlo simulations to describe the macroscopic UC luminescence processes by statistically analysing the microscopic interactions among multiple ions in the core-shell nanostructures. However, the Monte-Carlo simulations depend on accurate microscopic parameters to describe the complex coupling of the energy transitions and transfers among the ions. The spatial energy transfer and migration macroscopic model [20] was recently proposed to describe the UC luminescence dynamics in core-shell nanostructures with the predictions verified experimentally. The present study investigated the UC luminescence characterization in core-shell nanostructures using this macroscopic rate equation model to simultaneously consider the energy migration and energy transfer in NaYF₄: Yb³⁺/Er³⁺ core-shell nanostructures. The model predicts the upconversion emission decay lifetimes, emission intensities, and time-resolved spatial gradients of the excited ion population density as functions of the structure, shell thickness and excitation powers considering the energy migration between sensitizers. The analysis is useful for understanding the energy migration mechanism and manipulating the upconversion luminescence characteristics of core-shell nanostructures from fundamental principles.

THEORETICAL MODELS

In upconversion systems consisting of sensitizers and activators, the ET progress is recognized as the major factor producing upconverted photons, while EM processes are also essential for the system to maintain the UC luminescence. In core-shell UC nanostructures with non-uniform distributions of doped Ln³⁺, the EM process is not fast enough which results in non-uniform distributions of the excited sensitizers during the ET process. The long-range EM occurs across units in the core-shell nanostructure with a net excitation energy flux between adjacent units. The spatial energy transfer and migration macroscopic model [20] treats the net excitation energy migration among units as gradient-driven diffusion arising from the population density spatial gradient of the excited sensitizers. A spatial migration diffusion term is introduced into the model to predict the change rates of the excited ion population densities in the different spatial regions (core, shell and shell boundary) for the core-shell nanostructure as [20]:

$$\left\{ \begin{array}{l} \dot{N}_{S_2}(r,t) = q\sigma N_{S_1} - W_{S_2} N_{S_2} + k_{SS} \nabla^2 N_{S_2} \\ - \sum_{y \in (1...m)} W_{S_2-Ay} N_{S_2} N_{Ay} + \sum_{y \in (1...m)} W_{Ay-S_1} N_{Ay} N_{S_1}; \text{ core} \\ \dot{N}_{S_2}(r,t) = q\sigma N_{S_1} - W_{S_2} N_{S_2} + k_{SS} \nabla^2 N_{S_2}; \text{ shell} \\ \dot{N}_{S_2}(r,t) = q\sigma N_{S_1} - W_{S_2-b} N_{S_2} + k_{SS} \nabla^2 N_{S_2}; \text{ shell surface} \\ \dot{N}_{Ay}(r,t) = -W_{Ay} N_{Ay} + \psi_y, \quad 2 \leq y \leq m; \text{ core} \\ \sum_{x \in (1,2)} \dot{N}_{Sx}(r,t) = 0, \quad \sum_{y \in (1...m)} \dot{N}_{Ay}(r,t) = 0 \end{array} \right. \quad (1)$$

where W_{S_2-b} is the sensitizer surface relaxation rate arising from the surface-related interactions between S ions and surface defects, organic ligands and solvents, k_{SS} is defined as the diffusion constant of S ions representing the long-range effects of excitation migration. Due to the combination of the long-range macroscopic excitation migration diffusion term ($k_{SS} \nabla^2 N_{S_2}$) and the macroscopic energy transfer terms (containing rates of W_{S_2-Ay} and W_{Ay-S_1}), the model can be used to describe the spatial and temporal UC luminescence characteristics of core-shell nanostructures. This model more accurately describes the UC characteristics in nanostructures than the traditional Grant's macroscopic rate equations or Monte-Carlo simulations.

SIMULATIONS AND DISCUSSION

The core multi-shell nanostructures may be modified to manipulate the UC characteristics. However, most research has focused on the experimental studies of UC nanostructure designs, which has greatly increased the research times and provided limited information. Simulations can provide more information in shorter times to predict the UC characteristics of nanostructures. In this work, the macroscopic diffusion model was realized by a MATLAB program employing a time-marching method and a finite volume difference scheme to simulate the UC luminescence emission dynamics of core multi-shell nanoparticles for various core-shell structures, sizes and excitation conditions. The simulations considered three upconversion nanoparticles with NaYF₄: Yb³⁺, Er³⁺ (Yb³⁺ as sensitizer and Er³⁺ as activator) using the designs shown in Fig.1: NP-I, NaYF₄: 20% Yb³⁺, 2% Er³⁺@NaYF₄ core/inert shell; NP-II, NaYF₄: 20% Yb³⁺, 2% Er³⁺@ NaYF₄: 20% Yb³⁺ core/active shell and NP-III, NaYF₄: 20% Yb³⁺, 2% Er³⁺@NaYF₄: 20% Yb³⁺@ NaYF₄ core/active shell/inert shell. The predictions were then compared with measurements of the emission characteristics.

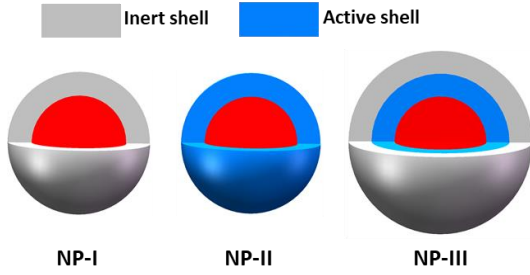


Fig. 1. Sketches of the NP-I, NP-II and NP-III nanostructures

Model verification

The parameters in Eq.(1), including the relaxation rates and the macroscopic energy transfer rates, were determined previously [20] and used here to simulate the UC emission spectra curves of all three nanostructure samples with 980 nm pulsed/continuous excitation. This section further verifies the accuracy of the rate equation model in Eq.(1) against experimental data using the known parameters to predict the steady-state upconversion emission characteristics which clarify the detailed interactions among the various levels.

The core diameters of the NP-I and NP-II samples were all 60 nm in the experiments. The inert shell thickness in NP-I was greater than 10 nm and the active shell thickness in NP-II was 6.6 nm. The luminescence properties of the samples were studied in the colloidal state. The steady-state spectra were measured using the Andor Shamrock SR-500i imaging spectrometer. A 980 nm CW laser was focused onto the UC samples as the excitation light to measure the steady-state upconversion emission spectra at various excitation powers. The red/654 nm (${}^4F_{9/2} \rightarrow {}^4I_{15/2}$) and green/540 nm (${}^2H_{11/2}, {}^4S_{3/2} \rightarrow {}^4I_{15/2}$) upconversion emissions dominated in the experiments so the 654 nm and 540 nm UC emissions are the focus of the analyses. Fig.2a compares the measured and simulated data for the intensity ratios of the 654 nm emissions to the 540 nm emissions obtained using the the rate equation model in Eq. (1) at various steady excitation power densities of 1.8~17.8 W/cm². The simulated emission ratios agree reasonably with the experimental data.

For multi-step energy transfer processes, the luminescence emission intensity, I , is usually proportional to the n^{th} power of the excitation power, P , that is $I \propto P^n$. For the 540 nm green emissions of NP-I, the power index of the I - P curve from the simulations was 1.15 which is close to the measured value of 1.12 when the NP-I sample was excited at weak power densities below 10 W/cm², as shown in Fig.2b. The predicted index, n , then

decreased as the excitation power density increased in the power range of (10~10⁴ W/cm²). These trends are consistent with other reported experimental data. The agreement between the theoretical and experimental results for the steady luminescence emissions for the NP-I sample verifies the rate equation model applicability.

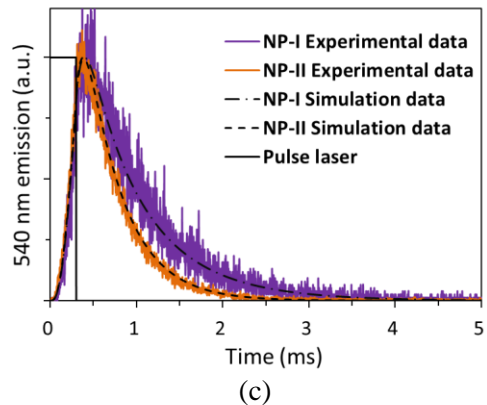
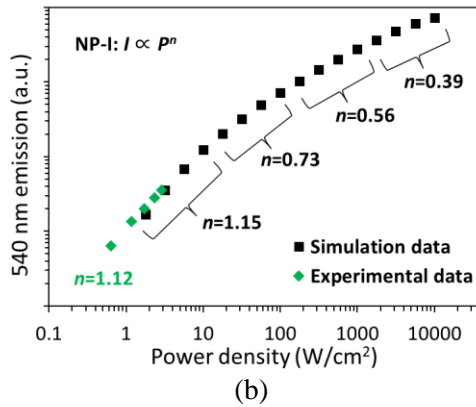
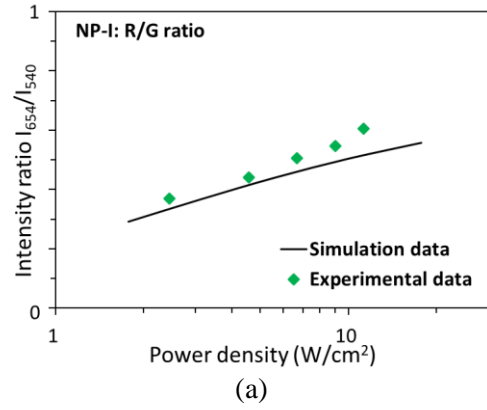


Fig. 2. (a) Red/Green emission intensity ratios for NP-I; (b) I-P relations for NP-I for 540 nm green emissions; (c) 540 nm UC emission decay curves for NP-I and NP-II with 980 nm pulsed excitation

The luminescence decay characteristics shown by the simulated 540 nm green emission decay curves for the NP-I and NP-II samples also agree well with the experimental results for 980 nm pulsed excitation (laser power, 11.1 W/cm²; pulse cycle, 10 ms; pulse width, 300 μ s) as shown in

Fig.2c. The simulation results based on Eq. (1) show that the active shell of the NP-II sample shortens the 540 nm emission decay time compared with that of the NP-I sample with the inert shell. The experimental observations of the energy migration and surface quenching effects in the core-shell nanostructures were numerically verified based on Eq. (1). Therefore, the verified model can be used to predict the emission characteristics of the nanostructure structures.

Influence of the multi-shell structure on the emission dynamics

The active shell with Yb^{3+} doping (for example, the NP-II and NP-III nanostructures) can be used to modulate the emissions and tune the lifetime by incorporating two additional pathways for the energy migration across the core-shell interface with surface-related quenching at the shell boundary. The model was used to investigate how these two mechanisms affect the upconversion dynamics with quantitative characterizations of the UC mechanisms in Ln^{3+} doped UC nanoparticles (UCNPs).

In the simulations, the NP-II UCNPs were assumed to be spherical with the same core diameter of 20 nm and different active shell thicknesses (5 nm, 10 nm and 15 nm). The 3-layer nanostructure of the NP-III UCNPs was assumed to have a thick epitaxial inert NaYF_4 shell that prevented surface-related quenching of Yb^{3+} to examine the effect of the energy migration in the structure on the upconversion luminescence. The excitation conditions were (1) CW 980 nm laser power density of 100 W/cm^2 for steady-state upconversion emissions and (2) Pulsed 980 nm laser power density peaks of $100 \text{ W/cm}^2 \sim 5 \times 10^4 \text{ W/cm}^2$ with a pulse duration of $1 \mu\text{s}$ for transient upconversion emission decay curves.

Yb^{3+} and Er^{3+} codoped systems have bright red and green upconversion luminescence. Fig.3 shows the simulated green/540 nm and red/654 nm UC emission decay curves of NP-II with various active shell thicknesses of (5 nm~15 nm) and the same excitation power of $5 \times 10^4 \text{ W/cm}^2$. The abscissa represents the process time. The rising edges of the UC emissions are delayed and the emission decay lifetimes grow longer with increasing active shell thickness. The decay lifetimes of the 540 nm emissions increase from $425 \mu\text{s}$ to $635 \mu\text{s}$ while the lifetimes of the 654 nm emissions increase from $523 \mu\text{s}$ to $688 \mu\text{s}$ when the shell thickness increases from 5 nm to 15 nm. These trends agree with the experimental observations of Zuo et al. [17].

Although the surface quenching effect with thicker shells with a larger surface area may accelerate the emission decay, a thicker active shell absorbs more excitation power which strengthens the UC emissions. On the other hand, the excitation energy in a thicker shell takes longer to migrate to the core across the core-shell interface. Therefore, the energy migration diffusion mechanisms of Yb^{3+} account for the prolonged luminescence characteristics. The energy migration diffusion strongly depends on the excited Yb^{3+} population density distribution while the boundary condition determines the diffusion direction. Therefore, different excited Yb^{3+} population density distributions will lead to energy migration diffusion forward towards the core due to the UC emissions or backwards towards the surface of the active shell due to surface quenching. These combined effects increase the UC luminescence of Er^{3+} and prolong the emission decay lifetimes in active shells doped with Yb^{3+} .

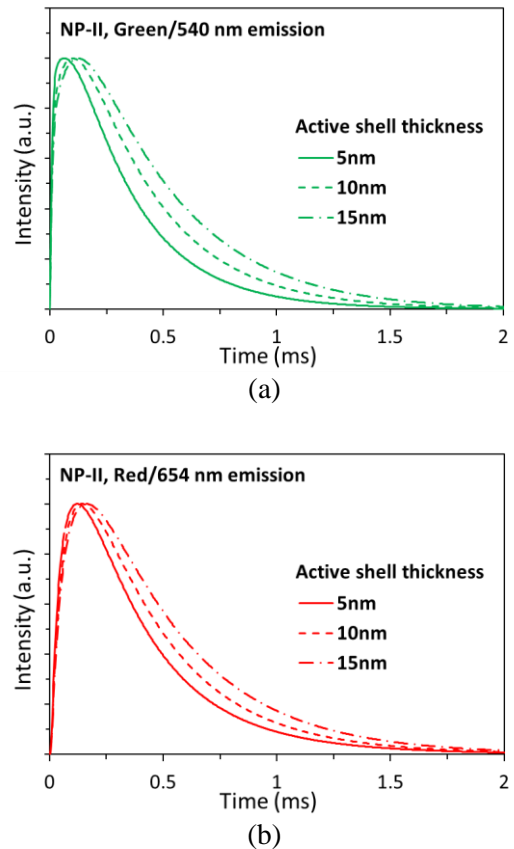


Fig.3. Simulated (a) 540 nm and (b) 654 nm UC emission decay curves for NP-II with an excitation power of $5 \times 10^4 \text{ W/cm}^2$

Fig.4 shows the simulated green/540 nm UC emission decay curves of NP-II with the same active shell thickness (5 nm) and various pulse

excitation powers ($100 \text{ W/cm}^2 \sim 5 \times 10^4 \text{ W/cm}^2$). The rising edge of the UC emissions occurs earlier while the emission decay lifetime is approximately constant with increasing excitation power. Thus, the excitation power has little effect on the emission decay rate. The rising edge time changes as the Yb^{3+} in the system becomes more active with high energy excitation rates. Initially, Yb^{3+} in the spherical core reaches its peak earlier by faster energy migration from the shell to the core. Thus, the energy migration has a greater effect on the rising edge time than the surface-related quenching.

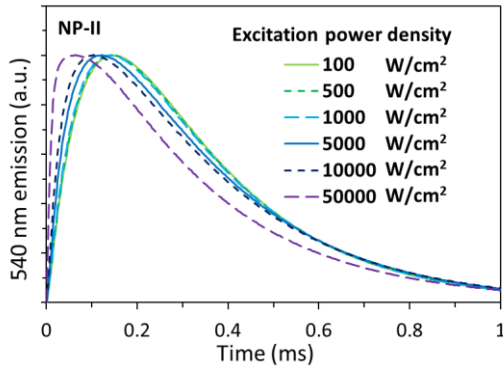
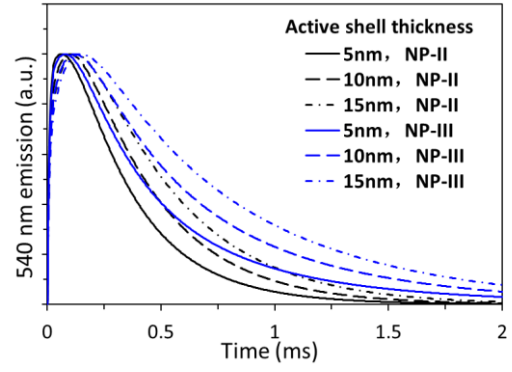
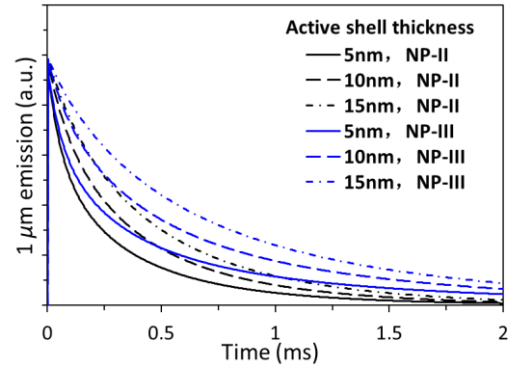


Fig.4. Simulated 540 nm UC emission decay curves of NP-II with an active shell thickness of 5 nm

The influence of the multi-layer shell on the nanostructure emission dynamics is further illustrated by the results in Fig.5 which show the simulated green/540 nm UC emission curves and the NIR/ $1\mu\text{m}$ DC (downconversion) emission decay curves for nanostructures NP-II (a single active shell) and NP-III (active-inert two layer shell) with various active shell thicknesses of (5 nm~15 nm) and the same excitation power density of $5 \times 10^4 \text{ W/cm}^2$. The results illustrate that the surface-related quenching of Yb^{3+} is effectively prevented by the additional inert shell in nanoparticle NP-III which lengthens the lifetimes of the UC and DC emissions for nanoparticle NP-III compared to those for nanoparticle NP-II. Actually surface deactivation caused by surface defects, organic ligands and solvents will provide additional relaxation pathways for the excited Yb^{3+} , which directly shortens the Yb^{3+} lifetimes and indirectly reduces the total excitation energy migrated to Er^{3+} . When protected by the inert shell, the increasing active shell thickness of nanoparticle NP-III still leads to longer emission decay lifetimes. Therefore, increasing the active shell thickness with or without the inert shell, the energy migration of the Yb^{3+} always prolongs the luminescence.



(a)



(b)

Fig.5. Simulated 540 nm UC emission curves (a) and NIR/ $1\mu\text{m}$ DC emission (b) decay curves of nanostructures NP-II and NP-III

The effect of the core-shell structure design on the luminescence intensity is demonstrated in Fig.6 which shows the simulated green/540 nm steady-state UC emission intensities represented by the population densities of the corresponding energy level N_{A6} for all three nanostructures (NP-I, NP-II, and NP-III) and various active shell thicknesses (5 nm~15 nm) with CW 980 nm laser excitation of 100 W/cm^2 . The simulations show that the active shell enhances the luminescence intensity 1.48 fold for NP-II with the 5 nm active shell thickness compared to the NP-I design with the same shell thickness and that the third inert shell layer wrapped around the active shell reduces the surface relaxation of Yb^{3+} which increases the luminescence 1.87 fold for NP-III with the 5 nm active shell thickness compared to the NP-I design with the same shell thickness. Therefore, the emission intensity of NP-III is largest while that of NP-I is smallest. In addition, the luminescence emission intensity increases with the active shell thickness for both the two-layer (NP-II) and three-layer (NP-III) nanostructures. The luminescence increases is 1.82 fold for NP-II and 1.89 fold for NP-III when the active shell thickness is increased from 5 nm to 15 nm.

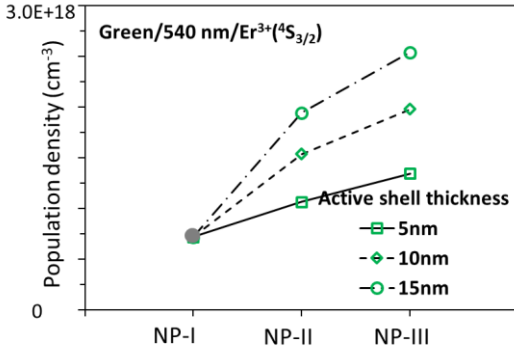


Fig.6. Simulated 540 nm steady-state UC emission intensities for all three nanostructures with 100 W/cm² power density

Energy migration in core multi-shell UC nanostructures

In the core-shell nanostructures, the energy migration is related to the excited Yb³⁺ population density distribution. From Eq.(1), the time-resolved spatial gradient of the excited Yb³⁺ population density, dN_{yb}/dr at the core-shell interface reflects the energy migration diffusion direction at the interface for whether the excitation energy migrates forwards from the shell to the core or backwards from the core to the shell. Fig.7 shows the simulated spatial gradients of the excited Yb³⁺ population density at the core-shell interface for the NP-II and NP-III nanostructures during the emission decay process for various active shell thicknesses.

The gradient dN_{yb}/dr decreases with time during the emission decay process (0~1.0 ms) and increases with the active shell thickness for both nanostructures. The energy diffusion goes in the same direction during the entire luminescence decay process for NP-III with the active shell and the inert shell, but reverses direction in NP-II with just a single active shell. The direction reverses since the excited Yb³⁺ in the NP-II core relax by transferring excitation energy to the adjacent Er³⁺ while the excited Yb³⁺ in the shell relax by transferring excitation energy to the surface quenchers. When the latter process is faster, the population density distribution of the excited Yb³⁺ reverses after some time. For NP-III, the lack of Yb³⁺ surface quenching leads to the excited Yb³⁺ population density always being higher in the active shell; thus, the energy migration direction remains unchanged. For NP-II, the direction reverses at t_0 equal to 275 μ s for the 5 nm active shell thickness, 625 μ s for the 10 nm thickness and 890 μ s for the 15 nm thickness. Thus, the reversal time increases with the active shell thickness which shows that

more excitation energy is converted to the upconversion luminescence in thicker shell structures.

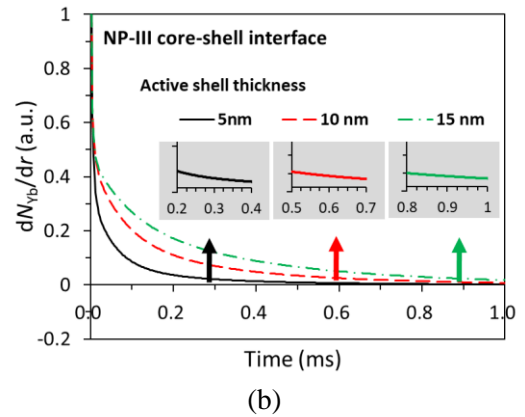
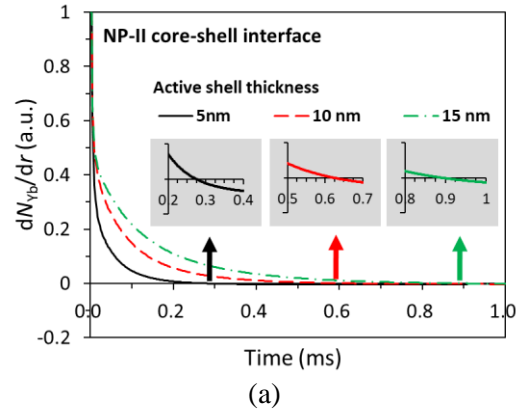


Fig.7. Spatial gradients of the excited Yb³⁺ population density at the core-shell interface, (a) NP-II and (b) NP-III

CONCLUSIONS

The current investigation modelled core-shell nanostructures made of NaYF₄ doped with Yb³⁺ and Er³⁺. The model predicted the upconversion emission decay lifetimes, intensity profiles and time-resolved spatial gradients of the excited Yb³⁺ population density for various structures, shell thicknesses and excitation powers.

The trends of the simulated emission decay curves agree well with measured data. The simulations show that the combined effects of the energy migration diffusion and the surface-related quenching promote the UC luminescence of Er³⁺ in active shells doped with Yb³⁺ and lengthen the emission decay lifetimes. The surface-related quenching of Yb³⁺ is effectively prevented by the additional inert shell in nanoparticle NP-III which leads to longer lifetimes of the UC and DC emissions than for nanoparticle NP-II. With and

without the inert shell, the energy migration diffusion mechanisms of Yb^{3+} in thicker active shells prolong the luminescence and enhance the emission intensity. The simulations also illustrate that the active shell enhances the luminescence intensity and that the inert shell wrapped around the active shell reduces the surface relaxation of Yb^{3+} which increases the luminescence. The predicted time-resolved spatial gradients of the excited Yb^{3+} population density distributions show when the energy excitation migrates forwards from the shell to the core or backwards from the core to the shell due to reversal of the excitation migration direction in the nanoparticles with the active shell. This improved macroscopic model provides an effective method for designing the upconversion luminescence characteristics of core-shell nanostructures from the fundamental physics that is more convenient and accurate than other simulation models or microscopic models.

ACKNOWLEDGEMENTS

The work was supported by the National Natural Science Foundation of China (No. 51976097) and the Science Fund for Creative Research (No. 51621062). The authors have no competing interests to declare.

NOMENCLATURE

N_{Sx}	sensitizer population density in the ground energy level ($x = 1$) or in the excited energy level ($x = 2$)
N_{Ay}	activator population density in the ground energy level ($y = 1$) or in other excited energy levels ($y = 2..m$)
q	excitation power density
σ	absorption cross section
r	space coordinates
t	time coordinates
W_{S2}	total relaxation rate of excited sensitizers
W_{Ay}	total relaxation rates of excited activators
W_{S2-Ay}	forward macroscopic energy transfer rates
W_{Ay-S1}	backward macroscopic energy transfer rates
ψ_y	activator population density change rates
k_{SS}	sensitizer energy migration diffusion constant
∇^2	Laplacian operator
W_{S2-b}	sensitizer surface-related quenching rate

REFERENCES

- [1] Auzel, F. Upconversion and anti-stokes processes with f and d ions in solids. *Chemical Society Reviews* **104**, 139-173 (2004).
- [2] Bünzli, J.-C. G., Comby, S., Chauvin, A.-S., Vandevyver C. D. B. New opportunities for lanthanide luminescence. *Journal of Rare Earths* **25**, 257-274 (2007).
- [3] Deng, R. R., Qin, F., Chen, R. F., Huang, W., Hong, M. H., Liu, X. G. Temporal full-colour tuning through non-steady-state upconversion. *Nature Nanotechnology* **10**: 237-242(2015).
- [4] Liu, Y. J., Liu, Y. Q., Yang, X. S., Zheng, X. L., Wen, S. H., Wang, F., Vidal, X., Zhao, J. B., Liu, D. M., Zhou, Z. G., Ma, C. S., Zhou, J. J., James, A. P., Xi, P., Jin, D. Y. Amplified stimulated emission in upconversion nanoparticles for super-resolution nanoscopy. *Nature* **543**, 229-233 (2017).
- [5] Tian, G. et al. Mn^{2+} dopant-controlled synthesis of NaYF_4 : Yb/Er upconversion nanoparticles for in-vivo imaging and drug delivery. *Advanced Materials* **24**, 1226-1231 (2012).
- [6] Yang, D. M., Ma, P. A., Hou, Z. Y., Cheng, Z. Y., Li, C. X., Lin, J. Current advances in lanthanide ion (Ln^{3+})-based upconversion nanomaterials for drug delivery. *Chemical Society Reviews* **44**, 1416-1448 (2015).
- [7] Kim, W. J.; Nyk, M. and Prasad, P. N. Color coded multilayer photopatterned microstructures using lanthanide (III) ion co-doped NaYF_4 nanoparticles with upconversion luminescence for possible applications in security. *Nanotechnology* **20**, 185301 (2009).
- [8] Yuan, C. Z., et al. Simultaneous multiple wavelength upconversion in a core-shell nanoparticle for enhanced near infrared light harvesting in a dye-sensitized Solar Cell. *ACS Applied Materials & Interfaces* **6**, 18018-18025 (2014).
- [9] Chen, X.; Peng, D. F.; Ju, Q.; Wang, F. Photon upconversion in core-shell nanoparticles. *Chemical Society Reviews* **44**, 1318-1330 (2015).
- [10] Chen, G. Y.; Ågren, H.; Ohulchanskyy, T. Y.; Prasad, P. N. Light upconverting core-shell nanostructures: nanophotonic control for emerging applications. *Chemical Society Reviews* **44**, 1680-1713 (2015).
- [11] Marques-Hueso, J., Peretti, R., Abargues, R., Richards, B. S., Seassal, C., Martínez-Pastor, J. P. Photonic crystal-driven spectral concentration for upconversion photovoltaics. *Advanced Optical Materials* **3**, 568-574(2015).
- [12] Kriek, G., Sarakovskis, A., Ignatans, R., Gabrusenoks, J. Phase transitions and upconversion luminescence in oxyfluoride glass ceramics containing $\text{Ba}_4\text{Gd}_3\text{F}_{17}$ nanocrystals. *Journal of the European Ceramic Society* **37** (4), 1713-1722 (2017).

- [13] Ahmed, E. H. et al. Enhanced UV upconversion emission using plasmonic nanocavities. *Optics Express* **24**, 259953 (2016).
- [14] Grant, W. J. C. Role of rate equations in the theory of luminescent energy transfer. *Physical Review B* **4**, 648-663 (1971).
- [15] Wang, J. et al. Enhancing multiphoton upconversion through energy clustering at sublattice level. *Nature Materials* **13**, 157-163 (2014).
- [16] Chen, X. et al. Confining energy migration in upconversion nanoparticles towards deep ultraviolet lasing. *Nature Communications* **7**, 10304 (2016).
- [17] Zuo, J., Sun, D. P., Tu, L. P., Wu, Y. N., Cao, Y. H., Xue, B., Zhang, Y. L., Chang, Y. L., Liu, X. M., Kong, X. G et al. Precisely tailoring upconversion dynamics via energy migration in core-shell nanostructures. *Angewandte Chemie International Edition* **57**, 3054-3058 (2018).
- [18] Zuo, J. et al. Revisit of energy transfer upconversion dynamics – the role of energy migration. *Science China: Technological Sciences* **61**, 1301-1308 (2018).
- [19] Zhou, B. et al. Probing energy migration through precise control of interfacial energy transfer in nanostructure. *Advanced Materials* **31**, 1806308 (2019).
- [20] Liu, J. F.; Fu, T. R. and Shi, C. L. Spatial energy transfer and migration model for upconversion dynamics in core-shell nanostructures. *The Journal of Physical Chemistry C* (2019) 10.1021/acs.jpcc.8b12300.

Activation and gas sorption performance in Zr-Co-Y getters on Ge substrates

Jie Guo^{1*}, Peng Wu¹, Jun Yuan², Lichun Sun¹, Qiong Li^{1*}, Bingzhe Li²

¹Yunnan Key Laboratory of Optoelectronic Information Technology, Yunnan Normal University, Kunming Yunnan, 650092, People's Republic of China

²Kunming Institute of Physics, Kunming Yunnan, 650000, People's Republic of China

The ternary ZrCo based getters are widely used in accelerator vacuum chambers and MEMS cavity. In this study, ZrCoY (Y is the rare earth element) getter thin films were deposited on polished Ge substrates in the uncooled infrared detectors by magnetron sputtering. Microstructure, sorption performance and activation mechanism were investigated. The grain size became larger and the FWHM of XRD diffraction peak decreased from 5.067 to 3.730 after the activation at 300°C for 45 minutes. The initial H₂ sorption speed reached 67.5 cm³·s⁻¹·cm⁻² and the attenuation of sorption performance firstly was 11% but decreased to 4.4% at the fifth hour which indicated that the good effect of ZrCoY getters. The total sorption was calculated to 2743.57 Pa·cm³·cm⁻². XPS showed that the getter film mainly existed as the form of ZrO₂ with a small amount of Zr. The addition of a Ni protective layer improved the sorption performance with initial sorption speed of 82 cm³·s⁻¹·cm⁻². The ZrCoY getter film on Ge substrates can be applied in uncooled infrared focal plane arrays (IRFPA).

Keywords: Non evaporable getters, ZrCoY, sorption performance, vacuum packaging

INTRODUCTION

The vacuum packaging in micro-electro-mechanical systems (MEMS) such as low lost uncooled infrared focal plane arrays (IRFPA) detectors is very important procedure to improve the devices performances and reliability. Undesired residual gases like H₂, CO, CO₂ and CH₄ after packaging have to be removed to maintain the vacuum conditions in the MEMS cavity [1-3]. Non-evaporable getters (NEG) are utilized for efficient sorption of sealed-off vacuum devices. The conventional bulk or sheet getters have been unsuitable for MEMS because of the limited space. The NEG thin films can be grown on the inner walls of vacuum chamber with lower activation temperature and better adhesion [4-5]. The pure metal or alloy like Ti, ZrTiV, ZrVFe have been applied in vacuum packaging for decades [6-9]. Recently, ZrCo based materials without toxic elements have attracted considerable interest because Co oxides can be deoxidized at low temperature which is benefit to decreasing the activation temperature. Zr-Co-RE (RE indicating rare earth elements) alloy getter materials exhibit a wide range of gas pumping and low activation temperature because of the excellent sorption performance of RE elements like Ce, La. In RE group [10], Yttrium (Y) is rich in the earth especially in China. Besides, it has been

demonstrated that the nickel (Ni) could reduce the activation temperature obviously because nickel plays a role of catalyst and can dissociate the hydrogen molecule at a lower energy level.

The NEG thin films in most of the research were grown on Si wafer. The NEG thin films in the vacuum MEMS devices usually need to be grown on the various substrates, such as germanium (Ge) window in IR detectors packing. It is important to understand the effect of Ge substrates on the film morphology, the activation property and sorption performance. In this paper, the highly porous ZrCoY thin films getters with Ni protect layer on Ge window substrates were firstly prepared by RF magnetron sputtering. The effect of Ni protect on the microstructure and morphology was discussed. Further, the effect of Ni protect layer on activation and H₂ gas sorption performance was studied.

EXPERIMENT

Films deposition

ZrCoY getter films were deposited on Ge substrates by RF magnetron sputtering. The Ge substrates were ultrasonically cleaned with acetone and alcohol in sequence, followed by washing in deionized water and heating at 300 °C for 30 min. The structure of the getter films from down up is the adjusting layer, the getter layer and the protective layer denoting Ge/Ti/ZrCoY/Ni. Ti film

* To whom all correspondence should be sent:

yunnugj@sohu.com

about 1 μm thickness was sputtered using the Ti (99.999%) target under the power 150 W, the Ar flow rate 80 sccm and the deposition pressure 1.0 Pa. ZrCoY getter films about 2 μm thickness were deposited by sputtering the alloy target under the power 80 W, the Ar flow rate 40 sccm and the deposition pressure 4.0 Pa. Ni film about 500 nm thickness was deposited using the same parameters as Ti film. The sputtering parameters were shown in Tab.1. Then the getter films were activated by annealing in the vacuum of 1.0×10^{-5} Pa at 300 ??? for 45 minutes.

Table 1. The sputtering parameters of Ti/ZrCoY/Ni getter films on Ge substrates

Films	Sputtering Power/W	Sputtering pressure/Pa	Thickness /μm
Ni	150	1	0.5
ZrCoY	80	4	2
Ti	150	1	1

Presentation of the experimental equipment

The microstructure was studied by X ray diffraction (Rigaku MSAL XD2) operated at 36kV and 20mA. The field emission scanning electron microscope (FEI Quanta FEG 450) with an integrated energy dispersive X-ray spectrometer (EDS) was used to analyze the morphology, cross-section and surface composition of the film. The componential analysis of the Zr-Co-Y thin films was investigated using Thermo Fisher Scientific EscaLab 250Xi X-ray photo-emission electron spectroscopy (XPS) measurements.

Gas sorption performance was tested by the dynamic method according to national standard of PRC GB8763-88 [11]. The two gas chambers were connected by capillary or orifice. The pressure of one chamber with getter was P_g . The other with inlet H_2 gas was P_m . In the test, the P_g remained 1.0×10^{-4} Pa unchanged and the P_m -time (t) relation was recorded. The sorption speed S ($cm^3 \cdot s^{-1} \cdot cm^{-2}$) and the sorption quantity Q ($Pa \cdot cm^3 \cdot cm^{-2}$) can be calculated by formula as followed:

$$S = F \frac{P_m - P_g}{P_g \cdot A}$$

$$Q = \int_0^t Q_i dt = \frac{F}{A} \int_0^t (P_m - P_g) dt$$

where $F = 71$ ml/s for H_2 is the conductance of the capillary tube. A (cm^2) is the area of the tested getter.

RESULTS AND DISCUSSION

Films microstructure before and after the activation

Fig.1 showed SEM images before and after activation of the films. The grain size became larger obviously from 20 nm to 60nm before and after the activation. During the heating activation process, the diffusion coefficient of the atoms increased. Therefore, the grain boundary was more likely to move which resulted in the growth of the grain. After the activation, the fresh and active surface was exposed [12-14,15].

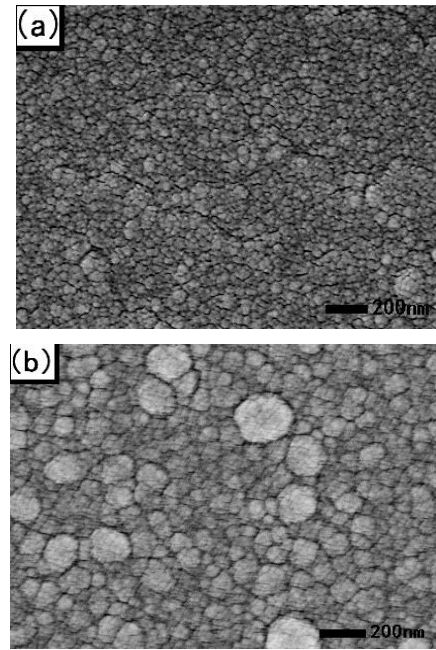


Fig.1. SEM images of ZrCoY getter films before (a) and after (b) activation

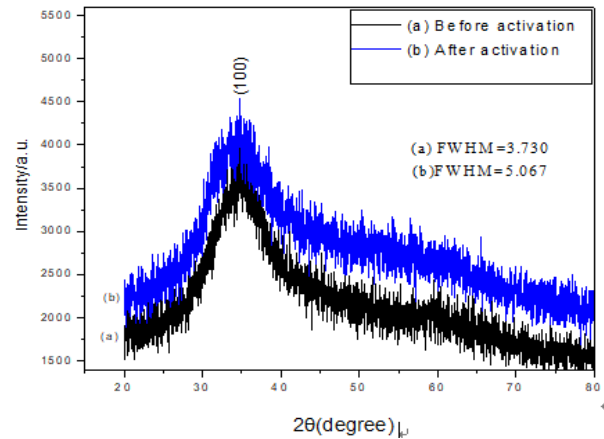


Fig.2. XRD pattern of ZrCoY getter films before and after activation

The XRD pattern before and after activation was shown in the Fig.2. The diffraction peak around 2θ

= 35° was (100) orientation according to the α -Zr hexagonal structure. The full width at half maximum (FWHM) of the peak became narrow from 5.067 to 3.730 because the activation process was accompanied by the growth of fine grains and the ordering of atoms [16].

Inspiratory performance analysis

Fig.3 showed the H₂ sorption performance of ZrCoY films after activation at 300 ° C for 45 min. The initial sorption speed reached 67.5 cm³·s⁻¹·cm⁻², then decreased slowly with the sorption quantity increasing. After activation, the bonds of the molecule broke and the gap between the grains increased, which significantly increased the surface area and improved the gas sorption properties of the

films. The rough surface and the interstitial space after activation are the main diffusion channels of the active gas molecules.

During the deposit of the vacuum MEMS devices, small amount of gas may release from the cavity materials. The change of the sorption speed with the time was investigated as shown in Tab.2. According to ASTM F798-97 (2002), the attenuation of the sorption speed is defined to the ratio of the real-time sorption speed to the initial sorption speed. The total sorption quantity is defined to the quantity at the termination of the sorption where the termination sorption speed is 5% of the initial speed that was 3.375 cm³·s⁻¹·cm⁻² in our experiment.

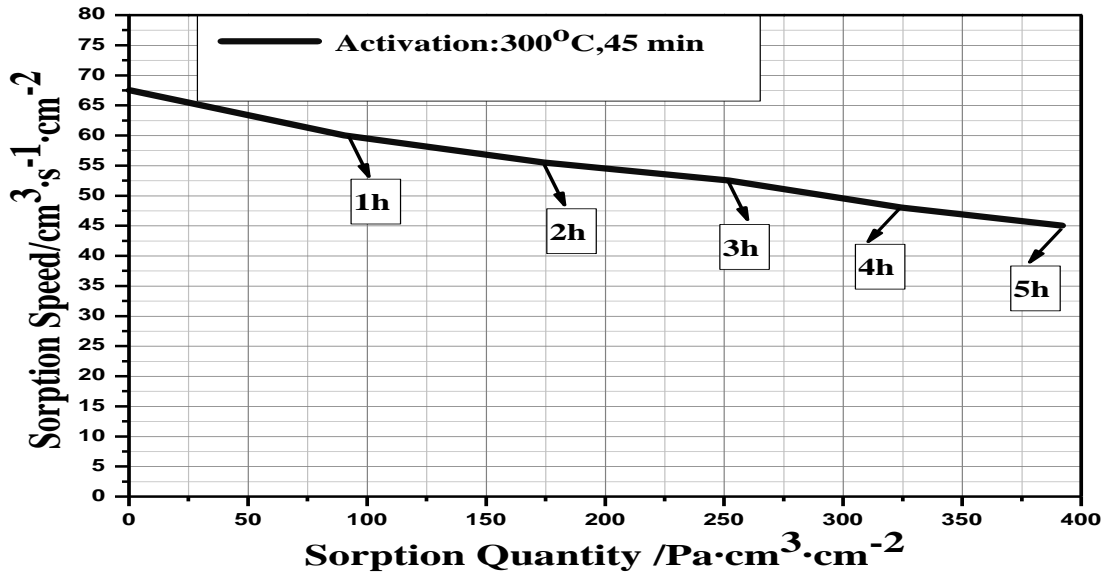


Fig.3. Hydrogen sorption performance curve of ZrCoY films on Ge substrates

Table 2. The change of the sorption speed with the time

Test time (h)	Real-time sorption speed (cm ³ s ⁻¹ cm ⁻²)	Attenuation (real-time/initial speed)
0	67.5	100%
0.5	63	93.33%
1	60	89%
1.5	58.5	86.7%
2	55.5	82.2%
2.5	54	80%
3	52.5	77.8%
3.5	51	77.6%
4	48	71.1%
4.5	46.5	68.9%
5	45	66.7%

The sorption speed gradually decreased with the time while the attenuation degree fade. From Tab.2, the attenuation rate decreased from 11% (100%-89%) in the first hour to 4.4% (71.1%-66.7%) in the fifth hour taking the initial sorption speed as the reference. It indicated that sorption of ZrCoY getters postponed the reduction of the vacuum degree. The empirical relation between the sorption speed and the quantity followed [17]:

$$\lg S = -\frac{Q}{A} + B \quad (1)$$

Where A and B are the parameters relating to the getter composition and the activation degree. The two parameters can be obtained by linearly fitting to $A=2108.77$, $B=1.83$ according to Fig.3. Then the formula (1) can be written as:

$$\lg S = -\frac{Q}{2108.77} + 1.83 \quad (2)$$

The total sorption Q can be obtained to $2743.57 \text{ Pa}\cdot\text{cm}^3\cdot\text{cm}^{-2}$ by substituting the termination sorption speed $3.375 \text{ cm}^3\cdot\text{s}^{-1}\cdot\text{cm}^{-2}$.

Sorption mechanism analysis

The sorption mechanism of ZrCoY getter was studied by XPS analysis as shown in Figs.4-6. Fig.4 was a full spectrum after sorption at room temperature in which the main elements of Zr, Co, O, Y and C can be found. The measured data were related to the evolution of the XPS spectra of Zr 3d, Co 2p, Y 3d, O 1s, and C 1s orbitals. The oxygen element came from the oxidation of the surface. The strong O1s peak was located at about 540 eV. The weak peak at 284 eV accorded to the C 1s binding energy, indicated a small amount of CO and CO₂ were absorbed before activation.

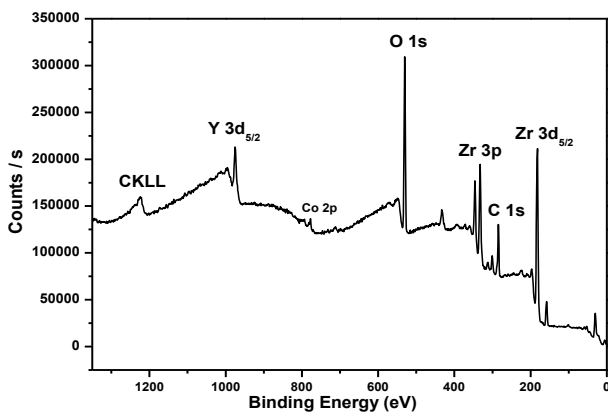


Fig.4. XPS spectrum of ZrCoY film after sorption

Fig.5 showed XPS spectrum of the Zr3d related peaks of ZrCoY films using the Gaussian-Lorentzian fitting after sorption. The two strong peaks at the electron binding energy 182 eV and 184.5 eV corresponded to Zr 3d5/2 and Zr 3d3/2 in ZrO₂ form or Zr⁴⁺. The weak peaks at 178 eV and 180.5 eV accorded to Zr 3d5/2 and Zr 3d3/2 in the natural form. The films mainly existed as the form of ZrO₂ with a small amount of Zr without metal hydroxide (Zr(OH)₂) and metal suboxides (ZrO_x, here $x < 2$) as other reports [18]. The composition of ZrO₂ and Zr was 90.78% and 9.22% respectively according to the area calculation. Obviously the abundant O₂ were absorbed and reacted with ZrCoY getter films after the activation, which proved the good sorption ability of the getter films.

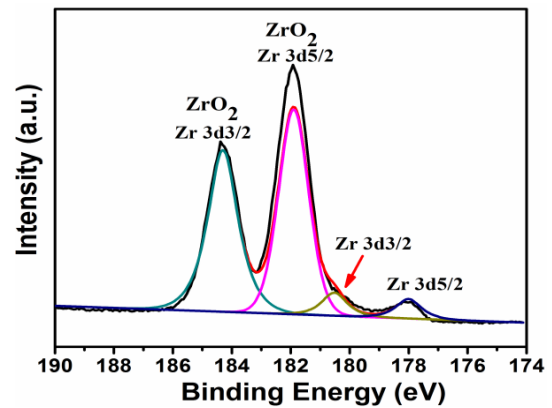


Fig.5. Zr 3d peaks in XPS spectrum after sorption

Fig.6 showed XPS spectrum of the Co 2p peak after sorption. The two characteristic peaks at 792 eV and 777 eV were accordance to Co 2p 1/2 and Co 2p 3/2 orbitals. There were obvious satellite peaks relating to the electronic vibration or Auger electron.

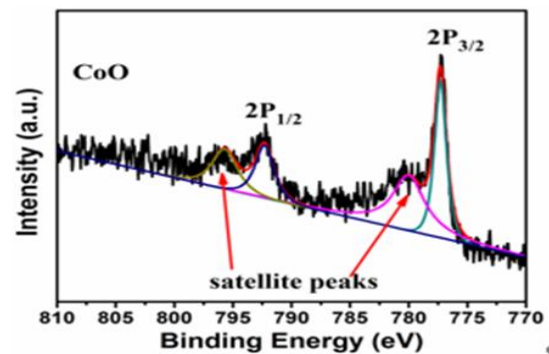


Fig.6. Co 2p XPS energy spectrum after sorption

The as-deposited and activated ZrCoY films were easily oxidized and absorbed the reactive gas in the air. The gas molecule was absorbed at the

surface and diffused to the certain depth from the surface which accompanied the energy absorption, the bond crack and new bond formation. So the gas molecule must be exhausted through the activation process. During the heating, Zr-O and Co-O bonds at the surface were broken resulted in the oxygen atoms diffusing into the bulk and Zr/Co metallic state appeared at the surface, which will realize the adsorption activity of the film.

Effect of Ni protective layer on the sorption performance in ZrCoY getter

Fig.7 showed the hydrogen sorption performance curve of ZrCoY getter films with and

without Ni protective layer. The Ni layer improved the sorption performance obviously. After being activated at 300 ° C for 45 min, the initial sorption speed improved from $67.5 \text{ cm}^3 \cdot \text{s}^{-1} \cdot \text{cm}^{-2}$ to $82 \text{ cm}^3 \cdot \text{s}^{-1} \cdot \text{cm}^{-2}$, indicating that the protective layer played a significant protective effect on the getter and reduced oxidation of the film. The getter without Ni layer had an open surface and a large active area so that the active gas was more likely to oxidize the getter surface to form a passivation film. In the structure with Ni layer, the crystal bond broke and the gap increased which significantly improved the sorption performance.

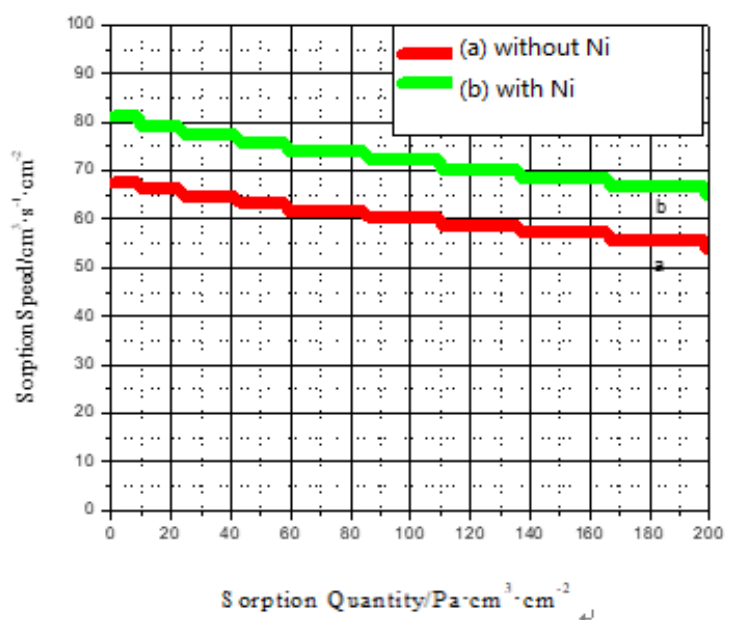


Fig.7. The sorption performance curves of ZrCoY film with and without Ni protective layer

CONCLUSIONS

ZrCoY (Y is the rare earth element) getter thin films were deposited on polished Ge substrates by magnetron sputtering. The microstructure, the surface morphology, the sorption performance and the activation mechanism were investigated. The total H₂ sorption quantity of ZrCoY getter films was estimated to about 2743.57 Pa·cm³·cm⁻². The sorption speed of Ni/ZrCoY film getters was 82 cm³·s⁻¹·cm⁻² which is 1.3 times than that of ZrCoY film getters. With the development to the inside of the film, O₂ gradually changed from adsorption state to oxidation state. The Ni protective layer effectively reduces the oxidation degree of ZrCoY film getter. The sorption properties of Ni/ZrCoY/Ti getter films in this paper ensure its application in

the uncooled infrared focal plane arrays (IRFPA). In addition, Ni protective layer provides a new passivation layer to improve the sorption properties in many vacuum sealed devices such as gyroscopes, accelerometers, micro-bolometers, pressure sensors, frequency resonators and atomic clocks. In the future, thicker Ni layer and other metal alloy protective layer can be applied to improve the sorption speed. ZrCo alloy with other rare earth elements like Ce will be investigated.

ACKNOWLEDGEMENTS

This study was supported by the National Natural Science Foundation of China (No. 61774130, 61705192).

REFERENCES

- [1] A. Moghadama, V. Dashtizad, A. Kafrou, H. Yoozbashizadeh, R. Ashirc, *Intermetallics* **57**, 51 (2015).
- [2] Z. B. Cekic, K. Ciric, M. Iordoc, S. Markovic, M. Mitric, D. Stojic, *J. Alloy. Compd.* **559**, 162 (2013).
- [3] Y. Xu, J. Cui, H. Cui, H. Zhou, Z. Yang, J. Du, *J. Elec. Mat.* **45**, 386 (2016).
- [4] Z. Cao, L. Ouyang, H. Wang, J. Liu, L. Sun, M. Felderhoff, M. Zhu, *Inter. J. Hydrogen Energy* **41**, 11242 (2012).
- [5] Y. Xu, J. Cui, H. Cui, H. Zhou, Z. Yang, J. Du, *J. Elec. Mater.* **45**, 386 (2016).
- [6] C. Boffito, B. Ferrario, P. Porta, L. Rosai, *Optoelec. Technol.* **18**, 1117 (1984).
- [7] C. Benvenuti, P. Chiggiato, F. Cicoira, Y. Aminot, V. Ruzinov, *Vacuum* **73**, 139 (2004).
- [8] R. Valizadeh, O. Malyshev, J. Colligon, A. Hannah, V. Vishnyakov, *J. Vac. Sci. Technol. A* **28**, 1404 (2010).
- [9] A. Moghadam, V. Dashtizad, A. Kafrou, H. Yoozbashizadeh, *Vacuum* **111**, 9 (2015).
- [10] O. Malyshev, R. Valizadeh, J. Colligon, A. Hannah, K. Middleman, S. Patel, V. Vishnyakov, *J. Vac. Sci. Technol. A* **27**, 521 (2009).
- [11] Test Methods of Gas Absorption Characteristic for Non-evaporation Gettering Materials and Products Chinese standard press, Beijing, 1989.
- [12] C. Benvenuti, P. Chiggiato, F. Cicoira, Y. Aminot, *J. Vac. Sci. Technol.* **16**, 148 (1998).
- [13] J. Bu, C. Mao, Y. Zhang, X. Wei, J. Du, *J. Alloy. Compd.* **529** 69 (2012).
- [14] C. Benvenuti, P. Chiggiato, A. Mongelluzzo, A. Prodromides, V. Ruzinov, C. Scheuerlein, M. Tadorelli, *J. Vac. Sci. Technol* **19**, 2925 (2001).
- [15] L. Tenchine, X. Baillin, C. Faure, P. Nicolas, E. Martinez, A. Papon, , *Sensor Actuat. A Phys.* **27**, 521 (2009).
- [16] C. Benvenuti, P. Chiggiato, P. Costa Pinto, A. Prodromides, V. Ruzinov, *Vacuum* **71**, 307(2003).
- [17] M. Mura, C. Paolin, *J. Vac. Sci. Technol.* **25**, 1234 (2007).
- [18] E. Bourim, H. Kim, and N. Chuang, *micromachines* **8**, 490 (2018).

Thermodynamic analysis of an innovative heat pump using indoor and outdoor air as heat source

Jing Li¹, Fan Yi¹, Xudong Zhao^{1*}, Xiaoman Bai^{2*}, Ali Badiei¹, Xiaoli Ma¹

¹Research Centre for Sustainable Energy Technologies, Energy and Environment Institute, University of Hull, Hull HU6 7RX, UK

²Environment Design Centre, School of Art and Medium, Hefei Normal University, Hefei, China, 230601

Heat recovery from exhaust air is an effective approach to carbon emission reduction for buildings in cold regions. This paper proposes a novel heat pump system to efficiently utilize the exhaust air. The system has two heat sources: exhaust air and ambient air. It consists of a condenser, two parallel evaporators and compressors, and two throttle valves. The exhausted indoor air is first used to heat the refrigerant in the medium-pressure evaporator. The exhaust air at a reduced temperature is then mixed with the ambient air to heat the low-pressure evaporator. The advantages of the mixed air source heat pump (MASHP) with two-stage evaporation over a conventional exhaust air heat pump (EAHP) include a larger heating capacity, higher waste heat recovery and lower carbon emission. Besides, the exhaust air can be employed for defrosting without additional power consumption. Thermodynamic performance of the system is investigated. Comparison is made with a conventional EAHP and a directly mixed air source heat pump with single-stage evaporation. The results indicate that under the conditions of exhaust air temperature of 20 °C, mass flow rate of 1.0 kg/s and ambient temperature of 0 °C, the profits for the proposed MASHP, conventional EAHP and MASHP with single-stage evaporation are about 11.5, 5.1 and 3.7 pound/day, respectively.

Keywords: heat pump, exhaust air, two-stage evaporation, heat recovery, profit

INTRODUCTION

Ventilation heat loss accounts for a large proportion of the building energy losses. Mechanical ventilation with heat recovery is able to provide the best indoor air-quality with low energy consumption. Thermal recovery from exhaust air has been widely dealt with in literature, in the form of either active or passive systems [1-3]. Among the technologies, exhaust air heat pumps (EAHP) is regarded as energy efficient heating system. It extracts heat from the exhaust air of a building which otherwise will be wasted and transfers the heat to the supply air, hot tap water and/or hydronic heating system. Extensive studies have been conducted on the EAHP, including the control algorithms [4], structural optimization [5], combination with other energy sources [6, 7], connection schemes [8], and economical performance [9]. Compared with other types of exhaust heat recovery methods, an EAHP avoids cross contamination between fresh and exhaust air, and can have a high recovery efficiency of more than 100% without any need of reheat for the fresh air [10]. The EAHPs have been commercialized. For example, new detached houses in Sweden are most often installed with an EAHP to minimize ventilation heat loss [11].

However, one challenge of EAHP is the limited heating capacity, leading to a high capital cost per kW and long payback period. The ventilation air stream for a typical house might be 30 litres per second and the maximum heat of recovery is about 720W at an ambient temperature of 0 °C. The indoor air exhausted into the environment may have a temperature of 5-10 °C higher than the ambient for the sake of an acceptable COP, thereby leading to a lower heat recovery. Between 2009 and 2013, thousands of brand new social homes were equipped with EAHPs in the UK, most owners and housing association tenants had reported increased electricity bills [12]. Moreover, there are heat losses through windows, walls and roofs. The heat recovered from the ventilation is not sufficient to meet the building energy demand. Additional heat is required to provide space heating and hot water, which may be from either electric or gas heater. This will always be accompanied by a higher operating cost or carbon emission.

In this paper, a novel heat pump system is proposed to efficiently make use of the exhaust air from the building. The exhaust air is only part of the energy sources. It is incorporated with outdoor air. The capacity of heat pump is therefore significantly larger than a conventional EAHP and the carbon emission from the building can be reduced. To the best of the authors' knowledge, it is the first time that exhaust air is mixed with ambient

* To whom all correspondence should be sent:
Xudong.zhao@hull.ac.uk

air to improve the performance of the heat pump system. The profit of the system based on the reduction in electricity consumption is analysed and compared with that a conventional EAHP system. Finally, the drawback of the novel system and future works are discussed.

SYSTEM DESCRIPTION

The heat pump is used to produce hot water for space heating (e.g., underfloor heating). The mixed air source heat pump (MASHP) with two-stage evaporators, MASHP with single-stage evaporator and conventional EAHP system are illustrated in Figs.1-3 respectively.

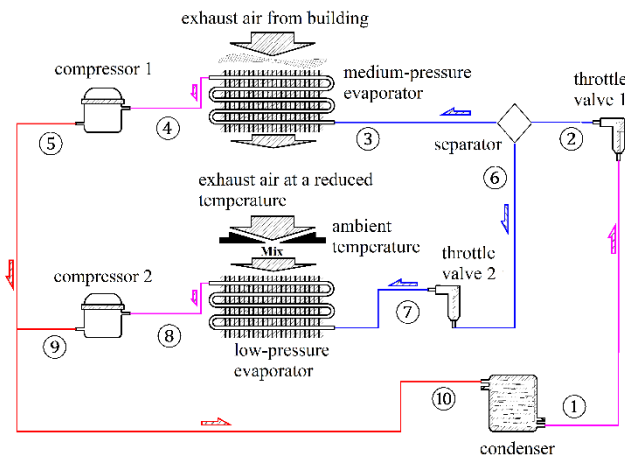


Fig.1. MASHP system with two-stage evaporators

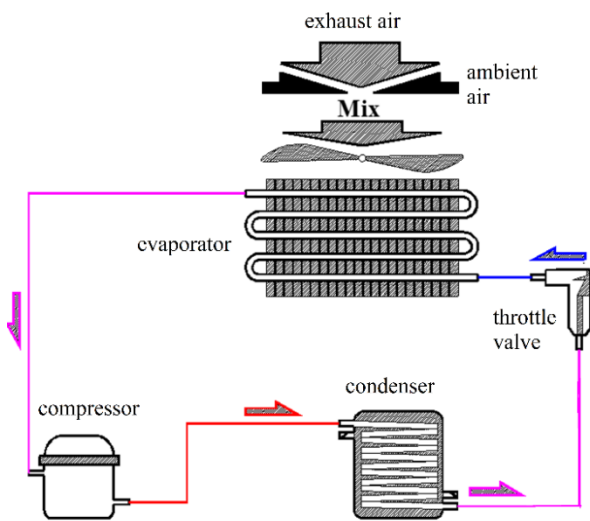


Fig.2. MASHP system with single-stage evaporator

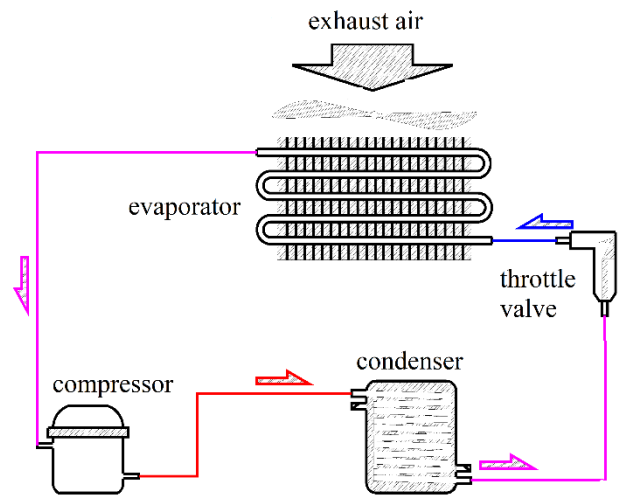


Fig.3. EAHP system

For the MASHP with two-stage evaporators, the refrigerant leaving the condenser is first throttled and is at binary phase state at the outlet of the throttle valve. Part of the liquid is further throttled and enters the low-pressure evaporator. The rest liquid and vapor flow into the medium-pressure evaporator. Vapor from the medium- and low-pressure evaporators is compressed by compressors 1 and 2, respectively. The vapor is then condensed in the condenser. The refrigerant circulates. The exhaust heat is first recovered by the medium-pressure evaporator and the exhaust air at a reduced temperature is further mixed with the ambient air. The thermodynamic states are marked in number in the figure.

The MASHP with single-stage evaporator in Fig.2 has not been reported in the literature either. It is simpler than that in Fig.1 and does not have the medium-pressure evaporator and compressor, which may lead to large thermodynamic irreversibility in the mixing process.

The EAHP in Fig.3 is commercially available. It does not have the low-pressure evaporator and compressor as compared with the MASHP with two-stage evaporators. Its heat source is just exhaust air from the building.

MATHEMATICAL MODELS

The COP of a heat pump is the ratio of the output heat to the input power. In this simulation emphasis is put on the thermodynamic cycle. The power consumption by fans and pumps are not considered. Therefore, the COP is defined by

$$COP = \frac{Q_{out}}{W_{ele}} = \frac{h_{cond,in} - h_{cond,out}}{h_{comp,out} - h_{comp,in}} \quad (1)$$

where:

$h_{cond,in}$ - specific enthalpy at the inlet of the condenser, J/kg;

$h_{cond,out}$ - specific enthalpy at the outlet of the condenser, J/kg;

$h_{comp,in}$ - specific enthalpy at the inlet of the compressor, J/kg;

$h_{comp,out}$ - specific enthalpy at the outlet of the compressor, J/kg.

The ventilation heat loss without recovery is

$$Q_{ven,l} = m_{ex}C_p(T_{ex} - T_{am}) \quad (2)$$

where:

m_{ex} - exhaust air flow rate, kg/s;

C_p - heat capacity, J/kg°C;

T_{am} - ambient temperature, °C;

T_{ex} - temperature of exhaust air leaving the building, °C.

The mixing of ambient and exhaust air for heat pump is rarely studied in the literature, and hence special attention is paid to the modelling of this process in this paper. The air temperature after mixing (i.e., air temperature at the low-pressure evaporator inlet) is calculated by

$$T_{mix,in} = \frac{m_{ex}T_{ex} + x \cdot m_{am}T_{am}}{m_{ex} + x \cdot m_{am}} = \frac{T_{ex} + x \cdot T_{am}}{1 + x} \quad (3)$$

$$x = \frac{m_{am}}{m_{ex}} \quad (4)$$

where:

m_{am} - ambient air flow rate, kg/s

The mixed air temperature leaving the evaporator is

$$\begin{aligned} T_{mix,out} &= T_{mix,in} - \frac{Q_{evap}}{m_{ex}(1+x)C_p} \\ &= T_{am} - \frac{\frac{Q_{evap}}{m_{ex}C_p} - (T_{ex} - T_{am})}{1+x} \end{aligned} \quad (5)$$

where:

Q_{evap} - low-pressure evaporator input heat for the MASHP with two-stage evaporation or evaporator input heat for EAHP and MASHP with single-stage evaporation, W;

The temperature drop of air through the evaporator is an important parameter in the design of the heat exchanger. A smaller temperature drop can provide a higher COP but more fan power is needed owing to a larger flow rate. The optimum temperature drop is then a compromise. For a fair comparison, a constant temperature drop of 5°C is

assumed for the low-pressure evaporator of the MASHP and conventional air source heat pump (ASHP).

$$\Delta T = T_{mix,out} - T_{mix,in} = 5 \quad (6)$$

$$C_p m_{ex}(1+x)\Delta T = Q_{evap} \quad (7)$$

$$\begin{aligned} \text{With } C &= \frac{Q_{evap}}{m_{ex}C_p(T_{ex}-T_{am})}, \\ x &= \frac{(T_{ex}-T_{am})C}{\Delta T} - 1 \end{aligned} \quad (8)$$

$$\begin{aligned} T_{mix,out} &= T_{am} - \frac{\frac{Q_{evap}}{m_{ex}C_p} - (T_{ex} - T_{am})}{1 + \frac{m_{am}}{m_{ex}}} \\ &= T_{am} - \Delta T \frac{C-1}{C} \end{aligned} \quad (9)$$

It indicates that at a given C , the mixed air temperature leaving the evaporator is independent on the exhaust air temperature. The relative increment of $T_{mix,out}$ by that of air leaving the evaporator of a conventional ASHP is

$$\Delta T_r = T_{mix,out} - (T_{am} - \Delta T) = \frac{\Delta T}{C} \quad (10)$$

The minimum temperature difference between the refrigerant and air in the evaporator shall take place at the air outlet, and is defined by

$$\Delta T_{min} = T_{mix,out} - T_{evap} \quad (11)$$

where

T_{evap} - refrigerant evaporation temperature, °C.

Profit is chosen as a key indicator in the comparison between the MASHP and conventional ASHP. It is the relative profit of the MASHP and defined by

$$\begin{aligned} Pro_{ex,heat} &= C_{heat}(W_{ele}COP_{mix} - W_{ele}COP_{am}) \\ &= C_{heat} \frac{C \cdot m_{ex}C_p(T_{ex}-T_{am})}{(COP_{mix}-1)} (COP_{mix} - COP_{am}) \end{aligned} \quad (12)$$

where:

$Pro_{ex,heat}$ - profit based on heat gain, £/s;

C_{heat} - price of heat, £/J;

W_{ele} -electricity input or consumption, W;

COP_{mix} - COP of the MASHP or EAHP system;

COP_{am} - COP of a traditional ASHP system operating at the same ambient and condensation temperature.

$Pro_{ex,heat}$ represents the net profit of heat gain by the MASHP and EAHP at the same electricity consumption. Because the MASHP and EAHP are expected to have a higher COP than a conventional ASHP the heat gain is higher at a given electricity input. Similarly, a comparison can be made based on the electricity consumption.

$$Pro_{ex,ele} = C_{ele} \left(\frac{Q_{gain}}{COP_{am}} - \frac{Q_{gain}}{COP_{mix}} \right) = C_{ele} \frac{C_{mex} C_P (T_{ex} - T_{am}) (COP_{mix} - COP_{am})}{(COP_{mix} - 1) COP_{am}} \quad (13)$$

where:

$Pro_{ex,ele}$ - profit based on reduction in electricity consumption, £/s;

C_{ele} - price of electricity, £/J;

$Pro_{ex,ele}$ represents the net profit of electricity reduction by the MASHP and EAHP at the same heat gain. The electricity inputs of the MASHP and EAHP are lower than that of a conventional ASHP at a given heat output due to a higher COP.

RESULTS AND DISCUSSION

In the following simulation, the price of electricity of 20 p/kWh and heat of 4p/kWh, compressor efficiency of 0.8, minimum temperature difference of heat transfer in the evaporator of 4 ~ 5 °C, minimum temperature drop of air through the evaporator of 5 °C, condensation temperature of 50 °C, exhaust air flow rate of 1.0 kg/s and ambient temperature of 0 °C are assumed. The refrigerant is R134a.

Performance of the EAHP

For the EAHP, the exhaust air is the only heat source of the heat pump. Because it has a higher temperature than the outdoor air, the COP will be higher than that of a conventional ASHP, resulting in more profit. The evaporator input heat shall not be larger than the ventilation heat loss. And the heat ratio C shall be less than 1. Otherwise the exhaust air leaving the evaporator will have a lower temperature than the ambient and the utilization of exhaust air might have no advantage over a conventional ASHP. Fig.4 shows the profit variation in the range of $C < 1$. The curves exhibit a parabola shape opening downward. As C increases from 0, the profit first increases and then reaches the maximum. Further increment in C leads to profit decrement. The C corresponding to the maximum profit is around 0.65. A larger C means a larger heat recovery from the exhaust air, but the temperature of exhaust air and the COP of the EAHP drop, as displayed in Fig.5. The maximum

profit is a compromise between the waste heat recovery from the exhaust air and COP of the heat pump.

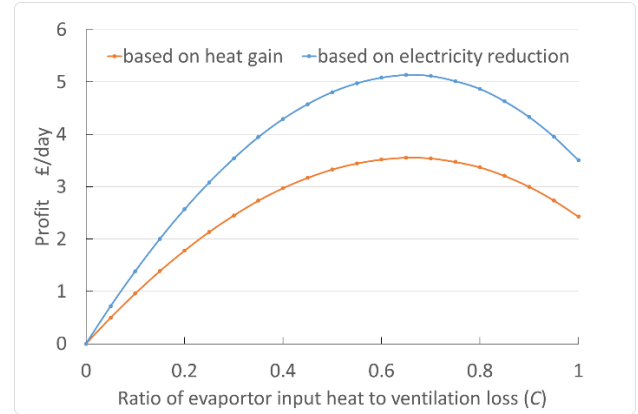


Fig.4. Variations of the profit with the input heat ($C \leq 1$)

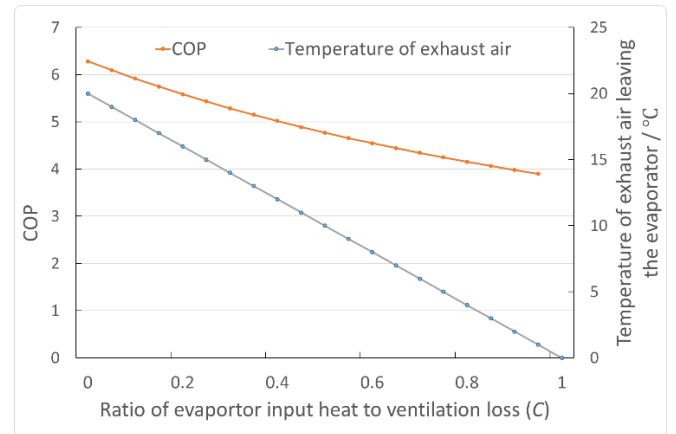


Fig.5. Variations of the temperature of exhaust air leaving the evaporator and COP with the input heat ($C \leq 1$)

The maximum profit for the EAHP based on heat gain and reduction in electricity consumption is about 3.55 and 5.13 £/day. The results indicate that in order to maximum the profit, the heat ratio (C) is less than 100%. However, when the heat pump is used for heat supply of the entire building, the evaporator input heat at design condition is normally larger than the ventilation heat loss (i.e., $C > 1$) because aside from the ventilation heat loss, there are heat losses through the windows, walls and roofs. To address this issue, the air ventilation can be facilitated intermittently. For example, a ventilation rate of 1 kg/s in a continuous operation mode can be adjusted to be 3 kg/s at 20 min intervals and 0 kg/s at 40 min intervals, as shown in Fig.6. For the intermittent ventilation, the daily

average ventilation heat loss is unvaried but the exhaust waste heat can be recovered more efficiently.

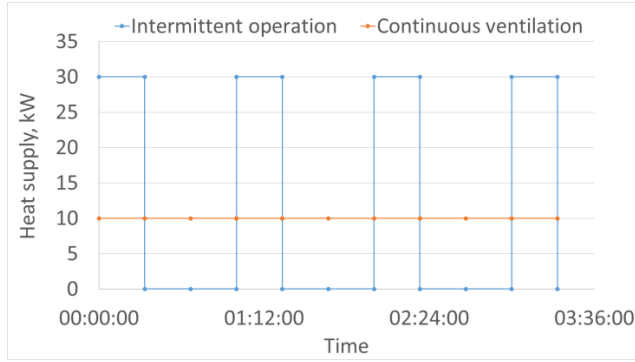


Fig.6. Control strategy for the ventilation

Performance of the MASHP with single-stage evaporator

For the MASHP with single-stage evaporator, the exhaust and ambient air are mixed directly. Although the principle is simple, analysis of this process is lacked. An insight to the mixing process is needed. Based on the established mathematical models, the following deductions can be made for the directly mixed air source heat pump when $C < 1$, $C = 1$ and $C > 1$.

(1) If $Q_{evap} < m_{ex}C_p(T_{ex} - T_{am})$, then
A higher x (i.e., a higher ambient air flow rate) leads to a lower $T_{mix,out}$ at a given the exhaust air flow rate. For the sake of a higher COP, there is no need to mix the exhaust air with the ambient air. This case occurs when the heat pump system is assisted by solar arrays and the heat pump provides only part of the energy required for heating. The MASHP will work in a similar way to the EAHP.

(2) If $Q_{evap} = m_{ex}C_p(T_{ex} - T_{am})$, then
 $T_{mix,out} = T_{am}$, which is independent on the mass flow rate of the ambient air.

(3) If $Q_{evap} > m_{ex}C_p(T_{ex} - T_{am})$, then

$$T_{ex} - T_{am} < \frac{Q_{evap}}{m_{ex}C_p} \quad (14)$$

$$\frac{Q_{evap}}{m_{ex}C_p} - (T_{ex} - T_{am}) > 0 \quad (15)$$

$$T_{mix,out} < T_{am} \quad (16)$$

For $C > 1$, the mixed air leaving the evaporator is at a temperature lower than the ambient temperature and therefore the evaporation temperature is always lower than the ambient temperature. Given the flow

rate of the exhaust air, a larger flow rate of ambient temperature leads to a higher temperature of the mixed air leaving the evaporator and thus a higher evaporation temperature and COP.

The profits based on the heat gain and electricity reduction are displayed in Fig.7. The profits increase slightly with the increment in the heat ratio (C). They are about 2.53 and 3.75 £/day. The curve shows that the profit is not influenced remarkably by the evaporator input heat. The reason behind this phenomenon is that the difference between the COPs of the MASHP and conventional heat pump (i.e. $COP - COP_{ref}$) is almost reversely proportional to C , as shown in Fig.8. On the other hand, the evaporator input heat is proportional to C . Due to the trade-off between $COP_{mix} - COP_{am}$ and C , The profits are almost constant.

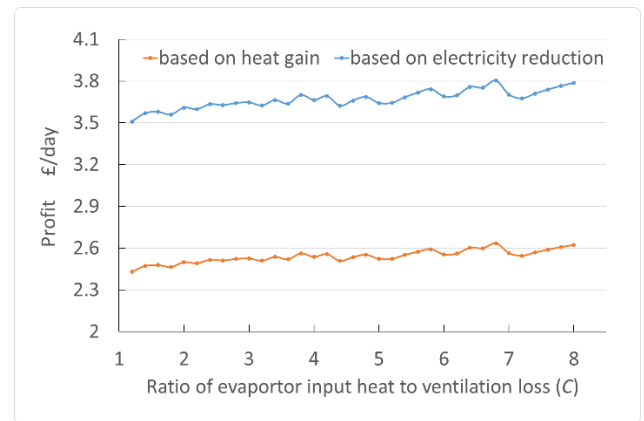


Fig.7. Variations of the profit with the input heat ($C > 1$)

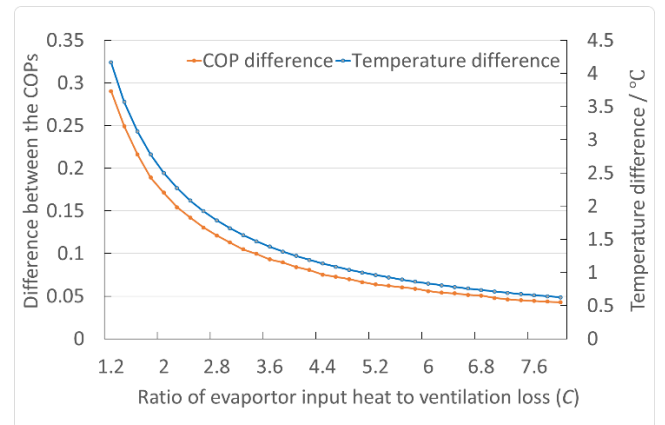


Fig.8. Variations of the COP difference and evaporation temperature difference with C

Variations of the ratio of ambient air flow rate to exhaust air flow rate (x), together with the mixed air temperature leaving the evaporator ($T_{mix,out}$), is

depicted in Fig.9. As the C increases, x goes up almost linearly, while $T_{\text{mix,out}}$ drops but the decrement becomes slower at a higher C . Given a temperature drop through the evaporator of 5°C , Q_{evap} influences the mass flow ratio, outlet temperature of air leaving the evaporator and the profit.

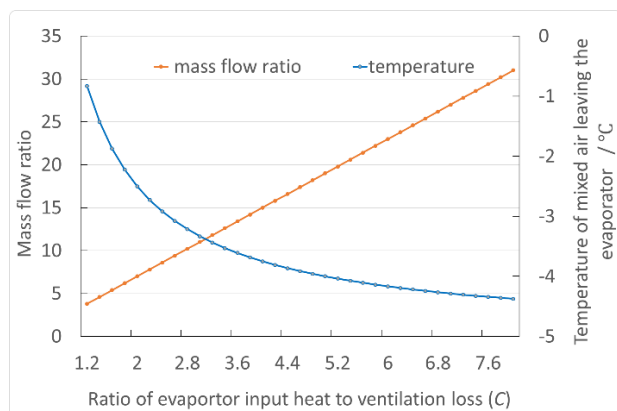


Fig.9. Variations of the mass flow ratio and mixed air temperature with the input heat (C)

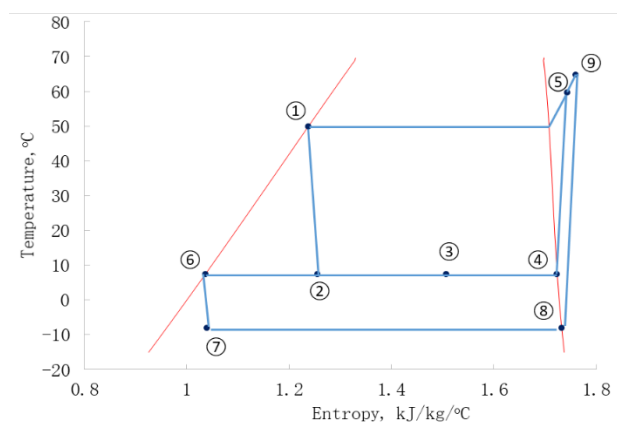


Fig.10. T - s diagram of the MASHP with two-stage evaporators

Performance of the MASHP with two-stage evaporators

The temperature-entropy (T - s) diagram of the MASHP with two-stage evaporators is illustrated in Fig.10. Similarly with those in Fig.1, the thermodynamic state points 1-10 represent the condenser outlet ①, throttle 1 outlet ②, medium-pressure evaporator inlet ③, medium-pressure evaporator outlet ④, compressor 1 outlet ⑤, throttle 2 inlet ⑥, throttle 2 outlet ⑦, low-pressure evaporator outlet ⑧ and compressor 2 outlet ⑨ and condenser inlet ⑩ (which is between ⑤ and ⑨), respectively.

Given the mass flow rate of exhaust air of 1.0 kg/s , the performance of the MASHP is influenced by the mass flow rate of the ambient air. The variations of the heat output and COP of the proposed heat pump with the mass flow ratio are displayed in Fig.11. The mass flow ratio (x) is defined by Eq.(4). The COP decreases while the heat output increases with the increment in x . The variations of the profits are depicted in Fig.12. Profits climb as x increases, which is due to an increasing heating capacity.

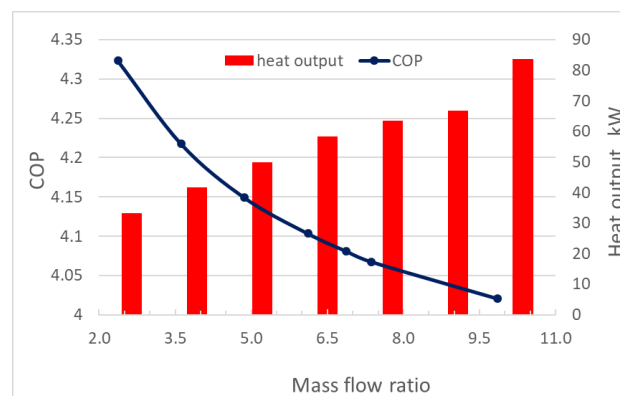


Fig.11. Variations of heat output and COP of the MASHP with the mass flow ratio

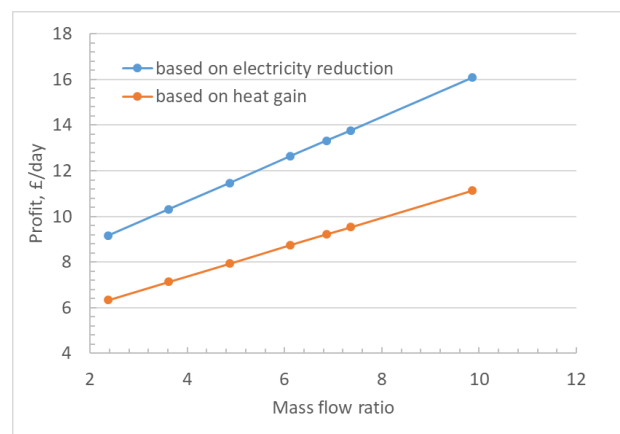


Fig.12. Variations of profits of the MASHP with the mass flow ratio

As a case study, parameter distribution of the MASHP with two-stage evaporators is exemplified in Tab.1 when the mass flow of ambient air is 4.87 (i.e., $x = 4.87$). The exhaust air is first used to heat the medium-pressure evaporator and then mixed with ambient air for the heating of the low-pressure evaporator. The temperature drop of exhaust air through the medium-pressure evaporator is 8.5°C and the mixed air leaving the low-pressure evaporator is at -3.1°C . The COP and heat output of the proposed heat pump are 4.15 and 50 kW . The

profit based on the reduction of electricity consumption is 11.5 £/day. Notably, the conventional ASHP operating at the same condensation temperature and ambient temperature is only 3.46.

Aside from the thermodynamic performance, the MASHP with two-stage evaporators have some technical advantages. Freezing is a serious problem of heat pumps applied in cold climate regions. A defrosting cycle is usually adopted and a considerable amount of electricity is needed, leading to a lower performance of the system. This problem can be overcome by the proposed heat pump. The exhaust air can be utilized for defrosting without additional electricity consumption.

Table 1. Parameter distribution of the MASHP with two-stage evaporators

Point	State	Temperature	Pressure	Flow rate	Quality
		°C	MPa	kg/s	%
1	liquid	50	1.32	0.30	0
2	binary	7.5	0.38	0.30	31.9
3	binary	7.5	0.38	0.14	68.4
4	vapor	7.5	0.38	0.14	100
5	vapor	59.7	1.32	0.14	100
6	liquid	7.5	0.38	0.16	0
7	binary	-8.0	0.22	0.16	10.8
8	vapor	-8.0	0.22	0.16	100
9	vapor	64.8	1.32	0.16	100
10	vapor	62.5	1.32	0.30	100

CONCLUSIONS

A direct mixing of the exhaust air and ambient air may cause significant thermodynamic irreversibility. The MASHP with single-stage evaporator has a profit of only about 3.7 £/day. The EAHP for recovery of the exhaust air without being mixed with the ambient temperature seems to be more profitable. To enable a ratio C of 0.65, the ventilation can be controlled. Given a compressor capacity of the heat pump, intermittent ventilation leads to a higher C than the continuous ventilation. The most beneficial system is the MASHP with two-stage evaporators and the profit is 11.5 £/day, which is significantly higher than that of the EAHP and MASHP with single-stage evaporator.

Despite of the superior thermodynamic performance, one more compressor is required. The capital cost of the system will be higher than a conventional ASHP and the payback period may not be shorter. To reduce the cost of the compressors, the vapor injection compressor will be

employed in the future work to recover the waste heat of exhaust air.

ACKNOWLEDGEMENTS

The authors would like to acknowledge our appreciation to the financial supports from the project titled ‘A low carbon heating system for existing public buildings employing a highly innovative multiple-throughout-flowing micro-channel solar-panel-array and a novel mixed indoor/outdoor air source heat pump’ funded by the UK BEIS.

NOMENCLATURE

- COP - Coefficient of performance;
 C_{ele} - Electricity price, £/kWh (about 0.20);
 C_{heat} - Heat price, £/kWh (about 0.04);
 C_p - Heat capacity;
 h - Enthalpy, J/kg;
 m_{am} - Flow rate of ambient air to be mixed, kg/s;
 m_{ex} - Exhaust air flow rate, kg/s;
 $Pro_{ex,ele}$ - Profit based on electricity reduction, £/day;
 $Pro_{ex,heat}$ - Profit based on heat gain, £/day;
 Q_{evap} - Evaporator input heat, W;
 $Q_{ven,l}$ - Ventilation heat loss without recovery, W;
 x - ratio of ambient air flow rate to exhaust air flow rate, %;
 T_{am} - Ambient temperature, °C;
 T_{ex} - Exhaust air temperature, °C;
 $T_{mix,in}$ - Mixed air temperature, °C;
 $T_{mix,out}$ - Mixed air temperature leaving the evaporator, °C;
 ΔT_{min} - Minimum temperature difference (about 5°C);
 W_{ele} - Electricity consumption.

REFERENCES

- [1] Gian Vincenzo Fracastoro, Matteo Serraino. Energy analyses of buildings equipped with exhaust air heat pumps (EAHP). *Energy and Buildings* **42**, 1283–1289 (2010).
- [2] Jörgen Wallin, Joachim Claesson. Improving heat recovery using retrofitted heat pump in air handling unit with energy wheel. *Applied Thermal Engineering* **62**, 823-829 (2014).
- [3] Dimitra Sakellari, Per Lundqvist. Modelling and simulation results for a domestic exhaust-air heat pump heating system. *International Journal of Refrigeration* **28**, 1048–1056 (2005).

- [4] Emmanouil Psimopoulos, Elena Bee, Joakim Widén, Chris Bales. Techno-economic analysis of control algorithms for an exhaust air heat pump system for detached houses coupled to a photovoltaic system. *Applied Energy* **249**, 355-367 (2019).
- [5] Ziyang Zhang, Chunlu Zhang, Meicai Ge, Yue Yu. A frost-free dedicated outdoor air system with exhaust air heat recovery. *Applied Thermal Engineering* **128**, 1041–1050 (2018).
- [6] Kuan Wang, Nianping Li*, Jinqing Peng*, Xiang Wang, Chunlei Wang, Meng Wang. A highly efficient solution for thermal compensation of ground-coupled heat pump systems and waste heat recovery of kitchen exhaust air. *Energy and Buildings* **138**, 499–513 (2017).
- [7] Zhongbing Liu, Weijiao Li, Ling Zhang, Zhenghong Wu, Yongqiang Luo. Experimental study and performance analysis of solar-driven exhaust air thermoelectric heat pump recovery system. *Energy & Buildings* **186**, 46–55 (2019).
- [8] Martin Thalfeldt, Jarek Kurnitski, Eduard Latõšov. Exhaust air heat pump connection schemes and balanced heat recovery ventilation effect on district heat energy use and return temperature. *Applied Thermal Engineering* **128**, 402–414 (2018).
- [9] Chen A, Liu H, Ran C, Wang C. Economic analysis on application of exhaust air heat recovery in existing public buildings in the severe cold regions. *Int Forum Energy, Environ Sci Mater*, 2015.
- [10] Lei Wang, Guoyuan Ma, Anna Ma, Feng Zhou, Fuping Li. Experimental study on the characteristics of triplex loop heat pump for exhaust air heat recovery in winter. *Energy Conversion and Management* **176**, 384–392 (2018).
- [11] Axell M, Karlsson F. IEA Heat Pump Centre, Europe: Heat pumps—Status and trends <https://www.google.com/search?client=firefox-ab&q=Axell+M%2C+Karlsson+F.+IEA+Heat+Pump+Centre%2C+Europe%3A+Heat+pumps%E2%80%94Status+and+trends+> (accessed 2.04.18)
- [12] Efficient' heating system left families with big bills". BBC News online. 10 Sep 2012. <https://www.bbc.co.uk/news/business-19511637>.

Screening of Antitumor and Hepatoprotective Activity Components from *Hedyotis diffusa*

Mengjiao Zhang[†], Hongyan Zhou, Siqing Niu, Xi Chen, Yunlan Li^{†*}

School of Pharmaceutical Science, Shanxi Medical University, Taiyuan 030001, P. R. China

Hedyotis diffusa is a traditional Chinese medicine used for the treatment of tumor and liver injury in clinic. But what are active ingredients that play the significant role in anticancer and liver protection are not yet know. The aim of this study was to screening for the effective components which had both antitumor and hepatoprotective activity in *Hedyotis diffusa*. The ethanol extract, ethyl acetate extract, total flavonoids and total triterpenoids from *Hedyotis diffusa* were prepared, and the antitumor activity and hepatoprotective effects of four extracts were screened by SRB method. The experimental results showed that four extracts could inhibit the proliferation to hepatoma carcinoma HepG-2 cells, and the total flavonoids had the strongest inhibitory effect on HepG-2. The inhibition rate of HepG-2 cells by 1000 $\mu\text{g/mL}$ total flavonoids could reach $84.9 \pm 2.7\%$. Only total flavonoids and total triterpenoids had protective effects on normal human hepatic HL-O2 cells, and the protective ratio of total flavonoids to HL-O2 was higher than that of total triterpenoids at the same concentration. In further experiments, five components including amentoflavone, quercetin, naringenin, kaempferol and rutin were selected from total flavonoids and used to screen for the antitumor activity and hepatoprotective effects. Furthermore, the amentoflavone and quercetin, which have both anticancer and hepatoprotective effects, were selected for further study. Finally, the selectivity of amentoflavone to liver cancer HepG-2 and normal human liver HL-O2 cells is higher than quercetin. Therefore, it is concluded that the main active components of *Hedyotis diffusa* against cancer and protect liver are total flavonoids and amentoflavone.

Keywords: Screening, antitumor activity, hepatoprotective activity, *Hedyotis diffusa*

INTRODUCTION

Hedyotis diffusa is an annual herb belonging to the genus Rubiaceae, mainly distributed in the south of China and some Asian countries, such as Indonesia, Japan, Malaysia, Nepal, Philippines, Sri Lanka, Thailand [1], and so on. *Hedyotis diffusa* is a traditional Chinese medicinal with long history. It was first reported that the *Hedyotis diffusa* has the effects of clearing heat, detoxifying, anti-inflammatory, anti-tumor [2-4], liver protection [5], antioxidant [6], and immune regulation [7] in "Guangxi Traditional Chinese Medicine". It was widely used for the treatment of tumor and liver injury in clinic up to now [8-10]. The liver is the most important metabolic organ of the human body [11]. When the liver was continuously exposed to alcohol, viruses, fat, harmful molecular metabolites and other factors that could cause liver damage and then it will lead to inflammation and liver function decline. Long-term liver damage can develop into chronic liver disease, which ultimately leads to liver cancer. The occurrence and development of liver disease were faced with a great threat to the maintenance of normal human activities. On the other hand, China's tumor morbidity and mortality have shown a clear upward trend according to

statistics, and cancer had become a serious public health problem. Due to the harmfulness of these two types of diseases (tumor and liver injury), the development of both anti-tumor and liver protective effects drugs had become a hot spot in human research. *Hedyotis diffusa* contains various active ingredients which simultaneously has the anti-tumor and the liver protection efficacy, including terpenoids, flavonoids, anthraquinones, alkaloids, organic acids, poly-saccharides, etc. The aim of this study was to find active ingredients with both anti-tumor and hepatoprotective activity in *Hedyotis diffusa*. The ethanol extract, ethyl acetate extract, total flavonoids and triterpenoids from *Hedyotis diffusa* were prepared through solvent extraction method, and the antitumor activity and hepatoprotective effects of four extracts were screened by Sulforhodamine B (SRB) method.

SRB test has been used as a common method for detecting cell proliferation and the inhibition rate of HepG-2 and the protection rate of HL-O2 by four different extracts including alcohol extract, ethyl acetate extract, total flavonoids and total triterpenoids. Screening out active ingredients with anti-cancer and liver-protecting activities from *Hedyotis diffusa*, which will be instructive for future mechanism of action work.

* To whom all correspondence should be sent:
liyulanr@163.com

Preparation of total triterpenoids

EXPERIMENTAL

Plant materials, Chemicals and reagents

Hedyotis diffusa was collected from Yangshuo, Guangxi and certified by Professor Tianai Gao from Shanxi Provincial Food and Drug Inspection Institute. Rutin (20140719), ursolic acid (20130321), kaempferol (20140710) and quercetin (20140716) were obtained from Tianjin Shilan Technology Co., Ltd. Amentoflavone (JZ15030111), naringenin (JZ15011710) were obtained from Nanjing Jingzhu Biotechnology Co., Ltd. Macroporous adsorbent resin AB-8 and polyamide resin were purchased from Chengdu Grecia Chemical Technology Co., Ltd. Cell culture media Dulbecco's modified Eagle's medium (DMEM), fetal bovine serum (FBS), PBS and pancreatin were obtained from Wuhan Dr. Bioengineering Co., Ltd. DMSO and Tris were purchased from Solarbio (Beijing, China). SRB and hydrogen peroxide were purchased from Sigma Aldrich Chemical. All the other reagents used were of high quality.

Preparation of alcohol extract and ethyl acetate extract

The *Hedyotis diffusa* was cut into small pieces about 5 mm and each 50 g of them was refluxed by 800 mL of 70% ethanol. The extraction solution was freeze-dried to obtain alcohol extracts. And then the alcohol extracts were made into an aqueous solution and extracted with ethyl acetate. After freeze-drying, ethyl acetate extracts were obtained.

Preparation of total flavonoids

The *Hedyotis diffusa* was cut into small pieces about 5 mm and each 50 g of them was refluxed by 800 mL of 70% ethanol about 2 hours. The filtrate of alcohol extract from *Hedyotis diffusa* was obtained by hot suction filtration. After cooling to room temperature, extracts with petroleum ether until the their layer was colorless. The aqueous layer solution was concentrated by rotary evaporator (DL-400, zhenzhou changcheng Co., Ltd) at 60°C under reduced pressure. The prepared aqueous solution was purified by macroporous adsorption resin [12-13] and polyamide resin (Chengdu grecia chemical technology co. LTD), and finally the total pure flavonoid extracts of *Hedyotis diffusa* were obtained.

Extraction with 70% ethanol reflux (v/v, 1:10) was performed for 3 times for each 50 g of *Hedyotis diffusa*. The pH of extraction to 12 was adjusted with sodium hydroxide solution and extracted with petroleum ether until the ether layer was nearly colorless, the water layer was taken. The pH of the water layer was adjusted from 2 to 3 with hydrochloric acid solution, and extracted with ethyl acetate until the ethyl acetate layer was nearly colorless, and the ethyl acetate layer was taken [14]. After purification by macroporous adsorption resin, the triterpene extracts of *Hedyotis diffusa* could be obtained.

Cell Lines and Cell Culture

The human cell lines used in this study were liver cancer hepatocellular carcinomas (HepG-2) cells and normal human hepatocyte cell line (HL-O2) cells, which were purchased from Wuhan Boster Biological Engineering Co., Ltd. (Wuhan, PR China). HepG-2 and HL-O2 cells were cultured in DMEM added with 10% heat-inactivated FBS, 100 U·mL⁻¹ penicillin and 100 µg·mL⁻¹ streptomycin in a constant temperature incubator with 5% CO₂ at 37°C. Passage was digested with 0.25% trypsin. According to cell growth, subculture was carried out for 2 to 3 days to ensure that all cells used for the experiment were in a logarithmic growth phase.

SRB assay

The inhibitory rate of liver cancer HepG-2 cells and the protection rate of normal human liver HL-O2 cells were determined by SRB method to compare the effects of different extracts. HL-O2 and HepG-2 cells in logarithmic growth phase were digested with trypsin and seeded in 96-well plates at a density of 2×10⁵ cells per well until cells attachment. The cells were treated with different extracts from *Hedyotis diffusa* (ethanol extracts, ethyl acetate extracts, total flavonoids and total triterpenoids) at 0, 62.5, 125, 250, 500 and 1000 µg/mL or five compounds in total flavonoids (amentoflavone, quercetin, naringenin, kaempferol, rutin) at 31.25, 62.5, 125, 250 and 500 µmol/L for 24 h, respectively. The cells were fixed with 50 µL of 30% trichloroacetic acid at 4°C for 1 h. The supernatant was discarded and the wells were rinsed 5 times with deionized water. After air drying, the cells were cultured in 100 µL of 0.4% SRB dissolved in 1% acetic acid for 30 min, washed with

5% acetic acid to remove the uncombined SRB colorant, air dried and dissolved in 10 mmol/L trisbase solution (pH 10.5). After blending, the absorbance (OD) values were measured at 515 nm by using a microplate reader (Thermo Scientific, USA). Cell inhibitory rates were calculated as the following formula: Inhibitory rates % = (absorbance of untreated cells-absorbance of treated cells) / absorbance of untreated cells × 100%.

Statistical Analysis

The dates were expressed in standard deviation ($X \pm SD$). *T*-test analysis was used to compare the differences between different groups. When $p < 0.05$, there was a statistical difference. All experiments were repeated three times in parallel.

RESULTS AND DISCUSSIONS

Result of total flavonoid purity determination

With UV full wavelength scanning from 400 to 800 nm, rutin has maximum absorption at 501 nm showed in Fig1. The standard curve was prepared with rutin as the standard. The linear regression equation was $Y = 10.88 X + 0.0043$, $r = 0.9984$.

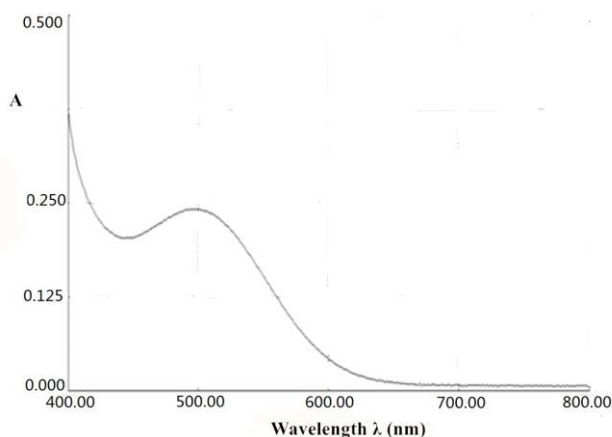


Fig.1. UV wavelength scanning for rutin

Calculate the total flavonoid purity according to the following formula [15]: Total flavonoids purity (%) = $DY / W \times 100\%$, *D* represents dilution multiple and *W* is sample quantity. The results were shown in Table 1, the purity of total flavonoids determined is 65.6 %.

Table 1. Determination of the purity of total flavonoids

No.	sample quantity (mg)	Absorbance	Purity (%)	Average purity (%)	RSD(%)
1	15.0	0.429	65.0		
2	15.0	0.437	66.3	65.6	0.66
3	15.0	0.432	65.5		

Result of total triterpenoid acid purity determination

With UV full wavelength scanning from 400 to 800 nm, ursolic acid has maximum absorption at 548 nm showed in Fig.2. The standard curve was prepared with ursolic acid as the standard. The linear regression equation was $Y = 5.9203 X - 0.01$, $r = 0.9994$.

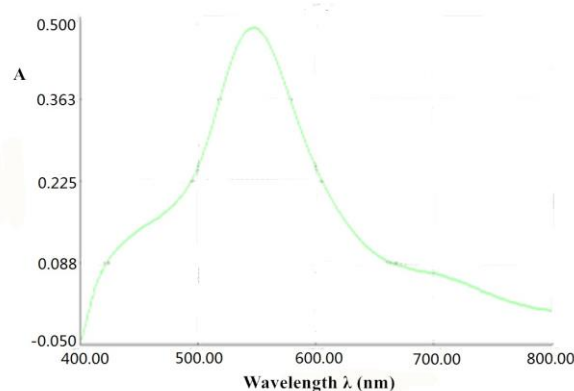


Fig.2. UV wavelength scanning for ursolic acid

Calculate the purity of total triterpenoid acid according to the following formula: Total triterpenoid acids purity (%) = $DY / W \times 100\%$, *D* represents dilution multiple, and *W* is sample quantity. The results are shown in Tab.2, the purity of total triterpenoid acids determined was 22.0 %.

Table 2. Determination of the purity of total triterpenoid acids

No.	sample quantity (mg)	Absorbance	Purity (%)	Average purity (%)	RSD (%)
1	25.0	0.415	23.4		
2	25.1	0.390	21.9	22.0	1.35
3	25.1	0.369	20.7		

Concentration selection of H₂O₂ Modeling

The inhibition rates of H₂O₂ at different concentrations (50 ~ 600 μmol/L) on HL-O2 cells were shown in Fig.3. The results showed that the survival rate of HL-O2 cells decreased with the increase of H₂O₂ concentration. When the concentration of H₂O₂ was 100 μmol/L, the survival rate of HL-O2 cells was significantly lower than that of the control group ($p < 0.05$). When the concentration of H₂O₂ was 200 μmol/L, the cell inhibition rate was about 60.0%. This concentration of H₂O₂ was selected for modeling.

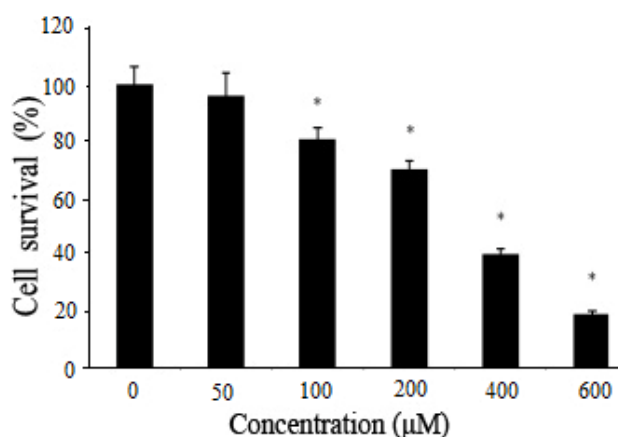


Fig.3. Cell survival rate of HL-O2 cells by different concentrations of H₂O₂. *($p < 0.05$) indicates that there is a significant difference in the survival rate of the H₂O₂ dosing group compared with the control group

Activity screening of four different extracted parts

The anticancer activities of alcohol extracts, ethyl acetate extracts, total flavonoids and total triterpenoid acid were shown in Fig.4 and the liver protective activities were shown in Fig.5. The results showed that the total flavonoids had the highest anticancer activity in the four extracts. The inhibitory rate of the total flavonoids on HepG-2 cells was 84.9±2.7%. Among the four extracts, only total flavonoids and total triterpenoid acids had hepatoprotective activities and the protective rates of 125 μg/mL and 250 μg/mL total flavonoids on HL-O2 cells were significantly higher than that of total triterpenoid acids at the same concentration ($p < 0.05$). In view of the fact that total flavonoids have the best anticancer activity and hepatoprotective activity in the four extracts, total flavonoids were identified as preferred sites. Compounds in total flavonoids were selected for

further screening for liver protection and anticancer activity.

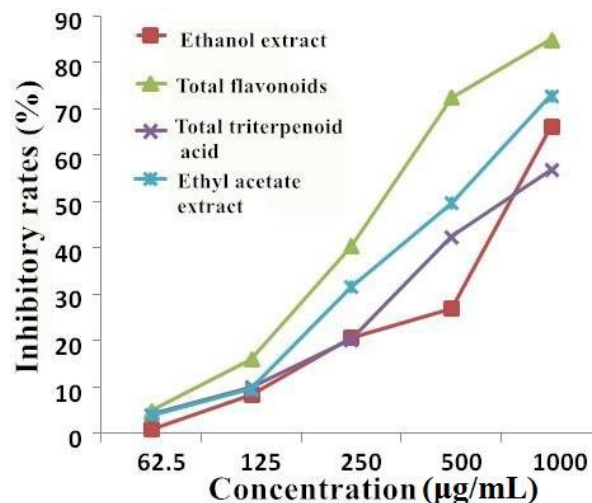


Fig.4. Inhibitory rates of four extracts on HepG-2 cells

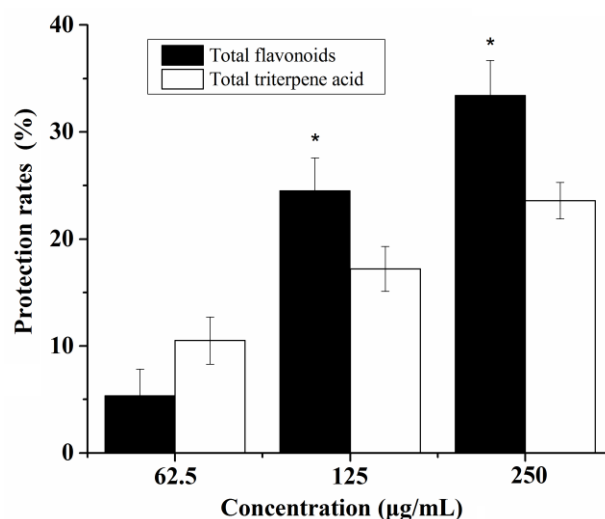


Fig.5. Protective rates of total flavonoids and total triterpenoid acids on HL-O2 cells. *($p < 0.05$) showed that there was a significant difference in the protective rate of total flavonoids compared with total triterpenoid acids

Activity screening of five different compounds in total flavonoids

Amentoflavone, quercetin, rutin, naringenin and kaempferol from total flavonoids were selected to screen for liver protection and anticancer activity. The liver protection activity was shown in Tab.3. From this results, it could be found that the compounds with better liver protective effect were amentoflavone and quercetin. The results showed that the protection rates of amentoflavone and quercetin on HL-O2 cells were higher than that

of other components. And the protection rate of 250 $\mu\text{mol/L}$ amentoflavone was significantly higher than that at the same concentration of quercetin and 125 $\mu\text{mol/L}$ bifendate ($p < 0.05$) (Fig.6).

Table 3. Protective effects of different flavonoids on HL-O2 cells

Compounds	Protection (%)		
	62.5 $\mu\text{mol/L}$	125 $\mu\text{mol/L}$	250 $\mu\text{mol/L}$
Amentoflavone	6.5 \pm 1.3	19.6 \pm 3.7	40.7 \pm 2.0
Quercetin	5.0 \pm 1.8	25.1 \pm 2.3	3.0 \pm 1.2
Rutin	9.4 \pm 2.4	—	—
Bifendate		10.7 \pm 3.0	

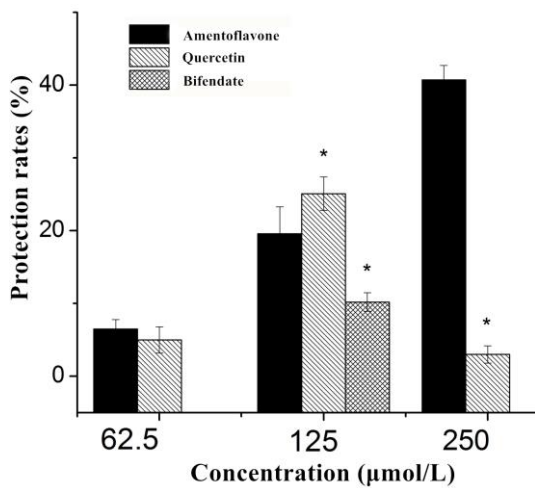


Fig.6. Protective rates of amentoflavone, quercetin and bifendate on HL-O2

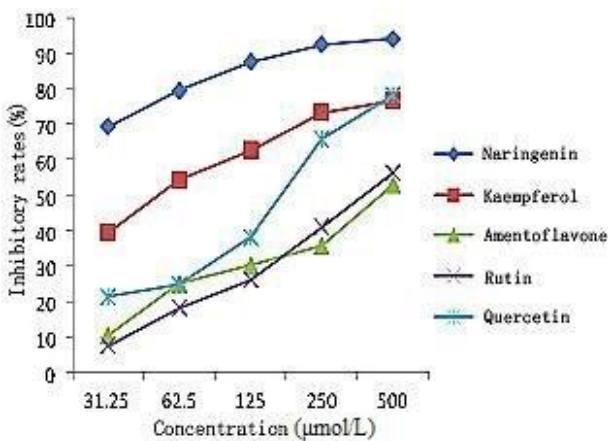


Fig.7. Inhibitory rates of five flavonoids on HepG-2 cells

Screening results of anticancer activities of Amentoflavone, quercetin, naringenin, kaempferol and rutin were shown in Fig.7. The inhibitory rates (%) of 500 $\mu\text{mol/L}$ amentoflavone and quercetin on HepG-2 cells were 56.2 \pm 8.1 % and 78.0 \pm 9.3 %, respectively. It can be seen from Fig.7 and Tab.3 that the compounds with anticancer activity and liver protective activity were quercetin and amentoflavone. HL-O2 and HepG-2 cells were treated with quercetin and amentoflavone for 48 h. The cell selectivity results were shown in Fig.8. From the selectivity results, it was found that the selectivity of amentoflavone was higher than that of quercetin at 500, 250, 125 and 62.5 $\mu\text{mol/L}$. Therefore, amentoflavone was selected as the preferred compound.

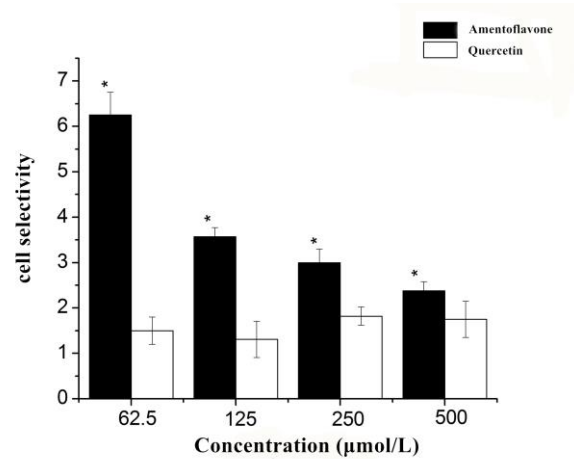


Fig.8. Results of selection of compounds. *($p < 0.05$) indicates a significant difference compared to quercetin

CONCLUSIONS

The inhibitory effect on HepG-2 cells and the protective effect on HL-O2 cells of different extracts from *Hedyotis diffusa* were investigated in this experiment. Ethanol extracts, ethyl acetate extracts, total flavonoids and total triterpenoids were separately prepared. The purity of total flavonoids could reach 65.6 %, and the purity of total triterpenic acids could reach 22.0 %. According to the screening results, all four extracts had inhibitory effect on HepG-2 cells, and the total flavonoids had the highest anticancer activity among the four extracts, and the inhibition rate of 1000 $\mu\text{g/L}$ total flavonoids on HepG cells could be up to 84.9 \pm 2.7%. And only the total flavonoids and total triterpenoid acids in the four extracts had hepatoprotective activity, and the protective rates of total flavonoids of 125 and 250 $\mu\text{g/mL}$ on HL-O2

cells were significantly higher than that the same concentration of total triterpenoid acids. Since the total flavonoids had the best anticancer activity and hepatoprotective activity, total flavonoids were selected for further activity screening. Amentoflavone, quercetin, naringenin, kaempferol and rutin were selected from total flavonoids. The results proved that amentoflavone and quercetin had better hepatoprotective activity, followed by rutin, but naringenin and kaempferol had no hepatoprotective activity. What's more, the protection rate of 250 $\mu\text{mol/L}$ amentoflavone was significantly higher than that in the same concentration of quercetin ($p < 0.05$). According to the screening results of anti-tumor activity, the amentoflavone and quercetin also had anticancer activity. The inhibition rates of 500 $\mu\text{mol/L}$ amentoflavone and quercetin on HepG-2 cells could reach $56.2 \pm 8.1\%$ and $78.0 \pm 9.3\%$ respectively. From the cell selectivity results, the selectivity of amentoflavone to HL-O2 and HepG-2 cells at 500, 250, 125, 62.5 $\mu\text{mol/L}$ was significantly different from that of quercetin ($p < 0.05$). Therefore, amentoflavone was screened as the preferred compound. In this experiment, the amentoflavone and total flavonoids in *Hedyotis diffusa* were screened as the active components that both had anticancer activity and liver protective activity, which provided a material basis for further research.

ACKNOWLEDGEMENTS

Financial support funded by National Natural Science Foundation of China (81973411), Shanxi Key Subjects Construction (FSKSC), National Science and Technology Major Project (2018ZX09101003-001-017), the Top Science and Technology Innovation Teams of Higher Learning Institutions of Shanxi Province, the Program for the Top Young and Middle-aged Innovative Talents of Higher Learning Institutions of Shanxi Province (2015), Shanxi Province Key Research and Development Project (201703D111033), the Project of Shanxi Key Laboratory for Innovative Drugs on Inflammation-based major disease "Anti-inflammatory Mechanism of Baihuadexhuangcao Flavone Baogan Capsule" (SXIDL-2018-05), Project of Center of Comprehensive Development, Utilization and Innovation of Shanxi Medicine (2017-JYXT-18), Research subject of graduate education reform in shanxi medical university (20141034) is gratefully acknowledged.

ABBREVIATIONS

RSD - relative standard deviation;
DMEM - Dulbecco's modified Eagle's medium;
SRB - Sulforhodamine B;
FBS - fetal bovine serum;
HepG-2 - liver cancer cells;
HL-O2 - normal human liver cells;

REFERENCES

- [1] Ye JH, Liu MH, Zhang XL. Chemical Profiles and protective effect of *Hedyotis diffusa* Willd in lipopolysaccharide-induced renal inflammation mice. *Int. J. of Molecular Sciences* **16** (11), 27252-27269 (2015).
- [2] Li Q, Wang X, Shen A, Zhang, Y. *Hedyotis diffusa* Willd overcomes 5-fluorouracil resistance in human colorectal cancer HCT-8/5-FU cells by downregulating the expression of P-glycoprotein and ATP-binding cassette subfamily G member 2. *Experimental & Therapeutic Medicine* **10** (5), 1845-1850 (2015).
- [3] Hu E, Wang D, Chen J. Novel cyclotides from *Hedyotis diffusa* induce apoptosis and inhibit proliferation and migration of prostate cancer cells. *International Journal of Clinical & Experimental Medicine* **8** (3), 4059-65 (2015).
- [4] Cai Q, Lin J, Wei, L. *Hedyotis diffusa* willd inhibits colorectal cancer growth in vivo via inhibition of stat3 signaling pathway. *International Journal of Molecular Sciences* **13** (5), 6117-6128 (2012).
- [5] G-Z Z, X-L P, N-H T. Natural biflavones as novel inhibitors of cathepsin B and K. *European Journal of Medicinal Chemistry* **41** (11), 1247-1252 (2006).
- [6] Gao X, Li C, Tang YL, Zhang, H (2015) Effect of *Hedyotis diffusa* water extract on protecting human hepatocyte cells (LO2) from H2O2-induced cytotoxicity. *Pharmaceutical Biology* 2015:1-8.
- [7] Kuo, Y J, Lin, J P, Hsiao, Y T. Ethanol extract of *Hedyotis diffusa* willd affects immune responses in normal balb/c mice in vivo. *Vivo* **29** (4), 453-460 (2015).
- [8] Wang RB. Treatment of liver diseases with traditional Chinese medicin. *Journal of Clinical hepatobiliary Disease* **31** (1), 2- 6 (2015).
- [9] Shen CY, Lin SY. Antineoplastic mechanism and clinical application of *Hedyotis diffusa*. *Henan traditional Chinese Medicine* **31** (11), 1304-1306 (2011).
- [10] Lin H, Mei QX, Kong XL. Clinical application and mechanism of *Hedyotis diffusa* in the treatment of liver diseases. *Asia-Pacific traditional Medicine* **07** (10), 173-175 (2011).

- [11] Andrade KQD, Moura FA, Santos JCD. Oxidative Stress and inflammation in hepatic diseases: therapeutic possibilities of N-Acetylcysteine. *Int. J. of Molecular Sciences* **16** (12), 30269-30308 (2015).
- [12] Yang PM, Dai L, Wei YL. Study on separation and purification of total flavonoids from *Hedyotis diffusa* by macroporous adsorption resin. *Journal of Beijing University of traditional Chinese Medicine* **33** (6), 417 – 420 (2015).
- [13] Mao XF, Luo JB. Study on extraction and separation of total flavonoids from *Hedyotis diffusa*. *Chinese medicinal materials* **25** (7), 499-500 (2002).
- [14] Meng RB, Tang QF, Zeng YC. Extraction and purification of total triterpenoid acid from *Hedyotis diffusa*. *Chinese Journal of Experimental prescription* **18** (24), 65-68 (2012).
- [15] Chai JX, Wan Y, Fu GM. Optimization of determination method for total flavonoids in *Eucommia ulmoides* leaves. *Chinese Journal of Food* **13** (4), 225- 230 (2013).

Comparative study on the quality control of trihydroxybenzophenones compounds

Siqing Niu^{1†}, Yunlan Li^{1,2,*}, Xi Chen¹, Mengjiao Zhang¹, Qingshan Li^{1,2*}

¹School of Pharmaceutical Science, Shanxi Medical University, Taiyuan 030001, P. R. China, Yunlan Li

²Shanxi University of Chinese Medicine, Key Laboratory of Innovative Drug for the Treatment of Serious Diseases Basing on the Chronic Inflammation

The quality control of three highly active anti-inflammatory and anti-oxidation structurally similar trihydroxybenzophenones, 4,5,2'-trihydroxy-2,5'-dichlorobenzophenone (LC), 4,5,2'-trihydroxy-2,5'-dibromobenzophenone (LB) and 4,5,2'-trimorpho- linyloxy-2,5'-dichlorobenzophenone (LMC) were developed in this paper. According to the common parent nucleus structure and characteristic groups of the three compounds, the quality comparison studies were illuminated from four aspects: traits, identification, inspection and content determination. The appearance, taste, solubility, melting point, melting range, absorption coefficient and acidity of the compound were examined in terms of properties. LC is a dark yellow powder crystal, LB is pale yellow needle one, and LMC is white one but a slight acid odor. They are all weakly acidic compounds. The melting points of both LC and LB are a little bit higher than 200°C, but LMC's is only 150°C. The absorption coefficients of three compounds are order of magnitude of 10⁴, they are 2.8 × 10⁴ (for LC), 3.0 × 10⁴ (for LB), 1.7 × 10⁴ (for LMC), respectively. The absorption coefficient of LB is the largest because of its highest conjugate structure. Three compounds were identified by chemical method, UV and HPLC method. Among them, the advantage of the chemical method is that it has an intuitive color reaction, so is simple in operation. The UV identification results shown that the maximum absorption wavelength of LMC is 230 nm, but the maximum absorption wavelengths of LB and LC are so similar (261 nm and 259 nm) that they are hard to separate. The HPLC method had very good specificity that it is able to identify the three compounds with completely accuracy. The contents of three compounds were determined severally by acid-base titration, UV and HPLC methods. The acid-base titration method is simple, accuracy, but its sensitivity is a little bit low. The HPLC is with high sensitivity, simple operation and universal applicability, UV had high accuracy and good repeatability. The quality of three batches of samples for three compounds were all in compliance with general Quality Control Standard of Pharmacopoeia including drying weight loss, ignition residue, heavy metal, and sulfate test. The results of these studies shown that the quality control of the three compounds are reliable, stable, accurate and controllable, and the contents of three compounds could be controlled in the range of 98.0 ~ 102.0%.

Keywords: Benzophenone, traits, identification, inspection, content determination

INTRODUCTION

Modern research had found that benzophenone halophenols have high activity in antitumor, antiinflammatory, antioxidation, antibacterial, antithrombosis, biological antifeeding, liver protection and diabetic nephropathy. The natural marine origin three patented compounds [1] including LC, LB and LMC researched by our laboratory group in this paper have good activity on the injury of vascular endothelial EA.hy 926 cells induced by H₂O₂. So the study of their quality control is extremely urgent. The comparative study on quality control of the three compounds had never been studied before. Since they not only have a common nucleus of diphenylketone, but also have characteristic groups, the comparative studies of quality control are meaningful for further predicting their biological activity and studying its *in vivo* detection, monitoring and drug metabolism. This research aims to describe a comparative study

on their quality standards including traits, identification, inspection and content determination [2-4]. Quality control researches about these three compounds could not only provide guidance for the preparation of raw materials and pharmaceuticals, but also offering quality standards for preclinical pharmaceuticals and pharmaceuticals for pharmacodynamics, toxicology research and new drug research and development.

EXPERIMENTAL

Chemicals and reagents

The standard substance (their purity were over 99.0% by HPLC analysis after three recrystallizations) and three compounds (their purity were over 98.0% by HPLC analysis) including LB, LC and LMC were all independently by our research group of Shanxi Medical University. The other chemicals used, such as silver nitrate, nitric acid, phosphoric acid, hydrochloric acid and sodium hydroxide, were obtained from Tianjin damao technology Co., Ltd (Tianjin, China). All solvents used were of HPLC grade. The

* To whom all correspondence should be sent:
liyulanrr@163.com

chromatographic solvents and reagents such as methanol and acetonitrile were purchased from Tianjin kemiu technology Co., Ltd (Tianjin, China). Deionized water was prepared using a Milli-Q water purifying system from Millipore Corp. (Bedford, MA).

Character check for three compounds

1. Solubility

Solubility is the property of a solid, liquid, or gaseous chemical substance called solute to dissolve in a liquid solvent to form a homogeneous solution of the solute in the solvent. The solubility of a substance fundamentally depends on the physical and chemical properties of the solute and solvent as well as on temperature, pressure and the pH of the solution. The extent of the solubility of a substance in a specific solvent is measured as the saturation concentration, where adding more solute does not increase the concentration of the solution and begin to precipitate the excess amount of solute. Excessive samples were added to 10 mL of solvent of the plugged triangular bottle and the bottle was placed into a 37°C thermostatic water bath shaker (BS-1E, Honghua instrument factory, China) for 48 h, then was centrifuged for 15 min at 5000 r/min with a centrifuge (TGL-16gR, Anting scientific instrument factory, Shanghai, China). The supernatant was filtered with 0.45 µm microporous filter membrane and the continuous filtrate were taken to determine the absorbance (OD) at the maximum absorption wavelength with a UV spectrophotometer (MAPADA-1200, Meipuda instruments co. LTD, Shanghai, China).

2. Melting point

Melting is a physical process that results in the phase transition of a substance from a solid to a liquid. The internal energy of a substance is increased, typically by the application of heat, resulting in its temperature to the melting point, at which the ordering of ionic or molecular entities in the solid breaks down to a less ordered state and the solid liquefies. 1 mg of dried sample was placed on glass plate and the initial temperature of the automatic melting point meter (SGW X-4, INESA instruments co. LTD, Shanghai, China) was set at 130°C. The glass plate with the sample was heated at a rate of 1.0 °C/min. The melting point of three compounds were the temperature at which it melts when heated it. The sample should be measured three times and the average value was taken as melting point.

3. Absorption coefficient

The absorption coefficient is a quantity that characterizes how easily a material or medium can be penetrated by a beam of light. 2 mg of samples were weighed precisely and 1000 mL of water was used to dissolve, diluted quantitatively to make a solution containing about 20 µg/mL, and then the solution were quantitatively half diluted to 10 µg/mL. The absorbance values were determined at the maximum absorption wavelength using five UV spectrophotometers (MAPADA-1200, MAPADA-1600 and MAPADA-1800, Shanghai, China; 1900, Shimadzu, Japan; Cary60, Agilent, USA) according to the General Rule 0401 of Part 4 in Chinese pharmacopoeia (2015 edition). The absorbance values (OD) of test solutions should be controlled between 0.3 and 0.7. The percentage absorption coefficients were calculated according to the following formula : $E_{cm}^{1\%} = A / c \times L$, where A refer to the absorbance values, c represented concentration with the unit (g / 100 mL), and L was thickness of object [5].

4. Acidity value

10 mg samples were added to 50 mL of water to prepare a solution. The solution was heated at 60 °C for 10 min, then cooled to 25°C, and filtered with 0.45 µm microporous membrane. The filtrate were taken to determine pH value according to general rule 0631 by pH acidity meter (pHS-2C , Shanghai lida instruments co. LTD, China).

Identification of three compounds

1. Chemical identification

One drop of FeCl₃ solution was added to the sample solution, and the changed color was used as the identification basis of phenol hydroxyl group. The dried samples were co-heated with an hydrous Na₂CO₃ powder until it turned to black from colorless, then 1 mL HNO₃ (0.1 mol/L) was added to adjust the solution to acidic. Finally, silver nitrate AgNO₃ was used to identify the phenolic hydroxyl, bromide and chloride groups. After AgNO₃ solution (0.1 mol/L) was added into above acidic solution, it was used as the basis for the identification of chlorine groups if white precipitate was generated, and light yellow precipitate would be generated as the basis for the identification of bromine groups.

2. UV identification

1 mg of sample was added to methanol to make a solution containing about 10 µg/mL LC, LB and

LMC. The solution was scanned by UV spectrophotometer from 200 to 400 nm to obtain the maximum UV absorption wavelength.

3. HPLC identification

HPLC analysis was carried out using a Agilent 1200 HPLC system (Agilent technology co. LTD, USA) which consisted of a photodiode array detector, an autosampler, and a degasser according to the General rule 0512 of Part 4 in Chinese pharmacopoeia (2015 edition). Chromatographic column was a Diamonsil C18 (250 mm × 4.6 mm, 5 μm) from Dikma Technologies (Beijing, China), and it's temperature was set at 25°C. The mobile phase for HPLC analysis consisted of 80% methanol and 20% water with a rate of 1 mL/min. The detection wavelength was the maximum absorption wavelength of each of the three compounds. Concentration of three compounds were all 200 μg/mL. Sample volume of 20 μL was injected. Prior to use, the mobile phase was filtered through a 0.45 μm hydrophilic membrane filter. The retention time of there compounds under this chromatographic condition was used for identification.

Limit inspection for general impurity

1. Drying weight loss

1.0 g of Samples which were dried to constant weight were measured precisely, and then were dried at 105°C for 30 min. The reduced mass of three samples before and after weighing was recorded and the lossed weight was calculated as the drying weight loss.

2. Residue on ignition and heavy metal

1.0 g of samples were placed in a crucible which had been ablated to a constant weight. The samples were heated slowly until full carbonization, and then 0.5 mL of concentrated H₂SO₄ (98.0%) were added to it, and the sulfur vapor was removed by low-temperature heating (55°C). Then the samples were ignited at 500°C until ashing completely, placed in the dryer to make it cold, then weighed precisely. The residue which left under ignited residue were used to check the content of heave metals according to the second method of General rule 0821 of Part 4 in Chinese pharmacopoeia (2015 edition)

3. Chloride check and sulfate check

2.0 g of the samples were added to 100 mL of water to make the mixed solution. The solution was

heated to a boil, then was cooled to 25°C. 25 mL of the filtrate was taken to check chloride according to General rule 0801 of Part 4 in Chinese pharmacopoeia (2015 edition). It would not be thicker than the control solution made of 5 mL of standard sodium chloride solution (0.01%). 25 mL of the filtrate which left under chloride check was taken to check sulfate according to general rule 0802 of Part 4 in Chinese pharmacopoeia (2015 edition). It will not be thicker than the control solution prepared from 1 mL of standard potassium sulfate solution (0.02%).

Content determination for the three compounds

1. Acid-base titration

4 mg of samples were weighed precisely, and added into 20 mL methanol to prepare test solution which concentration was about 200 μg/mL. The NaOH standard solution (0.01 mol/L) was taken as titrant. 20 mL of methanol was titrated with NaOH as blank correction. Phenolphthalein solution was used as indicator. The color of titration endpoint was shown as in Fig.1. The NaOH standard solution (0.01 mol/L) was used to titrate the sample solution which concentration was about 200 μg/mL. The initial volume and final volume of titrant were recorded, and the consumed volume of titrant NaOH standard solution were measured, thus the content of the sample was calculated as the following formula: Sample content (%) = ($V_{\text{NaOH}} \times c_{\text{NaOH}} \times M_{\text{sample}}$) × 100% / (1000 × w), where V_{NaOH} , c_{NaOH} , M_{sample} and w refer to the consumed volume (mL), concentration (mol/L) of NaOH standard solution, molar mass of measured compounds (g / mol) and the mass of weighing sample (g), respectively. The sample would be measured three times and then the average content (%) and RSD (%) value were calculated [6].



Fig.1. The color of titration endpoint for acid - base titration

2. UV-VIS spectrophotometry

10 mg of standard substances and the test three compounds were weighed precisely, transferred quantitatively into a 100 mL volumetric flask after

dissolution with methanol to prepare the corresponding standard store solution (100 µg/ mL), then stored in a refrigerator at 4°C [7-12]. With methanol, the standard store solution were proportionally diluted to different gradients solution which concentration were 0, 1, 5, 25, 50, 75, 100 µg / mL, respectively. The absorbance values OD of these solutions were measured by UV spectrophotometer at the maximum absorption wavelength for making standard curves with corresponding gradient concentration. In order to verify the precision of the method, the OD values of the standard substance solution (50 µg/mL) were measured six times by UV spectrophotometer under the maximum UV absorption wavelength of three compounds, and the RSD (%) value of these six measured OD were calculated. In order to verify the repeatability of the method, five portions test solution (50 µg/mL) were determined by UV spectrophotometer under the maximum UV absorption wavelength of three compounds, and their OD values were used to calculate the RSD (%) as the repeatability. 5 mg of the test samples were weighed precisely, and was added into a 100 mL volumetric flask and diluted to scale with methanol to prepare the test sample solution. To verify the recovery rate of the method, the nine samples of known concentrations were divided into three groups, and then each group was added with a 50 µg / mL control sample solution of 0.8 mL, 1.0 mL and 1.2 mL, respectively. Nine portions solutions were diluted with methanol, and the OD values were measured by UV spectrophotometer under the maximum UV absorption wavelength of three compounds, to calculate the recovery rate according to the following formula: The recovery rate (%) = (the measured quantity after added standard substance – the known quantity of sample) × 100% / the mass of added standard substance. Three batches of samples were taken to prepare 50 µg/mL of test solution and standard solution with methanol, respectively. The OD values of three batches samples were determined to calculate the content (%) according to standard curve.

3. HPLC chromatography

HPLC analysis as “3.3 HPLC identification” was carried out using a Agilent 1200 HPLC system to determinate contents of the three compounds. Chromatographic column was also Diamonsil C18 (250 mm × 4.6 mm, 5 µm), and the detect temperature was 25°C. The velocity of the mobile phase is 1 mL/min. Different chromatographic conditions [13-19] were shown in Tab.1.

Table 1. Different chromatographic conditions for three compounds

Comp.	Detection wavelength	
	(nm)	Mobile phase
LB	261	Methanol: water (75:25)
LC	259	Methanol: water (75:25)
LMC	230	Acetonitrile:water (60:40)

10 mg of standard substances and the test three compounds were weighed precisely, transferred quantitatively into a 100 mL volumetric flask after dissolution with methanol to prepare the corresponding standard store solution (100 µg/ mL), then stored in a refrigerator at 4°C. The standard and test substance store solutions were diluted to 50 µg/mL with mobile phase for detecting the degree of separation, tailing factor and theoretical plate number by HPLC according to the chromatographic conditions shown in Tab.1. With methanol, the standard store solution were proportionally diluted to 0, 1, 5, 25, 50, 75, 100 µg / mL as “5.2 UV-VIS spectrophotometry”. The peak area of these solutions were measured by HPLC to make a standard curve with corresponding concentration. The RSD (%) of the precision, accuracy, stability and repeatability of the experiments were also validated as “5.2 UV-VIS spectrophotometry”. The standard substance solution were diluted step by step and were detected to find LOD and LOQ which S/N equal to 3 and 10, respectively. Three batches of samples (about 50 µg / mL) of test solution and standard solution with mobile phase were determined to calculate the content (%) according to standard curve.

RESULTS AND DISCUSSIONS

The result of character check

The appearance, taste, solubility, melting point, melting range, absorption coefficient and acidity of three compounds were examined in terms of properties. LC is a dark yellow powder crystal, but LB is pale yellow needle one, and LMC is white and a slight acid odor.

Table 2. The result of physical constants

	LB	LC	LMC
Melting point (°C)	224	203	150
Percentage absorption coefficient $E_{cm}^{1\%}$	3×10^4	2.8×10^4	1.7×10^4
Acidity value	5.5 - 7.5	5.5 - 7.5	6.4 - 8.0

All these compounds are soluble in methanol and ethanol acetonitrile, dissolve in ethyl acetate, almost insoluble in dichloromethane, petroleum ether and water. The parts of their physical constants were determined and shown in Tab.2.

The result of identification

Refer to the General rule 0301, identification of the chemical identification were shown in Fig.2. After AgNO₃ solution (0.1 mol/L) was added into the HNO₃ acidic solution, phenolic hydroxyl was seen as Fig.2a, and light yellow precipitate would be bromine groups as Fig.2b, conclusively white precipitate was generated as chlorine groups as Fig.2c.

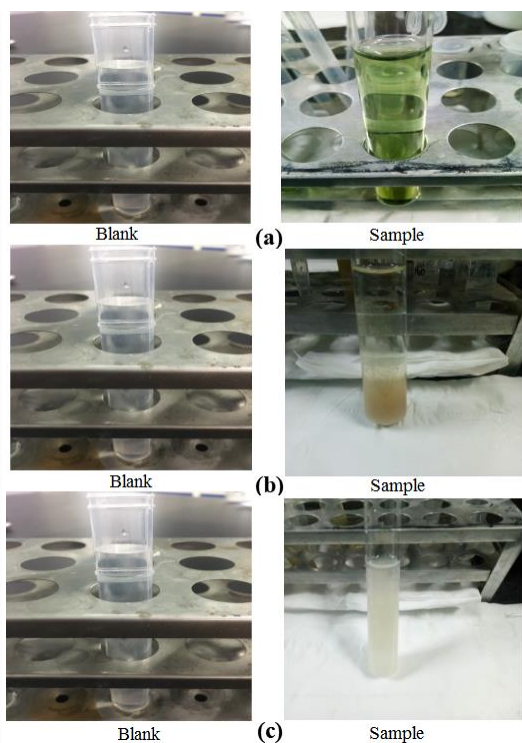


Fig.2. The phenomenon of the chemical identification (a) phenolic hydroxyl (b) bromide (c) chloride

The chemical identification results of three compounds were shown in Tab.3. The blank solution does not interfere with the identification. The chemical methods was specific for identification of three compounds's three batches samples.

Table 3. The result of chemical identification

	phenolic hydroxyl	bromide.	chloride
LB	+	+	
LC	+		+
LMC	-		+

UV wavelength scanning for these compounds were showed in Fig.3. With UV full wavelength scanning from 200 to 400 nm, the maximum absorption of LB, LC and LMC at 261, 259, and 230 nm, respectively. The UV identification results shown that the maximum absorption wavelength of LMC is 230 nm, but the maximum absorption wavelengths of LB and LC are so similar (261 nm and 259 nm) that they are hard to separate.

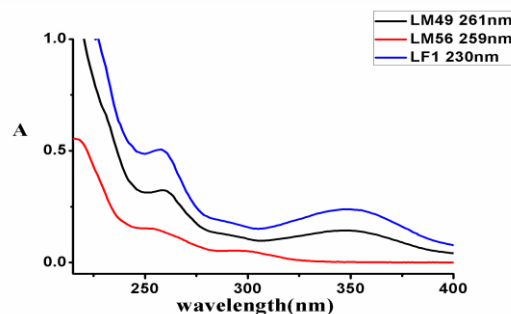


Fig .3. UV wavelength scanning for these compounds

Three compounds were identified by HPLC. The result of HPLC identificationa for these compounds shown in Fig.4. The retention time of LB, LC and LMC at 9.35, 9.905, and 8.947 min for three batches samples, respectively. The HPLC method had a very good specificity that it is able to identify the three compounds with completely accuracy.

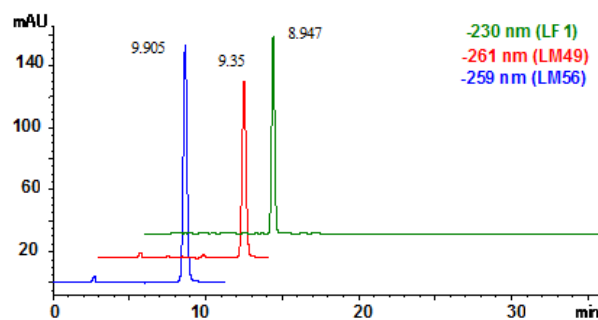


Fig .4. HPLC identificationa for these compounds

The result of limit inspection for general impurity

The weight loss would not exceed 0.5% according to the General rule 0831. According to the General rule 0841, the residue on ignition would not exceed 0.1%. The contents of heavy metals would not exceed 10 parts per million according to the General rule 0821. The solution of the examined chloride would not be thicker than the control solution made of 5 mL of standard sodium chloride solution (0.01%) according to the

General rule 0801. The solution of the examined sulfate would not be thicker than the control solution prepared from 1 mL of standard potassium sulfate solution (0.02%) according to the General rule 0802. Limit inspections for general impurity including the weight loss, residue on ignition, contents of heavy metals, solution of the examined chloride, solution of the examined sulfate, all complied with the limit of Part 4 in Chinese pharmacopoeia (2015 edition) for three batches samples of compounds.

The content determination for the three compounds

The contents of three compounds were determined by acid-base titration, UV and HPLC methods. Using UV method, the linear regression equation of LB, LC and LMC were: $Y = 0.034 X + 0.0048$ ($r = 0.9997$), $Y = 0.028 X + 0.0026$ ($r = 0.9994$), $Y = 0.0168 X + 0.0036$ ($r = 0.9991$) had been obtained, respectively. The results of methodo-logical validation for UV content determination were shown in the Tab.4.

Table 4. The result of methodological validation about UV method

Validation	LB	LC	LMC
RSD (%) for precision	1.4	1.0	1.2
RSD (%) for repeatability	1.5	1.6	1.7
RSD (%) for stability	1.4	1.3	1.4
Recovery rate (%)	98.3	99.2	101.6

Using HPLC method, the linear regression equation of LB, LC and LMC were: $Y = 43.207 X + 0.261$ ($r = 0.9997$), $Y = 50.482 X + 34.059$ ($r = 0.9993$), $Y = 45.15 X - 25.68$ ($r = 0.9996$) had been obtained, respectively. The results of methodological validation for HPLC content determination were shown in the Tab.5.

Table 5. The result of Methodological validation about HPLC method

Validation	LB	LC	LMC
RSD (%) for accuracy	0.8	0.8	0.9
RSD (%) for repeatability	1.1	1.0	1.1
RSD (%) for stability	1.7	0.8	1.7
Recovery rate (%)	99.8	100.2	99.8
LOD (ng/mL)	1.0	1.5	3.0
LOQ (ng/mL)	3.0	5.0	10.0

According to the results of method evaluation, the RSD (%) of the accuracy, stability and repeatability of the experiments were all within 2 %. All of these methodological verification could meet the requirements of quantitative analysis. The result of content determination was shown in Tab.6.

Table 6. The result of Content determination (n = 3)

Methods	LB	LC	LMC
UV- Content (%)	100.2	99.1	101.8
HPLC- Content (%)	99.9	99.5	100.2
Chemical- Content (%)	98.3	98.5	98.7

CONCLUSIONS

Through the comparative study of the quality of the three compounds, we can see that LC and LB are similar in appearance, solubility, melting point and other physical parameters due to their highly similar structures. But they can be identified easily by chemical and HPLC methods because they have their own characteristic groups. LMC is fundamentally different from LC and LB in appearance and melting point, which is due to the characteristic group of its structure. The general impurity test results of the three compounds were all in compliance with the General Quality Control Standard of Pharmacopoeia (2015). Among three methods for measuring the content of compounds, although the acid-base titration method is simple to operate, the accuracy and precision of the results were slightly lower than those of the other two methods because of the subjective error in judging the color of titration endpoint. The results of the three content determination methods shown that the quality control of the three compounds is all reliable, stable, accurate and controllable. The contents of three compounds could be controlled in the range of 98.0~102.0%. Through the research in this paper, the quality standards of the three compounds have been preliminarily established. The establishment of the quality standard can not only provide guidance for the production process of the compound, but also provide theoretical basis for later pharmacological and pharmacokinetic studies.

ACKNOWLEDGEMENTS

Financial support funded by National Natural Science Foundation of China (81973411), Shanxi key Subjects Construction (FSKSC), National Science and Technology Major Project (2018ZX09101003-001-017), the Top Science and

Technology Innovation Teams of Higher Learning Institutions of Shanxi Province, the Program for the Top Young and Middle-aged Innovative Talents of Higher Learning Institutions of Shanxi Province (2015), Shanxi Province Key Research and Development Project (201703D111033), the Project of Shanxi Key Laboratory for Innovative Drugs on Inflammation-based major disease “Anti-inflammatory Mechanism of Baihuadexhuangcao Flavone Baogan Capsule” (SXIDL-2018-05), Project of Center of Comprehensive Development, Utilization and Innovation of Shanxi Medicine (2017-JYXT-18), Research subject of graduate education reform in shanxi medical university (20141034) is gratefully acknowledged.

NOMENCLATURE

RSD - relative standard deviation;

UV - ultraviolet&visible spectrophotometry;

LOQ - limit of quantitation;

LOD - limit of determination;

S/N - Signal to noise ratio;

HPLC - High Performance Liquid Chromatography;

REFERENCES

- [1] Zhao WY, Feng XE, Ban SR (2010) Synthesis and in vitro antioxidant activity of novel halophenols. *Chinese journal of pharmaceutical chemistry* **20**, 264-268.
- [2] China Pharmacopoeia Committee. Pharmacopoeia of the People's Republic of China (Ed). China Chemical Industry Press, Beijing, 2015.
- [3] Liao B, Chen ZH (2003) Research and Formulation of Quality Standards for New Chemicals. *Chinese Journal of New Drugs* **12**, 164-168.
- [4] Liu ZL, Yuan BJ. Research and Formulation of Quality Standards for New Drugs Western Medicine) **28**, 6-9, 1993.
- [5] Wu MZ, Yuan BJ, Lu MI. Establishment and application of expert system for the formulation of new drug quality standards **19**, 453-456, 1993.
- [6] Zhang N, Guo DL Introduction to silver nitrate titration for chloride ion content determination in 93-98.
- [7] Lu W, Sun XM, Sun JJ. Comparison of two methods for the determination of Astragaloside. *Clinical Journal of Chinese Medicine* **8**, 43-45, 2016.
- [8] Wang YX, He JJ, Fang D. Exploration of the Methods by Quantitative Determination of VC in Common Fruits and Vegetables. *Anhui Agri. Sci. Bull* **21**, 20-22, 2015.
- [9] Zhang NJ, Liu Y. Study on Determination Content of Ioversol. *Guangzhou Chemical Industry* **43**, 146-148, 2015.
- [10] Xie Q, Wang W, Chen QX (2014) Comparative Study on Three Different Methods for the Determination of Total Phenolics in Chinese Olive **25**, 204-207, 2014.
- [11] Tang YL, Jing K. Improvement of the determination method of the assay of midodrine hydrochloride, **38**, 59-61, 2016.
- [12] Chen ZG, Shan GQ, Tan XQ. Determination of Quercetin Content in Raw Drug By Ultraviolet Spectrophotometry. *Progress in Veterinary Medicine* **37**, 122-124, 2016.
- [13] Li Y, Feng XE. Determination of 2,5'-Dibromo-4,5,2'-trihydroxydiphenylmethanone and Its Related Substances by HPLC. *Chin JMAP* **30**, 1104-1107, 2013.
- [14] Li J, He LL, Chou LY. Determination of Contents and Related Substance in Citrate Tando Spirone Tablets by Hplc. *Journal of Southwest University for Nationalities, Natural Science Edition* **42**, 183-187, 2016.
- [15] Li QX, Zheng SF. Determination of the Content and Related Substances of Metoprolol Succinate Using HPLC Method. **31**, 632-636, 2017.
- [16] Chen H, Zhu R. Content Determination of Allopurinol Sustained-release Tablets and Related Substances. *China Pharmacy* **24**, 80-82, 2013.
- [17] Zhao HL, Wang C, Xie DF. RP-HPLC Determination of Eplerenone and Its Related Substances. *Chin Pharm* **51**, 663-667, 2016.
- [18] Wang Y, Sun KL, Shi BY. Determination of related substances in cangrelor by HPLC. *Chinese Journal of New Drugs* **27**, 110-114, 2018.
- [19] Feng XE, Zhao WY, Liang TG. Study on the determination of 3-chloro-3',4'-dihydroxy diphenylmethanone and its related substances by RP-HPLC. *Chin Hosp Pharm* **31**, 185-187, 2011.

Simulation of the liquid distribution in the wall zone of a packed column: case study

T. St. Petrova*, D. B. Dzhonova-Atanasova

*Institute of Chemical Engineering, Bulgarian Academy of Sciences,
Acad. G. Bonchev Str., Bl. 103, 1113, Sofia, Bulgaria*

The maldistribution of the liquid phase in a packed column is essential for the efficiency of the mass transfer processes in it. One of the wide-spread methods to measure the liquid distribution in the packing layer includes liquid collecting device (LCD) mounted under the packed bed. The proper design of the LCD is very important for obtaining correct information about the hydrodynamics in the column. The most popular construction of LCD is composed of fixed number of concentric cylindrical sections, with equal or different cross-sectional surface areas. The number and width of these sections is determined so as to ensure enough resolution of the picture of the liquid flow. In this study an analysis and estimation of several variants for possible fragmentation of LCD are provided, based on a dispersion model simulations and calculation of the maldistribution factor. The simulation results are verified with experimental data for metal Raschig Super-Rings 1.5" (RSRM) with an improvement of the LCD. It is shown also, that model parameters identification depends on the LCD fragmentation, especially in the wall zone of the packed column. The present study defines a quantitative criterion for LCD design assessment, which is the fragmentation effect on the maldistribution factor. This solves the issue with the proper data collecting, necessary for obtaining the actual liquid distribution and for parameter identification of the dispersion model.

Keywords: Liquid Collecting Device, liquid distribution, open-structure random packings, modeling, wall zone

INTRODUCTION

The maldistribution of the liquid phase in packed beds and the measures to overcome or reduce it are essential for the efficiency of the mass transfer processes. Probably that is the reason of increasing interest during last years in the investigation of the liquid phase distribution and wall flow observations in columns with diameter $D_c \geq 0.4m$ [1, 2], as well as in the open structure random packings. An experimental study of liquid maldistribution in a 1.2 m diameter column with random packings (Raflux rings, Hiflow rings, RVT saddle rings, Raschig Super-Ring) [1], is followed by development of TUM-WelChem Cell Model for prediction of the liquid distribution in these packings [2]. Our previous papers [3-5] are concerned with experimental investigation [3] of liquid distribution in a column with a diameter of 0.47m and random packings, metal Raschig Super-Ring. The experimental results are used successfully as a base for refinement of a dispersion model [4, 5]. They are in conformity with the observations for an older type of a random packing, like Pall rings. The performance of Raschig Super-Rings and Pall rings was predicted by CFD modeling in a moving pilot plant, for a wide range of liquid loads with varied constant column tilt and different column motion frequencies [6]. A new

cell model, accounting for different liquid behaviour in the bulk and the wall cells, was created in [7], validated by experimental data of Pall rings.

The above mentioned random packings are characterized by a complex shape (a type of a lattice of curved thin lamellae), low pressure drop, and their liquid spreading capacity in the radial direction is much lower than conventional packings of older generations [8, 9].

The distribution of the liquid phase in the packing layer can be recorded by various experimental techniques - collection devices, tracer methods, non-invasive tomography methods, etc. In [7], for example, a tracer conducting method and a wire-mesh tomographic sensor are combined, which allows a two-dimensional picture of the phases/liquid distribution across the apparatus section and obtains the development of this distribution over time.

The liquid phase distribution is most often studied experimentally by liquid collecting devices (LCD) (see Tab.1). A LCD typically comprises coaxially positioned cylindrical pipes open from top and closed from bottom. They are mounted under the packed bed to measure the distribution of the superficial velocity of the liquid flowing in the packing from the liquid distributor at the top of the apparatus. With a sufficient number of sections of the LCD, a detailed picture is obtained of the distribution and the radial spreading of the liquid

* To whom all correspondence should be sent:
tanch066@yahoo.com

phase in the apparatus. Often, in countercurrent flow of the gas and liquid phases, the collecting device is combined with the gas inlets [8, 13]. The LCD can also be mobile [12], in order to measure the radial distribution for different heights of the layer or to obtain a two-dimensional (radius and angle) pattern of distribution.

One important aspect in the design of collecting devices is the problem of correctly measuring the wall flow in a column with liquid flow with or without gas flow. The width of the section located next to the column wall should be appropriately selected [16]. Tab.1 shows the part of the cross-section area of the section collecting the wall flow,

accepted in existing investigations. If it is too big, a portion of the liquid coming from the bulk [11, 12, 15, 17] will be collected in addition to the wall flow, thus giving an inaccurate measured value. For example, the authors of [17] used a collecting device of four concentric cylindrical rings with the same area, i.e., the cross-section area of the section collecting the wall flow was 25% of the entire column cross-section area with a diameter $D_c = 0.3m$. In [11, 15] a 15 mm wide section was selected, which corresponded to 11.64% of the entire column diameter $D_c = 0.5m$.

Table 1. Previous studies of liquid distribution in packed beds by LCD

Reference	D_c [m]	δw [mm]	Area ratio [%]	Packing, size [mm]
Baker et al. (1935) [17]	0.3	20	25	Spheres, Saddles
Porter and Templeman (1968) [18]	0.3	3.2	4	ceramic Raschig rings - 12.7 metal Raschig rings - 25.4 ceramic Intalox saddles - 12.7 metal Pall ring- 15.9
Dutkai and Ruckenstein (1968) [10]	0.3	3.2	4	ceramic Raschig rings-10, 15, 20, 25 ceramic Intalox saddles-15, 25 ceramic Berl saddles - 25 plastic Pall ring - 35
Gunn and Al-Saffar (1993)[8]	0.3	25	30.56	Metal Nutter ring - 25 Plastic IMTP - 25 Plastic Pall rings - 25 Metal Super Intalox saddles- 25
Hoek (1983) [12]	0.5	10	16	Glass Raschig rings-10, 20, 30 Ceramic Intalox saddles - 15 polypropylene Intalox saddles - 50 metal Pall rings- 25
Stikkelmann (1989) [13]	0.5	12.7	10	Plastic Torus saddles - 25 Plastic Ralu ring - 25/38 Metal IMTP- 25 Metal Pall ring- 25
Kouri and Sohlo (1996) [11]	0.5	15	11.64	Ceramic Intalox saddles - 38 Plastic Pall rings - 25/ 50
Yin et al. (2000) [19]	0.6	4.7	3.12	Metal Pall ring - 25.4
Zhu (2005) [16]	0.3	12	15.13	Metal Pall ring - 25.4
Dzhonova et al. (2007) [20] Dzhonova et al. (2018) [3, 4] Petrova et al. (2018) [5]	0.47	5	4.21	Metal IMTP - 40/ 50/ 70 Plastic Ralu ring - 25/ 50 Metal Raschig Super rings - 12.5/ 25/ 37.5/ 50/ 75 plastic Raschig Super rings -15 / 50
Hanusch et al. (2017, 2018) [1, 2]	1.2	24	3.96	Metal Raflux ring - 35-5/ 50-5 Metal RVT saddle rings - 50-4/ 70-5 Plastic Hiflow ring - 50-6/ 90-7

A similar technique was used in [13] in a 0.5m diameter column to investigate the liquid distribution in 3rd generation packings of 25-38 mm sizes. The wall-flow collecting section has a

width of $\frac{1}{2}$, or about 10% of the entire cross-section.

The choice of a smaller width, <5 mm, for the wall-adjacent section and a cross-section area about

4% of the entire cross section limits the mixing of the wall flow with the bulk zone liquid, but may also measure a smaller wall flow of the actual, especially in countercurrent gas flow and at higher velocities of the liquid phase [16].

The choice of other researchers [8, 21] of the wall section width was within 1 packing element diameter (for element sizes up to 25 mm), and in columns with diameters of 0.291m and 0.3m, respectively. In [21], it is mentioned that the wall flow can be removed prior to reaching the collector by specially designed auxiliary device.

As can be seen from the literature survey, the number and the cross-section area magnitude of the concentric sections of the LCD are essential to obtain a correct picture of the radial distribution of the liquid, particularly for the measuring wall effects and the development of the wall flow for packings of different generation and in columns of various diameters. The existing models that provide analytical or numerical solutions for radial liquid distribution after a packing layer are based on experimental data obtained for specific conditions for this distribution through different types of LCDs. So far, the effect of "fragmentation" in the LCD on the parameters in model solutions has not been studied.

The present work defines and solves the following tasks:

- Influence of the number and width of the sections in the wall-adjacent area of the LCD on the picture of liquid radial distribution in a packed column;

- Influence of "fragmentation" in the LCD on the identification of parameters in the dispersion model; verification of simulation results and estimation by the maldistribution factor of LCD through real experimental data in a column with a diameter of 0.47m and RSRM 1.5" packing.

The first task was solved by simulating the various options for fragmentation of the LCD in the wall zone using the dispersion model [4, 5]. Eight variants of virtual fragmentation of the original LCD used in [3, 4] were tested calculating for each of them a maldistribution factor, as an integral characteristic of the model radial liquid distribution. The obtained results confirm the observation reported by other authors, that the most important is the width of the section collecting the wall flow. They also confirm the experimental data for the bulk zone liquid distribution from our previous studies [3, 4], as well as those of other authors [1, 14] for columns of a larger diameter.

The second task is consequence of the fact that with the data measured by the primary design of the

LCD used in our previous studies [4, 5], the dual identification of the model parameters turns out impossible, due to automodelity of residual variance in respect to one of the parameters (residual variance independence of the parameter). It is shown that Variant 2 of the LCD enables the dual parameter identification by the global minimum of the residual variance. This is achieved by means of simply dividing the section next to the wall-adjacent section of the primary structure and retaining its width. With the parameter values so identified, the adequacy of the model is proven by the example of a metal Raschig Super-ring (RSRM) 1.5" packing. The comparison between the experimental and model values of the maldistribution factor for the original and the improved LCD design proves the advantages of the latter.

SIMULATION AND ESTIMATION OF RADIAL LIQUID MALDISTRIBUTION IN LCD

It was experimentally found [3] that the liquid irrigation density in the central (bulk) zone of the original LCD (i.e, from 1st to 5th section, all sections are 8) did not change significantly with the liquid load, as well as with the packing redumpings. The same observation was confirmed through dispersion model simulations [5]. Therefore, it was decided to investigate theoretically only the column cross-section zone after the 5th section to the column wall, and to consider different variants of fragmentation of this zone and their effect on the liquid irrigation density distribution and the maldistribution factor. The latter is used as an integral estimation of the liquid distribution.

Eight variants of "fragmentation" of each section in the wall zone (after 5th section) of the original LCD, have been examined. The original LCD with 8 sections is presented by Variant 1. For all variants the first two sections are merged because their areas are too small. For each other variant, the fragmentation of 7th and 8th section is different. Section 6 is divided into three parts (sub-sections) with different areas for Variants 2 to 8. The fragmentation of section 7 starts from 2 sub-sections (Variant 2) to 3 or 4 sub-sections (Variant 3 and 4), with different combinations of areas. The area fragmentation of the last section is kept unchanged for Variants 1 - 4 (4.2 %), and then starts to increase from 6.3% (Variant 5) to 16.3% (Variant 8).

On the scheme (Fig.1), all 8 virtual variants are presented graphically for better visibility. The variant numbers are presented horizontally; the

fragmentation sub- sections areas in percentages for each variant are given vertically. In the authors' software, created for calculation of the theoretical distribution of the radial liquid irrigation density by the dispersion model, the radii of the LCD sections are set as external data.

Tab.2 gives the radii corresponding to the fragmentation after 5th section for each of the variants, as well as the calculated maldistribution factors [2, 4] by the following formula:

$$M_f = \frac{1}{F_0} \sum_{i=1}^{ns} F_i \left| \frac{L_i - L_0}{L_0} \right| \quad (1)$$

In Eq. (1) the ratio F_i/F_0 represents the ratio of the area of the respective section i to the entire area of the LCD (i.e. column cross-section), m^2 , ns is the number of sections of the LCD, L_i/L_0 is the dimensionless theoretical or experimental irrigation density in the section i of LCD, limited between the radii r_{i-1} and r_i ($r_i > r_{i-1}$). Theoretical mean density in i^{th} section of LCD is obtained from dispersion model according to:

$$f_i = \frac{2}{r_i^2 - r_{i-1}^2} \int_{r_{i-1}}^{r_i} f(r, z) r dr \quad (2)$$

The solution of the dispersion model, $f(r, z)$ at uniform initial liquid distribution has the form [5]:

$$f^u(r, z) = A_0 + \sum_{n=1}^{\infty} A_n' J_0(q_n r) \exp(-q_n^2 z), \quad (3)$$

$$A_0 = \frac{C}{1+C}, \quad A_n' = \frac{2(q_n^2/B - 2C)}{[(q_n^2/B - 2C)^2 + q_n^2 + 4C]} J_0(q_n)$$

As can be seen from Eqs. (1) and (3), the theoretical maldistribution factor and the solution depends on r , z and dispersion model parameters B, C and D for the respective packing and current packing layer height $z = DH/R^2$.

Since we are interested in the influence of fragmentation in the wall zone area along the radius, the maldistribution factor in Tab.2 is calculated from the solution in Eq. (3) at preselected values of z , B, C and D , for the corresponding $r = R_m/R$, F_i/F_0 and ns , for each considered variant.

The analysis of the results obtained in Tab.2 leads to the following conclusions:

- The additional fragmentation after 5th section in the wall zone of the LCD does not cause a significant variation of the maldistribution factor, if the cross-section area of the wall-adjacent section, where the wall flow is measured, is not changed;

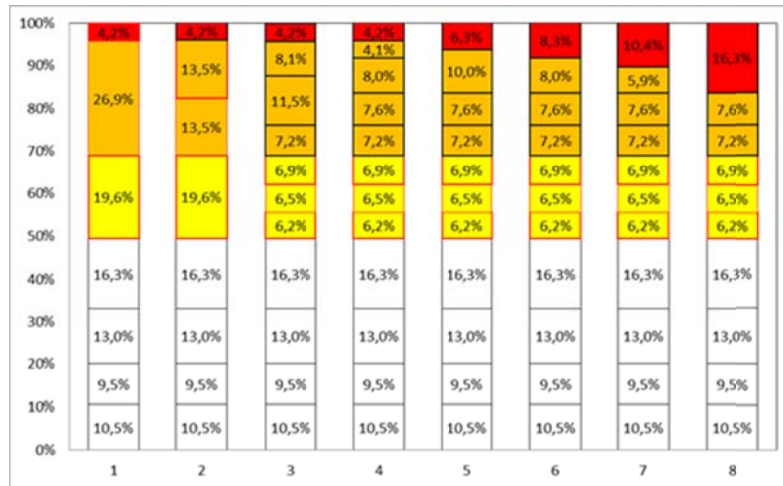


Fig.1. Scheme of fragmentation variants of original LCD in the wall zone of the column after the 5th section: fraction of section area in % versus number of variants

- When increasing the area of the wall-adjacent section to the technologically reasonable and practically defined limits (between 3 and 16% of the total cross-section area of the column), the theoretical maldistribution factor decreases.

In fact, this decrease is due to the increase in the F_w/F_0 ratio for Variants 5 to 8 from 6 to 16%. According to the dispersion model, the model wall flow is dimensionless and its value does not depend

on r , but only on the height of the layer and the value of parameters B, C and D . If only the area of the last section increases, the wall flow will not change, but the theoretical M_f will be artificially much lower than the actual value. For example, for parameter values close to those in Tab.2 and for LCD Variant 1, the experimental maldistribution factor value for RSRM 1.5" is about 0.28 [3], i.e. close to the theoretical 0.26. While for Variant 8 the

theoretical M_f value is 0.1560 or 44% lower. Therefore, it is appropriate to choose such a variant of section fragmentation in the wall zone, for which the theoretical and experimental maldistribution

factors do not differ by more than 10%. It is envisaged to obtain experimental confirmation of this conclusion in our future work, which will require a reconstruction of the LCD.

Table 2. Sections radii of LCD, corresponding to the fragmentation after 5th section, for each of the 8 variants and calculated respective maldistribution factors

No. Variant	1	2	3	4	5	6	7	8
	R_{in}, m							
No. section								
1+2	0.076	0.076	0.076	0.076	0.076	0.076	0.076	0.076
3	0.105	0.105	0.105	0.105	0.105	0.105	0.105	0.105
4	0.135	0.135	0.135	0.135	0.135	0.135	0.135	0.135
5	0.165	0.165	0.165	0.165	0.165	0.165	0.165	0.165
6	0.195	0.195	0.175	0.175	0.175	0.175	0.175	0.175
7	0.23	0.213	0.185	0.185	0.185	0.185	0.185	0.185
8	0.235	0.23	0.195	0.195	0.195	0.195	0.195	0.195
9		0.235	0.205	0.205	0.205	0.205	0.205	0.205
10			0.22	0.215	0.215	0.215	0.215	0.215
11			0.23	0.225	0.2275	0.225	0.2225	0.235
12			0.235	0.230	0.235	0.235	0.235	
13				0.235				
ns	7	8	11	12	11	11	11	10
M_f^{model} $B=10, C=1.5,$ $D=0.0022m$	0.2615	0.2615	0.2615	0.2615	0.2411	0.2219	0.2037	0.1560

A complementary conclusion of the study is that the value of the maldistribution factor strongly depends on the parameter B and less on the parameter C , which has been already observed in the model solution in our previous work [5]. Since the parameter C is determined exactly by the experimental data measured in the wall zone of the column, it is very important which variant of the LCD fragmentation is selected. Subsequently, this will also affect the identification of the other two parameters in the model.

In the above-mentioned work, it was shown that dual identification of B and D is not possible due to automodelity of residual variance for RSRM 0.7", 1.5" and 3", and a hybrid method for their determination is proposed.

However, it is necessary to investigate and verify for a real example, whether the dividing of the wall zone of a particular LCD is not the cause of the automodelity.

INFLUENCE OF THE WALL ZONE FRAGMENTATION ON THE PARAMETERS' IDENTIFICATION – CASE STUDY

A modification of the LCD wall zone area in the pilot installation described in [3, 4] corresponding to Variant 2 (Tab.2) is made. Section 7 is divided into two parts with the same area, as it is too large compared to the remaining sections of the LCD (Fig.2). In this modification the areas of the

remaining sections have been kept unchanged, especially the outermost one, in which the wall flow is collected. Experiments were carried out to measure the radial distribution with the modified LCD after a layer of a packing RSRM 1.5" at a layer height $H = 0.6m$ with two different types of initial liquid irrigation - uniform and on the wall. The range of initial liquid flow rates, the number of redumpings of the packing layer, and the measurement technique are described in details in [3].

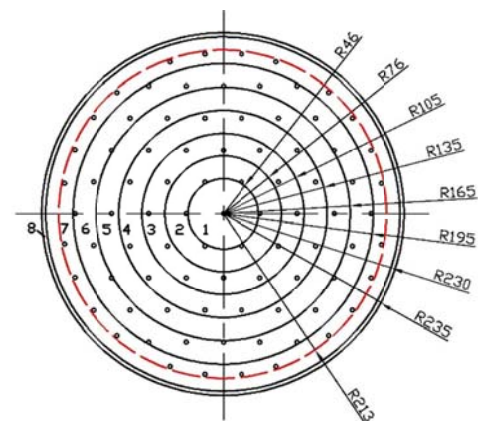


Fig.2. Scheme of LCD radial fragmentation (Variant 1) [5]. (Red dashed line dividing 7th section corresponds to Variant 2.)

With the experimental data obtained, the value of parameter C was recalculated on the base of four sections because of the division of the 7th section.

The newly obtained value $C = 0.993$ for the packing RSRM 1.5” is close to the previous one - 0.981, calculated without division of the 7th section. With the calculated value of $C = 0.993$ a dual identification of the parameters B and D of the dispersion model is performed. The criterion for reaching their optimal values is the minimum of the residual variance between the experimental and model mean density of irrigation, across all sections of the modified LCD.

Fig.3 shows the results of double identification as a contour map. A global minimum of the residual variance of $0.1302e-01$ for the model parameters’ values $B = 9, D = 0.00275m, C = 0.993$ was identified, indicated by arrow.

Adequacy verification of the obtained model parameters was made. The reproducibility variance of the experiments carried out is $S_0^2 = 0.674e-02$ of a sample size $m' = n - ns = 16$ of $n = 24$ and $ns = 8$ sections of the modified LCD with $n_i = 3$ redumpings (parallel experiments) of the packing layer.

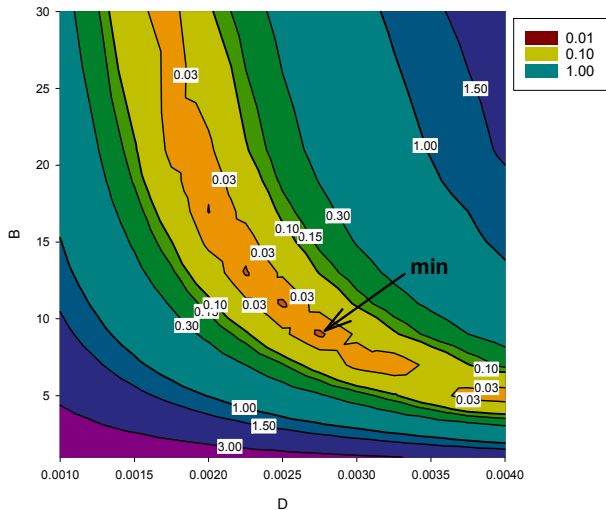


Fig.3. A contour map of residual variance as a function of model parameters B and D

The minimum residual variance between experimental and model mean densities of irrigation in all sections of LCD,

$$S_A^2 = \left(\sum_{i=1}^{ns} n_i (f_{iexp} - f_{imod})^2 \right) / (ns - 1) \text{ is } 0.1302e-01$$

Table 3. Experimental and theoretical values of density of irrigation in the modified LCD and average relative error $\delta\%$ in sections

No. section	I+II	III	IV	V	VI	VII	VIII	IX
f_{ie}	0.908	0.964	0.967	0.985	0.889	0.5709	0.589	4.67
f_{ic}	0.9995	0.9958	0.9815	0.9355	0.8246	0.6762	0.5331	4.667
$\delta, \%$	9.15	3.19	1.48	-5.29	-7.81	15.56	-10.49	-0.06

for volume of the sample $m = ns - 1 = 7$.

At a level of significance $\alpha = 0.05$, Fisher's criterion shows adequacy:

$$F = \frac{\min(S_A^2)}{S_0^2} = 1.931 < F(m, m') = 2.66 \quad (4)$$

The experimental and theoretical values of the irrigation density in the modified LCD along with the average relative error $\delta\%$ by section are given in Tab.3.

The results confirm the assumption that splitting of section 7 of the original LCD is sufficient to ensure that both parameters B and D are identified by a new value of the third parameter C of the dispersion model.

For comparison, the model and experimental maldistribution factors for the original LCD - Variant 1 and three sizes of packings, obtained in our previous work (Fig.4), are calculated too. It can be seen that the relative error between the model and experimental values of the maldistribution factor is highest ($\sim 24\%$) for the smallest packing size, for the data obtained using the LCD of Variant 1.

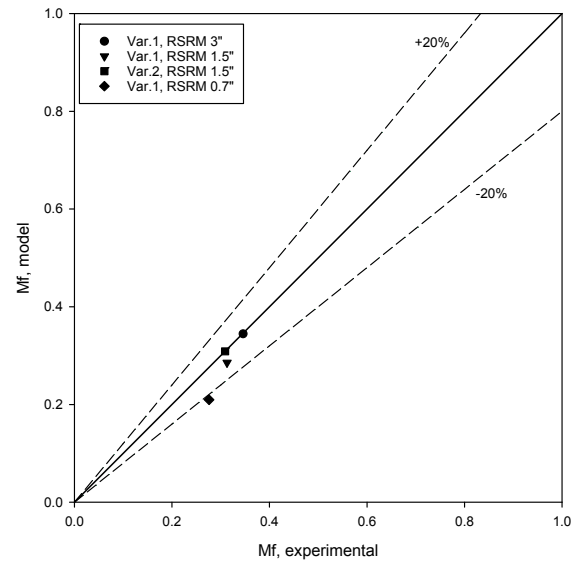


Fig.4. Comparison between experimental and model maldistribution factors for RSRM 0.7, 1.5 and 3”, at optimal values of model parameters for Variant 1 [5] and Variant 2

This deviation is probably due to insufficiently precise determination of the parameter C in the wall zone, its value being much lower (0.630) compared to the C values for the other two sizes - 0.981 and 1.541. It is known that parameter C depends on the diameter of the packing [22], as well as on the coefficient of radial spreading D , but for lattice- type packings, it is difficult to determine which dimension is the characteristic one. According to [20], this size is the width of the lamella of the packing element. This characteristic width increases with the nominal size of the packing. This is connected with the increase in the coefficient of radial spreading D , as well as in the wall flow.

It should be noted that after the modification, the model and experimental maldistribution factor for the examined case study for the packing RSRM 1.5" completely coincided, whereas for one-parameter identification and the experiment of Variant 1, the relative error was 8.7%.

CONCLUSIONS

The present study examines the effect of different fragmentation of the LCD in the column wall zone on the dispersion model's solution and the identification of its parameters, as well as on the experimental data obtained in the LCD. Eight variants of virtual dividing into sub- sections in the wall zone of the original LCD used in [3, 4] were tested. For each of them, the integral characteristic called maldistribution factor [2], of the radial liquid distribution obtained by the model, was computed. The results confirm the observation, reported by other authors, that the width of the section collecting the wall flow is the most important.

It is shown that Variant 2 of the LCD fragmentation (Tab.2) solves the no-minimum issue in two-parameter identification by simply dividing the section next to the last one and retaining the latter's width. With the proposed modification of the LCD, experiments with a RSRM 1.5" packing were performed and the adequacy of the model was proven for the identified parameter values. The comparison between the experimental and model maldistribution factor for the original and the improved LCD design confirms the advantages of the latter.

The presented procedure for evaluation of the effect of the LCD wall zone fragmentation, by calculation of the respective maldistribution factor, suggests a quantitative criterion for proper design of the experimental set-up. The increase of

the wall section width should be accompanied with difference between values of the maldistribution factors (experimental and theoretical) not exceeding 10 % in order to be sure to obtain a correct flow distribution in LCD.

ACKNOWLEDGMENTS

This work is supported by the National Science Fund under Contract DN07/14/15.12.2016.

NOMENCLATURE

A_0, A_n^u - coefficients of dispersion model solution for uniform initial irrigation;

B - dispersion model parameter, a criterion for exchange of liquid between the column wall and the packing;

C - dispersion model parameter, expresses the equilibrium distribution of entire liquid flow between the wall and the packing when equilibrium state is attained $z \rightarrow \infty$;

D - dispersion model parameter, coefficient of radial spreading of liquid, m;

D_c - column diameter, m;

d_p - diameter of a single packing element, m;

H - packing layer height, m;

F_i - area of section i in LCD, m^2 ;

F_0 - column cross-section area or that of LCD, m^2 ;

F_w - area of the section next to the column wall, m^2 ;

$f(r, z)$ - dimensionless dispersion model solution for uniform initial irrigation;

\bar{f}_i - the mean dimensionless density of irrigation in i -th annular section of the LCD, delimited by the radii r_{i-1} and r_i ($r_i > r_{i-1}$);

L_i/L_0 - ratio of local to mean irrigation densities, in section i of LCD;

M_f - maldistribution factor for radial liquid distribution in packed column cross-section, or in LCD;

m, m' - degree of freedom for reproductive and residual variances, respectively;

n - sample size of experimental data, measured in LCD, packing redumpings are included;

ns - number of sections in LCD;

R - column radius, m;

$r = r'/R$ - dimensionless radial coordinate;

r' - radial coordinate, m;

q_n - the roots of the characteristic equation, following from boundary condition in [5];

S_0^2 - reproductive variance for experimental data, with parallel experiments (packing redumpings);

S_A^2 - residual variance between model and experimental values;

$z = DH/R^2$ - dimensionless axial coordinate;

Greek symbols

α - significance level in Fisher criteria;

δ - mean relative error, in %, between experimental and model densities of irrigation;

δ_w - width of the wall flow collecting section (Tab.1), mm;

Subscripts

ic - calculated values in section *i* of LCD;

ie - experimental values in section *i* of LCD;

in - inner radii of sections in LCD;

w - wall

Superscripts

model - model;

exp - experimental;

REFERENCES

- [1] F. Hanusch, S. Rehfeldt, H. Klein. Liquid maldistribution in random packed columns: experimental investigation of influencing factors, *Chem. Eng. Technol.* **41**(11), 2241-2249 (2018).
- [2] F. Hanusch, V. Engel, R. Kender, S. Rehfeldt, H. Klein. Development and application of the TUM-WelChem cell model for prediction of liquid distribution in random packed columns, *Chemical Engineering Transactions* **69**, 739- 744 (2018).
- [3] D. Dzhonova-Atanasova, T. Petrova, Kr. Semkov, S. Darakchiev, K. Stefanova, S. Nakov, R. Popov. Experimental investigation of liquid distribution in open structure random packings as a basis for model refinement. *Chemical Engineering Transactions* **70**, 2077- 2082 (2018).
- [4] D. Dzhonova-Atanasova, Kr. Semkov, T. Petrova, S. Darakchiev, K. Stefanova, Svetoslav Nakov, R. Popov. Liquid distribution in a semi-industrial packed column - experimental and theory. *Food Science & Appl. Biotechnology* **1**(1), 19-25 (2018).
- [5] T. Petrova, Kr. Semkov, D. Dzhonova-Atanasova. Modeling of liquid distribution in a packed column with Open-structure random packings, *Chemical Engineering Transactions*, **70**, 1051-1056 (2018).
- [6] M. Schultes, J. Brauer, P. Chen, S. Doong. Marinization of mass transfer columns for FLNG applications. *Chem. Eng. Trans.* **69**, 301-306 (2018).
- [7] F. Van Holt, J. Brinkmann, M. Grunewald. Experimental and theoretical studies on local liquid phase distribution in packed columns. *Chemical Engineering Transactions*, **69**, 391-396 (2018).
- [8] D. J. Gunn, H. B. S. Al-Saffar. Liquid distribution in packed columns. *Chem. Eng. Sci.*, **48**, 22, 3845-3854 (1993).
- [9] S. Schug. Untersuchung der fluiddynamik in packungskolonnen mittels computertomographie. PhD thesis, Technischen Fakultät, Friedrich - Alexander Universität, Erlangen-Nurnberg, Germany, 2018.
- [10] E. Dutkai, E. Ruckenstein. Liquid distribution in packed columns. *Chem. Eng. Sci.* **23**, 1365-1373 (1968).
- [11] R. J. Kouri, J. J. Sohlo. Liquid and gas flow patterns in random packings. *Chem. Eng. J.*, **61**, 95-105 (1996).
- [12] P. J. Hoek, Large and small scale liquid maldistribution in a packed column. PhD Thesis, Delft University of Technology, Netherlands, 1983.
- [13] R. M Stikkelmann. Gas and liquid maldistribution in packed columns. PhD Thesis, Academisch Boeken Centrum, TU Delft, The Netherlands, 1989.
- [14] F. Yin. Liquid maldistribution and mass transfer efficiency in randomly packed distillation columns. PhD thesis, University of Alberta, Edmonton, Alberta, Canada, 1999.
- [15] T. Dang-Vu, H. Doan, A. Lohi, Y. Zhu. A new liquid distribution factor and local mass transfer coefficient in a random packed bed, *Chemical Engineering Journal*, **123**, 81–91 (2006)
- [16] Y. Zhu. Liquid distribution and its effect on local mass transfer in a packed column of Pall rings. Theses and dissertations., Master thesis, Paper 417, Ryerson University, Toronto, Ontario, Canada, 2005.
- [17] T. Baker, H. Chilton, H. Vernon. The course of liquid flow in packed towers. *Trans. Am. Inst. chem. Engrs.* **13**, 296 (1935).
- [18] K. Porter, V. Barnett, J. Templeman. Liquid flow in packed columns. Part II: The spread of liquid over random packings, *Trans. Inst. Chem. Eng.* **46** (3), 69-94 (1968).
- [19] F. H. Yin, Z. C. Wang, A. Afacan, K. Nandakumar, K. T. Chuang. Experimental study of liquid flow maldistribution in random packed columns. *Can. J. Chem. Eng.*, **78**, 449-457 (2000).
- [20] D. Dzhonova-Atanasova, N. Kolev, Sv. Nakov. Determination of liquid radial spreading coefficients of some highly effective packings. *Chem. Eng. Technol.*, **30**, 2, 202-207 (2007).
- [21] V. Stanek, V. Kolar. Distribution of liquid over a Random Packing. VIII. Distribution of the Density of Wetting in a Packing for an Arbitrary Type of Initial Condition. *Coll. Czech. Chem. Commun.*, **38**, 2865-2873 (1973).
- [22] V. Staněk, V. Kolář. Distribution of liquid over a random packing. IV. Verification of the boundary condition of liquid transfer between a packed bed and the wall of a cylindrical column, and evaluation of its parameters. *Collect. Czechoslov. Chem. Commun.*, **33**, 1062-1077 (1968).

Influence of ZnS Sputtering Power on Film Adhesion and $\text{Cu}_2\text{ZnSnS}_4$ Solar Cells

Wang Lu¹, Guo Jie^{1*}, Hao Ruiting^{2*}, A. Aierken², Sun Lichun¹, Qiong Li², Liu Bin¹, Gu Kang², Sun Shuaihui¹

¹ Yunnan Key Laboratory of Optoelectronic Information Technology, Yunnan Normal University, Kunming, Yunnan, 650500, People's Republic of China

² Key Laboratory of Renewable Energy Advanced Materials and Manufacturing Technology Ministry of Education, Yunnan Normal University, Kunming, Yunnan, 650500, People's Republic of China

The stacking precursors Mo/ZnS/SnS/Cu were sputtered on soda-lime glass (SLG) substrates using different sputtering power of ZnS changing from 50 W to 140 W. $\text{Cu}_2\text{ZnSnS}_4$ (CZTS) thin films were obtained by annealing the precursors. The effects of ZnS sputtering powers on the morphology, microstructure and adhesion in ZnS and followed CZTS thin films were investigated. ZnS thin films with different power were hexagonal wurtzite with (008) preferred orientation. The compressive stress in ZnS thin film increased by an order of magnitude with sputtering power from 50 W to 140 W. When sputtering power of ZnS was lower than 80 W or higher than 110 W, the crack and even falling off phenomenon were observed in the annealed CZTS thin films. From 80 W to 110 W, the surface of CZTS thin film was even but more holes and secondary phases appeared at higher power of 110 W. The CZTS solar cell was fabricated with ZnS thin films sputtered at 80 W, which showed the open circuit voltage of 572 mV, the short circuit current density of 14.23 mA/cm² and the conversion efficiency of 3.34 %.

Keywords: $\text{Cu}_2\text{ZnSnS}_4$, ZnS, stress, films adhesion

INTRODUCTION

$\text{Cu}_2\text{ZnSnS}_4$ (CZTS) is a direct bandgap semiconductor material, with band gap of 1.4~1.5 eV. It has similar photovoltaic performance to $\text{CuIn}_x\text{Ga}(1-x)\text{Se}_2$, making it an ideal absorber layer for thin film solar cells. Besides, CZTS solar cells attract the attention of researchers all over the world because of earth-abundant elements and non-toxic, [1-6]. In 2013, IBM Corporation, Solar Frontier and Tokyo Chemical Industry Co., Ltd. jointly developed CZTSSe thin-film solar cell with photoelectric conversion efficiency of 12.6%, which is the highest in copper-based solar cell [7], but it still far from the theoretical maximum efficiency of 31% [8],[9]. The magnetron sputtering has the advantages of flexible target selection and easy control of deposition parameters. Araki et al. [10] reported the effect of six different stacking orders on the properties of CZTS films, and the Mo/Zn/Cu/Sn structure was optimized with an efficiency of 1.79 %. Katagiri et al. [11] prepared CZTS thin films by co-sputtering Cu/ZnS/SnS targets, studying the effect of sulfurization on phase formation. Katagiri et al. [12] also reported that the annealing caused the loss of Zn and Sn, resulting in

the conversion efficiency decreasing. The Zn and Sn elemental targets are replaced by the binary sulfide targets ZnS and SnS, which can further promote grain growth and reduce formation of secondary phases and the holes on the surface of the CZTS film [13][14]. Shin et al. studied three different structures of CZTS precursors and found that Mo/ZnS/SnS₂/Cu sequence can obtain better phase purity [15]. However, the residual stress of films could be affected by the growth process like the temperature or the power [16]. Li et al. found that the films had crack and peel off after annealing in magnetron-sputtered CZTSSe. Since the thermal expansion coefficient of Cu and its sulfide is higher than that of ZnS and SnS, a large stress occurs. Placing Cu on the top layer, as SLG/Mo/ZnS/SnS/Cu, will reduce the possibility of film cracking and shedding [17]. On the other hand, in process of sputtering, the internal stress of ZnS thin film will not only lead to red shift of absorption edge and narrow band gap [18-20], [23], but also cause films to crack or even fall off after annealing. In the growth conditions of ZnS thin films, sputtering power has a great influence on structure, grain growth and surface roughness, it also one of the important factors affecting film stress and

To whom all correspondence should be sent:

E-mail: ynnugj@sohu.com

adhesion [13],[18]. The quality of ZnS thin film as bottom layer has crucial influence on the crystal quality, photoelectric performance and internal stress of CZTS thin film. In this paper, the CZTS precursor was prepared by sputtering Mo/ZnS/SnS/Cu. ZnS thin films were sputtered with different powers. The influence of sputtering power on the structure, morphology, adhesion and photovoltaic performance of CZTS films and solar cells were studied.

EXPERIMENTAL

CZTS thin film precursors were deposited at room temperature on 20mm × 20mm soda lime glasses by magnetron sputtering Mo, ZnS, SnS, and Cu target in sequence. The background vacuum was 10⁻⁵ Pa and Ar pressure was 0.3 Pa. The Mo bottom electrodes about 1.2 μm thickness were firstly sputtered under 100 W power. The sputtering parameters were shown in Tab.1. The sputtering power of ZnS is 50 W, 80 W, 110 W, and 140 W, with the composition of precursors was adjusted to Cu/(Zn+Sn) ≈ 0.8 and Zn/Sn ≈ 1.2. The four samples at different ZnS power were marked as A1, A2, A3 and A4 respectively. After characterizing the crystal structure of ZnS, SnS with 50 W power and Cu with 100 W power were sputtered on ZnS. The precursors were placed in a graphite boat and annealed in the furnace filling with high-purity nitrogen gas to remove air. The heating temperature was 260°C for 30 minutes then cooling in nature. Then, the temperature was raised to 580 °C for 30 min in sulfur powder and a CZTS film was obtained. The surface and cross-section morphology, crystal structure of ZnS and CZTS thin films were characterized by field emission scanning electron microscopy (SEM: FEI Nova Nano450) and X-ray diffraction (XRD: Rigaku Ultima IV). Hereafter, the 50 nm thick CdS as buffer layer was deposited on the CZTS film by chemical bath method (CBD). The window layer i-ZnO (50 nm) and ZnO:Al (200 nm) were prepared by RF sputtering. The current density-voltage (J-V) characteristics of the CZTS solar cells were measured by a solar simulator under the standard AM1.5 spectrum using a Keithley 2420 source meter unit. The whole sample of 20mm×20mm area was illuminated with the intensity of 100 mW/cm². The light intensity of the solar simulator was calibrated with a standard monocrystalline Si reference solar cell. Finally, the top grids electrodes of Au with 150nm thickness were fabricated by thermal evaporation.

Table 1. Sputtering parameters for ZnS

Target	Sample	Sputtering power		Film thickness
		[W]		[nm]
ZnS	A1	50		270.4
	A2	80		221.0
	A3	110		196.9
	A4	140		152.6

RESULTS AND DISCUSSION

Morphology and structure

As shown in Fig.1, SEM images of four samples have uniform surface, clear grain boundary and no cracks. With increase of sputtering power, the grain size of ZnS increased gradually due to the increasing of atoms energy and surface migration. The atoms are likely to aggregate resulting in an increase in grain size [21].

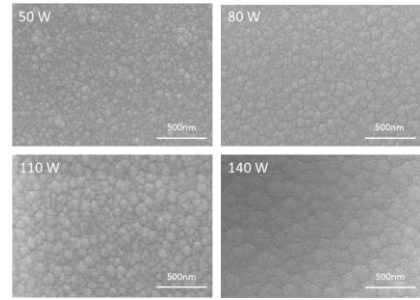


Fig.1. SEM images of ZnS films at different sputtering power

Fig.2 showed XRD patterns of ZnS thin films at different sputtering power. Three peaks at $2\theta=28.5^\circ$, 47.5° , 56.3° , which correspond to (008), (110) and (118) diffraction planes in the hexagonal structure.

The microstructure parameters of ZnS films at different sputtering power was shown in Tab.2. As sputtering power increased from 50W to 140W, the (008) diffraction peak intensity increased by six times with the full width at half maximum (FWHM) decreasing. In addition, a smaller angle shift of (008) peak position indicated the lattice constant became larger.

The lattice difference will result in the residual stress in the film. The calculation of the film stress is based on the biaxial strain model [22]. The strain along the c-axis ϵ_{zz} can be estimated by the relation:

$$\epsilon_{zz} = \frac{C_{film} - C_{bulk}}{C_{bulk}} \quad (1)$$

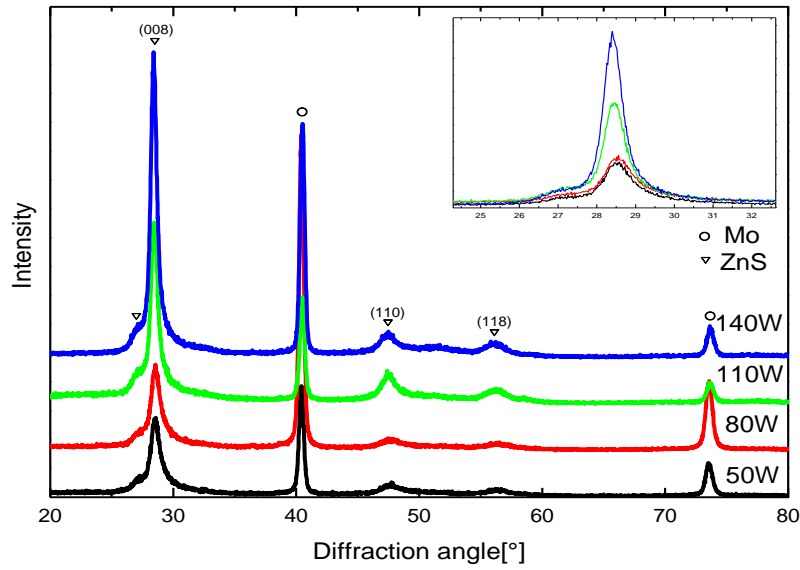


Fig.2. XRD patterns of ZnS films at different sputtering power

Table 2. Microstructure parameters of ZnS films at different sputtering power

Sputtering power [W]	2θ [°]	Intensity	FWHM	Lattice a_0 [Å]	Residual stresses [GPa]
bulk	28.602	—	—	3.1183	0
50	28.579	3908.33	0.666	3.1208	-0.1866
80	28.559	7508.33	0.633	3.1229	-0.3430
110	28.460	15833.3	0.574	3.1336	-1.1422
140	28.400	26575.0	0.525	3.1400	-1.6201

Being c_{bulk} the strain-free lattice constant of bulk ZnS (3.1183 Å) and c_{film} the lattice constant of ZnS films measured by XRD. Further, the biaxial film stress σ is related to the measured c-axis strain by the relation:

$$\sigma_{film} = \frac{2c_{13}^2 - c_{33}(c_{11} + c_{12})}{2c_{13}} \cdot \epsilon_{zz} \quad (2)$$

For the elastic constants c_{ij} , the data of single crystalline ZnS have been used: $c_{11}=208.8$, $c_{33}=213.8$, $c_{12}=119.7$, $c_{13}=104.2$ GPa. [21] The residual stresses of all ZnS thin film showed the compressive stress, and increased by an order of magnitude as the power increases from 50W to 140W.

Morphology and structure of CZTS thin Films with different ZnS power

CZTS thin films images with different

ZnS sputtering power before and after annealing were shown in Fig.3. The four precursors before annealing has smooth and dense surface as shown in Fig.3a. During annealing treatment, sample A1 and A4 had obvious cracking and peeling. The poor crystal quality of ZnS at low power resulted in the poor adhesion in A1. The peeling of A4 may be due to the thermal expansion coefficient differency between the substrates and Cu, SnS layers. The interface stress was caused by the structural mismatching of small grain of A1 and large grain of A4. These stresses lead films to poor adhesion, resulting in cracking and shedding [24, 25]. On the contrary, sample A2 and A3 did not crack or fall off, which indicated that sputtering power of ZnS was between 80W and 110W can bring lower stress and better crystal quality of ZnS and CZTS films.

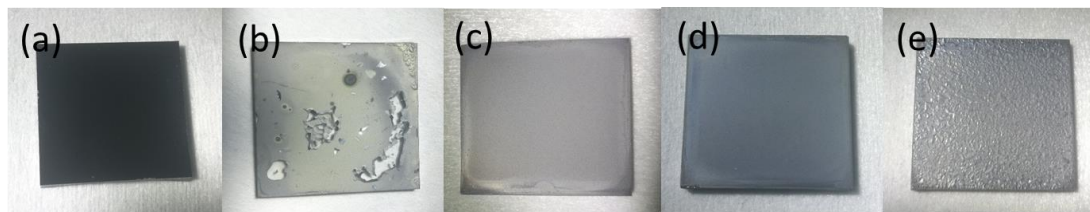


Fig.3 CZTS films images before annealing (a) and after annealing at different ZnS power 50 W (b), 80 W (c), 110 W (d) and 140 W (e)

The surface and section morphology of A2 and A3 samples were analysed by SEM as shown in Fig.4. The surface grains of CZTS film in A2 are larger than that in A3. There were obvious pores and cracks on the surface of A3 (Fig.4c). Fig.4b showed more than $2\mu\text{m}$ grain and dense morphology in

A2. The A3 was non-uniformity with many small grains and holes at the bottom as shown in Fig.4d. The holes will cause the traps and the recombination centers at the CZTS/Mo interface, reducing the photoelectric conversion efficiency of CZTS solar cells [26].

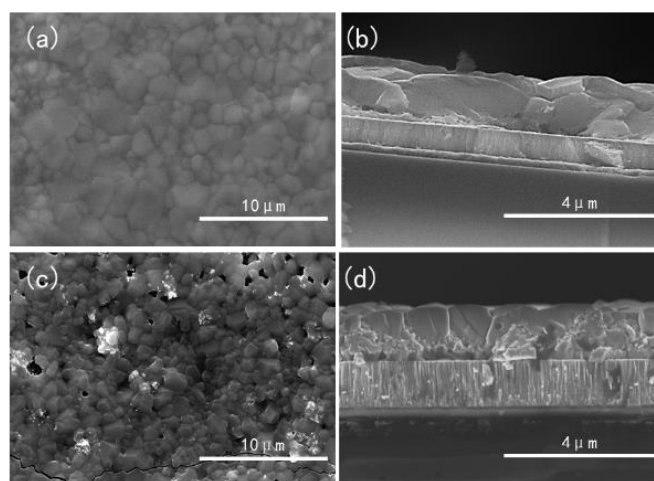


Fig.4. SEM images of surface and cross-section in sample A2 (a, b) and A3 (c, d)

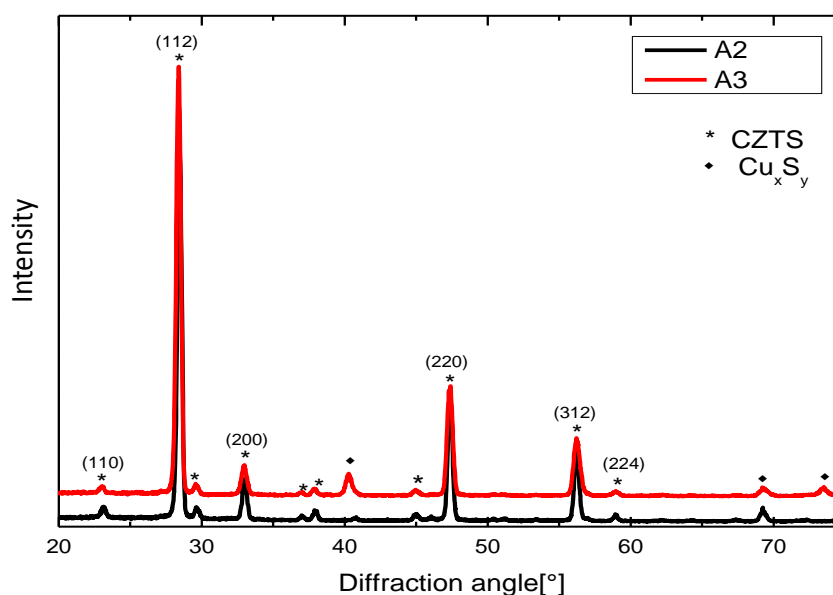


Fig.5. XRD patterns of sample A2 and A3

The reaction mechanism of CZTS films has been studied deeply [27, 28]. Due to the strong migration ability of Cu, it will firstly react with SnS to form a mesophase Cu_2SnS_3 , then react with Zn to form CZTS. Fig.5 was XRD pattern of the sample A2, A3 after annealing. Three main diffraction peaks at $2\theta = 28.53^\circ, 47.33^\circ, 56.18^\circ$ corresponded to the (112), (220), (312) crystal planes, correlating well with ICDD value of kesterite CZTS (ICDD No: 00-026-0575). Compared with A2, A3 had a Cu_xS_y phase ($x=1.9, 3.1; y=1.5, 1.6$), Cu_2SnS_3 , and SnS phases at $2\theta = 40.4^\circ, 69.3^\circ$ and 73.6° . The formation of these secondary phases may be due to the higher sputtering power to obtain a dense ZnS film, which cannot be fully combined with the Cu_2SnS_3 phase to form $\text{Cu}_2\text{ZnSnS}_4$.

Electrical characteristics of CZTS solar cells

The J - V curve of CZTS solar cells fabricated by A2 and A3 thin films were shown in Fig.6. CZTS solar cell fabricated by A2 had better short-circuit current of 14.23 mA/cm^2 and fill factor of 0.41, thus having relatively higher photoelectric conversion efficiency of 3.3%. The open voltage of the two samples was close. The short current of sample A3 was inferior due to the more traps which enhanced the photogenerated carrier nonirradiation recombination at the CZTS/Mo interface as shown in the SEM images in Fig.4. Further, the secondary phases with insufficient react also led to the increase of series resistance [29]. Experiments showed that under fixed conditions, when sputtering power of ZnS was about 80 W, the CZTS solar cell obtained better photoelectric performance.

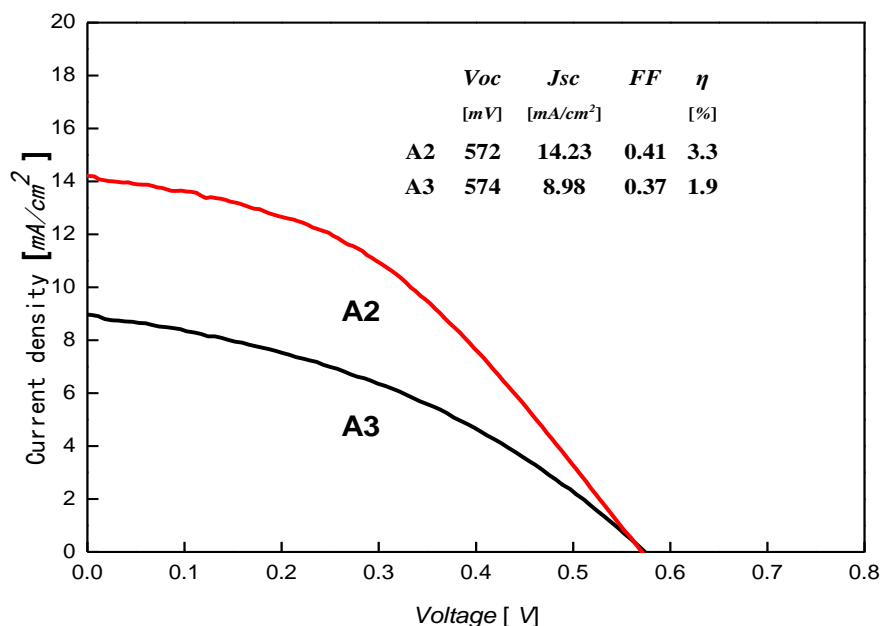


Fig.6. J - V curve and the photoelectrical performance for A2 and A3 solar cells

CONCLUSION

CZTS solar cells were prepared by magnetron sputtering with stacking sequence SLG/Mo/ZnS/SnS/Cu. The adhesion was a crucial influence factor on the quality of the thin films. In this paper, the adhesion of CZTS thin film was optimized by adjusting the sputtering power of ZnS, which is helpful to increase the

yield rate for the low-cost solar cell fabrication and other functional material including ZnS thin films. The film morphology and crystal structure were studied under the sputtering power of ZnS from 50 W to 140 W. The results showed that residual stress would remain in the film which would crack or even fall off when the power lower than 80 W and higher than 110 W. The photoelectric conversion efficiency of CZTS solar cells under the optimal ZnS

power was 3.3%. However, the effects of other factors such as the temperature on the adhesion still need to be explored, and the efficiency of CZTS solar cell will be anticipated to improve.

ACKNOWLEDGEMENTS

This study was supported by the National Natural Science Foundation of China (No. 61774130, 61705192, 61534008).

REFERENCES

- [1] A Walsh, S Chen, S Wei, Kesterite Thin-Film Solar Cells: Advances in Materials Modelling of Cu₂ZnSnS₄. *Advanced Energy Materials* **2**, 400-409 (2012).
- [2] D B Mitzi, O Gunawan, T K Todorov, The path towards a high-performance solution-processed kesterite solar cell. *Solar Energy Materials and Solar Cells* **95**, 1421-1436 (2011).
- [3] A Polizzotti, I L Repins, R Noufi, et al. The state and future prospects of kesterite photovoltaics. *Energy & Environmental Science* **6**, 3171-3182 (2013).
- [4] T K Todorov, J Tang, S Bag, et al. Beyond 11% efficiency: characteristics of state-of-the-art Cu₂ZnSn(SSe)₄ solar cells. *Advanced Energy Materials* **3**, 34-38 (2013).
- [5] G. Raikova, P. Carpanese, Z. Stoyanov; D. et al. Inductance correction in impedance studies of solid oxide fuel cells. *Bulgarian chemical communications* **41**, 199-206 (2009).
- [6] G. Krishnamurthy, M. Sona Bai, Oxidation of lindane in contaminated water under solar irradiation in the presence of photocatalyst and oxidizing agents. *Bulgarian chemical communications* **42**, 161-166 (2010).
- [7] W. Wang, M. T. Winkler, O. Gunawan, Device Characteristics of CZTSSe Thin Film Solar Cells with 12.6% Efficiency. *Adv. Energy Mater.* **4**, 1029-1036 (2014).
- [8] W. Shockley, H. Queisser, Detailed Balance Limit of Efficiency of pn Junction Solar Cells, *J. Appl. Phys.* **32**, 510-519 (1961).
- [9] C. Henry, Limiting efficiencies of ideal single and multiple energy gap terrestrial solar cells, *J. Appl. Phys.* **51**, 4494-4500 (1980)
- [10] H. Araki, et al., Preparation of Cu₂ZnSnS₄ thin films by sulfurization of stacked metallic layers, *Thin Solid Films* **517**, 1457-1460 (2008).
- [11] H. Katagiri, K. Jimbo, M. Tahara, The influence of the composition ratio on CZTS-based thin film solar cells, *Proc. of Mater. Res. Soc. Symp.* **113**, 1165-M04 (2009).
- [12] H Katagiri, K Saitoh, Development of thin film solar cell based on Cu₂ZnSnS₄ thin films. *Solar Energy Materials and Solar Cells* **65**, 141-148 (2001).
- [13] D H Son, D H Kim, S N Park, Growth and Device Characteristics of CZTSSe Thin-Film Solar Cells with 8.03% Efficiency. *Chem. of Mater.* **2**, 5180-5188 (2015).
- [14] J. Li, Y. Zhang, H. Wang, On the growth process of Cu₂ZnSn(SSe)₄ absorber layer by selenizing Cu₂ZnSn(SSe)₄ precursors and its photovoltaic performance, *Sol. Energy Mater. Sol. Cells* **132**, 363-371 (2015).
- [15] Shin S W, Pawar S M, Park C Y, Studies on Cu₂ZnSnS₄ (CZTS) absorber layer using different stacking orders in precursor thin films. *Solar Energy Materials and Solar Cells* **95**, 3202-3206 (2011).
- [16] S Y Shao, Z X Fan, J D Shao, Study of Residual Stress in ZrO₂ Thin Films, *Acta Opt. Sin.* **24**, 437-441 (2004)
- [17] Li J J, Fabrication and research of CZTSSe thin film solar cells by magnetron sputtering and post-selenization process, Ph.D's Thesis, Tianjin, Nankai University, 2016
- [18] A. Le Donne, D. R.A Cavalcoli, M Mereu, Study of the physical properties of ZnS thin films deposited by RF sputtering. *Mater. Sci. in Semi. Processing* **71**, 128-130 (2017).
- [19] G Laukaitis, S Lindroos, S Tamulevicius, Stress and morphological development of CdS and ZnS thin films during the SILAR growth on GaAs, *Appl. Surf. Sci.* **185**, 134-139 (2001).
- [20] S Rodrigues, A G Rolo, A Khodorov, Determination of residual stress in PZT films produced by laser ablation with X-ray diffraction and Raman spectroscopy, *J. Euro. Ceram. Soc.* **30**, 521-525, (2010).
- [21] P F Gui, Z R Zheng, Y J Zhao, Study on the mechanism and measurement of stress of TiO₂ and SiO₂ thin-films, *Acta Phys. Sin.* **55**, 6459 (2006)
- [22] A. Segmuller, M. Murakami, In Analytical Techniques for Thin Films, Springer, 1988.
- [23] E. Mollwo, In Landoldt-Börnstein. Zahlenwerte und Funktionen aus

- Naturwiss. u. Technik. Neue Serie, Springer, 1982.
- [24] J Xie, B Li, Y J Li, Study on ZnS thin films prepared by RF magnetron sputtering technique, *Acta. Phys. Sin.* **59**, 5749-5754 (2010).
- [25] X P Song, X Yang, Study on preparation and properties of ZnS thin films, *Journal of Functional Materials* **11**, 1734-1736 (2006).
- [26] C. Hong, S. Shin, K. Gurav, Comparative study on the annealing types on the properties of Cu₂ZnSnS₄ thin films and their application to solar cells, *Applied Surface Science* **334**, 180-184 (2015).
- [27] A Fairbrother, X Fontané, V Izquierdo, On the formation mechanisms of Zn-rich Cu₂ZnSnS₄ films prepared by sulfurization of metallic stacks. *Solar Energy Materials and Solar Cells* **112**, 97-105 (2013).
- [28] R Schurr, A Hölzing, S Jost, The crystallization of Cu₂ZnSnS₄ thin film solar cell absorbers from co-electroplated CuZnSn precursors. *Thin Solid Films* **517**, 2465-2468 (2009).
- [29] S.M. Pawar, A.V. Moholkar, I.K. Kim, Effect of laser incident energy on the structural, morphological and optical properties of Cu₂ZnSnS₄ (CZTS) thin films, *Current Applied Physics* **10**, 565-56 (2010).

Numerical calculation of the permeability of fibrous porous medium

Zh.K. Akasheva^{1,2*}, B.K. Assilbekov^{1,2}, A.A. Kudaikulov²

¹ *Satbayev University, 22a Satbayev Str., Almaty, Kazakhstan, 050000*

² *LLP "KBTU BIGSoft", 140 Baitursynov Str., of.502, Almaty, Kazakhstan, 0500000*

Single-phase flow through a fibrous porous medium is numerically simulated. The simulation is based on the numerical solution of incompressible Navier-Stokes equations in irregular domains, where the irregular boundary is represented by its level-set function. This numerical method is used to search the Reynolds number below which the fluid flow in porous medium obeys linear Darcy's law for different kinds of porous medium. Also, the calculation results, which obtained using a simple and snap meshes, are compared with analytical solution. The results show that the simple mesh is effective enough and can be used instead of snap mesh in OpenFOAM.

Keywords: permeability, porous medium, mesh size, numerical calculation

* To whom all correspondence should be sent:
zhibek_akasheva@mail.ru

INTRODUCTION

Understanding of fluid flow mechanics through a porous medium is important in the design of many porous materials [1].

There are various approaches for fluid flow calculation in porous medium at pore-scale. In particular, pore network models [2-4] have been widely used to understand multiphase fluid displacement in porous media. Pore-network models are computationally efficient, and they are a viable tool for understanding multiphase flow at the pore scale. However, these methods are based on simplified geometries and physics, which limit their predictive capabilities [5].

Lattice Boltzmann model has been used to simulate flow through the true pore geometry of a porous media, for both single and multiphase flow. Lattice Boltzmann model is used to simulate two-fluid-phase flow at the pore scale [6]. However, the application of this model to multiphase flow is limited by the admissible range of fluid properties due to restricted numerical stability and its high computational cost.

Other approaches that use exact geometry as input to fluid flow numerical simulations in porous media include: volume of fluids [7, 8], smoothed particle hydrodynamics [9], level set [10], and density functional method [11]. Kudaikulov *et al.* predicted theoretically and numerically the permeability of an ordered fibrous porous medium for normal flows [12]. The theoretical prediction of velocity profile allows investigating in detail the fluid flow at the pore-scale or microscale.

In this work, numerical calculations are performed using the OpenFOAM finite volume library. Error analysis on the accuracy of numerical calculations is performed, and also, where possible, there is a comparison with the analytical solution.

MATHEMATICAL FORMULATION OF THE PROBLEM

This paper examines single-phase flow in fibrous porous media where porous material is represented as parallel periodic cylinders of equal radius (Fig.1a). Therefore, the domain with one cylinder in the middle can be considered. The flow direction is perpendicular to the axes of cylinders. Fig.1b shows boundary conditions used for this problem (L is the domain size).

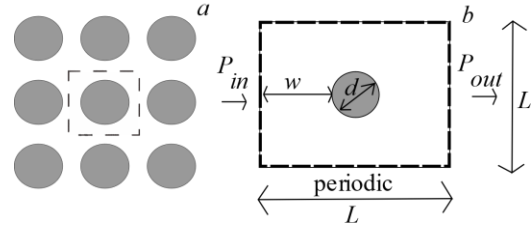


Fig.1. Periodically arranged cylinders

This model is based on numerical solution of the incompressible flow in irregular domains, where irregular boundary is represented by its level-set function [12]. The flow is described using the Navier-Stokes equations:

$$\frac{\partial \vec{u}}{\partial t} + \vec{u} \cdot \nabla \vec{u} = -\nabla P + \frac{1}{Re} \nabla^2 \vec{u} \quad (1)$$

$$\nabla \cdot \vec{u} = 0 \quad (2)$$

where u is the velocity, m/s; P is the pressure, Pa; and Re is the Reynolds number.

Initial condition for the velocity of fluid flow:

$$\vec{u}(0, x, y) = 0 \quad (3)$$

Boundary conditions on the boundaries of the domain (dashed lines on Fig.1b) are:

$$u(x = 0, y) = u(x = L, y) \quad (4)$$

$$u(x, y = 0) = u(x, y = L) \quad (5)$$

$$P(x = 0, y) = P_{in} \quad (6)$$

$$P(x = L, y) = P_{out} \quad (7)$$

$$P(x, y = 0) = P(x, y = L) \quad (8)$$

where P_{in} is the inlet pressure, Pa; P_{out} the outlet pressure, Pa.

No-slip boundary condition is used on the surface of the cylinders:

$$u(t, x, y)|_{d\Omega} = 0 \quad (9)$$

where $d\Omega$ is the surface of the cylinder.

SEARCHING OF REYNOLDS NUMBER FOR LINEAR DARCY'S LAW

Reynolds number below which the fluid flow in porous medium obeys linear Darcy's law in isotropic and anisotropic porous media is found in this section.

Whitaker examined that the linear Darcy's law is valid for Reynolds numbers $Re \ll 1$ using the method of volume averaging [13]. To investigate this condition, it is sufficient to calculate the permeability in linear Darcy's law, which is written as following for single-phase flow:

$$U = \frac{K P_{in} - P_{out}}{\mu L} \quad (10)$$

where K is the absolute permeability, m^2 ; μ is the dynamic viscosity, Pa*s; and U the is volume-averaged velocity:

$$U = \frac{1}{V} \int_V u dV \quad (11)$$

where V is the volume, m^3 .

In isotropic medium, all cylinders in the model are located at the same distance from each other and the coordinates of one cylinder are $x_c=0.5$ and $y_c=0.5$ and have a diameter of $d=0.4$. In anisotropic medium, cylinder C in the model is shifted relative to other cylinders (y_c has a different values) as shown in Fig.2. For this case, we move the location of the cylinder (y_c coordinate) and study the relation between the Reynolds number and permeability.

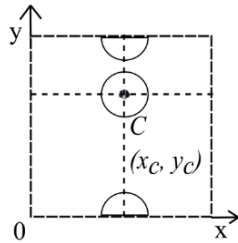


Fig.2. Anisotropic porous medium

Tabs.1-3 present the results of numerical calculation (v^{-1} (inverse kinematic viscosity), U , Re and K (absolute permeability)) for anisotropic porous medium for cylinders with $d=0.2$ and locations of middle cylinder $y_c=0.5, 0.6$ and 0.7 , respectively.

Table 1. Calculation results for $d=0.2$ and $y_c=0.5$

v^{-1}, m^2s	U, ms^{-1}	Re	K, m^2
0.01	$1.57*10^{-4}$	$3.14*10^{-7}$	$1.57*10^{-2}$
0.1	$1.57*10^{-3}$	$3.14*10^{-5}$	$1.57*10^{-2}$
1	$1.57*10^{-2}$	$3.14*10^{-3}$	$1.57*10^{-2}$
10	$1.57*10^{-1}$	$3.13*10^{-1}$	$1.57*10^{-2}$
100	$8.36*10^{-1}$	$1.67*10^0$	$8.36*10^{-3}$

Table 2. Calculation results for $d=0.2$ and $y_c=0.6$

v^{-1}, m^2s	U, ms^{-1}	Re	K, m^2
0.01	$1.82*10^{-4}$	$3.63*10^{-7}$	$1.82*10^{-2}$
0.1	$1.82*10^{-3}$	$3.63*10^{-5}$	$1.82*10^{-2}$

1	$1.82*10^{-2}$	$3.63*10^{-3}$	$1.82*10^{-2}$
10	$1.81*10^{-1}$	$3.62*10^{-1}$	$1.81*10^{-2}$
100	$8.48*10^{-1}$	$1.70*10^0$	$8.48*10^{-3}$

Table 3. Calculation results for $d=0.2$ and $y_c=0.7$

v^{-1}, m^2s	U, ms^{-1}	Re	K, m^2
0.01	$2.57*10^{-4}$	$2.57*10^{-7}$	$2.57*10^{-2}$
0.1	$2.57*10^{-3}$	$2.57*10^{-5}$	$2.57*10^{-2}$
1	$2.57*10^{-2}$	$2.57*10^{-3}$	$2.57*10^{-2}$
10	$2.55*10^{-1}$	$2.55*10^{-1}$	$2.55*10^{-2}$
100	$8.54*10^{-1}$	$8.54*10^0$	$8.54*10^{-3}$

Fig.3 demonstrates the $K-Re$ relationships for the anisotropic porous medium (cylinders with $d=0.2$ and locations of middle cylinder $y_c=0.5, 0.6$ and 0.7 , respectively).

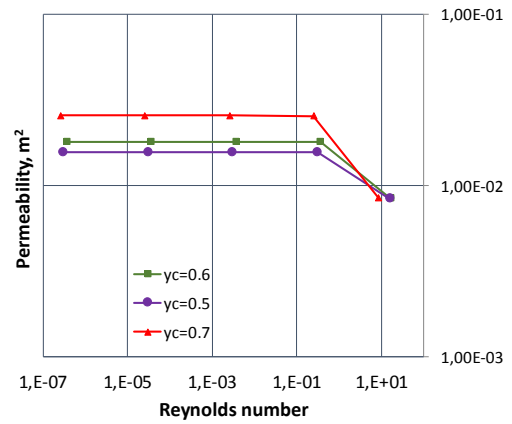


Fig.3. The $K-Re$ for $d=0.2$ and $y_c=0.5, 0.6$ and 0.7 , respectively

Fig.4 shows streamlines for the anisotropic porous medium (cylinders with $d=0.2$ and locations of middle cylinder $y_c=0.5, 0.6$ and 0.7 , respectively) for kinematic viscosities $0.01 m^2/s$ and $0.1 m^2/s$.

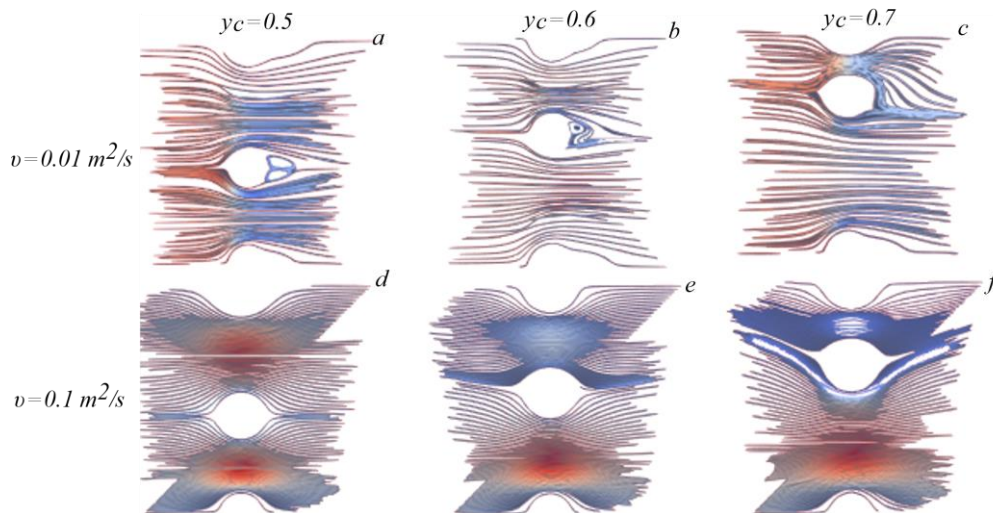


Fig.4. Streamlines for $d=0.2$ and $y_c=0.5, 0.6$ and 0.7 for $v=0.01 m^2/s$ and $v=0.1 m^2/s$ as indicated

From the numerical results, it can be seen that at lower values of Reynolds number, when vorticity does not occur, the linear Darcy's law is fulfilled. It is known that vorticity occurs at high values of Reynolds number [14] and appear inactive zones, therefore the permeability of porous medium depends not only on the geometry of porous medium, but also on the fluid flow properties (see Fig.4).

COMPARISON OF SIMPLE AND SNAP MESH

Results of numerical calculation using different computational meshes (simple and snap) are compared and affection of geometric inaccuracy on the results is studied in this section.

The simple structured mesh in the OpenFOAM is created using BlockMesh utility, which creates parametric meshes with grading and curved edges. The principle behind BlockMesh is to decompose the domain geometry into a set of 1 or more three dimensional, hexahedral blocks. Edges of the blocks can be straight lines, arcs or splines. Each block of the geometry is defined by 8 vertices, one at each corner of a hexahedron [15].

The snap mesh is created using SnappyHexMesh utility, which is a mesh generator that takes an already existing mesh (usually created with BlockMesh) and chisels it into the required mesh. SnappyHexMesh generates 3D meshes containing hexahedra and split-hexahedra automatically from triangulated surface geometries, or tri-surfaces. The mesh approximately conforms to the surface by iteratively refining a starting mesh and morphing the resulting split-hex mesh to the surface [16]. Fig.5a shows a simple mesh, Fig.5b shows a snap mesh in OpenFOAM.

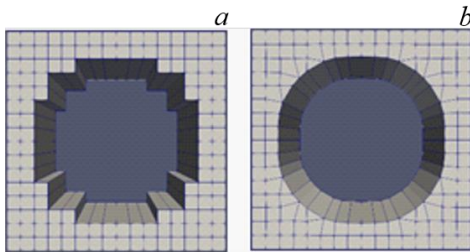


Fig.5. Simple (a) and snap (b) meshes

NUMERICAL RESULTS DISCUSSION

The optimal mesh size selection was studied in this section in order to achieve reliable calculation results while using the computational resources effectively. On one extreme, a rough mesh produces inaccurate results and on other hand, a too high-resolution mesh requires a large memory and

high computational time. Therefore, mesh adaptation methods and an optimal choice of mesh resolution are necessary. Main parameters for optimal size selection are the diameter of cylinder d and parameter w (see Fig.1b).

$$w = \frac{L-d}{2} \quad (12)$$

The accuracy of cylinder's surface depends on the mesh size. Therefore, the mesh resolution should be correlated with d and w . For our case the optimum mesh resolution was found by calculating the relative error of each mesh size relative d and w .

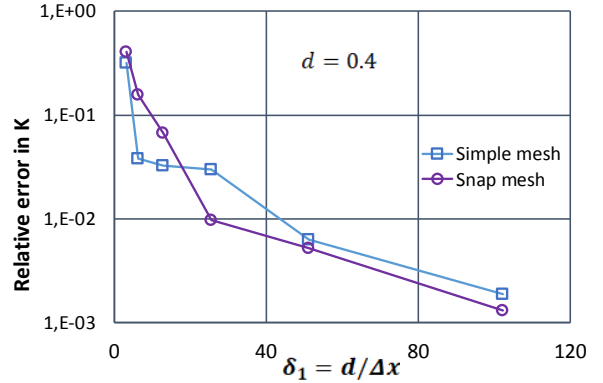


Fig.6. Relative error of average velocity for $d=0.4$ (simple and snap meshes)

The following formulas are used to calculate the relative errors of calculated permeability using simple and snap meshes:

$$RE = \frac{K_N - K_T}{K_T} \times 100\% \quad (13)$$

$$RE_1 = \frac{K_{simple_{n \times n}} - K_{simple_{512 \times 512}}}{K_{simple_{512 \times 512}}} \times 100\% \quad (14)$$

$$RE_2 = \frac{K_{snap_{n \times n}} - K_{snap_{512 \times 512}}}{K_{snap_{512 \times 512}}} \times 100\% \quad (15)$$

where K_N is the numerical value of permeability, K_T is the theoretical value of permeability, K_{simple} is the permeability using simple mesh, K_{snap} is the permeability using snap mesh, n is the number of nodes along the x and y axes, respectively.

The calculation results for $d=0.4$ for simple and snap meshes are given on Fig.6 and Tab.4.

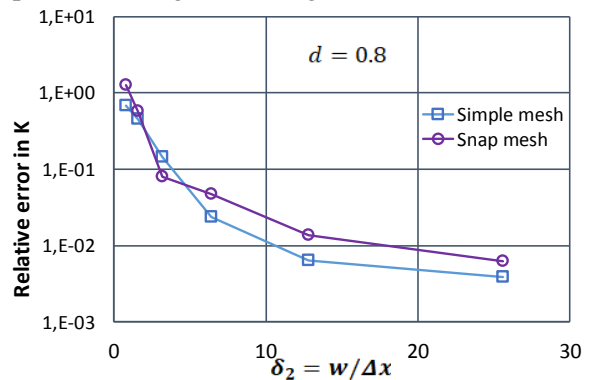


Fig.7. Relative error of average velocity for $d=0.8$ (simple and snap meshes)

The calculation results for $d=0.8$ for simple and snap meshes are given on Fig.7 and Tab.5.

Note that δ_1 is the ratio between the diameter of cylinder and mesh size ($\delta_1=d/\Delta x$) and δ_2 is the ratio between the parameter w and mesh size ($\delta_2=w/\Delta x$).

Table 4. Results for $d=0.4$ using simple and snap meshes

Mesh	δ_1	δ_2	K_{simple}, m^2	RE_1 of K_{simple}	K_{snap}, m^2	RE_2 of K_{snap}
8x8	6.4	0.8	$3.31 \cdot 10^{-3}$	$6.78 \cdot 10^{-1}$	$4.18 \cdot 10^{-5}$	1.27
16x16	12.8	1.6	$2.65 \cdot 10^{-3}$	$4.52 \cdot 10^{-1}$	$2.90 \cdot 10^{-5}$	$5.79 \cdot 10^{-1}$
32x32	25.6	3.2	$1.56 \cdot 10^{-3}$	$1.43 \cdot 10^{-1}$	$1.98 \cdot 10^{-5}$	$7.87 \cdot 10^{-2}$
64x64	51.2	6.4	$1.78 \cdot 10^{-3}$	$2.35 \cdot 10^{-2}$	$1.92 \cdot 10^{-5}$	$4.67 \cdot 10^{-2}$
128x128	102.4	12.8	$1.84 \cdot 10^{-3}$	$6.39 \cdot 10^{-3}$	$1.86 \cdot 10^{-5}$	$1.37 \cdot 10^{-2}$
256x256	204.8	25.6	$1.83 \cdot 10^{-3}$	$3.86 \cdot 10^{-3}$	$1.85 \cdot 10^{-5}$	$6.16 \cdot 10^{-3}$
512x512	409.6	51.2	$1.82 \cdot 10^{-3}$	0	$1.84 \cdot 10^{-5}$	0

Table 5. Results for $d=0.8$ using simple and snap meshes

Mesh	δ_1	δ_2	K_{simple}, m^2	RE_1 of K_{simple}	K_{snap}, m^2	RE_2 of K_{snap}
8x8	3.2	2.4	$2.29 \cdot 10^{-2}$	$3.18 \cdot 10^{-1}$	$4.71 \cdot 10^{-2}$	$4.04 \cdot 10^{-1}$
16x16	6.4	4.8	$3.48 \cdot 10^{-2}$	$3.82 \cdot 10^{-2}$	$3.88 \cdot 10^{-2}$	$1.56 \cdot 10^{-1}$
32x32	12.8	9.6	$3.47 \cdot 10^{-2}$	$3.27 \cdot 10^{-2}$	$3.58 \cdot 10^{-2}$	$6.71 \cdot 10^{-2}$
64x64	25.6	19.2	$3.26 \cdot 10^{-2}$	$2.95 \cdot 10^{-2}$	$3.39 \cdot 10^{-2}$	$9.59 \cdot 10^{-3}$
128x128	51.2	38.4	$3.33 \cdot 10^{-2}$	$6.25 \cdot 10^{-3}$	$3.37 \cdot 10^{-2}$	$5.18 \cdot 10^{-3}$
256x256	102.4	76.8	$3.35 \cdot 10^{-2}$	$1.86 \cdot 10^{-3}$	$3.36 \cdot 10^{-2}$	$1.30 \cdot 10^{-3}$
512x512	204.8	153.6	$3.36 \cdot 10^{-2}$	0	$3.36 \cdot 10^{-2}$	0

COMPARISON OF NUMERICAL RESULTS WITH ANALYTICAL SOLUTION

The comparison of numerical results with analytical solution [17] is provided in this section.

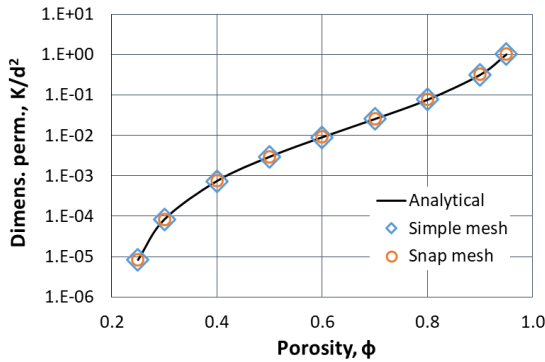


Fig.8. Comparison of numerical and analytical permeabilities

Tab.6 and Fig.8 present numerical results for simple and snap meshes for different radii of the cylinder (R), porosity (ϕ) and numerical predictions of dimensionless permeability using simple mesh (K_{simple}/R^2), snap mesh (K_{snap}/R^2) and dimensionless analytic permeability ($K_{analytic}/R^2$). Also, Tab.6 shows the comparison of relative errors of calculated permeability using simple and snap meshes, which are compared against the analytical values from [17].

It can be seen that the results are almost the same (relative error between the meshes is less than 1%); therefore simple mesh can be used for calculation in OpenFOAM to save the computation time and power.

Table 6. Numerical results obtained using simple and snap meshes

Mesh	R, m	ϕ	K_{simple}/R^2	K_{snap}/R^2	$K_{analytic}/R^2$	RE of K_{simple}	RE of K_{snap}
128x128	0.1261	0.95	$1.02 \cdot 10^0$	$1.31 \cdot 10^0$	$1.01 \cdot 10^0$	$1.17 \cdot 10^{-2}$	$2.09 \cdot 10^{-2}$
128x128	0.1784	0.90	$3.19 \cdot 10^{-1}$	$3.23 \cdot 10^{-1}$	$3.32 \cdot 10^{-1}$	$7.34 \cdot 10^{-3}$	$2.13 \cdot 10^{-2}$
128x128	0.2523	0.80	$7.73 \cdot 10^{-2}$	$7.79 \cdot 10^{-2}$	$7.62 \cdot 10^{-2}$	$1.42 \cdot 10^{-2}$	$2.21 \cdot 10^{-2}$
128x128	0.3090	0.70	$2.55 \cdot 10^{-2}$	$2.60 \cdot 10^{-2}$	$2.54 \cdot 10^{-2}$	$2.69 \cdot 10^{-3}$	$2.13 \cdot 10^{-2}$
128x128	0.3568	0.60	$8.91 \cdot 10^{-3}$	$9.15 \cdot 10^{-3}$	$9.01 \cdot 10^{-3}$	$1.13 \cdot 10^{-2}$	$1.57 \cdot 10^{-2}$
256x256	0.3989	0.50	$2.95 \cdot 10^{-3}$	$2.98 \cdot 10^{-3}$	$2.95 \cdot 10^{-3}$	$1.14 \cdot 10^{-3}$	$9.05 \cdot 10^{-3}$
256x256	0.4370	0.40	$7.33 \cdot 10^{-4}$	$7.51 \cdot 10^{-4}$	$7.42 \cdot 10^{-4}$	$1.32 \cdot 10^{-2}$	$1.14 \cdot 10^{-2}$
512x512	0.4720	0.30	$8.15 \cdot 10^{-5}$	$8.43 \cdot 10^{-5}$	$8.30 \cdot 10^{-5}$	$1.77 \cdot 10^{-2}$	$1.58 \cdot 10^{-2}$
1024x1024	0.4886	0.25	$8.22 \cdot 10^{-6}$	$8.40 \cdot 10^{-6}$	$8.29 \cdot 10^{-6}$	$8.45 \cdot 10^{-3}$	$1.36 \cdot 10^{-2}$

CONCLUSIONS

The permeability of fibrous porous medium is numerically calculated in this paper. The optimal mesh size is selected depending on the parameter w and the diameter of the cylinder d . The Reynolds number below which the flow obeys the linear Darcy's law is investigated for isotropic and anisotropic porous media.

The computational results show that the simple mesh is effective enough and can be used instead of snap mesh in OpenFOAM. From the Tab.6 it can be concluded that the correlation between the diameter of cylinder and mesh is effective enough for $\delta_1=51.2$ and $\delta_2=38.4$ and can be applied for calculation of more complex porous medium. Numerical calculation results are in excellent agreement with analytical solution [17] for the flow in porous medium.

ACKNOWLEDGEMENTS

This work has been supported financially as part of the sub-project APP-JRG-17/0448F "Development and implementation of an integrated software product for a comprehensive solution of production stimulation problems on hydrocarbon fields" funded under the project "Stimulation of Productive Innovations". We thank PhD Ali Qaseminejad Raeini for his insightful comments on this work.

REFERENCES

- [1] M.J. Blunt, *Multiphase flow in permeable media. A pore-scale perspective*. Cambridge Univ. Press, 2017.
- [2] M.J. Blunt, P. King, *Transp. Porous Media*, **6**(4), 407 (1991).
- [3] K. E. Thompson, *AIChE Journal* **48** (7), 1369 (2002).
- [4] M. Piri, M.J. Blunt, *Physical Review E* **71** (2), (2005).
- [5] M.J. Blunt, *Curr. Opin. Colloid Interface Sci.* **6** (3), 197 (2001).
- [6] C. Pan, M. Hilpert, C.T. Miller, *Water Resour. Res.* **40** (1), (2004).
- [7] A.Q. Raeini, M.J. Blunt, B. Bijeljic, *J. Comput. Phys.*, **231**, 5653 (2012).
- [8] H. Huang, P. Meakin, M.B. Liu, *Water Resour. Res.* **41** (12), (2005).
- [9] A.M. Tartakovsky, N. Trask, K. Pan, B. Jones, *Computat. Geosci.* **20** (4), 1 (2015).
- [10] M. Sussman, P. Smereka, S. Osher, *J. Comput. Phys.* **114** (1), 146 (1994).
- [11] O. Dinariev, N. Evseev, *Computat. Geosci.* **20** (4), 1 (2015).

- [12] A. Kudaikulov, C. Josserand, A. Kaltayev, *Mathematical Modeling of Technological Processes, Series of Communications in Computer and Information Science, Book Series.* - Springer **549**, **85** (2015).
- [13] S. Whitaker, *Transp. Porous Media* **1**, 3 (1986).
- [14] G.K. Batchelor, *An introduction to fluid dynamics*, Cambridge Univ. Press, 2000.
- [15] <https://cfd.direct/openfoam/user-guide/v6-blockmesh/>
- [16] <https://cfd.direct/openfoam/user-guide/v6-snappyhexmesh/>
- [17] A.S. Sangani, A. Acrivos, *Int.J.Multiphase flow*, **8**(3), 193 (1982).

BULGARIAN CHEMICAL COMMUNICATIONS

Instructions about Preparation of Manuscripts

General remarks: Manuscripts are submitted in English by e-mail or by mail (in duplicate). The text must be typed double-spaced, on A4 format paper using Times New Roman font size 12, normal character spacing. The manuscript should not exceed 15 pages (about 3500 words), including photographs, tables, drawings, formulae, etc. Authors are requested to use margins of 3 cm on all sides. For mail submission hard copies, made by a clearly legible duplication process, are requested. Manuscripts should be subdivided into labelled sections, e.g. **Introduction, Experimental, Results and Discussion**, etc.

The title page comprises headline, author's names and affiliations, abstract and key words.

Attention is drawn to the following:

a) **The title** of the manuscript should reflect concisely the purpose and findings of the work. Abbreviations, symbols, chemical formulas, references and footnotes should be avoided. If indispensable, abbreviations and formulas should be given in parentheses immediately after the respective full form.

b) **The author's** first and middle name initials, and family name in full should be given, followed by the address (or addresses) of the contributing laboratory (laboratories). **The affiliation** of the author(s) should be listed in detail (no abbreviations!). The author to whom correspondence and/or inquiries should be sent should be indicated by asterisk (*).

The abstract should be self-explanatory and intelligible without any references to the text and containing not more than 250 words. It should be followed by key words (not more than six).

References should be numbered sequentially in the order, in which they are cited in the text. The numbers in the text should be enclosed in brackets [2], [5, 6], [9–12], etc., set on the text line. References, typed with double spacing, are to be listed in numerical order on a separate sheet. All references are to be given in Latin letters. The names of the authors are given without inversion. Titles of journals must be abbreviated according to Chemical Abstracts and given in italics, the volume is typed in bold, the initial page is given and the year in parentheses. Attention is drawn to the following conventions:

a) The names of all authors of a certain publications should be given. The use of “*et al.*” in

the list of references is not acceptable.

b) Only the initials of the first and middle names should be given.

In the manuscripts, the reference to author(s) of cited works should be made without giving initials, e.g. “Bush and Smith [7] pioneered...”. If the reference carries the names of three or more authors it should be quoted as “Bush *et al.* [7]”, if Bush is the first author, or as “Bush and co-workers [7]”, if Bush is the senior author.

Footnotes should be reduced to a minimum. Each footnote should be typed double-spaced at the bottom of the page, on which its subject is first mentioned.

Tables are numbered with Arabic numerals on the left-hand top. Each table should be referred to in the text. Column headings should be as short as possible but they must define units unambiguously. The units are to be separated from the preceding symbols by a comma or brackets.

Note: The following format should be used when figures, equations, etc. are referred to the text (followed by the respective numbers): Fig., Eqns., Table, Scheme.

Schemes and figures. Each manuscript (hard copy) should contain or be accompanied by the respective illustrative material as well as by the respective figure captions in a separate file (sheet). As far as presentation of units is concerned, SI units are to be used. However, some non-SI units are also acceptable, such as °C, ml, l, etc.

The author(s) name(s), the title of the manuscript, the number of drawings, photographs, diagrams, etc., should be written in black pencil on the back of the illustrative material (hard copies) in accordance with the list enclosed. Avoid using more than 6 (12 for reviews, respectively) figures in the manuscript. Since most of the illustrative materials are to be presented as 8-cm wide pictures, attention should be paid that all axis titles, numerals, legend(s) and texts are legible.

The authors are asked to submit **the final text** (after the manuscript has been accepted for publication) in electronic form either by e-mail or mail on a 3.5” diskette (CD) using a PC Word-processor. The main text, list of references, tables and figure captions should be saved in separate files (as *.rtf or *.doc) with clearly identifiable file names. It is essential that the name and version of

the word-processing program and the format of the text files is clearly indicated. It is recommended that the pictures are presented in *.tif, *.jpg, *.cdr or *.bmp format, the equations are written using "Equation Editor" and chemical reaction schemes are written using ISIS Draw or ChemDraw programme.

The authors are required to submit the final text with a list of three individuals and their e-mail addresses that can be considered by the Editors as potential reviewers. Please, note that the reviewers should be outside the authors' own institution or organization. The Editorial Board of the journal is not obliged to accept these proposals.

EXAMPLES FOR PRESENTATION OF REFERENCES

REFERENCES

1. D. S. Newsome, *Catal. Rev.–Sci. Eng.*, **21**, 275 (1980).
2. C.-H. Lin, C.-Y. Hsu, *J. Chem. Soc. Chem. Commun.*, 1479 (1992).
3. R. G. Parr, W. Yang, *Density Functional Theory of Atoms and Molecules*, Oxford Univ. Press, New York, 1989.
4. V. Ponec, G. C. Bond, *Catalysis by Metals and Alloys* (Stud. Surf. Sci. Catal., vol. 95), Elsevier, Amsterdam, 1995.
5. G. Kadinov, S. Todorova, A. Palazov, in: *New Frontiers in Catalysis* (Proc. 10th Int. Congr. Catal., Budapest, 1992), L. Guzzi, F. Solymosi, P. Tetenyi (eds.), Akademiai Kiado, Budapest, 1993, Part C, p. 2817.
6. G. L. C. Maire, F. Garin, in: *Catalysis. Science and Technology*, J. R. Anderson, M. Boudart (eds), vol. 6, Springer-Verlag, Berlin, 1984, p. 161.
7. D. Pocknell, *GB Patent 2 207 355* (1949).
8. G. Angelov, PhD Thesis, UCTM, Sofia, 2001.
9. JCPDS International Center for Diffraction Data, Power Diffraction File, Swarthmore, PA, 1991.
10. *CA* **127**, 184 762q (1998).
11. P. Hou, H. Wise, *J. Catal.*, in press.
12. M. Sinev, private communication.
13. <http://www.chemweb.com/alchem/articles/1051611477211.html>.

CONTENTS

A. A. Genbach, K. K. Shokolakov, D. Y. Bondartsev, I. K. Iliev, A. Terziev, Research of specific destruction energy of the porous coatings at power units	5
A. S. Askarova, S. A. Bolegenova, S. A. Bolegenova, R. K. Manatbayev, V. Yu. Maximov, Zh. K. Shortanbayeva, A. O. Nugymanova, A. S. Bergaliyeva, 3D computer simulation of heat and mass transfer processes to improve the energy efficiency of combustion chambers.....	11
A. S. Askarova, S. A. Bolegenova, V. Yu. Maximov, S. A. Bolegenova, N. R. Mazhrenova, Zh. K. Shortanbayeva, R. K. Manatbayev, M. R. Mamedova, Numerical simulation of turbulent combustion of pulverized coal flame	19
C. Dulucheanu, T. L. Severin, A. Potorac, L. Irimescu, J. Javorova, Influence of the initial structure on the critical points in solid-state phase transformation of some hypoeutectoid steels	26
Dan Wang, Li Wang, Rui Xu, Xingan Wu, Yunlan Li, Comparison of antiviral activity of realgar and nano-realgar against herpes simplex virus type II (HSV-2) <i>in vitro</i>	34
I. Klinovitskaya, D. Kalygulov, S. Plotnikov, P. Lay, Increasing the efficiency of photovoltaic cells based on Kazakhstan silicon	41
I. V. Khromushin, Yu. V. Yermolaev, N. K. Kasmamytov, T. I. Aksenova, T. Tusseyev, L. A. Stanbay, Radiation modification of $\text{BaCe}_{0.85}\text{Nd}_{0.15}\text{O}_{3-\delta}$	49
J. F. Liu, T. R. Fu, Simulations of the macroscopic energy migration diffusion characteristics in upconversion core-shell nanostructures	55
Jie Guo, Peng Wu, Jun Yuan, Lichun Sun, Qiong Li, Bingzhe Li, Activation and gas sorption performance in Zr-Co-Y getters on Ge substrates	63
Jing Li, Fan Yi, Xudong Zhao, Xiaoman Bai, Ali Badiei, Xiaoli Ma. Thermodynamic analysis of an innovative heat pump using indoor and outdoor air as heat source	69
Mengjiao Zhang, Hongyan Zhou, Siqing Niu, Xi Chen, Yunlan Li, Screening of Antitumor and Hepatoprotective Activity Components from <i>Hedyotis diffusa</i>	77
Siqing Niu, Yunlan Li, Xi Chen, Mengjiao Zhang, Qingshan Li, Comparative study on the quality control of trihydroxybenzophenones compounds	84
T. St. Petrova, D. B. Dzhonova-Atanasova, Simulation of the liquid distribution in the wall zone of a packed column: case study	91
Wang Lu, Jie Guo, Hao Ruiting, A. Aierken, Sun Lichun, Qiong Li, Liu Bin, Gu Kang, Sun Shuaihui, Influence of ZnS Sputtering Power on Film Adhesion and $\text{Cu}_2\text{ZnSnS}_4$ Solar Cells	99
Zh. K. Akasheva, B. K. Assilbekov, A. A. Kudaikulov, Numerical calculation of the permeability of fibrous porous medium	106

